JAAVSO

Volume 51
Number 1
2023

The Journal of the American Association of Variable Star Observers

Visual Photometry: Testing Hypotheses Concerning Bias and Precision

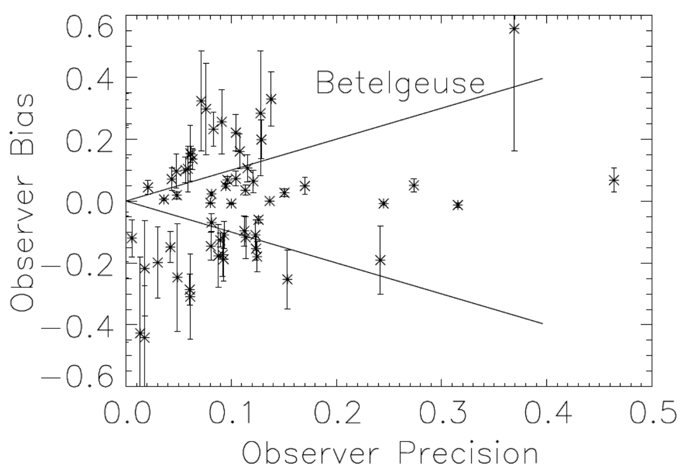

Bias (average of residual around the fitted curve) compared with precision (standard deviation around the average) for the observers of Betelgeuse. The straight lines show where the quantities are equal *in magnitude*.

Also in this issue...

- Photometric Distance to the RR Lyrae Star SW Andromedae Using Period-Luminosity-Metallicity Relationships
- Combined Spectroscopic and Photometric Analysis of Flares in the Dwarf M Star EV Lacertae
- Studies of R CrB Star Pulsation Using ASAS-SN Photometry
- 13 New Light Curves and Updated Mid-Transit Time and Period for Hot Jupiter WASP-104 b with EXOTIC

Complete table of contents inside...

The American Association of Variable Star Observers
185 Alewife Brook Parkway, Suite 410, Cambridge, MA 02138, USA

ISSN 0271-9053 (print)
ISSN 2380-3606 (online)

JAAVSO

The Journal of
The American Association
of Variable Star Observers

Volume 51
Number 1
2023

AAVSO
185 Alewife Brook Parkway,
Suite 410, Cambridge, MA 02138
USA

ISSN 0271-9053 (print)
ISSN 2380-3606 (online)

Publication Schedule

The Journal of the American Association of Variable Star Observers is published twice a year, June 15 (Number 1 of the volume) and December 15 (Number 2 of the volume). The submission window for inclusion in the next issue of JAAVSO closes six weeks before the publication date. A manuscript will be added to the table of contents for an issue when it has been fully accepted for publication upon successful completion of the referee process; these articles will be available online prior to the publication date. An author may not specify in which issue of JAAVSO a manuscript is to be published; accepted manuscripts will be published in the next available issue, except under extraordinary circumstances.

Page Charges

Page charges are waived for Members of the AAVSO. Publication of unsolicited manuscripts in JAAVSO requires a page charge of US $100/page for the final printed manuscript. Page charge waivers may be provided under certain circumstances.

Publication in *JAAVSO*

With the exception of abstracts of papers presented at AAVSO meetings, papers submitted to JAAVSO are peer-reviewed by individuals knowledgeable about the topic being discussed. We cannot guarantee that all submissions to JAAVSO will be published, but we encourage authors of all experience levels and in all fields related to variable star astronomy and the AAVSO to submit manuscripts. We especially encourage students and other mentees of researchers affiliated with the AAVSO to submit results of their completed research.

Subscriptions

Institutions and Libraries may subscribe to JAAVSO as part of the Complete Publications Package or as an individual subscription. Individuals may purchase printed copies of recent JAAVSO issues via Amazon KDP.

Instructions for Submissions

The *Journal of the AAVSO* welcomes papers from all persons concerned with the study of variable stars and topics specifically related to variability. All manuscripts should be written in a style designed to provide clear expositions of the topic. Contributors are encouraged to submit digitized text in MS WORD, LATEX+POSTSCRIPT, or plain-text format. Manuscripts should be submitted through the JAAVSO submission portal (https://www.aavso.org/apps/jaavso/submit/) or may be mailed electronically to journal@aavso.org or submitted by postal mail to JAAVSO, 185 Alewife Brook Parkway, Suite 410, Cambridge, MA 02138, USA.

Manuscripts must be submitted according to the following guidelines, or they will be returned to the author for correction:

Manuscripts must be:
1) original, unpublished material;
2) written in English;
3) accompanied by an abstract of no more than 100 words.
4) not more than 2,500–3,000 words in length (10–12 pages double-spaced).

Figures for publication must:
1) be camera-ready or in a high-contrast, high-resolution, standard digitized image format;
2) have all coordinates labeled with division marks on all four sides;
3) be accompanied by a caption that clearly explains all symbols and significance, so that the reader can understand the figure without reference to the text.

Maximum published figure space is 4.5" by 7". When submitting original figures, be sure to allow for reduction in size by making all symbols, letters, and division marks sufficiently large.

Photographs and halftone images will be considered for publication if they directly illustrate the text.

Tables should be:
1) provided separate from the main body of the text;
2) numbered sequentially and referred to by Arabic number in the text, e.g., Table 1.

References:
1) References should relate directly to the text.
2) References should be keyed into the text with the author's last name and the year of publication, e.g., (Smith 1974; Jones 1974) or Smith (1974) and Jones (1974).
3) In the case of three or more joint authors, the text reference should be written as follows: (Smith et al. 1976).
4) All references must be listed at the end of the text in alphabetical order by the author's last name and the year of publication, according to the following format: Brown, J., and Green, E. B. 1974, *Astrophys. J.*, **200**, 765.
   Thomas, K. 1982, *Phys. Rep.*, **33**, 96.
5) Abbreviations used in references should be based on recent issues of JAAVSO or the listing provided at the beginning of *Astronomy and Astrophysics Abstracts* (Springer-Verlag).

Miscellaneous:
1) Equations should be written on a separate line and given a sequential Arabic number in parentheses near the right-hand margin. Equations should be referred to in the text as, e.g., equation (1).
2) Magnitude will be assumed to be visual unless otherwise specified.
3) Manuscripts may be submitted to referees for review without obligation of publication.

Online Access

Articles published in JAAVSO, and information for authors and referees may be found online at: https://www.aavso.org/apps/jaavso/

The Journal of the American Association of Variable Star Observers
Volume 51, Number 1, 2023

Table of Contents continued on next page

Variable Star Data

Editorial

Tools for Writers

Nancy D. Morrison
Editor-in-Chief, Journal of the AAVSO

Department of Physics and Astronomy and Ritter Observatory, MS 113, The University of Toledo, 2801 W. Bancroft Street, Toledo OH 43606; jaavso.editor@aavso.org

Received June 10, 2023

1. Introduction

Communication of research results is an essential part of science, and publication is an essential part of communication. For readers, students, and historians of science, the sequence of ideas from one paper to the next traces the evolution of scientific thought. Writing helps sharpen one's scientific reasoning. For all these reasons, writing is an essential skill for a scientist.

It is commonly said that the introduction is the hardest part of a paper to write. For example, the website Grammarly has extensive dicussion on this topic.[1] Although its advice is aimed at academic theses, which tend to be more expansive than journal articles, the main ideas are also applicable here.

The introduction to a paper is typically the first section, and it often consists of more than one paragraph. It typically has three parts.

1. Importance of the problem; why the reader and astronomers in general should care.

2. Survey of relevant previous work, with citations to specific papers. This part is essential to place your work in context.

3. The aim/thesis/main point of the paper in one or a few sentences.

If the paper is long and complicated or if its organization is unconventional, it is customary for the last paragraph of the introduction to provide a brief outline of what material appears in each section.

A good introduction doesn't always conform strictly to this model. For example, Maravelias and Kraus (2022) did a great job of stating the importance of their problem and providing a literature review along the way.

In this essay, the next section discusses part 2 above, and the third section part 1.

2. Writing the brief literature summary

If your expertise is still in development, you can also draw inspiration from (not copy!) text written by other astronomers on the topic. Be sure to use your own words. It is sometimes possible to express other authors' ideas better than they did.

There is no need to go back to the dawn of the subject area. A good background source may be one that is a few years old and cited by several papers related to yours. In the review, include work you used to guide your research, but also provide context with parallel, independent results by others. You should not give a false impression of being the only game in town (Hughes, Benz, and Prato 2023). Deciding what to include takes judgment, and experience helps. As with other writing, it's better to include too much material than too little, because it's easier to remove material from a manuscript than to add. Once your submitted article reaches the peer review stage, an expert referee can help.

Don't just list references. Limit yourself to the most important ones, and briefly summarize each one's contribution to the field. Cadmus (2015) provides a nice literature summary in the section named "Background."

A helpful tool for searching the literature is the NASA Astrophysics Data System (ADS).[2] For any given paper, it links to both the papers cited by that paper and also those that cite the paper. Perhaps you have a reference paper for background, but it's a few years old. To find more recent work, use the "Paper Form" option in ADS to bring up the reference paper and click "citations" to find papers that cited the reference paper. If you want to look for review articles, you can search for the journal *Annual Reviews of Astronomy and Astrophysics* (bibliographic code ARA&A).

For more general searches, use the "Modern Form" option. You can search for papers by a given author, about a given star, or about a given topic/keyword in either the abstract or the full text. By changing my search options, I have at times found completely new information. I think of it as trying to see through a dense forest. Changing your line of sight will give you new views through the trees.

You shouldn't cite papers that you haven't at least skimmed. Therefore, following this advice involves reading a lot of papers. By so doing, you will acquire the familiarity with the topic that will give your introduction an expert feel. Don't worry if you don't understand every technical detail in every paper. With time, you'll acquire the skill of gleaning the information that you need and can understand, while leaving the more difficult

[1] https://www.grammarly.com/blog/how-to-write-an-introduction/

[2] https://ui.adsabs.harvard.edu

information for later. Not least, one of the best ways to learn to write is to read many papers.

3. Writing the first paragraph

Some writers have difficulty producing the first paragraph of an article. A useful starting point for such people—as for those whose native language is not English—may be a large language model such as ChatGPT.[3] Much is being written, in many contexts, about large language models. Recently, American Astronomical Society Editor-in-Chief Ethan Vishniac (2023) has written a thoughtful, skeptical editorial about the applicability of ChatGPT to writing scientific papers.

I have only limited experience with ChatGPT. From a variety of reading, I understand that it is not trustworthy regarding factual material, because it is designed for mimicking patterns in existing texts, which may not be accurate. It is known to output false information, or to "hallucinate." Another recurring theme is that it cannot be trusted to do literature searches.

It may be useful for producing "boilerplate" prose for an introductory paragraph. I tried it out with the question, "Why are RR Lyrae stars important in astronomy?" and received a chatty but nicely written, fairly sensible paragraph about period-luminosity relations, metallicity dependences, the cosmic distance scale, and so forth. I did not check whether this output was a verbatim copy of something on the Internet, nor did I try the prompt a second time to see how the output changed—tests that might have been instructive.

To my follow-up question about who has done research on RR Lyrae stars in the past ten years, it returned mostly nonsense. I have difficulty envisioning how this software could be helpful in writing a methods/observations section, an analysis section, a discussion section, or a conclusions section.

I also tried to use it to improve a paragraph written by a former student, with mixed results. The grammar and phrasing were improved, but the logically poor sentence order was unchanged.

If you want to try using ChatGPT, or another large language model, you should do the following:

• Rigorously fact check the output.

• Restyle the output so that it harmonizes with your own writing style. Remember, I suggested using ChatGPT as a starting point. If your own grammar needs improvement, you might consider using the grammar checker on Grammarly, the website referred to above.

• In the acknowledgements section of the paper, describe how you used the large language model, as you would any other advanced software, and how you adapted the output.

Adventurous folks may want to try an open-source application such as LLaMA, which is advertised as a ChatGPT equivalent that can run on a high-end laptop.[4] The fact that it is open source means that a specialist can decipher how the algorithm was trained and get insight into its workings.

Readers are encouraged to email me their thoughts about use of large language models. Best wishes for your writing!

References

Cadmus, R. R., Jr. 2015, *J. Amer. Assoc. Var. Star Obs.*, **43**, 3.

Hughes, A. M., Bentz, M., and Prato, L. 2023, "Citation Ethics in Publishing," American Astronomical Society, Washington, DC.[5]

Maravelias, G., and Kraus, M. 2022, *J. Amer. Assoc. Var. Star Obs.*, **50**, 49.

Vishniac, E. T. 2023, *Bull. Amer. Astron. Soc.*, **55**, 016. (https://doi.org/10.3847/25c2cfeb.c3619710).

[3] https://openai.com

[4] https://arstechnica.com/information-technology/2023/03/you-can-now-run-a-gpt-3-level-ai-model-onyour-laptop-phone-and-raspberry-pi/

[5] https://aas.org/posts/news/2023/06/citation-ethics-publishing

Photometric Distance to the RR Lyrae Star SW Andromedae Using Period-Luminosity-Metallicity Relationships

Talon Dow
Jakob Bergstedt
Emily Payne
Tyce Olaveson
Hayley Kerkman
Lesilie Greer
Stephen McNeil

Brigham Young University-Idaho, Department of Physics, Rexburg, ID 83460; address correspondence to mcneils@byui.edu

Received July 15, 2022; revised March 24, 27, 2023; accepted March 29, 2023

Abstract Cáceres and Catelans' period-luminosity-metallicity equations give us a way to measure the photometric distance to RR Lyrae stars using absolute magnitude equations that rely on the specific photometric filter (V, i, and z), the period, and the metallicity. Over a period of two weeks, 76 images of the RR Lyr Star SW Andromedae were taken in the B, V, i, and z bands. Using Source Extractor Kron (SEK) photometry method, the apparent magnitudes were plotted and converted into periods and amplitudes. Together with previously measured values for the metallicity and interstellar extinction, we calculated a photometric distance to SW Andromedae of 516 ± 14 parsecs to 527 ± 14 depending on the chosen metallicity. This distance is comparable to the parallax distance obtained from GAIA EDR3 data of 510 ± 7 parsecs.

1. Introduction

In the optical passbands RR Lyrae stars are connected to the metallicity by a luminosity-metallicity relationship (Clementini *et al.* 2003; Catelan *et al.* 2004; Marconi *et al.* 2015; Muraveva *et al.* 2018; Garofalo *et al.* 2022), and in the near and mid-infrared passbands by a period-luminosity-metallicity (PLZ) relationship (Catelan *et al.* 2004; Marconi *et al.* 2015; Muraveva *et al.* 2015; Neeley *et al.* 2019). Catelan *et al.* (2004) derived the following relation for the V-band:

$$M_V = 2.288 + 0.822\,\mathrm{LogZ} + 0.108\,(\mathrm{LogZ})^2 \qquad (1)$$

Cáceres and Catelan (2008) published the following PLZ equations in the i and the z bands:

$$M_i = 0.908 - 1.035\,\mathrm{LogP} + 0.220\,\mathrm{LogZ} \qquad (2)$$
$$M_z = 0.839 - 1.295\,\mathrm{LogP} + 0.211\,\mathrm{LogZ}, \qquad (3)$$

with the LogZ in these equations being related to the metallicity by:

$$\mathrm{LogZ} = [\mathrm{M/H}] - 1.765 \qquad (4)$$

$$[\mathrm{M/H}] = [\mathrm{Fe/H}] + \log(0.638 \times 100.3 + 0.362) \qquad (5)$$

This paper examines the light curves for the RR Lyr star SW Andromedae using Bessel B and V filters, and SDSS/PanSTARRS i and z filters. The period and apparent magnitude will then be determined, and a distance calculated using the absolute magnitudes determined by the Cáceres and Catelan equations. This photometric distance will then be compared to the parallax distance found by GAIA EDR3 (Gaia Collaboration *et al.* 2021).

SW And has been studied by both recent surveys, including multicolor photometry (Barcza and Benkő 2014), and in the older uvbyβ photometry system (McNamara and Feltz 1977). However, there have been no papers that have used observed photometric data to determine the photometric distance to SW And using Cáceres and Catelans' equations. The general properties of SW And were obtained from SIMBAD (Wenger *et al.* 2000) and the AAVSO International Variable Star Index (VSX; Watson *et al.* 2014). This basic information is listed in Table 1.

There are a variety of published values for the metallicity of SW And, with the metallicity values ranging from –0.06 to –0.21 for metallicities based on spectra (see Table 2 for a list). For this paper, the two values of [Fe/H] = –0.06 and –0.21 will be used to see how this range affects the distance measurements.

2. Observations

Observations were made using the remote telescopes operated by the Las Cumbres Observatory (Brown *et al.* 2013). The telescopes were 0.4-meter with SBIG 6303 cameras, located at the Canary Islands (Spain), Fort Davis (Texas, USA), and Haleakala (Hawaii, USA). We collected images through B, V, i, and z filters. For each of these passbands, a cadence was created starting on 28 September 2020 and ending on 18 October 2020. The B band had an exposure time of 22 seconds, the V band 16, the i band 12, and the z band 38. A total of 76 images were obtained from each filter after poor quality images were thrown out. An image taken in the V filter during this observing run can be seen in Figure 1 (SW And is in the center of the image).

All images were processed using the data pipeline created by Our Solar Siblings (Fitzgerald 2018). The pipeline cleaned up all the raw images through image reduction and calibration, including noise reduction, cosmic ray removal, and flat fielding effects. This pipeline also created photometry files using both aperture photometry and point spread function photometry. For each of the four filters, six different photometry algorithms were used. These methods were Dominion Astrophysical Observatory

Table 1. General information of SW And.

Right Ascension (J2000)	$00^h\ 23^m\ 43.0896^s$
Declination (J2000)	+29° 24' 03.6265"
Period	0.44226 day
Parallax (GAIA EDR3)	1.9615 ± 0:0284 mas
Radial Velocity	–20.80 km/s
Spectral Type	A7III-F8III

Table 2. Calculated metallicity [Fe/H] based on spectra.

Value	*Measurement*
–0.06	Clementini et al. (1995)
–0.07	Liu et al. (2013)
–0.20	Lambert et al. (1996)
–0.21	Takeda (2022)

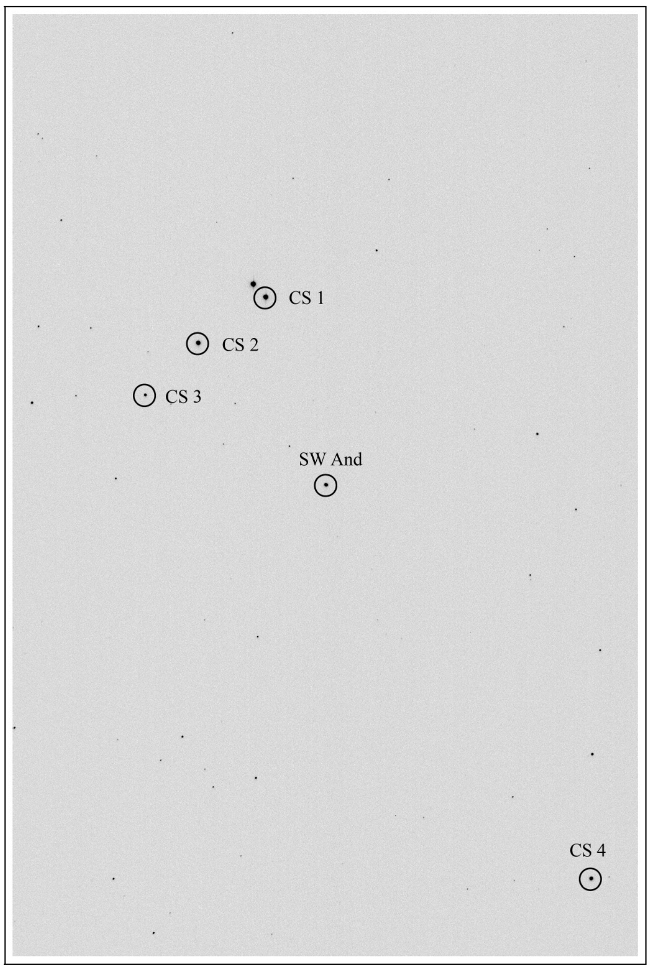

Figure 1. LCO Image of SW And using a Bessel V filter. Comparison stars (CS) used are indicated. The image is 29 × 19 arcminutes in size with north up and east to the left.

Photometry (DAOPHOT; Stetson 1987), DoPHOT (Schechter *et al.* 1993), Point Spread Function with Source Extractor (PSFEx; Bertin 2011), Source Extractor Aperture (SEX) and Source Extractor Kron (SEK) (Bertin and Arnouts 1996), and Aperture Photometry Tool (APT; Laher *et al.* 2012a, 2012b). The cleanest data set was found using the photometry method of Source Extractor using a Kron radius (SEK), so this method is the one used in this study for all the photometry.

3. Methods

After the data were processed using the OSS pipeline, a PYTHON program called ASTROSOURCE (Fitzgerald *et al.* 2020) was used to determine the period and amplitude and generate light curves for each of the filters. The ASTROSOURCE software analyzes the star field in each image and identifies suitable comparison stars by choosing those stars with the least variance. The star catalogs used depended on which catalog covered that part of the sky and which one was more sensitive to that particular magnitude and color. For the B, V, and i bands, the APASS star catalog (Levine *et al.* 2018) was used, and for the z band the SDSS star catalog (Alam *et al.* 2015) was used. See Table 3 for the calibrated apparent magnitudes for the comparison stars.

To account for the interstellar dust that affects the stellar magnitudes, observations in the B filter were made to help adjust the measurements in other filters by using the interstellar reddening E(B–V). The value for E(B–V) was chosen to be 0.039 based on the value found on the Galactic Dust Reddening and Extinction web page found at the NASA/IPAC Infrared Science Archive (Schlegel *et al.* 1998; Schlafly and Finkbeiner 2011). The extinction for each filter was then calculated using the extinction law equations as found in Cardelli *et al.* (1989). The calibrated apparent mid-point magnitudes, corrected for interstellar extinction, are shown in Table 4. The errors quoted in the table are from both the estimated noise from individual measurements as well as the measured standard deviation of the calibration fit.

4. Results

As can be seen from Figures 2, 3, 4, and 5, our light curves obtained are reminiscent of RRab type stars with a steep rise and gradual fall.

The Cáceres and Catelan equations mentioned previously allow us to take our derived periods and metallicity and convert them into an absolute magnitude. The periods were estimated using three different methods, Phase Dispersion Minimization (PDM; Stellingwerf 1978), String Method (SM; Dworetsky 1983), and the Lomb–Scargle periodogram (VanderPlas 2018). Since all three methods gave similar results, we averaged all three methods through all four filters and came up with a period of 0.44214 ± 0.00018 day. This aligns closely with the published period value on the AAVSO website (VSX) of 0.442262 day, giving us some confidence in our method of period analysis.

The measured periods and light curve amplitudes can be seen in Table 5, a Lomb-Scargle periodogram in Figure 6, and a PDM likelihood plot in Figure 7. The results were also

Table 3. Calibrated apparent magnitudes for comparison stars.

Star	*R.A. (deg)*	*Dec. (deg)*	*Filters*	*B Magnitude*	*V Magnitude*	*i magnitude*	*z Magnitude*
CS 1	5.964772	29.49598	B,V	8.720 ± 0.090	8.328 ± 0.046	—	—
CS 2	6.004061	29.47281	B,V,i,z	9.151 ± 0.085	8.739 ± 0.046	8.645 ± 0.019	8.905 ± 0.019
CS 3	6.034822	29.44641	i,z	—	—	10.041 ± 0.020	10.069 ± 0.028
CS 4	5.775393	29.20150	z	—	—	—	9.032 ± 0.020

Table 4. Calibrated apparent mid-point magnitudes (corrected for extinction) for SW And.

Filter	*m*	*Error*
B_0	9.602	0.088
V_0	9.400	0.046
i_0	9.493	0.0094
z_0	9.788	0.019

Table 5. Period and light curve amplitudes for B, V, i, and z filters.

Filter	*DM Period*	*PDM Period*	*LS Period*	*Amplitude*
B	0.44200	0.44200	0.44220	1.386
V	0.44240	0.44190	0.44240	1.014
i	0.44200	0.44281	0.44240	0.653
z	0.44200	0.44200	0.44219	0.580

Table 6. Absolute magnitudes (M) and extinction (A) for SW And.

Filter	*M*	*A*
V	1.069 ± 0.051	0.121
i	0.887 ± 0.022	0.0826
z	0.926 ± 0.021	0.0595

Table 7. Photometric distance to SW And.

Filter	*Distance [Fe/H] = –0.06*	*Distance [Fe/H] = –0.21*
V	447 ± 32	464 ± 33
i	518 ± 19	526 ± 19
z	584 ± 21	592 ± 21
Viz	516 ± 14	527 ± 14

compared to TESS data (Ricker *et al.* 2015), obtained through the software PERANSO (Paunzen and Vanmunster 2016), which can be seen in Figures 8 and 9. The TESS data spanned the time from 8 October 2019 to 31 October 2019. As can be seen from the almost perfect observed light curve from the TESS data, their period has a much lower experimental error. Using PERANSO and the ANOVA method (Schwarzenberg-Czerny 1996) for period analysis, a TESS period of 0.442263 ± 0.000020 day is found. This is the period which will be used in all our calculations, since it has the smallest measurement error.

5. Discussion and analysis

The purpose of this research was to determine if the photometric distance as calculated through period-luminosity-metallicity equations for RR Lyr stars from Catelan *et al.* (2004) and Cáceres and Catelan (2008) agrees with GAIA EDR3 parallax distances. In order to calculate the photometric distance to SW And we used the standard distance equation:

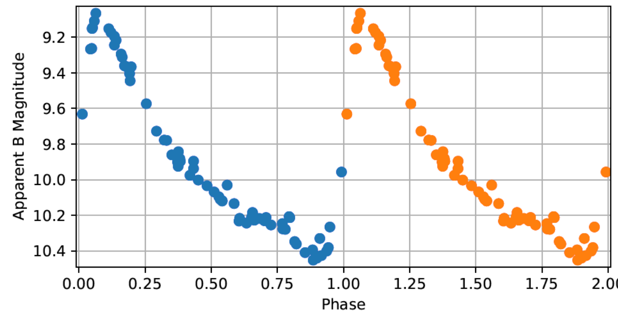

Figure 2. B filter phased light curve for SW And.

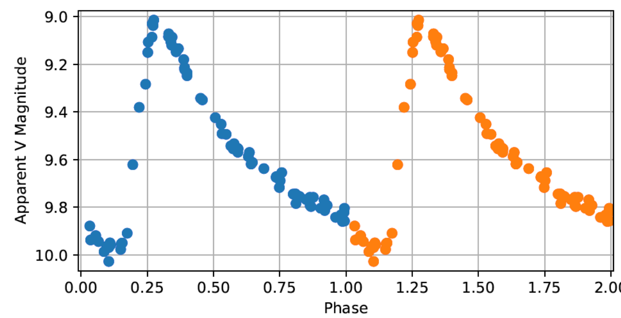

Figure 3. V filter phased light curve for SW And.

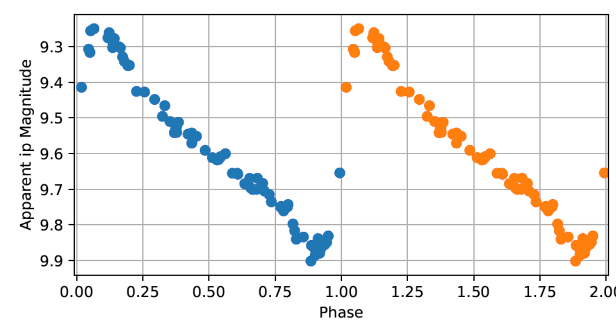

Figure 4. i filter phased light curve for SW And.

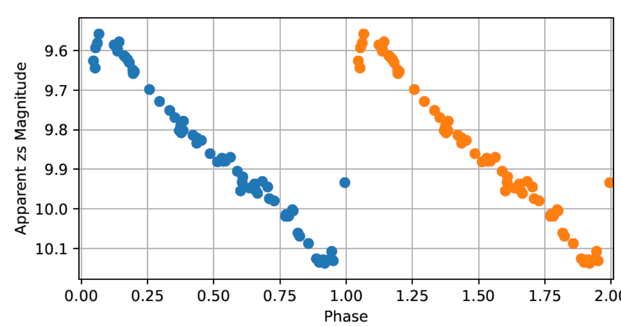

Figure 5. z filter phased light curve for SW And.

$$d = 10^{(m - M - A + 5) / 5}, \qquad (6)$$

where m is our measured apparent mid-magnitude in each filter, M is the absolute magnitude as calculated using the Cáceres and Catelan equations (using the period and metallicity), and A is the extinction at a specific wavelength and is based on an interstellar reddening of E(B–V) = 0.039 as discussed previously in section 3. This information is found in Table 6.

Using the values given in Table 6, an average photometric distance to SW And is calculated through all three filters of 516 ± 14 parsecs for [Fe/H] = –0.06 and 527 ± 14 for [Fe/H] = –0.21. These averages compare relatively well to the parallax distance obtained from GAIA EDR3 data of 510 ± 7 parsecs and roughly overlap the GAIA data within the margin of error. However, as can be seen in Table 7, individual filter distances can either be well below or well above the GAIA distance. Although the i filter distance compares relatively well with GAIA, the other two filters are clearly a couple of standard deviations away from this average. A possible reason for the V filter being off at a value of [Fe/H] = –0.06 is that this is really beyond the metal-rich end for the data range cited in Catelan *et al.* (2004). However, [Fe/H] = –0.21 is not, but suffers from the same underestimation. As a comparison, at least in the V filter, the data was also used in the PZ relationship developed by Garofalo *et al.* (2022) for RR Lyr field stars, which gave a distance of 455 ± 4 to 465 ± 3 for the range of Fe/H of –0.06 to –0.21. These calculated distances are almost the same, albeit with a smaller error, as the distances using Cáceres and Catelans' PZ equation.

6. Conclusion

The goal of this project was to test the validity of Cáceres and Catelans' period-luminosity-metallicity equations for RR Lyr field stars using SW And. The validity is tested by comparing our calculated photometric distance, based on the magnitudes derived using the PLZ equations, to the calculated parallax distance from GAIA EDR3 data. Using the data we acquired and previously measured interstellar reddening and metallicity values, the average distance (through V, i, and z filters) was calculated to be 516 ± 14 parsecs or 527 ± 14 parsecs, depending on the metallicity used. Both of these averages are within one standard deviation of the current parallax distance as measured by GAIA, 510 ± 7 parsecs. This seems to support the validity of Cáceres and Catelans' equations in this limited study of just one RR Lyr field star. The i filter distance matched GAIA the best, and may suggest a better correlation to distance, but to confirm that would require considerably more i filter data using other RR Lyr stars. Since the distance is dependent on metallicity and interstellar reddening, having definitive values for both [Fe/H] and E(B–V) would help with reducing the error on the photometric distance. The discrepancy in distance for the various filters will need to be looked at further in any future studies, since taking a straight average of V, i, and z may have complications tied to how well the PLZ equations actually fit the data used to develop those equations in the different filters.

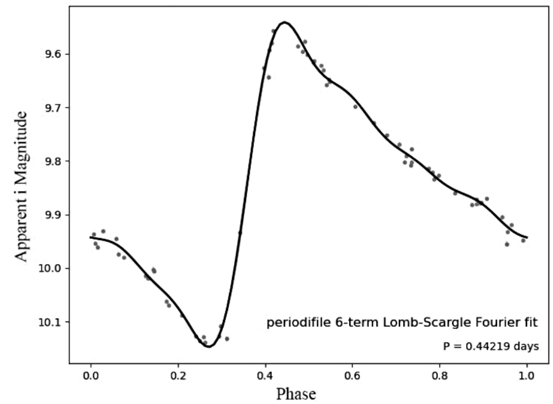

Figure 6. Lomb-Scargle light curve fit using the i filter.

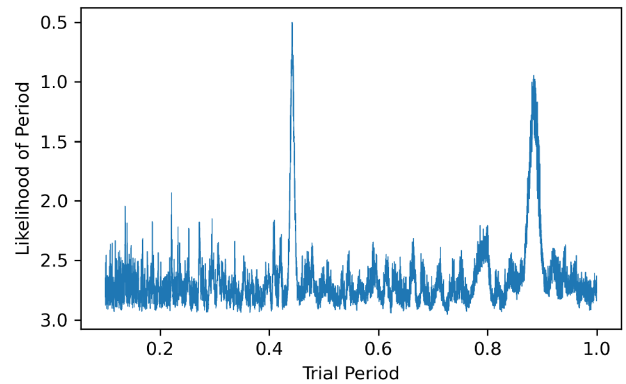

Figure 7. Likelihood plot for the period of SW And.

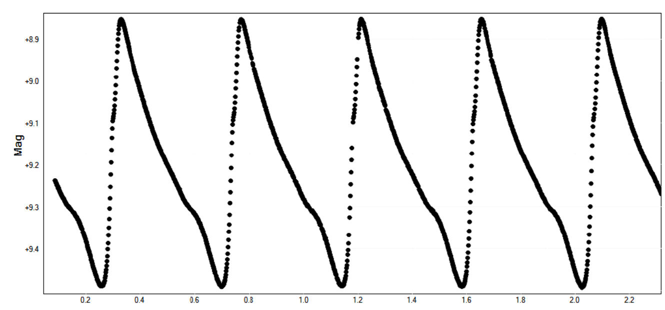

Figure 8. TESS light curve for SW And over several periods.

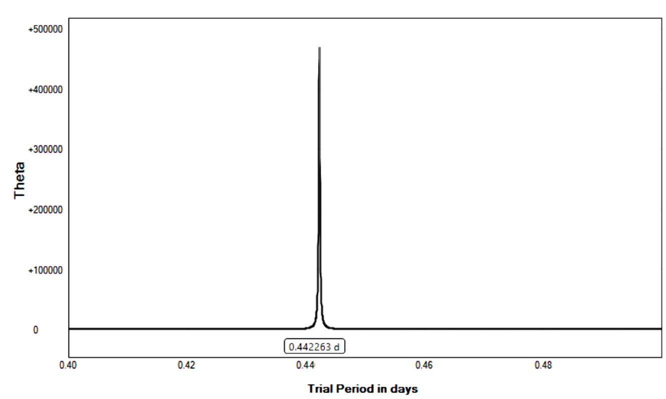

Figure 9. Peranso period analysis of the TESS light curve using the ANOVA method.

7. Acknowledgements

The authors would like to acknowledge Michael Fitzgerald and Our Solar Siblings for providing this research opportunity and providing our group with a plethora of knowledge concerning variable stars and RR Lyr stars.

This research made use of Peranso (www.peranso.com), a light curve and period analysis software. This research has also made use of the Aladin Sky Atlas, SIMBAD, and VizieR developed at CDS, Strasbourg Observatory, France. We acknowledge with thanks the variable star observations from the AAVSO International Database contributed by observers worldwide and used in this research.

References

Alam, S., *et al.* 2015, *Astrophys. J., Suppl. Ser.*, **219**, 12 (DOI: 10.1088/0067-0049/219/1/12).

Barcza, S., and Benkő, J. M. 2014, *Mon. Not. Roy. Astron. Soc.*, **442**, 1863 (DOI: 10.1093/mnras/stu978).

Bertin, E. 2011, in *Astronomical Data Analysis Software and Systems XX*, eds. I. N. Evans, D. J. Mink, A. H. rots, ASP Conf. Proc. 442, Astronomical Society of the Pacific, San Francisco, 435.

Bertin, E., and Arnouts, S. 1996, *Astron. Astrophys., Suppl. Ser.*, **117**, 393 (DOI: 10.1051/aas:1996164).

Brown, T. M., *et al.* 2013, *Publ, Astron. Soc. Pacific*, **125**, 1031 (DOI: 10.1086/673168).

Cáceres, C., and Catelan, M. 2008, *Astrophys. J., Suppl. Ser.,* **179**, 242 (DOI: 10.1086/591231).

Cardelli, J. A., Clayton, G. C., and Mathis, J. S. 1989, *Astrophys. J.*, **345**, 245 (DOI: 10.1086/167900).

Catelan, M., Pritzl, B. J., and Smith, H. A. 2004, *Astrophys. J., Suppl. Ser.*, **154**, 633 (DOI: 10.1086/422916).

Clementini, G., Carretta, E., Gratton, R., Merighi, R., Mould, J. R., and McCarthy, J. K. 1995, *Astron. J.*, **110**, 2319 (DOI: 10.1086/117692).

Clementini, G., Gratton, R., Bragaglia, A., Carretta, E., Di Fabrizio, L., and Maio, M. 2003, *Astron. J.*, **125**, 1309 (DOI: 10.1086/367773).

Dworetsky, M. 1983, *Mon. Not. Roy. Astron. Soc.*, **203**, 917.

Fitzgerald, M. T., Cutts, R., Salimpour, S., and Slater, S. 2018, *Robotic Telesc. Student Res. Education Proc.*, **1**, 1.

Fitzgerald, M., Gomez, E., Salimpour, S., and Wibowo, R. 2020, *J. Open Source Software*, in review.

Gaia Collaboration, Brown, A. G. A., *et al.* 2021, *Astron. Astrophys.*, **649A**, 1 (DOI: 10.1051/0004-6361/202039657).

Garofalo, A., Delgado, H. E., Sarro, L. M., Clementini, G., Muraveva, T., Marconi, M., and Ripepi, V. 2022, *Mon. Not. Roy. Astron. Soc.*, **513**, 788 (DOI: 10.1093/mnras/stac735).

Laher, R. R., Gorjian, V., Rebull, L. M., Masci, F. J., Fowler, J. W., Helou, G., Kulkarni, S. R., and Law, N. M. 2012a, *Publ. Astron. Soc. Pacific*, **124**, 737.

Laher, R. R., *et al.* 2012b, *Publ. Astron. Soc. Pacific*, **124**, 764.

Lambert, D. L., Heath, J. E., Lemke, M., and Drake, J. 1996, *Astrophys. J., Suppl. Ser.*, **103**, 183 (DOI: 10.1086/192274).

Levine, S., Henden, A., Terrell, D., Welch, D., and Kloppenborg, B. 2018, in *AAS/Division for Planetary Sciences Meeting Abstracts, Vol. 50*, AAS/Division for Planetary Sciences Meeting Abstracts #50, 315.03.

Liu, S., Zhao, G., Chen, Y.-Q., Takeda, Y., and Honda, S. 2013, *Res. Astron. Astrophys.*, **13**, 1307 (DOI: 10.1088/1674-4527/13/11/003).

Marconi, M., *et al.* 2015, *Astrophys. J.*, **808**, 50 (DOI: 10.1088/0004-637X/808/1/50).

McNamara, D. H., and Feltz, K. A., Jr. 1977, *Publ. Astron. Soc. Pacific*, **89**, 699 (DOI: 10.1086/130212).

Muraveva, T., Delgado, H. E., Clementini, G., Sarro, L. M., and Garofalo, A. 2018, *Mon. Not. Roy. Astron. Soc.*, **481**, 1195 (DOI: 10.1093/mnras/sty2241).

Muraveva, T., *et al.* 2015, *Astrophys. J.*, **807**, 127 (DOI: 10.1088/0004-637X/807/2/127).

Neeley, J. R., *et al.* 2019, *Mon. Not. Roy. Astron. Soc.*, **490**, 4254 (DOI: 10.1093/mnras/stz2814).

Paunzen, E., and Vanmunster, T. 2016, *Astron. Nachr.*, **337**, 239 (DOI: 10.1002/asna.201512254).

Ricker, G. R., *et al.* 2015, *J. Astron. Telesc. Instrum. Syst.*, **1**, 014003 (DOI: 10.1117/1.JATIS.1.1.014003).

Schechter, P. L., Mateo, M., and Saha, A. 1993, *Publ. Astron. Soc. Pacific*, **105**, 1342.

Schlafly, E. F., and Finkbeiner, D. P. 2011, *Astrophys. J.*, **737**, 103 (DOI: 10.1088/0004-637X/737/2/103).

Schlegel, D. J., Finkbeiner, D. P., and Davis, M. 1998, *Astrophys. J.*, **500**, 525 (DOI: 10.1086/305772).

Schwarzenberg-Czerny, A. 1996, *Astrophys. J., Lett.*, **460**, L107 (DOI: 10.1086/309985).

Stellingwerf, R. F. 1978, *Astrophys. J.*, **224**, 953 (DOI: 10.1086/156444).

Stetson, P. B. 1987, *Publ. Astron. Soc. Pacific*, **99**, 191.

Takeda, Y. 2022, *Mon. Not. Roy. Astron. Soc.*, **514**, 2450 (DOI: 10.1093/mnras/stac1431).

VanderPlas, J. T. 2018, *Astrophys. J., Suppl. Ser.*, **236**, 16 (DOI: 10.3847/1538-4365/aab766).

Watson, C., Henden, A. A., and Price, C. A. 2014, AAVSO International Variable Star Index VSX (Watson+, 2006–2014; https://www.aavso.org/vsx).

Wenger, M., *et al.* 2000, *Astron. Astrophys., Suppl. Ser.*, **143**, 9 (DOI: 10.1051/aas:2000332).

The First Precision Photometric Observations and Analyses of the Totally Eclipsing, Solar Type Binary, V1302 Herculis

Ronald G. Samec
Pisgah Astronomical Research Institute, 318 Monti Drive, Anderson, SC 29625; ronaldsamec@gmail.com

Daniel Caton
Dark Sky Observatory, Department of Physics and Astronomy, Appalachian State University, 525 Rivers Street, Boone, NC 28608-2106; catondb@appstate.edu

Danny Faulkner
Johnson Observatory, 1414 Bur Oak Court, Hebron, KY 41048; dfaulkner@answersingenesis.org

Received August 26, 2022; revised May 2, 10, 2023; accepted May 10, 2023

Abstract CCD, BVRI light curves of the W UMa variable V1302 Her were taken on 24, May, 07, and 23. 24, 27 June 2020 at the Dark Sky Observatory, North Carolina, USA, with the 0.81-m reflector of Appalachian State University. From our present observations, which include three primary eclipses and three secondary eclipses, we determined a linear and a quadratic ephemeris:

JD Hel MinI = 2459027.6675±0.0033 + 0.3162911±0.0000003 × E

JD Hel MinI = 2459027.6764±0.0033d + 0.31629542±0.00000087 × E +

0.00000000027±0.00000000005 × E2

From our 16-year period study, the period is found to be increasing. This could be due to mass transfer making the mass ratio decrease (q = M2 / M1; all pairs of values should be corrected with a phase shift of 0.5). A Wilson-Devinney analysis reveals that the system is an A-type (more massive component is the hottest) overcontact W UMa binary with a fairly extreme mass ratio (q = 0.2426 ± 0.0003, 1 / q = M1 / M2 = 4.1). Its Roche Lobe fill-out is ~23%. One hot spot was needed in the solution. The temperature difference of the components is only ~263 K, with the more massive component as the slightly hotter one, so that in the present observations, it is an A-type W UMa binary. The inclination is high, 87.0 ± 0.2, resulting in a total primary eclipse.

1. History and observations

The variability of V1302 Her (GSC 3101-0683, 1SWASP J175239.07+434931.5) was detected in the FOV of the Algol-type binary V338 Her by the ROTSE1 experiment (Akerlof *et al.* 2000; ROTSE1 J175239.04+434936.7, Liakos and Niarchos 2009, see Figure 1.). They classified it as a contact variable with an ephemeris of HJD Min I = 2454610.3476169 + 0.3162897 d * E (Pejcha 2005). A nearby X-ray source, 1RXS J175245.6+435128, is likely associated with this star (Pejcha 2006). It is classified as a contact variable with a maximum V magnitude of 12.33 and amplitude of V ~ 0.4.

The system was observed by the All Sky Automated Survey as ASASSN-V J051858.09+365806.2 (Shappee *et al.* 2014; Kochanek *et al.* 2017), see Figure 2.). They give a V_{mean} = 11.33, an amplitude of 0.4, and EW designation, J–K = 0.467. The initial report was given in American Astronomical Society meeting #238 (Canton *et al.* 2021). Their ephemeris is:

$$\text{HJD Min I} = 2457070.80679 + 0.3995827\text{E d} \times \text{E} \quad (1)$$

From the ASAS-SN curves we were able to phase the data with Equation 1 and do parabola fits to the primary and secondary minima to locate two times of minimum within 0.001 phase of each minimum. We also included the ASAS-SN HJD Min I in our period study.

This system was observed as a part of our professional collaborative studies of interacting binaries at Pisgah Astronomical Research Institute from data taken from DSO observations.

The observations were taken by D. Caton, R. Samec, and D. Faulkner. Reduction and analyses were done by Ron Samec.

Our 2017 BVRI light curves were taken at Dark Sky Observatory, on 24, May, 07, and 23. 24, 27 June 2020 with a thermoelectrically cooled (–35° C) 1KX1K FLI camera and Bessell BVRI filters.

These observations consisted of 680 measurements in B, 707 in V, 717 in R, and 707 in I. The listed magnitudes are delta magnitudes in V–C. HJD are Heliocentric Julian dates. The probable error of a single observation was 4 mmag in B, V, and R, and 3 mmag in I. The nightly C–K values stayed constant throughout the observing run with a precision of about 1%. Exposure times varied from 45 s in B and 20 s in V to 15 s in R and I. To produce these images, nightly images were calibrated with 25 bias frames, at least five flat frames in each filter, and ten 300-second dark frames. Table 1 gives the BVRI observations.

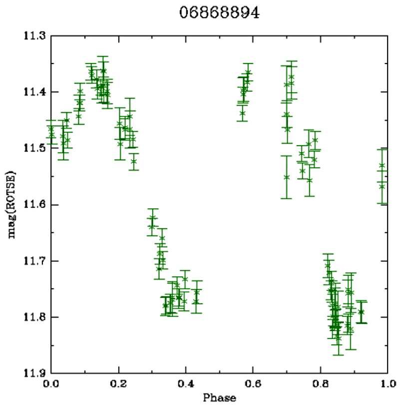

Figure 1. ROTSE light curves (Geske *et al.* 2006).

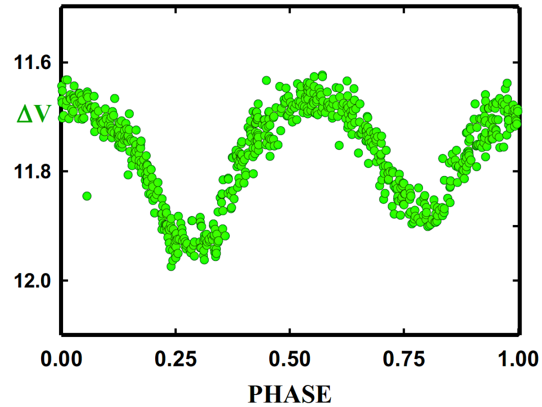

Figure 2. ASAS-SN data light curves (Shappee *et al.* 2014; Kochanek *et al.* 2017).

Table 1. Sample of first ten *V1302 Her B, V, R, I* observations.

ΔB (V–C)	HJD 2458900+	ΔV (V–C)	HJD 2458900+	ΔR (V–C)	HJD 2458900+	ΔI (V–C)	HJD 2458900+
2.619	93.8085	2.747	93.8064	2.742	93.8042	2.781	93.8044
2.619	93.8105	2.743	93.8076	2.764	93.8054	2.788	93.8056
2.626	93.8125	2.751	93.8089	2.753	93.8066	2.795	93.8069
2.621	93.8140	2.754	93.8110	2.753	93.8079	2.799	93.8081
2.619	93.8155	2.755	93.8130	2.758	93.8099	2.803	93.8101
2.621	93.8170	2.756	93.8145	2.766	93.8117	2.803	93.8120
2.620	93.8186	2.762	93.8161	2.763	93.8133	2.804	93.8135
2.617	93.8201	2.755	93.8176	2.743	93.8148	2.794	93.8150
2.608	93.8216	2.762	93.8191	2.767	93.8163	2.795	93.8166
2.610	93.8232	2.754	93.8206	2.768	93.8179	2.807	93.8181

Note: First ten data points of V1302 Her B, V, R, I observations. The complete table is available through the AAVSO ftp site at ftp://ftp.aavso.org/public/datasets/3851-Samec-511-v1302her.txt (if necessary, copy and paste link into the address bar of a web browser).

Table 2. The photometric target data.

Star	Name	R.A. (2000) h m s	Dec. (2000) ° ′ ″	V	J–K
V1302 Her	GSC 03101 0683 2MASS J17523906+4349293 UCAC3 268-144343 UCAC4 670-064717 Gaia DR2 1346420948207784704	17 52 39.0640592463[3]	+43 09 29.337600715[1]	11.373	0.469 ± 0.0333
C (comparison)	GSC 03101 1257	17 52 52.8323207873[4]	+43 50 48.212826632[4]	10.12 (0.03)	0.501 ± 0.047
K (check)	GSC 03101 0995	17 53 06.0206513889[4]	+43 52 6.243839274	9.752	0.246 ± 0.033

[1] *ICRS (IAU 2013).* [2] *2MASS (Skrutskie* et al. *2006).* [3] *UCAC3 (U.S. Naval Observatory 2012).* [4] *UCAC3 (Zacharias, N.,* et al. *2010).*

2. Photometric targets

The photometric targets (variable, comparison (C), and check (K) stars) of this paper are noted in Table 2. The finding chart with variable (V), comparison, and check stars is shown in Figure 3.

3. Period determination

Seven mean times of minimum light were calculated from our present observations (BVRI data), which included four primary and three secondary eclipses:

HJD I = 2458993.81742 ± 0.00106, 2459024.81490 ± 00007, 2459023.86008 ± 0.00056, 2459027.66111 ± 0.000128

HJD II = 2459024.65805 ± 0.00031, 2459023.71008 ± 0 0.00052, 2459027.82066 ± 0.00025.

These minima were weighted as 1.0 in the period study.

In addition, eight times of low light were calculated from ASAS-SN data and were weighted 0.1. Twenty times of minimum were taken from IBVS (Hübscher *et al.* 2010, 2012; Liakos and Niachos 2009; Pejcha 2005, 2006; Nelson 2015, 2017). This gave us a period study with an interval of ~16 years.

From these timings, two ephemerides have been calculated, a linear and a quadratic one:

$$\text{JD Hel Min I} = 2459027.65873 \pm 0.00080\,\text{d} + 0.31629036 \pm 0.00000072 \times \text{E} \quad (2)$$

$$\text{JD Hel Min I} = 2459027.66132 \pm 0.00054\,\text{d} + 0.31629221 \pm 0.00000017 \times \text{E} + 0.000000000121 \pm 0.000000000011 \times \text{E}^2 \quad (3)$$

The plotted residuals of the quadratic term are given in Figure 4. The errors are too small to be given in the figure or are nonexistent (from visual timings or times of single ASAS-SN observations, usually within 0.001s of the fitted minima). These are used in the absence of enough observed minima to do a period study. They have been found to work well in this situation.).

The study given here covers a time interval of 16 years. It does show an orbital period that is increasing, as shown in the O–C curve. This might be due to mass transfer to the more massive, primary component making the mass ratio more extreme.

The quadratic ephemeris yields a $\dot{P} = 1.7(0.5) \times 10^{-7}$ d/yr or a mass exchange rate of

$$dM/dt = (\dot{P}\,M_1 M_2)/(3P(M_1 - M_2)) = 8(3) \times 10^{-8}\,M_\odot/\text{yr}$$

in a conservative scenario (the primary component is the gainer; see van der Sluys 2021). The O–C table of minima with linear and quadratic residuals is shown in Table 3. The initial ephemeris for the table and to begin the calculation was

$$\text{JD Hel Min I} = 2459027.661109 + 0.3162897000 \times \text{E}.$$

4. Light curve characteristics

The curves are of good accuracy, averaging about 2% photometric precision. The amplitude of the light curve varies from 0.506 to 0.581 mag for I to B. The O'Connell effect, an indicator of spot activity, was 0.017–0.040 mag, B to I, indicating that magnetic activity is likely. The difference in minima, 0.062 to 0.046 B to I, indicates overcontact light curves in poor thermal contact. A total eclipse occurs at our secondary minima and lasts some 34 minutes. Complete light curve characteristics are given in Table 4.

5. Light curve solution

The 2MASS, J–K = 0.469 ± 0.033 for the binary star. These correspond to ~K0.5V ± 2.5, which yields a temperature of 5250 ± 200 K. Fast rotating binary stars of this type are noted for having strong magnetic activity, so the binary is of solar type with a convective atmosphere.

The B, V, R, and I curves were pre-modeled with Binary Maker 3.0 (Bradstreet and Steelman 2002). Fits were determined in all four filter bands and like parameters (like inclination) were averaged. The solution was that of an overcontact eclipsing binary. The parameters were then averaged (q = 0.21, fill-out = 0.0875, i = 86°, T_1 = 4950, with one 15° cool spot, T-FACT = 0.7) and input into a four-color simultaneous light curve calculation using the Wilson-Devinney Program (Wilson and Devinney 1971; Wilson 1990, 1994; van Hamme and Wilson 1998). A solution is arrived at when all parameter corrections are smaller than their associated standard deviations for each parameter. The solution was computed in Mode 3 and converged to a solution. In the case of the Wilson program (a differential corrections routine) this means that the corrections to the parameters are made at each iteration until they are smaller than their standard deviations. Convective parameters, g = 0.32, A = 0.5 were used. An eclipse duration of ~34 minutes was determined for our secondary eclipse and the light curve solution. The more massive component is the coolest one, making the system a W-type W UMa contact binary. We tried third light but that did not solve any fitting issues. The spotted solution follows in Table 5. At the request of the referee a non-spotted was undertaken. This solution is also given in Table 5. The goodness of fit parameter, Sum(W*Res**2), shows that the spotted solution is considerably better.

The BV and RI solution plots are given in Figures 5 and 6. The geometric surface (Roche Lobes) at quadratures is shown

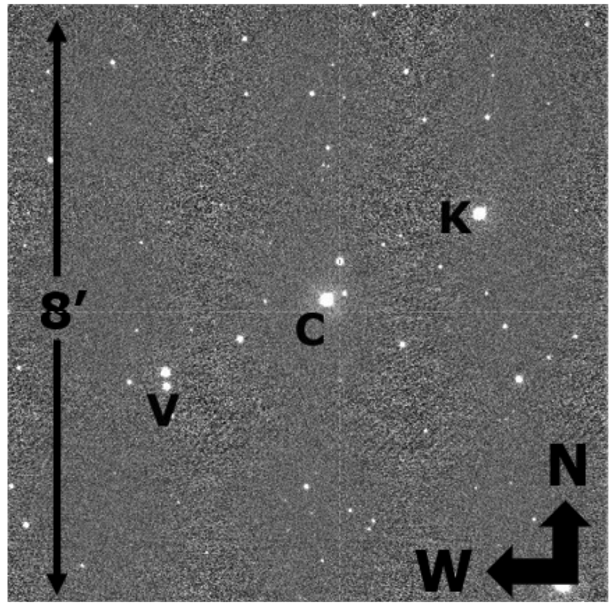

Figure 3. The finding chart for V1302 Her with variable (V), comparison (C), and check stars (K).

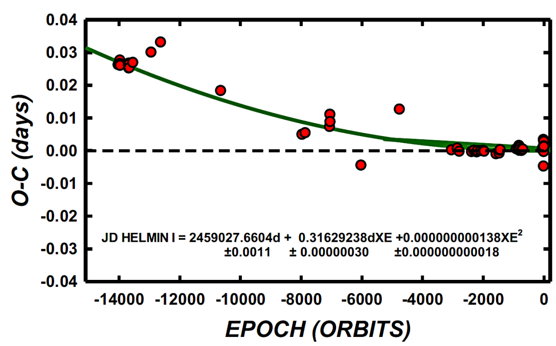

Figure 4. The plotted residuals of the quadratic term. Errors are smaller than the point size for regular minima (not times of low light).

Table 3. O–C residuals of minima, V1302 Her.

	Epoch (JD–2400000.0000)	Cycle	Initial Res.	Linear Res.	Quad. Res.	Wt.	Reference
1	53258.3739 ± 0.0008	18240.5	–0.0049	0.0095	0.0004	1.0	Pejcha (2005)
2	54591.5278 ± 0.0001	14025.5	–0.0121	–0.0004	–0.0009	1.0	Hübscher *et al.* (2010)
3	54609.3997 ± 0.0002	13969.0	–0.0106	0.0011	0.0007	1.0	Liakos and Niarchos (2009)
4	54610.3475 ± 0.0001	13966.0	–0.0117	0.0000	–0.0004	1.0	Liakos and Niarchos (2009)
5	54610.5055 ± 0.0002	13965.5	–0.0118	–0.0002	–0.0005	1.0	Liakos and Niarchos (2009)
6	54611.4540 ± 0.0002	13962.5	–0.0122	–0.0005	–0.0009	1.0	Liakos and Niarchos (2009)
7	54699.3835 ± 0.0003	13684.5	–0.0112	0.0002	0.0003	1.0	Liakos and Niarchos (2009)
8	54700.3326 ± 0.0003	13681.5	–0.0110	0.0005	0.0005	1.0	Liakos and Niarchos (2009)
9	54701.2817 ± 0.0004	13678.5	–0.0107	0.0007	0.0008	1.0	Liakos and Niarchos (2009)
10	54701.4384 ± 0.0004	13678.0	–0.0122	–0.0007	–0.0007	1.0	Liakos and Niarchos (2009)
11	54703.3363 ± 0.0003	13672.0	–0.0120	–0.0006	–0.0005	1.0	Liakos and Niarchos (2009)
12	54704.4433 ± 0.0006	13668.5	–0.0120	–0.0006	–0.0005	1.0	Liakos and Niarchos (2009)
13	54706.3421 ± 0.0003	13662.5	–0.0110	0.0005	0.0005	1.0	Liakos and Niarchos (2009)
14	54707.4480 ± 0.0004	13659.0	–0.0121	–0.0007	–0.0006	1.0	Liakos and Niarchos (2009)
15	54744.2977 ± 0.0004	13542.5	–0.0101	0.0012	0.0015	1.0	Hübscher *et al.* (2010)
16	54934.5507[2]	12941.0	–0.0054	0.0056	0.0066	0.2	Nelson (2017)[1]
17	55659.4811 ± 0.0055	10649.0	–0.0110	–0.0016	0.0018	0.2	Nelson (2014, 2017)
18	56507.4476 ± 0.0008	–7968.0	–0.0172	–0.0095	–0.0051	1.0	Hübscher (2014)
19	56540.3425 ± 0.0008	–7864.0	–0.0164	–0.0088	–0.0043	0.5	Hübscher (2014)
20	56794.8016 ± 0.0005	–7059.5	–0.0124	–0.0053	–0.0009	1.0	Nelson (2015)
21	56799.3916 ± 0.0055	–7045.0	–0.0086	–0.0015	0.0029	1.0	Hübscher *et al.* (2015)
22	56799.5475 ± 0.0007	–7044.5	–0.0108	–0.0038	0.0007	1.0	Hübscher *et al.* (2015)
23	57183.9985[1]	–5829.0	–0.0099	–0.0037	0.0004	0.1	Shappee 2014
24	56757.9535[1]	–7176.0	–0.0127	–0.0056	–0.0011	0.1	Shappee 2014
25	56757.9538[1]	–7176.0	–0.0125	–0.0053	–0.0009	0.1	Shappee 2014
26	56857.9030[1]	–6860.0	–0.0107	–0.0038	0.0006	0.1	Shappee 2014
27	57296.7571[1]	–5472.5	–0.0086	–0.0026	0.0013	0.1	Shappee 2014
28	57048.1516[1]	–6258.5	–0.0104	–0.0039	0.0004	0.1	Shappee 2014
29	58027.7101[1]	–3161.5	–0.0012	0.0033	0.0054	0.1	Shappee 2014
30	56797.9671[1]	–7049.5	–0.0098	–0.0027	0.0017	0.1	Shappee 2014
31	57522.9120 ± 0.0010	–4757.5	–0.0009	0.0047	0.0081	0.5	Nelson (2014, 2017)
32	58993.8174 ± 0.0003	–107.0	–0.0007	0.0018	–0.0006	0.5	Present observations
33	59024.6581 ± 0.0001	–9.5	0.0017	0.0041	0.0015	1.0	Present observations
34	59024.8149 ± 0.0008	–9.0	0.0004	0.0028	0.0002	1.0	Present observations
35	59023.7101 ± 0.0008	–12.5	0.0026	0.0050	0.0024	1.0	Present observations
36	59023.8601 ± 0.0006	–12.0	–0.0056	–0.0032	–0.0057	1.0	Present observations
37	59027.6611 ± 0.0001	0.0	0.0000	0.0024	–0.0002	1.0	Present observations
38	59027.8207 ± 0.0003	0.5	0.0014	0.0038	0.0012	0.5	Present observations

[1] *Times of low light.* [2] *Visual.*

in Figures 7a, b, c, and d. The system dimensions are given in Table 6 and the estimated system absolute parameters are given in Table 7. These are based on the system radii from the Wilson program and the densities from Roche lobe calculations using the period input into Binary Maker 3.

6. Discussion

V1302 Her is a A-type, overcontact W UMa binary. Since the eclipses were total, the mass ratio, $q = 0.24$ ($1/q = 4.12$), is well determined with a fill-out of 23(1)%. The system has a fairly extreme mass ratio and a component temperature difference of ~263 K, so it is in good thermal contact. One spot was needed in the final modeling. The inclination of ~87° resulted in a total eclipse in the secondary ($p_{shift} = 0.5$, from the binary maker hand fit). Its photometric spectral type indicates a surface temperature of ~5250 K for the primary1 component, making it a solar type binary. Such a main sequence star would have a mass of ~0.86 $M_\odot$ (K0.5V) and the secondary (from the mass ratio) would have a mass of ~0.21 $M_\odot$ (making it very much undersized). The temperature of the primary component (~5513 K) of a main sequence star would make it of type G7V instead of M5V as indicated by its mass. This is probably due to substantial magnetic (dark spots) activity causing the more massive component to have a suppressed surface temperature. The period of this binary indicates that it is increasing. This could be due to mass exchange with the flow toward the more massive component making the mass ratio more extreme ($dM/dt = +8.11 \times 10^{-8} M_\odot/s$).

Radial velocity curves are needed to obtain absolute (not relative or estimated) system parameters.

Table 4. Light curve means and differences at quadratures, V1302 Her.

Filter	Phase Mag Min I	Phase Mag Max I
	0.00	0.25
B	2.644 ± 0.021	2.063 ± 0.025
V	2.775 ± 0.013	2.215 ± 0.017
R	2.761 ± 0.081	2.248 ± 0.021
I	2.799 ± 0.020	2.293 ± 0.022

Filter	Phase Mag Min II	Phase Mag Max II
	0.50	0.75
B	2.582 ± 0.016	2.080 ± 0.025
V	2.712 ± 0.018	2.247 ± 0.017
R	2.729 ± 0.011	2.290 ± 0.021
I	2.753 ± 0.020	2.333 ± 0.022

Filter	Min I–Max I	Max II–MaxI	Min –Min II
B	0.581 ± 0.046	0.017 ± 0.017	0.062 ± 0.037
V	0.560 ± 0.030	0.032 ± 0.032	0.063 ± 0.032
R	0.513 ± 0.102	0.042 ± 0.042	0.032 ± 0.092
I	0.506 ± 0.043	0.040 ± 0.040	0.046 ± 0.040

Filter	Min II–Max I	Min I–Max II	Min II–Max II
B	0.519 ± 0.041	0.564 ± 0.046	0.502 ± 0.041
V	0.497 ± 0.035	0.528 ± 0.030	0.465 ± 0.035
R	0.481 ± 0.032	0.471 ± 0.102	0.439 ± 0.032
I	0.460 ± 0.042	0.466 ± 0.043	0.420 ± 0.042

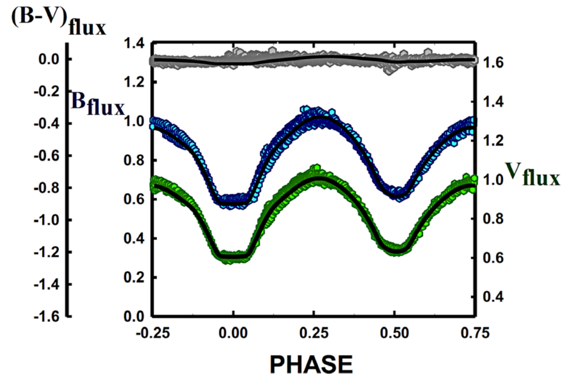

Figure 5. B,V light curve solution overlying the normalized flux curves. B is in blue and V in green. Gray is B–V.

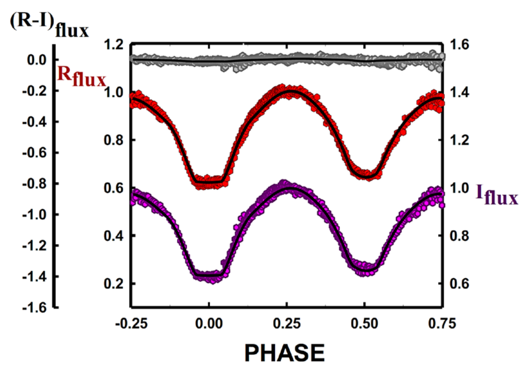

Figure 6. R,I light curve solution underlying the normalized flux curves. R is in red and I in purple. Gray is R-I.

Table 5. Light curve solutions of V1302 Her.

Parameters	Spotted Solution	Unspotted Solution
λ_B, λ_V, λ_R, λ_I (nm)	440, 550, 640, 790	440, 550, 640, 790
g_1, g_2	0.32	0.32
A_1, A_2	0.5	0.5
Inclination (°)	87.0 ± 0.2	85.3 ± 0.3
T_1, T_2 (K)1	5250, 5513 ± 2	5250, 5607 ± 2
$\Omega_1 = \Omega_2$	2.301 ± 0.001	2.301 ± 0.002
$q(m_1/m_2)$[1]	0.2426 ± 0.0003	0.2422 ± 0.0003
Fill-outs: F1, F2 (%)	23.0 ± 0.51	22 ± 11
$L_1/(L_1+L_2)_I$	0.7480 ± 0.0005	0.7379 ± 0.0006
$L_1/(L_1+L_2)_R$	0.7427 ± 0.0005	0.7307 ± 0.0006
$L_1/(L_1+L_2)_V$	0.7350 ± 0.0006	0.7202 ± 0.0007
$L_1/(L_1+L_2)_V$	0.7194 ± 0.0008	0.6985 ± 0.0009
JD_o (days)	2459027.66191 ± 0.00006	2459027.66281 ± 0.00007
Period (days)	0.3163106 ± 0. 0000015	0.3163083 ± 0.0000018
P-shift$_2$	0.5 added to phase	0.5
Dimensions		
$r_1/a, r_2/a$ (pole)	0.480 ± 0.001, 0.255 ± 0.002	0.480 ± 0.001, 0.254 ± 0.002
$r_1/a, r_2/a$ (side)	0.522 ± 0.002, 0.266 ± 0.003	0.521 ± 0.001, 0.265 ± 0.002
$r_1/a, r_2/a$ (back)	0.548 ± 0.002, 0.307 ± 0.006	0.548 ± 0.002, 0.305 ± 0.004
Spot I, Primary Component	*Polar Hot Spot Region*	
Colatitude (°)	32.19 ± 0.26	
Longitude (°)	59 ± 1	
Radius (°)	19.4 ± 0.1	
T-Factor	1.195 ± 0.003	
[3]Sum(W*Res**2)	0.774315	1.193995

[1] The errors are given by the Wilson code. Fill-out errors are determined from the combined errors of possible mass ratios and potentials (referee's note: these are underestimated). [2] The P-Shift = 0.5 means that in the normal sense (for ease in modeling), all primaries are replaced by secondaries and vv., (1↔2). [3] Goodness of fit parameter N.

Table 6. Estimates of V1302 Her system dimensions.

R_1, R_2 (pole, $R_\odot$)	0.961 ± 0.002	0.509 ± 0.005
R_1, R_2 (side, $R_\odot$)	1.044 ± 0.003	0.532 ± 0.006
R_1, R_2 (back, $R_\odot$)	1.097 ± 0.004	0.613 ± 0.012

Table 7. Estimated absolute parameters.[1]

Parameter	*Star 1*	*Star2*
Mean Radius ($R_\odot$)	1.003	0.552
Mean density	1.111 ± 0.004	1.803 ± 0.006
Mass ($M_\odot$)	0.87	0.21
Log g	4.34	4.29

[1] *Using light curve solution units, a = 1, a is calculated for Wilson program, and the semi-major axis. The density is in g/cm³ a = 2.00 $R_\odot$ (Binary Maker, Bradstreet and Steelman 2002).*

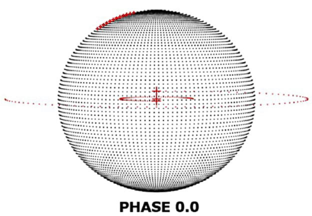

Figure 7a. Geometrical representation at phase 0.0

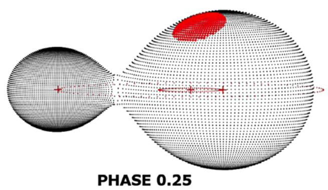

Figure 7b. Geometrical representation at phase 0.25.

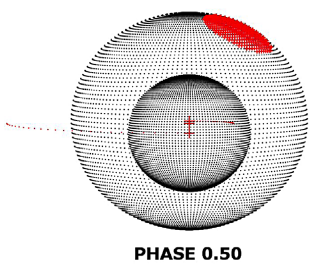

Figure 7c. Geometrical representation at phase 0.50.

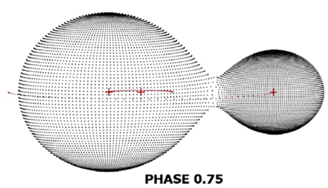

Figure 7d. Geometrical representation at phase 0.75.

References

Akerlof, C. *et al.* 2000, *Astron. J.*, **119**, 1901.
Bradstreet, D. H., and Steelman, D.P. 2002, *Bull. Amer. Astron. Soc.*, **34**, 1224.
Caton, D. B., Samec, R., and Faulkner, D. 2021, *Bull. Amer. Astron. Soc.*, **53**, e-id 2021n6i215p05.
Geske, M. T., Gettel, S. J., and McKay, T. A. 2006, *Astron. J.*, **131**, 633.
Hübscher, J. 2014, *Inf. Bull. Var. Stars*, No. 6118, 1.
Hübscher, J., and Lehmann, P. B. 2015, *Inf. Bull. Var. Stars*, No. 6149, 1.
Hübscher, J., Lehmann, P. B., Monninger, G., Steinbach, H.-M. and Walter, F. 2010, *Inf. Bull. Var. Stars*, No. 5918, 1.
Hübscher, J., Lehmann, P. B., and Walter, F. 2012, *Inf. Bull. Var. Stars*, No. 6010, 1.
International Astronomical Union. 2013, International Earth Rotation and Reference Systems Service, International Celestial Reference System (ICRS; https://www.iers.org/IERS/EN/Science/ICRS/ICRS.html).
Kochanek, C. S., *et al.* 2017, *Publ. Astron. Soc. Pacific*, **129**, 104502.
Liakos, A., and Niarchos, P. 2009, *Inf. Bull. Var. Stars*, No. 5897, 1.
Nelson, R. H. 2014, AAVSO O–C database (https://www.aavso.org/bob-nelsons-o-c-files).
Nelson, R. H. 2015, *Inf. Bull. Var. Stars*, No. 6131, 1.
Nelson, R. H. 2017, *Inf. Bull. Var. Stars*, No. 6195, 1.
Pejcha, O. 2005, *Inf. Bull. Var. Stars*, No. 5645, 1.
Pejcha, O. 2006, *Inf. Bull. Var. Stars*, No. 5699, 15.
Shappee, B. J., *et al.* 2014, *Astrophys. J.*, **788**, 48.
Skrutskie, M. F., *et al.* 2006, "The Two Micron All Sky Survey," *Astron. J.*, **131**, 1163.
U.S. Naval Observatory. 2012, UCAC-3 (http://www.usno.navy.mil/USNO/astrometry/optical-IR-prod/ucac).
van der Sluys, M. 2021, "Binary evolution in a nutshell (BEiaNS)."[1]
van Hamme, W. V., and Wilson, R. E. 1998, *Bull. Amer. Astron. Soc.*, **30**, 1402.
Wilson, R. E. 1990, *Astrophys. J.*, **356**, 613.
Wilson, R. E. 1994, *Publ. Astron. Soc. Pacific*, **106**, 921.
Wilson, R. E., and Devinney, E. J. 1971, *Astrophys. J.*, **166**, 605.
Zacharias, N., *et al.* 2010, *Astron. J.*, **139**, 2184.

[1] van der Sluys (2021), "Binary evolution in a nutshell (BEiaNS)" (https://astro.ru.nl/~sluys/Binaries/files/BinaryEvolutionNutshell_letter.pdf).

Combined Spectroscopic and Photometric Analysis of Flares in the Dwarf M Star EV Lacertae

David Boyd
West Challow Observatory, OX12 9TX, UK; davidboyd@orion.me.uk

Robert Buchheim
Lost Gold Observatory, Gold Canyon, Arizona; bob@rkbuchheim.org

Sean Curry
Yank Gulch Observatory, Talent, Oregon; sxcurry@gmail.com

Frank Parks
Tierrasanta Astrophysics Observatory, San Diego, California; fgparks@mac.com

Keith Shank
Carollton, Texas; kasism@verizon.net

Forrest Sims
Desert Celestial Observatory, Gilbert, Arizona,; forrest@simsaa.com

Gary Walker
Maria Mitchell Observatory, Nantucket, Massachusetts; bailyhill14@gmail.com

John Wetmore
AZ Desertskies Observatory, Gilbert, Arizona; john@azdesertskies.com

James Jackman
ASU School of Earth and Space Exploration, Tempe, Arizona; jamesjackman@asu.edu

Received September 2, 2022; revised March 15, April 3, 2023; accepted April 3, 2023

Abstract We report results of an observing campaign to study the dwarf M flare star EV Lacertae. Between October 2021 and January 2022 we obtained concurrent B band photometry and low resolution spectroscopy of EV Lac on 39 occasions during 10 of which we observed flares with amplitude greater than 0.1 magnitude. Spectra were calibrated in absolute flux using concurrent photometry and flare-only spectra obtained by subtracting mean quiescent spectra. We measured B band flare energies between Log E = 30.8 and 32.6 erg. In the brightest flares we measured temporal development of flare flux in H I and He I emission lines and in the adjacent continuum and found that flux in the continuum subsided more rapidly than in the emission lines. Although our time resolution was limited, in our brightest flare we saw flux in the continuum clearly peaking before flux in the emission lines. We observed a progressive decrease in flare energy from Hβ to Hδ. On average we found 37% of B band flare energy appeared in the Hβ to Hε emission lines with the remainder contributing to a rise in continuum flux. We measured black-body temperatures for the brightest flares between 10,500 ± 700 K and 19,500 ± 500 K and found a linear relationship between flare temperature and continuum flux at 4170 Å. Balmer lines in flare-only spectra were well fitted by Gaussian profiles with some evidence of additional short-lived blue-shifted emission at the flare peak.

1. Introduction

Stellar flares are explosive events that occur when magnetic reconnection in the corona accelerates charged particles down into the chromosphere, heating the plasma and releasing energy across the electromagnetic spectrum (Benz and Güdel 2010; Allred *et al.* 2015). Flare output at visual wavelengths has been modelled as a combination of a fast, short-lived rise in the continuum produced by hot black-body radiation and a slower rise and decay in Balmer emission (see Kowalski *et al.* 2013 for references). Flares occur more often in stars of later spectral type, becoming most frequent in young, rapidly rotating, magnetically active M dwarfs (see for example results from TESS in Günther *et al.* 2020 and NGTS in Jackman *et al.* 2021). As M dwarfs are the most common stars in the galaxy, they are also the most common hosts of exoplanetary systems. The space weather environment around these stars will have a profound effect on the habitability of their planets and this has stimulated an increasing level of interest in understanding the nature and frequency of stellar flares.

EV Lac is a well-known flare star with mass 0.350 ± 0.020 $M_{\odot}$, radius 0.353 ± 0.017 $R_{\odot}$, luminosity 0.0128 ± 0.0003 $L_{\odot}$, and effective temperature 3270 ± 80 K (Paudel *et al.* 2021). It has a rotation period of 4.378 days (Pettersen 1980), faster than the 5.78-day mean rotation period of M dwarfs in both the K2 and SDSS surveys (Popinchalk *et al.* 2021). Fast rotation contributes to development of a strong magnetic field. Its spectral type has been variously described as dM3.5e (Reid *et al.* 1995), M4.0V (Lépine *et al.* 2013), and M4.5e (Joy and Abt 1974). Several multi-wavelength campaigns to observe flares in EV Lac have been published (see for example Paudel *et al.* 2021 and references therein) but have had limited success in recording flares concurrently with photometry and spectroscopy.

2. Observing campaign

Here we report the results of a campaign by a group of well-equipped amateur observers located in the USA and Europe, in which Jackman participated as our professional advisor and mentor, to specifically address that deficit by obtaining and analysing concurrent photometry and spectroscopy of EV Lac. The campaign was coordinated through biweekly online meetings and is part of a larger coordinated program of observations covering several flare stars. Members of the group obtained photometric and/or spectroscopic observations using the resources listed in Table 1 whenever circumstances permitted. Equipment is located at the observer's home unless stated otherwise. Photometric observations were reported to databases managed by the AAVSO (Kafka 2022) and BAA (BAA Photometry Database 2022). A shared project Google Drive was used to manage spectroscopic observations, including a timeline recording when concurrent photometric and spectroscopic observations had been obtained.

Observations reported here run from October 2021 to January 2022. During that time, we recorded 107 photometry sessions and 72 spectroscopy sessions including 39 in which photometry and spectroscopy were obtained concurrently. In these 39 sessions we identified 10 containing flares with B-magnitude amplitudes greater than 0.1 magnitude and which form the basis of this analysis. A journal of these ten sessions is given in Table 2. Analysis of our data was performed with custom Python software which made extensive use of the Astropy package (Astropy Collaboration 2018).

3. Photometric observations

Photometric observations were mostly made with 0.35- and 0.5-m telescopes, using Astrodon dielectric Johnson-Cousins (J-C) B-band photometric filters. This passband was chosen as light output from flares increases towards shorter wavelengths (Paudel *et al.* 2021; Kowalski *et al.* 2013) but recording efficiency in the UV passband is generally low with our observing equipment and with atmospheric transmission at our low altitudes. A small number of observations were made with smaller telescopes using J-C V band filters to observe changes in the color index of EV Lac during flares. Photometric images were bias, dark, and flat corrected and instrumental magnitudes obtained by aperture photometry using the software AIP4WIN (Berry and Burnell 2005) or Maxim DL (Diffraction Limited 2023). Comparison star magnitudes were obtained from the AAVSO chart for EV Lac (AAVSO 2022) and used to convert instrumental to standard magnitudes in the J-C system. In order to establish a consistent timeframe between datasets recorded concurrently, observation times were obtained from internal computer clocks regularly synchronized to internet time servers (NIST, NPL 2023) and were recorded in FITS headers as Julian Date (JD). Heliocentric corrections were not applied. Exposures ranged between 20 and 120 seconds depending on aperture used and conditions. B band photometric observations listed in Table 2 and used in this analysis totalled 38.7 hr.

4. Spectroscopic observations

Spectroscopic observations covered the wavelength range 3750 Å to 7000 Å and were made with ALPY (R ~ 500) and LISA (R ~ 1000) spectroscopes (Shelyak Instruments 2022) auto-guided on 0.3- and 0.4-m telescopes using 23-μ slits to match typical atmospheric seeing at the observing sites. Spectra were usually integrated for 300 seconds. Spectra were processed with the ISIS spectral analysis software (Buil 2021). Spectroscopic images were bias, dark, and flat corrected, geometrically corrected, sky background subtracted, spectral profile extracted, and wavelength calibrated using integrated ArNe calibration sources. Spectra of a nearby star with a known spectral profile from the MILES library of stellar spectra (Falcón-Barroso *et al.* 2011) situated as close as possible in airmass to EV Lac at the time of observation were obtained

Table 1. Equipment used by members of the group.

Observer	*Photometry Equipment*	*Spectroscopy Equipment*
Boyd (DB)	0.35 m SCT + B filter	0.28 m SCT + LISA
Buchheim (RB)	—	0.41 m SCT + ALPY
Curry (SC)	0.11 m refractor + B, V filters	0.11 m refractor + ALPY
Parks (FP)	0.11 m refractor + B filter	0.2 m Newtonian + LISA
Shank (KS)	—	0.35 m SCT + LISA
Sims (FS)	0.11 m refractor + B, V, R_c filters	0.35 m CDK + LISA
Walker (GW)	0.5 m CDK + U, B, V, R_c filters at Sierra Remote Observatory, Auberry, CA	—
Wetmore (JW)	—	0.28 m SCT + LISA

Table 2. Journal of photometric and spectroscopic observations used in this analysis.

Observing Session	Date	Start of Photometry (JD)	Duration of Photometry (hr)	No. of Images	Band	Observer Initials	Start of Spectroscopy (JD)	Duration of Spectroscopy (hr)	No. of Spectra	Resolving Power	Observer Initials
1	2021 Oct 30	2459517.675	3.925	360	B	GW	2459517.676	4.217	51	500	RB
2	2021 Nov 4	2459522.686	3.922	360	B	GW	2459522.655	4.385	53	500	RB
3	2021 Nov 13	2459531.666	3.904	360	B	GW	2459531.593	5.695	62	500	RB
4	2021 Nov 15	2459533.665	3.900	360	B	GW	2459533.623	4.559	55	500	RB
5	2021 Nov 18	2459536.665	3.917	360	B	GW	2459536.599	4.996	58	500	RB
6	2021 Nov 21	2459540.296	4.378	530	B	DB	2459540.301	4.180	50	1000	DB
7	2021 Nov 26	2459544.608	3.903	1405	B & V	FP FS GW	2459544.580	5.000	57	500	RB
8	2021 Dec 12	2459560.557	5.254	160	B	GW	2459560.636	2.423	24	1000	JW
9	2022 Jan 13	2459593.261	3.033	410	B	DB	2459593.262	3.159	38	1000	DB
10	2022 Jan 14	2459594.280	2.546	350	B	DB	2459594.287	2.043	25	1000	DB

both immediately before and immediately after the spectra of EV Lac. By adopting a parameterization of atmospheric transmission as a function of airmass (Vidal-Madjar 2010), we were able to correct for instrumental and atmospheric losses at the airmass of each spectral image. Spectroscopic observations listed in Table 2 and used in to this analysis totalled 40.8 hr.

5. Analysis of photometric data

Visual examination of the photometric light curves in the 39 sessions with concurrent spectroscopy identified 10 sessions in which flares rose above the quiescent level with B magnitude amplitudes greater than 0.1 magnitude. This threshold was chosen as our subsequent analysis found that, at the low resolving power of our spectra, poorly-defined or lower amplitude flares did not yield spectra of sufficient quality for the quantitative analysis described here. In these 10 sessions we identified the 12 flares shown in Figure 1. Flares come in many forms, ranging from rapidly rising and falling to slowly rising and gradually decaying, with new flares starting before quiescence is reached. The start and end times of flares were identified by visual inspection of the photometric light curves as the times at which the flux level started to rise above the quiescent level and either returned to the quiescent level, a second flare began, or the observing session finished. All light curves were thus divided into flares and quiescent regions. The regions identified as flares are marked in red in Figure 1. The magnitude scale of each light curve in Figure 1 is chosen to show maximum detail. All were recorded with similar sized telescopes so have similar noise levels.

The median quiescent B magnitude during each observing session was calculated and converted to an absolute quiescent B magnitude using the distance modulus of EV Lac determined from its distance of 5.05 parsec derived from the parallax measured by Gaia (Bailer-Jones *et al.* 2021). The mean B band quiescent luminosity in erg/s during each observing session was calculated from the absolute quiescent B magnitude using B band solar luminosity and absolute solar B magnitude on the Vegamag system (Bohlin and Gilliland 2004) as transmitted through the same B band filter profile used for our observations. The mean B band quiescent magnitude and luminosity over all observing sessions were 11.89 ± 0.04 mag and $3.14 \pm 0.11 \times 10^{29}$ erg/s, respectively. The small uncertainties indicate that the quiescent energy output of EV Lac was relatively stable between October 2021 and January 2022.

Each photometric B magnitude was converted to a B band luminosity in the same way and the B band luminosity of any flare present was obtained by subtracting the mean B band quiescent luminosity for that session. These B band flare luminosities were integrated over the time span of each photometric exposure to find the energy in erg contributed to the flare by that exposure. The total energy emitted by the flare in the B band was then found by integrating these contributions through the duration of the flare. Table 3 gives information about times, magnitudes, and energies of the 12 flares. It also includes measurements of the $t_{1/2}$ and equivalent duration parameters which are described in section 8.

We also recorded a series of V magnitude measurements concurrently with B magnitudes on 26 November 2021, enabling us to derive the B–V color index shown in Figure 2. The uncertainty on individual B–V values was 0.02 mag. The mean B–V color index of EV Lac during quiescence prior to the first flare on that date was 1.66 ± 0.02 mag. Given the consistency of our quiescent B magnitudes noted in Table 3, we assume this to be representative of the quiescent color index of EV Lac on other dates. In Figure 2 we show B–V peaking at 1.37 mag and 0.98 mag during the two flares recorded on that date.

6. Analysis of spectroscopic data

The mean B magnitude during each spectrum was calculated by converting photometric B magnitudes obtained within the exposure time of the spectrum to fluxes, averaging these fluxes over the duration of the spectrum, and converting this back to a B magnitude. Using the procedure described in Boyd (2020), each spectrum was then calibrated in absolute flux in FLAM units as erg/cm^2/s/Å using this concurrently obtained mean B magnitude. This procedure made use of CALSPEC spectra (Bohlin *et al.* 2014) to establish a zero point B magnitude for the B band filter used for these observations. Given the relatively small distance of EV Lac we assume negligible interstellar reddening. Reiners *et al.* (2018) report a radial velocity for EV Lac of 0.19 km/s, and the heliocentric radial velocity of EV Lac varied by less than 10 km/s during our observations. As these are below a level which would affect our analysis, no velocity corrections were made.

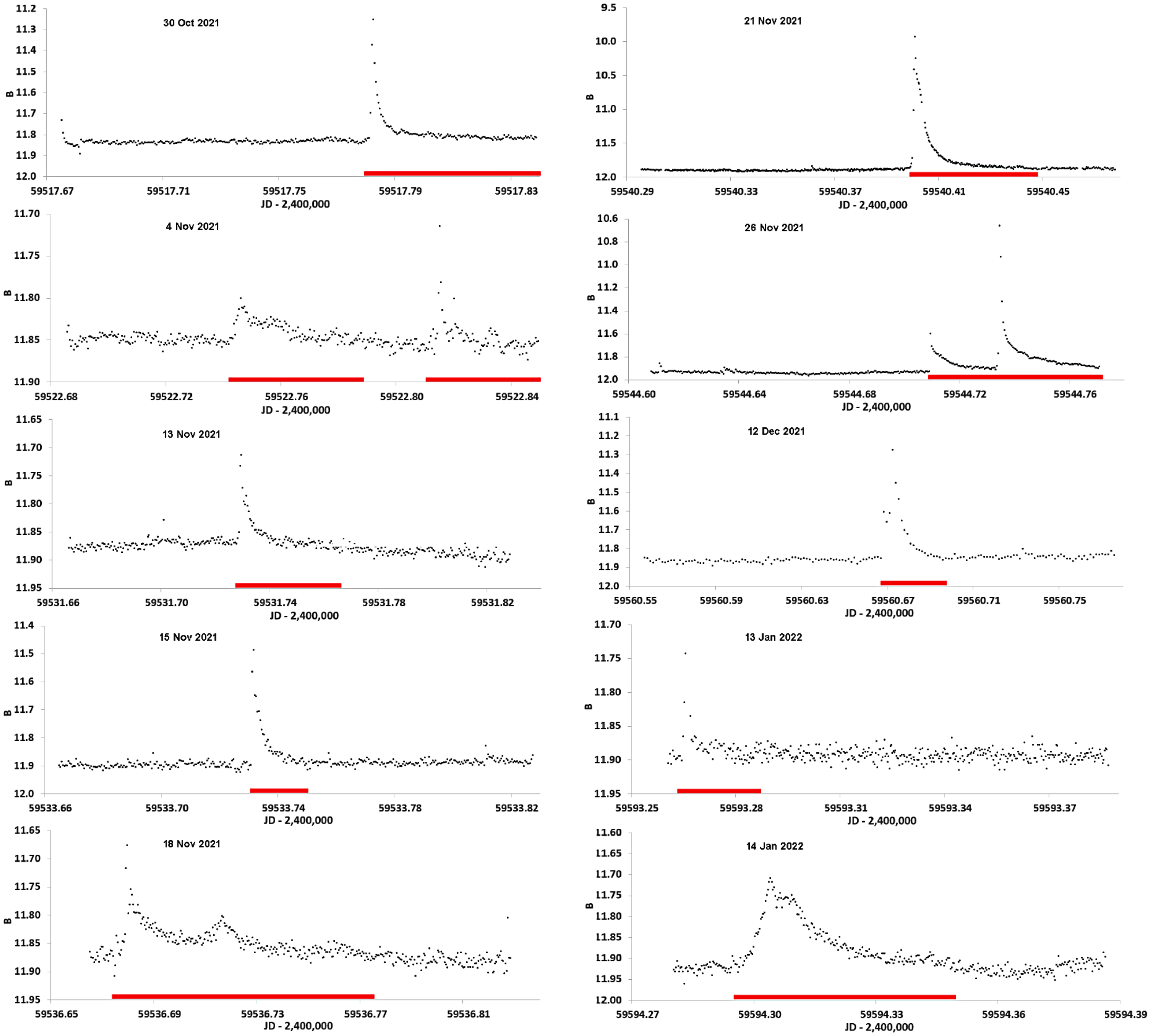

Figure 1. B magnitude light curves of 12 EV Lac flares showing in red the regions identified as flares.

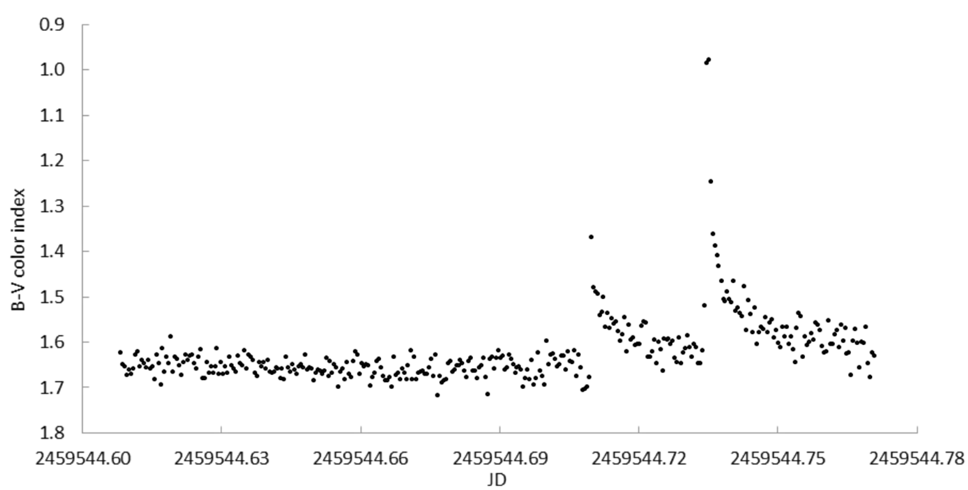

Figure 2. B–V color index of EV Lac on 26 November 2021.

Table 3. Parameters of 12 recorded flares of EV Lac.

Flare No.	Date	Start Time of Flare (JD)	Rise Time of Flare (min)	Decay Time of Flare (min)	Quiescent B-band Mag. (mag)	Peak B-band Mag. (mag)	B-band Magnitude (mag)	B-band Amplitude Log (erg)	B-band $t_{1/2}$ (min)	Equivalent Duration
1	2021 Oct 30	2459517.779	4.6	80.9	11.84	11.25	0.58	31.90	1.95	4.0
2	2021 Nov 4	2459522.741	7.2	57.7	11.85	11.80	0.05	31.17	21.03	0.8
3	2021 Nov 4	2459522.811	5.9	34.1	11.85	11.72	0.14	30.77	1.20	0.3
4	2021 Nov 13	2459531.727	3.3	48.9	11.88	11.71	0.17	31.33	3.82	1.1
5	2021 Nov 15	2459533.73	1.9	28.0	11.89	11.49	0.40	31.55	2.43	1.9
6	2021 Nov 18	2459536.675	7.2	139.4	11.87	11.68	0.20	31.94	3.82	4.6
7	2021 Nov 21	2459540.397	5.4	68.8	11.90	9.93	1.97	32.61	1.67	22.0
8	2021 Nov 26	2459544.709	0.7	30.1	11.94	11.60	0.34	31.72	2.44	2.9
9	2021 Nov 26	2459544.733	2.0	52.2	11.94	10.66	1.28	32.23	1.34	9.5
10	2021 Dec 12	2459560.667	7.9	39.6	11.86	11.28	0.58	32.07	5.31	6.1
11	2022 Jan 13	2459593.264	2.9	27.1	11.90	11.69	0.20	31.05	1.99	0.6
12	2022 Jan 14	2459594.296	11.4	70.1	11.92	11.71	0.22	31.94	15.84	4.8

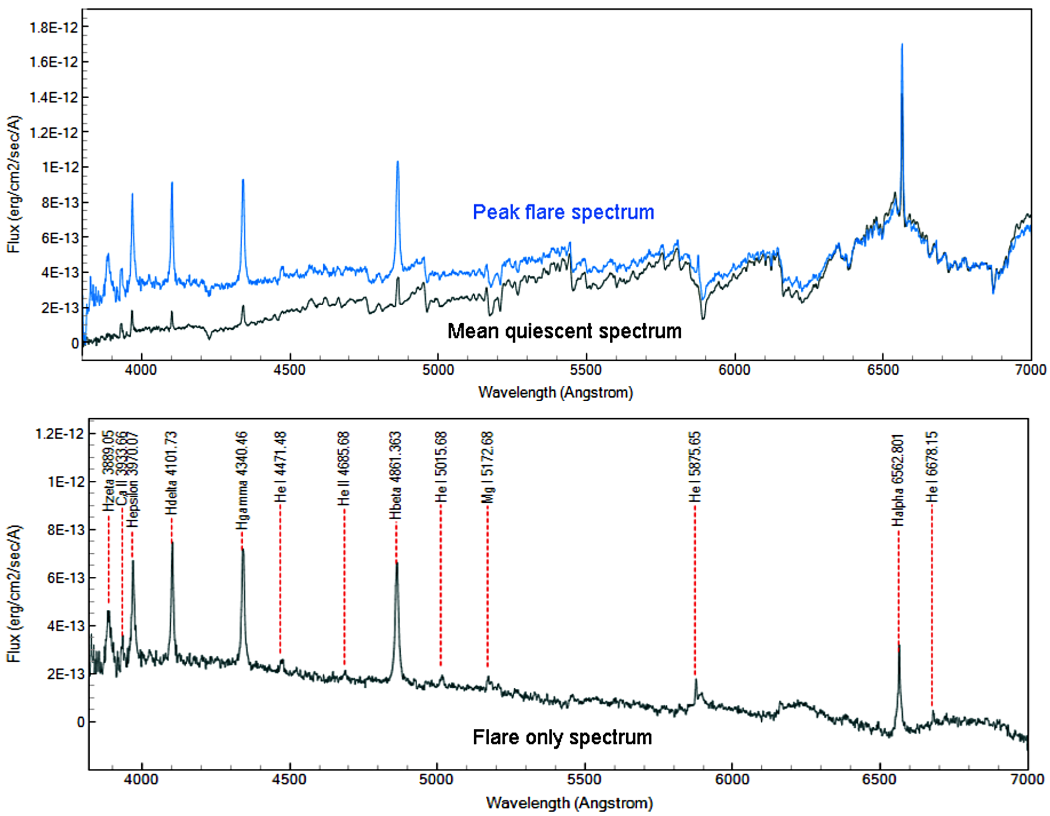

Figure 3. Mean absolute flux quiescent and peak flare spectra of EV Lac on 21 November 2021 (upper) and the peak flare-only spectrum with identified emission lines (lower).

For each observing session, all our absolute flux spectra during quiescence were averaged to find a mean absolute flux quiescent spectrum. Given that all spectra in a session are likely to have been recorded under similar conditions and processed taking account of varying airmass, we consider the standard deviation of quiescent flux at each wavelength to give a realistic estimate of the uncertainty in measuring the flux at that wavelength for all spectra in that session. By averaging over the wavelength range of each Balmer line we could also obtain an estimate of the uncertainty in the flux in these lines. Dividing the mean absolute quiescent flux in each observing session by its standard deviation at each wavelength gives an estimate of the SNR of spectral flux at that wavelength for that session. We found SNR to vary between 10 and 30 for most sessions except below ~4000 Å, where throughput started to fall due to declining equipment efficiency.

7. Calculating flare-only spectra

The mean absolute flux quiescent spectrum of EV Lac for the observing session on 21 November 2021 is shown in Figure 3 (upper). TiO molecules form in the atmosphere of cool M-type stars and produce the deep absorption bands seen in this spectrum (Gray and Corbally 2009). Also shown is the spectrum recorded at the peak of the flare. Subtracting the mean quiescent spectrum from the peak flare spectrum gives the peak flare-only spectrum.

This is shown in Figure 3 (lower) which identifies H I and He I emission lines plus a weak line of He II 4686 Å and possibly the Mg I triplet at 5167, 5173, and 5184 Å (Gray and Corbally 2009). See Table 5 below for the energy emitted in lines which could be measured reliably. The likely presence of He II in emission indicates a high temperature. The "humps" in the flare-only spectrum above 6000 Å are likely to be the result of TiO absorption bands becoming shallower during a flare relative to their depth in quiescence because of molecular dissociation during the flare.

As a check on our measurements of B-band flare energy from photometry in section 5, each flare-only spectrum was multiplied by the transmission profile of our B filter to give the B band flux in the spectrum in erg/cm^2/s. This was integrated over the time interval of each spectrum and multiplied by $4\pi d^2$, where d is the distance to EV Lac, to give the B band energy in each flare-only spectrum in erg. This assumes energy is being emitted isotropically into a sphere of radius d, although in practice emission from the flare is likely to be anisotropic. Nevertheless, it is conventional to assume isotropic emission for the purpose of calculating total energy emission. Integrating the energy recorded in each flare-only spectrum over all spectra in the flare gives a consistency check on the total B band energy in the flare. Comparing this with the measurement we obtained for the B band flare energy from photometry we find that, averaging over all flares, the two estimates of flare energy agree to within 2%.

8. Empirical flare parameters

Several parameters have been proposed in the literature to characterize properties of flares. One is $t_{1/2}$, defined by Kowalski *et al.* (2013) as the time interval between half maximum on the rise of the flare and the same height on its decay, in other words, the duration of the flare measured at half maximum. This is independent of the shape of the flare profile. We measured the $t_{1/2}$ times for the flares in our B band photometry and these are listed in Table 3.

Another measure that has been widely adopted for the longevity of flares is the equivalent duration defined in Gershberg (1972) as the ratio of flare-only energy in a specific band, in our case the B band, to quiescent luminosity in the same band. This is also independent of the flare profile. Table 3 contains our measurements of equivalent duration for each flare.

Table 4. Black-body temperatures for the four most energetic peak flare-only spectra.

Flare No.	*Date*	*JD of Spectrum*	*Black-body Temperature (K)*
7	2021 Nov 21	2459540.399	19,500 ± 500
7	2021 Nov 21	2459540.403	13,300 ± 600
9	2021 Nov 26	2459544.738	12,300 ± 400
10	2021 Dec 12	2459560.674	10,500 ± 700

9. Black-body temperature of continuum during flares

To estimate the equivalent black-body temperature of the flare-only continuum during a flare, we performed a non-linear least-squares fit of a Planck function to the continuum of flare-only spectra in the region 4120–5150 Å, excluding any emission or absorption features. In most cases the flux level of the individual flare-only spectra was too low to yield a reliable fit. However, we were able to obtain reasonable fits of black-body temperatures for four spectra at the peak of the three most energetic flares numbered 7, 9, and 10 in Table 3. These temperatures are listed in Table 4 and Figure 4 shows the black-body spectrum fitted to the peak flare-only spectrum on 21 November 2021. The uncertainty in temperature is from the covariance in the non-linear least squares fit. In Table 4, the first spectrum of flare 7 is at the flare peak, while the second immediately follows the peak.

We also attempted to fit a Planck function to a similar region of the continuum for each of the mean quiescent spectra, excluding emission or absorption features. The mean black-body temperature and standard deviation we found over all quiescent spectra was 3097 ± 251 K. From Pecaut and Mamajek (2013) the mean quiescent B–V color index of 1.66 mag observed on 26 November 2021 corresponds to spectral type M4V and effective temperature around 3200 K. Given the difficulty of measuring the low flux levels in this region of quiescent spectra, we consider the agreement with spectral type M3.5V and effective temperature 3270 ± 80 K given in Paudel *et al.* (2021) to be acceptable.

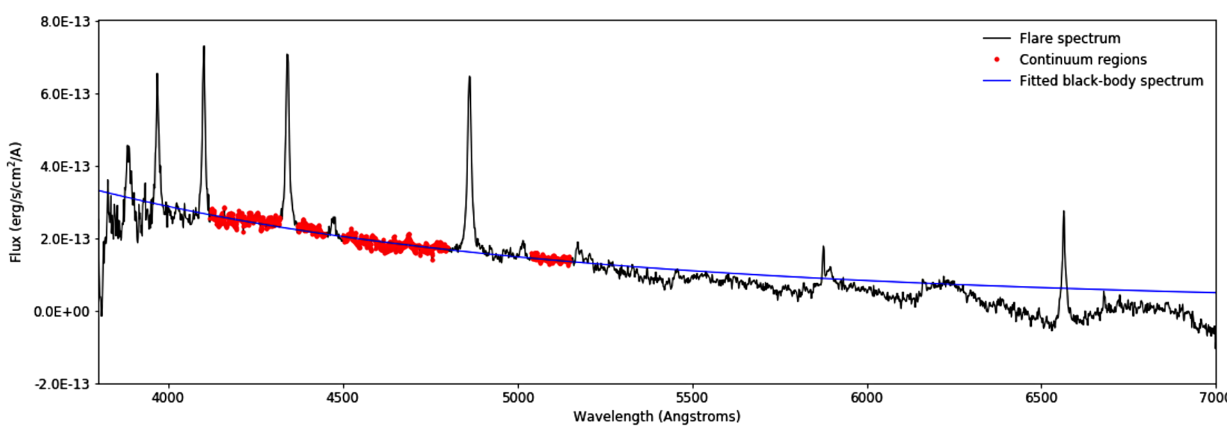

Figure 4. Fitted black-body spectrum for the peak flare-only spectrum on 21 November 2021 showing the continuum regions used for the fit.

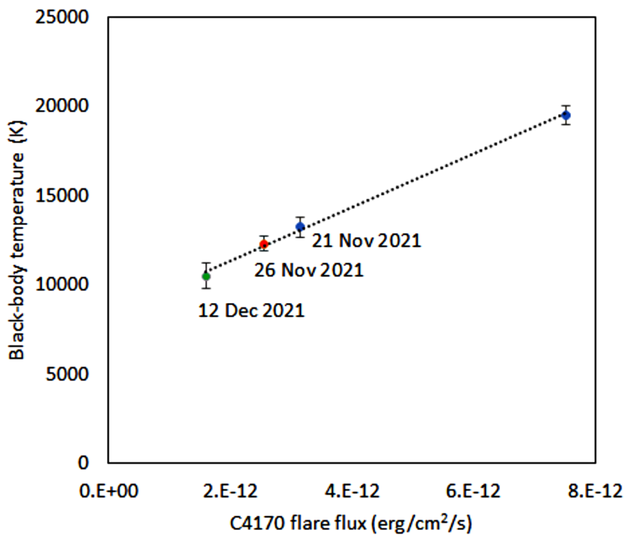

Figure 5. Black-body temperature vs flare flux in the C4170 region for the four most energetic flare-only spectra.

The peak black-body temperature of 12,300 K on 26 November 2021 contrasts with an effective temperature of around 4850 K from the peak B–V color index of 0.98 (Pecaut and Mamajek 2013). Whereas the peak black-body temperature is derived from the spectral energy continuum profile at the peak of the flare, the B-V color index is an indication of the effective temperature of the M dwarf star as a whole, increased above its quiescent level by the presence of the flare.

Kowalski *et al.* (2013) defined a region of the blue continuum labeled C4170 centered on 4170 Å with width 30 Å which could be used to provide a measure of flux level in the continuum. We integrated the flux in this region under the four flare-only spectra in Table 4 and used this to investigate a potential correlation between flare continuum flux in this region and black-body temperature at the peak of a flare. Figure 5 shows that, for flares in this temperature range, there does appear to be a linear relation between the black-body temperature derived from a fit to the continuum and the integrated flux in the C4170 region of the continuum.

In each of these three flares the black-body temperature of the following spectrum recorded five minutes later had dropped to below 4000 K and the integrated flux in the C4170 region had fallen below 10^{-12} erg/cm^2/s. This demonstrates how quickly temperature in a flare drops and energy in the flare dissipates after the initial sharp release of energy.

10. Analysis of flare energy in emission lines

In previous studies, higher resolving powers have often been used to examine in detail the behavior of individual emission lines (see for example Johnson *et al.* 2021). Working at lower resolving power and covering a wide wavelength range, we record several Balmer lines in our spectra. To find the energy emitted during a flare in a specific emission line, we first linearly interpolated the continuum under the line between regions of the continuum outside the line and integrated the area between the line profile and the interpolated continuum to obtain the integrated flux in the line in erg/cm^2/s. In doing this we were careful to set the continuum regions used for interpolation far enough away from the peak wavelength of the line that they did not include wings of the line which expanded at the peak of a flare, as shown in Figure 10. We then did the same with the mean quiescent spectrum to find the integrated flux in the line during quiescence and subtracted this from the integrated flux in the line to obtain the flux in the line from the flare in erg/cm^2/s. The flare flux in the line was then multiplied by the time interval between spectra and integrated over all spectra in the flare to get the total flux emitted by the flare in the line in erg/cm^2. Finally, this was multiplied by $4\pi d^2$, where d is the distance to EV Lac, to give the total energy in erg emitted by the flare in that emission line, again assuming isotropic emission.

The uncertainty in measuring flare energy in emission lines accrues mainly from two sources. One is the uncertainty in the flux level at each line as determined from the standard deviation in quiescent flux described earlier. The other is the uncertainty in defining the level of the interpolated continuum under emission lines because of local variations in the continuum on either side of the line. Both these sources propagate into the uncertainty in flare energy in an emission line.

Table 5 lists flare energy in the Hα to Hε Balmer lines for each flare where this is measurable. At our resolving power, the Hε line is blended with the Ca II H line, while the nearby Ca II K line is well resolved. On the basis that the two calcium lines

Table 5. Energy emitted in H I and He I 5876 Å emission lines during each flare.

Flare No.	*Date*	*Hα ($\times10^{30}$ erg)*	*Hβ ($\times10^{30}$ erg)*	*Hγ ($\times10^{30}$ erg)*	*Hδ ($\times10^{30}$ erg)*	*~Hε ($\times10^{30}$ erg)*	*He I 5876 ($\times10^{30}$ erg)*
1	2021 Oct 30	9.3 ± 1.8	8.2 ± 0.4	6.8 ± 0.4	6.4 ± 0.4	5.5 ± 1.1	—
2	2021 Nov 4	1.1 ± 1.9	4.4 ± 0.5	2.6 ± 0.4	2.5 ± 0.4	1.9 ± 1.2	—
3	2021 Nov 4	—	0.6 ± 0.3	0.1 ± 0.4	0.4 ± 0.4	—	—
4	2021 Nov 13	9.8 ± 2.8	5.2 ± 0.6	2.4 ± 0.8	1.8 ± 0.7	0.1 ± 2.2	—
5	2021 Nov 15	5.6 ± 1.3	4.3 ± 0.3	3.9 ± 0.3	2.3 ± 0.3	2.4 ± 0.8	—
6	2021 Nov 18	5.5 ± 2.7	12.6 ± 0.7	10.6 ± 0.6	8.0 ± 0.6	7.3 ± 1.6	—
7	2021 Nov 21	45.7 ± 1.2	47.0 ± 0.9	36.9 ± 1.4	25.1 ± 1.5	18.1 ± 11.6	15.4 ± 0.1
8	2021 Nov 26	7.9 ± 0.8	5.9 ± 0.3	4.8 ± 0.4	3.5 ± 0.5	0.8 ± 0.9	1.9 ± 0.1
9	2021 Nov 26	32.9 ± 1.3	26.8 ± 0.6	18.3 ± 0.7	13.3 ± 0.9	4.5 ± 1.6	4.3 ± 0.1
10	2021 Dec 12	8.8 ± 1.0	11.0 ± 0.6	8.6 ± 0.8	5.7 ± 0.8	6.2 ± 2.1	5.8 ± 0.1
11	2022 Jan 13	0.7 ± 1.0	1.6 ± 0.5	1.3 ± 0.5	1.5 ± 0.6	1.5 ± 4.3	—
12	2022 Jan 14	28.0 ± 3.7	18.6 ± 1.0	13.5 ± 0.9	12.5 ± 1.3	9.2 ± 8.2	2.8 ± 0.2

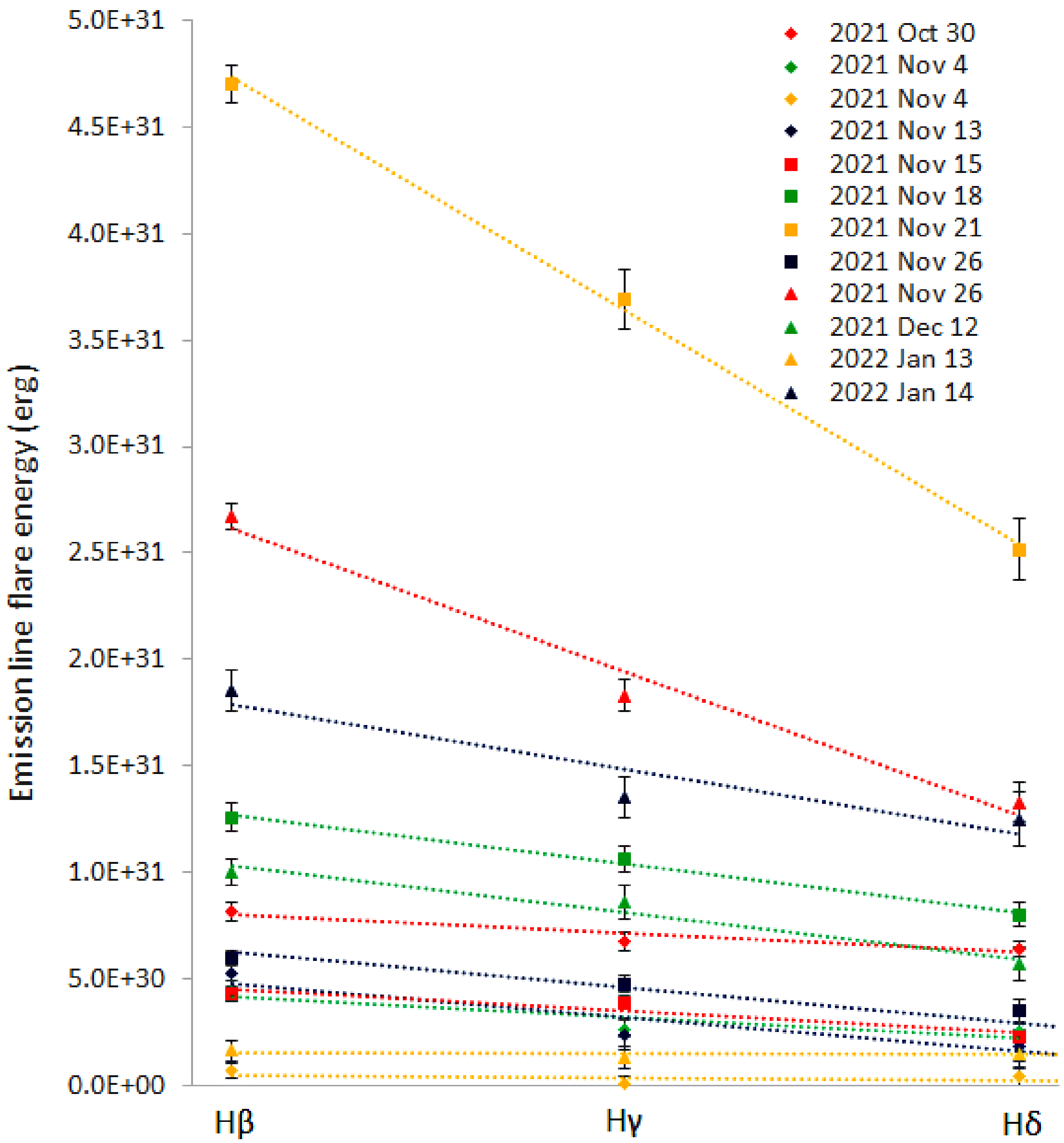

Figure 6. Decrement of Balmer line flare energy from Hβ to Hδ.

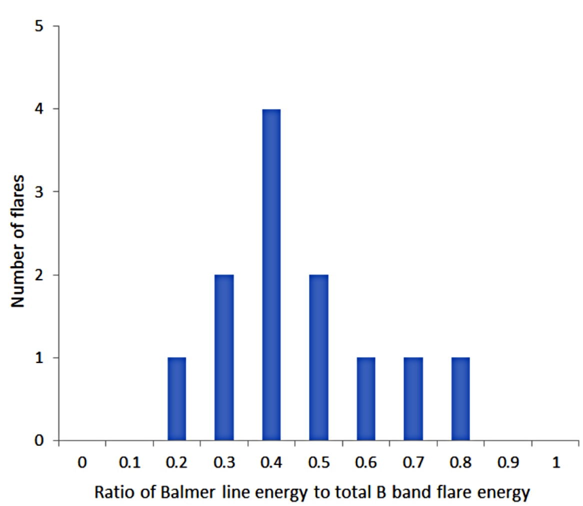

Figure 7. Histogram of the ratio for each flare of the total flare energy in the Hβ to Hε lines to the total flare energy emitted in the B band.

have broadly similar strength (Rauscher and Marcy 2006), we constructed a pseudo Hε line, labelled ~Hε, by subtracting the Ca II K flux from the Hε + Ca II H line flux. There is visible evidence in some of the R = 1000 spectra of emission lines of He I 4471, 5016, 5876, and 6678 Å and He II 4686 Å, but only the He I 5876 Å line yields credible values in some of the larger flares and these are also included in Table 5. Figure 6 shows that, particularly in the more energetic flares, flare energy decreases progressively from Hβ to Hδ.

For each flare we aggregated the total flare energy in the Hβ to Hε lines, all of which lie within the B band, and calculated the ratio of this to the total flare energy emitted in the B band. Figure 7 shows a histogram of this ratio for all flares. The median percentage contribution of these emission lines to the total energy emitted in the B band is 37%, with lower and upper quartiles of 30% and 47%. This indicates that approximately 63% of the B band energy in these flares was in the continuum.

11. Temporal evolution of Balmer emission lines during flares

As mentioned in the introduction, stellar flares have been modelled as a combination of a short-lived rise in the continuum followed by a slower increase in hydrogen Balmer emission. Our typical spectral integration time of 300 seconds limits our ability to resolve events in time, as calculations of flux are quantified per spectrum. The smaller the time difference between events, the lower the probability they would occur during different spectra and thus be resolved. In less energetic flares where spectra have lower SNR, the sequence of events is also less clearly defined. To investigate temporal evolution during flares, we have therefore again focused on the three largest flares which all have B band flare energies greater than 10^{32} erg.

For each of these flares we calculated how the integrated flare flux in the Hα, Hβ, Hγ, Hδ, and He I 5876 emission lines changed as the flares progressed. We also calculated the changing flare flux level in the continuum adjacent to each line. Figure 8 shows how the flare flux in these emission lines and in the adjacent continuum varied as a function of time since each flare started. Line flux in each spectrum is marked as connected dots in red, continuum flux similarly in blue.

We described earlier how we estimated uncertainty in the spectral flux at Balmer emission lines from the standard deviation of flux in our quiescent spectra and from the uncertainty in defining the interpolated continuum under these lines. By combining these flux uncertainties in our flare and quiescent spectra, we calculated uncertainties in our flare-only spectra for the flux in Balmer emission lines and in the continuum flux at these lines. In Figure 8, one standard deviation of uncertainty in line flux is shown as red bands and in continuum flux as blue bands. In general, uncertainties increase as the flux in spectra decreases. Although, as we shall see in Figure 10, growth in the continuum at Hα in flares tended to be small, the Hα emission lines in these flares grew strongly and could be well measured, as shown in Table 5.

During the largest flare on 21 November 2021, each of the emission lines peaked one spectrum later than their adjacent continuum. In the other two flares, emission lines and continuum peaked during the same spectrum. There were two flares on 26 November 2021 (see Figure 1), with flux dropping to almost zero between them. It is notable that flux in the continuum decayed more quickly following the peak than flux in the Balmer lines. It appears in Figure 8 that there is a pattern with shorter wavelength Balmer lines decaying more quickly. Flux in the He I 5876 Å line remained high for longer than the Balmer lines before then decaying rapidly. This is similar to behavior reported in Hawley and Pettersen (1991) for AD Leo. We also noted that the peak in B band photometry always occurred during the same spectrum as the peak in continuum flux. This may be expected as the peak in continuum flux is a major driver for the photometric peak.

To quantify the tendency for shorter wavelength Balmer lines to decay more quickly, we measured the $t_{1/2}$ times of the Hα to Hδ Balmer lines in the three largest flares. This is the time interval between half maximum flux on the line rising and the same height on its decay, in other words the duration of the line measured at half maximum. These times are listed in Table 6. Uncertainties in flux are propagated into uncertainties in time. Figure 9, which plots these times along with linear fits to the data for each flare, shows that the duration of flares in Balmer lines is indeed positively correlated with their wavelength. This behavior is similar to that shown in Figure 18 and related text in Kowalski *et al.* (2013). Note also that the $t_{1/2}$ times of the Balmer lines in flares are several times longer than the $t_{1/2}$ times measured in the peaks of B band photometry given in Table 3. Again, this is consistent with the continuum decaying faster during flares relative to the decay in Balmer emission.

12. Spectral evolution of Balmer emission lines

Figure 10 compares Balmer line profiles in flux calibrated spectra at flare peak and quiescence on 21 November 2021. This shows that absolute flux in the Hβ, Hγ, and Hδ lines and in the continuum adjacent to these lines increased considerably relative to the quiescent level during the flare, whereas at Hα the continuum in quiescence was already higher and increased relatively little during the flare. Flare energy in the Hα line was broadly similar to that in the Hβ line as Table 5 shows.

To measure the Full Width at Half Maximum (FWHM) in Angstroms of Balmer emission lines during flares, we fitted Gaussian profiles to the Balmer lines in flare-only spectra after subtracting the interpolated continuum under the line. In most cases the line profiles were well fitted by a Gaussian profile, but in spectra at the peak of the larger flares we saw an excess of flux in the wings of the lines, particularly towards shorter wavelengths. In Figure 11 we show Gaussian fits to the Hβ line in the first three spectra of the largest flare peak on 21 November 2021. In the first two spectra there is clearly additional emission in the form of low wings which are more extensive on the blue side of the line and reach to around –1500 km/s. Although these wings are relatively poorly defined in our spectra, we attempted to model them by including an additional wide, low amplitude Gaussian component in the fits for the first two spectra. We found that the peaks of these additional components were displaced by around –100 km/s relative to the Hβ line and had FWHM of ~1600 km/s. This suggests that there was short-lived, blue-shifted emission in the Hβ line at the start of the flare.

In Figure 12 we show how FWHM of the Hα to Hδ lines varied during the course of the large flare on 21 November 2021. After a brief expansion, the lines rapidly settled back to their pre-outburst width.

To investigate the relationship in time between the changing flux (in Figure 8) and width (in Figure 12) of the Balmer lines as a flare evolves, we show in Figure 13 plots of flux vs FWHM for the Hα to Hδ lines during the peak of the large flare on 21 November 2021. The trajectories all follow a counter-clockwise loop whose direction of travel is marked with an arrow. All lines except Hα reach their maximum width in the spectrum before the lines reach their peak flux.

13. Summary and conclusions

Working as a collaborative group of small telescope scientists, we observed 12 flares of the dwarf M star EV Lac

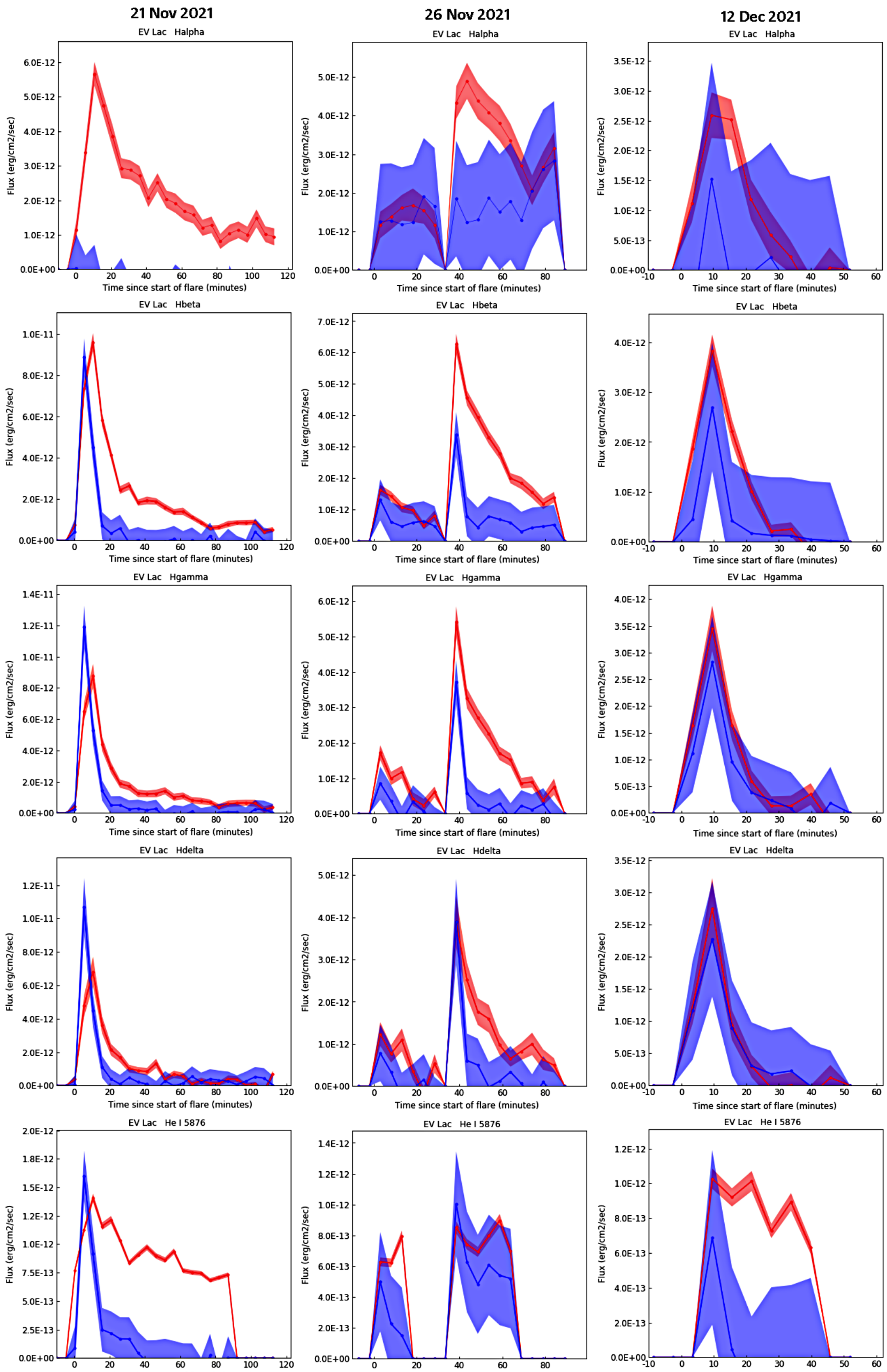

Figure 8. Temporal evolution of emission line flux and continuum flux in the three largest flares.

Table 6. $t_{1/2}$ times of Balmer emission lines in the three largest flares.

Flare No,	*Date*	*Hα $t_{1/2}$ (min)*	*Hβ $t_{1/2}$ (min)*	*Hγ $t_{1/2}$ (min)*	*Hδ $t_{1/2}$ (min)*
7	2021-Nov-21	32 ± 3	16 ± 2	12 ± 2	13 ± 2
9	2021-Nov-26	36 ± 5	20 ± 4	13 ± 4	12 ± 2
10	2021-Dec-12	18 ± 2	15 ± 2	12 ± 2	10 ± 2

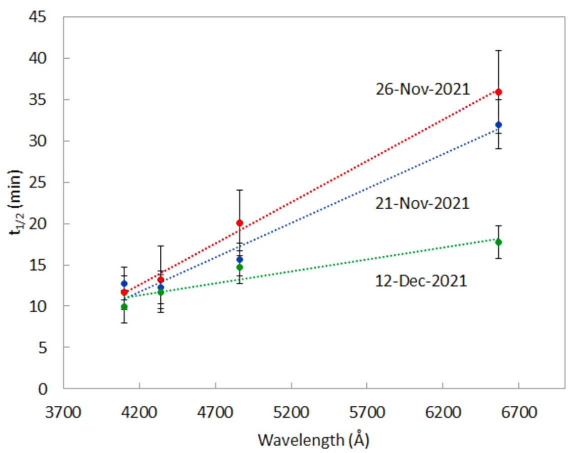

Figure 9. $t_{1/2}$ time vs wavelength for the three largest flares showing a positive correlation between Balmer line flare duration and wavelength.

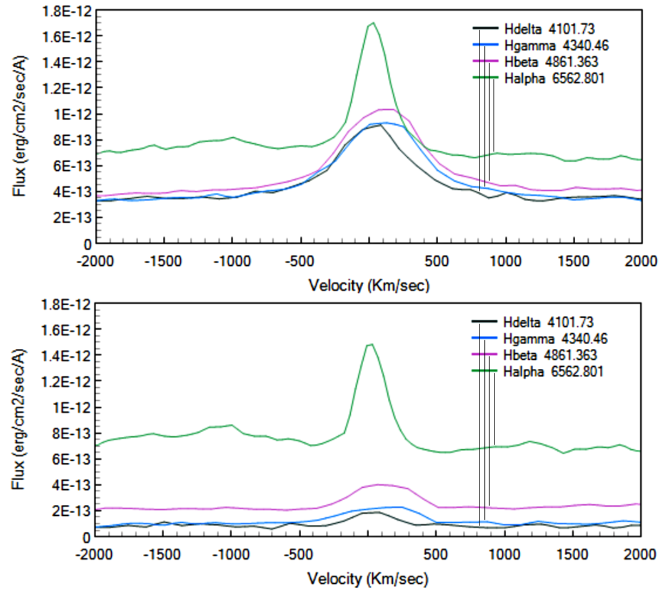

Figure 10. Balmer line profiles at flare peak (upper) and quiescence (lower) on 21 November 2021.

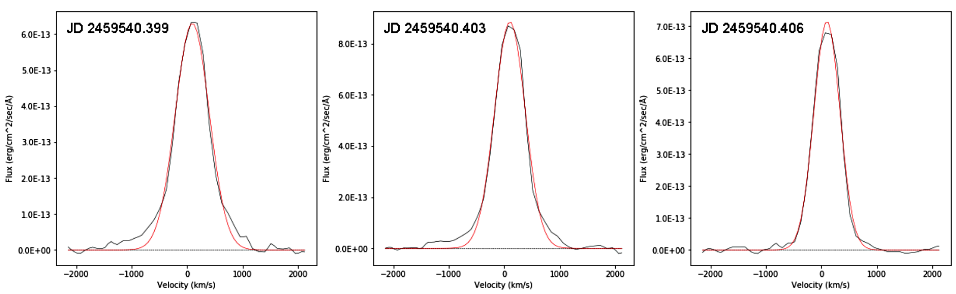

Figure 11. Gaussian fits to Hβ emission lines in the first three flare-only spectra during the flare peak on 21 November 2021. Data are marked as a solid black line, the Gaussian fit as a solid red line, and the continuum level as a dotted black line.

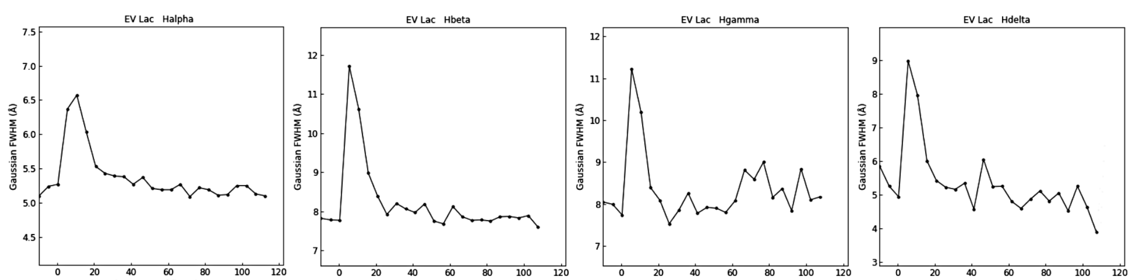

Figure 12. Evolution of FWHM in Hα to Hδ lines during the flare on 21 November 2021.

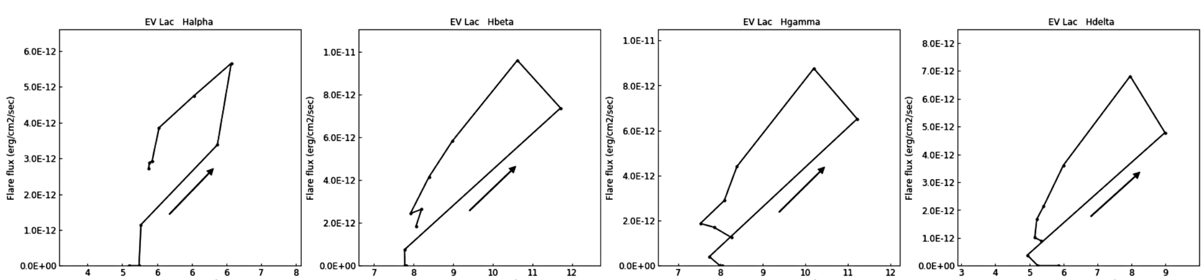

Figure 13. Relationship between flare flux and FWHM for the Hα to Hδ lines during the flare peak on 21 November 2021. The arrows show the direction of travel in time.

with B-band amplitude greater than 0.1 magnitude for which we concurrently recorded low resolution spectroscopy and B-band photometry. We calibrated our spectra in absolute flux using the B-band photometry and calculated B-band flare energies in the range Log E = 30.8 to 32.6 erg. We subtracted mean quiescent spectra to obtain flare-only spectra, calculated the energy emitted in Balmer emission lines during each flare, and monitored how this changed as flares evolved. Although our time resolution was limited by the length of our spectral exposures (300 sec), we observed in the brightest flare that flux in the continuum clearly peaked before flux in the Balmer emission lines. We found that flux in the continuum decayed faster than flux in emission lines and that shorter wavelength Balmer lines decayed faster. By fitting a Planck function to the blue continuum of the three brightest flares, we obtained their black-body temperatures.

Several publications (for example Alekseev *et al.* 1994; Abdul-Aziz *et al.* 1995; Osten *et al.* 2005; Paudel *et al.* 2021) have reported on optical band photometric and spectroscopic observations of EV Lac. These have mostly used meter-class telescopes and have rarely managed to obtain concurrent photometric and spectroscopic observations because of constraints on observing schedules. We have attempted to remedy that deficit through a coordinated campaign of concurrent photometric and spectroscopic observations of flares using amateur-sized telescopes. Our data can be compared with and potentially used to constrain the predications of flare models.

14. Acknowledgements

We thank our referee for a very thorough and helpful review. We acknowledge with thanks the resources provided by the AAVSO and BAA in support of the amateur community. Our research made use of NASA's Astrophysics Data System Bibliographic Services and the SIMBAD database operated at CDS, Strasbourg, France. The work of the Astropy collaboration has been extensively used in the analysis of our data.

References

AAVSO. 2022, Variable Star Plotter (VSP, https://www.aavso.org/apps/vsp/).
Abdul-Aziz, H. *et al.* 1995, *Astron. Astrophys., Suppl. Ser.*, **114**, 509.
Alekseev, I. Y. *et al.* 1994, *Astron. Astrophys.*, **288**, 502.
Allred, J. C., Kowalski, A. F., and Carlsson, M. 2015, *Astrophys. J.*, **809**, 104.
Astropy Collaboration, *et al.* 2018, Astron. J., **156**, 123.
Bailer-Jones, C. A. L., Rybizki, J., Fouesneau, M., Demleitner, M., and Andrae, R. 2021, *Astron. J.*, **161**, 147.
Benz, A. O., and Güdel, M. 2010, *Annu. Rev. Astron. Astrophys.*, **48**, 241.
Berry, R., and Burnell, J. 2005, *The Handbook of Astronomical Image Processing*, Willmann-Bell, Richmond, VA.
Bohlin, R. C., and Gilliland, R. L. 2004, *Astron. J.*, **127**, 3508.
Bohlin, R. C., Gordon, K. D., and Tremblay, P.-E. 2014, *Publ. Astron. Soc. Pacific*, **126**, 711.
Boyd, D. 2020, "A method of calibrating spectra in absolute flux using V magnitudes" (https://britastro.org/sites/default/files/absfluxcalibration.pdf).
British Astronomical Association. 2022, BAA Photometry Database (https://britastro.org/photdb).
Buil, C. 2021, ISIS Integrated Spectrographic Innovative Software (http://www.astrosurf.com/buil/isis-software.html).
Centre de Données astronomiques de Strasbourg. 2007, simbad Astronomical Database (http://simbad.u-strasbg.fr/simbad).
Diffraction Limited. 2023, MaxIm DL image processing software (https://diffractionlimited.com/product/maxim-dl).
Falcón-Barroso, J. Sánchez-Blázquez, P., Vazdekis, A., Ricciardelli, E., Cardiel, N., Cenarro, A. J., Gorgas, J., and Peletier, R. F. 2011, *Astron. Astrophys.*, **532A**, 95.
Gershberg, R. E. 1972, *Astrophys. Space Sci.*, **19**, 75.
Gray, R. O., and Corbally, C. J. 2009, *Stellar Spectral Classification*, Princeton Univ. Press, Princeton, NJ.
Günther, M. N., *et al.* 2020, *Astron. J.*, **159**, 60.
Hawley, S. L., and Pettersen, B. R. 1991, *Astrophys. J.*, **378**, 725.
Jackman, J. A. G., *et al.* 2021, *Mon. Not. Roy. Astron. Soc.*, **504**, 3246.
Johnson, E. N., *et al.* 2021, *Astron. Astrophys.*, **651A**, 105.
Joy, A. H., and Abt, H. A. 1974, *Astrophys. J., Suppl. Ser.*, **28**, 1.
Kafka, S. 2022, variable star observations from the AAVSO International Database (https://www.aavso.org/aavso-international-database-aid).
Kowalski, A. F., Hawley, S. L., Wisniewski, J. P., Osten, R. A., Hilton, E. J., Holtzman, J. A., Schmidt, S. J., and Davenport, J. R. A. 2013, *Astrophys. J., Suppl. Ser.*, **207**, 15.
Lépine, S. Hilton, E. J., Mann, A. W., Wilde, M., Rojas-Ayala, B., Cruz, K. L., and Gaidos, E. 2013, *Astron. J.*, **145**, 102
National Institute of Standards and Technology. 2022, NIST Internet Time Servers (https://tf.nist.gov/tf-cgi/servers.cgi).
National Physical Laboratory. 2022, MSF radio time signal (https://www.npl.co.uk/msf-signal).
Osten, R. A., Hawley, S. L., Allred, J. C., Johns-Krull, C. M., and Roark, C. 2005, *Astrophys. J.*, **621**, 398.
Paudel, R., *et al.* 2021, *Astrophys. J.*, **922**, 31.
Pecaut, M. J., and Mamajek, E. E. 2013, *Astrophys. J., Suppl. Ser.*, **208**, 9.
Pettersen, B. R. 1980, *Astron. J.*, 85, 871.
Popinchalk, M., Faherty, J. K., Kiman, R., Gagné, J., Curtis, J. L., Angus, R., Cruz, K. L., and Rice, E. L. 2021, *Astrophys. J.*, **916**, 77.
Rauscher, E., and Marcy, G. W. 2006, *Publ. Astron. Soc. Pacific*, **118**, 617.
Reid, I. N. Hawley, S. L., and Gizis, J. E. 1995, *Astron. J.*, **110**, 1838.
Reiners, A., *et al.* 2018, *Astron. Astrophys.*, **612A**, 49.
Shelyak Instruments. 2022, (https://www.shelyak.com).
Vidal-Madjar, A. 2010, *Astron. Astrophys.*, **523A**, 57.

σ Octantis

Bill Rea
Richmond, New Zealand; rea.william@gmail.com

Received December 2, 2022; revised February 3, March 3, 2023; accepted March 15, 2023

Abstract We examine data from three Sectors of observations from NASA's Transiting Exoplanet Survey Satellite (TESS) for the δ Scuti star σ Octantis = HD 177482. We were unable to conclude that it is a hybrid δ Sct/γ Dor variable as reported in earlier literature because the evidence for the presence of active γ Dor frequencies was absent from one Sector's data and only weakly statistically significant in the other two. We report that several of the δ Sct frequencies showed statistically significant amplitude modulation between the three TESS Sectors.

1. Introduction

On the HR diagram the δ Scuti variables lie at the intersection of the main sequence and the classical instability strip. Diagrams showing the location of different types of pulsating variables, such as Figure 3.2 of Catelan and Smith (2015), often show the regions occupied by roAp, δ Sct, SX Phe, γ Dor, and RR Lyr variables overlapping to some extent. Of particular interest for asteroseismology are stars which lie in the overlapping regions of δ Sct and γ Doradus variables because these stars should pulsate in both pressure and gravity modes (p- and g-modes), which are the pulsation modes of δ Sct and γ Dor variables, respectively.

Although the prototype for the class, δ Sct, was known to be variable since Campbell and Wright (1900), as a class they were not recognized as a distinct group of variable stars until Eggen (1956). The discovery of the γ Dor class of variables is usually credited to Balona *et al.* (1994), but it is clear that they drew on evidence from a number of authors published over the previous 20 years and conference papers on them had appeared earlier such as Krisciunas (1993). However, it has also been known almost as long as they have been recognized as a separate class of pulsators that the two regions overlap so that a single star may pulsate with both δ Sct and γ Dor frequencies (Breger and Beichbuchner 1996). Such stars are known as hybrid δ Sct/γ Dor stars.

σ Octantis = HD 177482 (see Table 1 for some basic data) was first identified as a δ Sct by McInally and Austin (1978) based on observations obtained using the Optical Craftsmen 61-cm telescope at University of Canterbury's Mt. John Observatory and, apart from the paper of Crouzet *et al.* (2018), has been little studied since then. It was the subject of two very short papers by Coates *et al.* (1981) and Tsvetkov (1982) which did little more than establish a single pulsation period of 0.097 day together with its amplitude of $\Delta V = 0.025$ magnitudes and a conjecture that it pulsates only in the fundamental mode. The 848 observations in the American Association of Variable Star Observers International Database (AAVSO; Kafka 2022) were obtained in a few short observing sessions in 1981, 1986, and 1989. The 1981 observations contributed to Coates *et al.* (1981) but the later work, by the Auckland Photoelectric Observers Group, does not appear to have led to further analysis and publication.

Based on four Antarctic winter seasons of photometry from 2008 to 2011, Crouzet *et al.* (2018) recently reported that σ Oct was a hybrid δ Sct/γ Dor pulsator, and they reported 21 active frequencies, 17 within the δ Sct range and four within the γ Dor range. Crouzet *et al.* (2018) reported that four of the δ Sct frequencies showed amplitude modulation, confirming Bowman *et al.* (2016), who studied 983 δ Sct stars observed by *Kepler*, and reported that 61.3% exhibited amplitude modulation. In particular, the amplitude of σ Oct's main frequency of the first two seasons' observations (2008 and 2009), approximately 10.49 cycles d^{-1}, decreased by a factor of almost 10 during the final seasons of observations (2010 and 2011) meaning that it was no longer the highest amplitude frequency. They further reported that the γ Dor frequencies had low amplitudes.

The unpublished report of Rea (2019), based on 350 high resolution spectra from two, two-week observing runs, also concluded that σ Oct had both δ Sct and γ Dor pulsations active and hence should be considered a hybrid δ Sct/γ Dor variable.

This paper analyzes data from the Transiting Exoplanet Survey Satellite (TESS) (Ricker *et al.* 2014), which observed σ Oct in sectors 12, 27, and 39 of its mission. Table 2 gives the date ranges for the observations within these sectors. This provides a useful set of data to check the conclusions of these previous works and look for any changes in the active frequencies.

The remainder of the paper is structured as follows. section 2 gives details of the data used, section 3 presents the results of the frequency analyses carried out, section 4 contains the discussion, and section 5 gives our conclusions.

Table 1. Basic data on σ Oct.

Parameter	*Value*	*Source*
R.A.	$21^h\ 08^m\ 46.85^s$	VSX
Dec.	–88° 57' 23.4"	VSX
Spectral Type	F0IV	VSX/SIMBAD
Period	0.097 d/2.3 h	VSX
Magnitude	5.45 V	VSX
Amplitude	0.05 V	VSX
Distance	90.09 pc ± 0.50	Gaia
TIC	468184895	TASOC

Notes: TIC is the TESS Input Catalogue number. The sources are: the Variable Star Index (VSX; Watson et al. *2014); SIMBAD (CDS Strasbourg 2007); Gaia Collab. (2020), and TASOC (2023).*

2. Data and methods

2.1. Data

The raw data for this paper were downloaded from the TESS Asteroseismic Science Operations Center (TASOC; https://tasoc.dk). Sector 12 data were downloaded on 30 Jun 2020, Sector 27 data on 30 Nov 2020, and Sector 39 data on 19 May 2022.

The reported corrected flux was converted to magnitudes using the value for σ Oct's magnitude in the V band as reported on the TASOC web site as the mean value for each observation run. Observations were discarded if the value in the Pixel Quality Field (PQF) was non-zero or either the date or the corrected flux was recorded as not-a-number (nan). Table 2 summarizes the date ranges and number of usable data points for each sector's observations.

2.2. Frequency analysis

Frequency analysis was carried out using three software packages. Analysis was primarily carried out using FAMIAS (Zima 2008), an interactive package in which the user guides each step of the frequency analysis process. A minimum signal-to-ratio (SNR) of four was used with FAMIAS to determine if an extracted frequency was statistically significant. Frequency analysis was also carried out using SigSpec (Reegen 2011), which uses the spectral significance rather than the signal-to-noise ratio as the statistical quantity to determine if a frequency is significant. Details of the spectral significance can be found in Reegen (2007). Briefly, the significance spectrum is based on an analytical solution of the probability that a discrete Fourier transform (DFT) peak of a given amplitude does not arise from white noise in a non-equally spaced data set which is typical of astronomical light curves. The underlying Probability Density Function (PDF) of the amplitude spectrum generated by white noise can be derived explicitly if both frequency and phase are incorporated into the solution. The spectral significance depends on frequency, amplitude, and phase in the DFT, and takes into account the time-domain sampling. Reegen (2007) states that the spectral significance is an unbiased statistical estimator.

SigSpec operates in a batch processing mode. The user provides a file of data and sets analysis options in an initialization file. SigSpec then reads both files and proceeds to analyze the data without further input from the user. A minimum spectral significance of five was used with SigSpec to determine if a frequency was statistically significant. This is equivalent to an SNR of four used with FAMIAS.

The package Period04 (Lenz and Breger 2005) Version 1.2 was also used, primarily as a check on the frequencies reported by FAMIAS. Period04 is an interactive package in which the user guides each step of the analysis. The frequencies and amplitudes reported by Period04 were sufficiently close to those of FAMIAS that the results obtained from Period04 are not reported separately. For example, in the Sector 12 data the first 25 identified frequencies where the same for Period04 and FAMIAS.

Recently Rea (2022a, b) proposed a simple modification to the method of frequency analysis which involved breaking up the frequency range to be analyzed into non-overlapping ranges and particularly suited frequency analysis software which used batch processing such as SigSpec. The method of splitting the frequency range was subjective and based on a visual inspection of the grouping of frequencies in the periodogram. The periodogram in Figure 2 did not have particularly clear gaps in the manner of either Rea (2022a) Figure 6 or Rea (2022b) Figure 4. Nevertheless, we split the full range into six sub-ranges in two different ways. Table 4 gives the ranges; the results part of the Table will be discussed further below. The reasoning is as follows and one possible alternative is also given:

Table 2. Details of the TESS data used in this paper.

Sector	*JD Range*	*Days of Observations*	*Usable Data Points*	*Amplitude (Mag.)*
12	1624.96–1652.89	27.93	19,086	0.0531
27	2036.28–2059.77	23.49	16,156	0.0525
39	2361.77–2389.72	27.95	19,337	0.0547

Notes: The JD Range gives the observation dates as Barycentric Julian Date –2457000. The final column reports the maximum amplitude of the light curve during the sector.

Table 3. A summary of the significant frequencies reported by FAMIAS (SNR > 4) and SigSpec (significance > 5).

	FAMIAS			*SigSpec (0–50)*		
Sector	*DScuti*	*GDor*	*Other*	*DScuti*	*GDor*	*Other*
12	20	0	0	483	45	6
27	24	3	0	368	41	5
39	26	2	0	460	47	7
				SigSpec (0–25)		
12	—	—	—	380	45	7
27	—	—	—	312	40	4
39	—	—	—	375	46	7

Notes: The frequency range used for γ Dor (GDor) was 0.3 to 3 cycles d^{-1}, for δ Scuti (DScuti) > 3 cycles d^{-1}; frequencies outside these ranges were classified as "other." The first set of results for SigSpec covers the frequency range 0 to 50 cycles d^{-1}, and the second set covers the range 0 to 25 cycles d^{-1}.

Table 4. The numbers of significant frequencies reported in the two restricted range analyses using SigSpec.

Range	*Sector 12*	*Sector 27*	*Sector 39*
0–3	0	3	0
3–7	0	0	0
7–9.5	6	9	4
9.5–11.1	25	23	19
11.1–16	72	54	69
16–50	40	32	33
Total	143	121	125
11.1–12.5	20	23	23
12.5–50	90	62	80
Total	141	120	126

0–3 This range included the γ Dor frequencies and lower. An alternative would have been to extend this range to a frequency of around four cycles d^{-1} because there were a number of low peaks in the periodogram, one of which is the frequency G1 of Table 6, above the three cycles d^{-1} cutoff.

3–7 This frequency range appears devoid of any peaks in the periodogram apart from the G1 frequency just mentioned.

7–9.5 There is a very small gap in the periodogram at around 9.5 cycles d^{-1} where there are no distinct peaks visible.

9.5–11.1 In common with the previous frequency range there is a very small gap in the periodogram at around 11.1 cycles d^{-1} where there are no distinct peaks visible.

11.1–16 This frequency range was sparsely populated with frequency peaks with the last visually important peak just inside the cut-off frequency.

16–50 The final frequency range had no visually important peaks. We also ran an analysis on the range 16–25 cycles d^{-1} but this gave identical numbers of frequencies as the longer (to 50 cycles d^{-1}) range and are not reported separately.

A second restricted range analysis was run splitting the range 11.1–50 cycles d^{-1} as follows:

11.1–12.5 This split took advantage of a clear region of very low peaks in the periodogram around 12.5 cycles d^{-1}.

12.5–50 Given the spacing between the visually important peaks above 12.5 cycles d^{-1} the final group of frequencies was analyzed as a single group. We also ran an analysis of the 12.5–25 cycles d^{-1} range but these gave identical numbers of frequencies as the longer (to 50 cycles d^{-1}) range and are not reported separately.

User-written R Code (R Core Team 2019) was used to prepare the data, plot the light curves, and further analyze the output of FAMIAS, PERIOD04, and SIGSPEC. An important task carried out in R was to check whether each statistically significant frequency matched a distinct feature in the periodogram or was a spurious frequency resulting from the pre-whitening process used by all three packages; see Balona (2014) for a study of these types of spurious frequencies.

3. Results

Figure 1 presents the full light curves for the three sectors' observations. The approximately one-day data gaps were caused by the data download from the satellite to the ground.

Figure 2 presents the periodograms of the data and of the residuals after all significant frequencies were fitted and removed. The lower panel presents the spectral window for the Sector 12 data as generated by FAMIAS. The periodograms and spectral windows for Sectors 27 and 39 were not sufficiently different from Sector 12 to warrant reporting them separately.

Initially, frequency analysis was carried out to 100 cycles d^{-1} because Bedding *et al.* (2020) had reported statistically significant frequencies in some δ Sct stars up to 80 cycles d^{-1}. The periodogram for the σ Oct was featureless beyond 22 cycles d^{-1} for all three sectors' data and so subsequent analysis was reduced to cover the frequency range 0 to 25 cycles d^{-1}.

The default frequency range for SIGSPEC is 0 to 50 cycles d^{-1} and this was initially run. Because of the featureless periodogram above 25 cycles d^{-1}, a second set of analyses was run using the range of 0 to 25 cycles d^{-1}. Both sets of results are reported here in Table 3.

A summary of the results of the frequency analyses by FAMIAS and SIGSPEC are presented in Table 3. The frequency ranges for δ Sct, γ Dor were guided by Catelan and Smith (2015) Table 9.1. 0.3–3 cycles d^{-1} were classified as γ Dor frequencies; frequencies above three cycles d^{-1} were classified as δ Sct. Frequencies below 0.3 cycles d^{-1} were classified as Other.

Table 4 reports the number of significant frequencies reported by SIGSPEC when the two restricted range analyses were carried out.

A total of 41 distinct significant frequencies were reported by FAMIAS from the three sectors of observations. Of these only 13 frequencies in the δ Sct range were statistically significant in all three sectors. Table 5 presents details of these 13 frequencies using their ordering from the Sector 12 data.

γ Dor frequencies were reported by FAMIAS; details of these frequencies are presented in Table 6. Included in this Table is the 3.55 cycles d^{-1} frequency, which is above the usual cut-off frequency for γ Dor and hence could have been classified as a δ Sct frequency and included in Table 5. However, one should note that Grigahcene *et al.* (2010), in their Figure 2, showed that for hybrid γ Dor/δ Sct stars the γ Dor and δ Sct frequency ranges should not overlap. If we had taken their gap into account, which depends on a precise measure of the effective temperature, this particular frequency should perhaps be classified as Other.

Figure 3 presents a plot of the residuals after the 20 statistically significant frequencies identified by FAMIAS had been fitted to the Sector 12 data. Light curves of the residuals for Sectors 27 and 39 were also generated but are not reported separately.

4. Discussion

A feature of the light curves of all three sectors in Figure 1 was the extremely complex light curve which is typical of many δ Sct stars. Such complexity is the result of numerous pulsation frequencies being active in the star at the same time. Qualitatively, the light curve from Sector 39 does appear slightly different from the previous two Sectors in that the switching between high and low amplitude periods seems to be more frequent. When analyzed by FAMIAS there were more significant frequencies active in the Sector 39 data than Sector 12 (28 in Sector 39 and 20 in Sector 12), but the number of significant frequencies only differed by one between Sector 27 and Sector 39. A natural question which arises, particularly from the often abrupt changes in amplitude, which sometimes occur in a matter of only a few minutes, is whether this phenomenon is purely the result of numerous frequencies being active, or whether data exhibit some sort of deterministic chaos. When investigating the first option it was clear when fitting models to the data that even the inclusion of only the ten highest amplitude frequencies gave excellent fits and reproduced the often abrupt changes in amplitude well, meaning they were the result of beating between close frequencies. It can be seen in Table 5 that frequencies D3, D7, and D10 all had their highest amplitudes in the Sector 39 data. While there are empirical tests for chaotic behavior, such as those outlined in Sprott (2003), preliminary

Table 5. A summary of significant δ Sct frequencies.

No.	Frequency Sector 12	Frequency Sector 27	Frequency Sector 39	Amplitude Sector 12	Amplitude Sector 27	Amplitude Sector 39	Crouzet et al. (2018)
D1	10.49119	10.493168	10.492485	10.37	9.28	10.58	Y
	(68.984)	(67.383)	(99.237)	(0.69)	(0.67)	(0.58)	
D2	10.74000	10.740016	10.741156	3.09	3.23	3.18	Y
	(20.398)	(22.681)	(29.504)	(0.67)	(0.64)	(0.55)	
D3	9.35991	9.361072	9.361837	2.87	3.70	3.95	Y
	(19.996)	(26.882)	(43.653)	(0.67)	(0.64)	(0.55)	
D4	10.25491	10.252704	10.252759	2.80	2.76	2.78	Y
	(18.901)	(20.623)	(27.513)	(0.67)	(0.65)	(0.56)	
D5	11.42736	11.429488	11.429921	2.64	2.49	2.52	Y
	(16.922)	(18.187)	(19.914)	(0.67)	(0.64)	(0.55)	
D6	10.44644	10.43784	10.442393	1.95	1.81	1.99	Y
	(13.050)	(13.303)	(18.939)	(0.69)	(0.67)	(0.55)	
D7	9.71791	9.716448	9.719637	1.71	2.53	2.72	Y
	(11.940)	(18.568)	(29.584)	(0.69)	(0.66)	(0.58)	
D8	9.76803	9.769648	9.771518	1.49	1.42	1.52	Y
	(10.045)	(10.438)	(15.930)	(0.69)	(0.67)	(0.59)	
D9	9.13974	9.141888	9.140001	1.28	1.16	1.31	Y
	(9.185)	(8.342)	(14.046)	(0.67)	(0.64)	(0.55)	
D10	8.80680	8.795024	8.794724	1.11	2.13	3.06	Y
	(8.421)	(16.653)	(32.285)	(0.69)	(0.68)	(0.55)	
D11	10.91721	10.918768	10.914689	1.08	1.19	0.81	N
	(7.109)	(8.130)	(7.303)	(0.67)	(0.66)	(0.57)	
D12	11.75672	11.752944	11.755519	0.61	0.80	0.83	Y
	(4.334)	(5.533)	(6.659)	(0.67)	(0.64)	(0.55)	
D13	14.80867	14.823648	14.782507	0.48	0.41	0.39	N
	(4.541)	(4.372)	(4.410)	(0.67)	(0.64)	(0.57)	

Notes: Signal to noise (SNR) ratio is given in parentheses as reported by FAMIAS (Zima 2008) present in all three sectors of the TESS data. Amplitude is in millimagnitudes together with the the 3-σ confidence interval. Crouzet et al. *(2018) indicates whether the frequency was reported in their Tables B.1 or B.2.*

Table 6. The significant γ Dor frequencies from Sectors 12, 27, and 39 with the SNR below each frequency.

No.	Sector 12 Frequency (SNR)	Sector 12 Amplitude (3sigma)	Sector 27 Frequency (SNR)	Sector 27 Amplitude (3 σ)	Sector 39 Frequency (SNR)	Sector 39 Ampltiude (3 σ)	Crouzet (2018)
G1	3.547780	0.387	3.547376	0.392	3.545798	0.382	N
	(4.812)	(0.67)	(4.618)	(0.63)	(5.112)	(0.55)	
G2	—	—	0.697984	0.558	—	—	N
	—	—	(5.856)	(0.63)	—	—	
G3	—	—	2.845136	0.447	2.774739	0.438	Y
	—	—	(4.880)	(0.63)	(5.613)	(0.55)	
G4	—	—	0.614992	0.454	—	—	Y
	—	—	(4.831)	(0.64)	—	—	
G5	—	—	—	—	1.407943	0.440	N
	—	—	—	—	(4.219)	(0.55)	

Notes: The amplitude is in millimagniudes and the figure in brackets is the 3-σ uncertainty. The final column indicates whether the frequency was also reported in Crouzet et al. *(2018) Table B.1.*

analysis of the light curves and residuals showed no evidence of chaos. With the apparent adequacy of the models composed only of sinusoids, no further analysis of this type was carried out.

Table 5 presents details of the 13 δ Sct frequencies which were active in all three Sectors of the TESS data. As may be seen in the final column of the Table, 11 of these frequencies were also reported by Crouzet *et al.* (2018) in either their Table B.1 or B.2, indicating their stability over decadal time spans. The early estimates of the dominant photometric frequency reported by McInally and Austin (1978), Coates *et al.* (1981), and Tsvetkov (1982) give a somewhat lower frequency than either Crouzet *et al.* (2018) or the present analysis of the TESS data. Given the short time baselines and higher levels of observational uncertainties in these early papers, we cannot conclude that these were genuinely different frequencies.

The frequency 10.058734 which was reported in the Crouzet *et al.* (2018) Table B.2 was also present in the Sector 27 data with an amplitude of 0.8 mmag and in the Sector 39 data with an amplitude of 0.67 mmag. These amplitudes were similar to that in their 2011 season's data.

Of the 13 frequencies listed in Table 5 four underwent significant changes in amplitude at at least the 3-σ level.

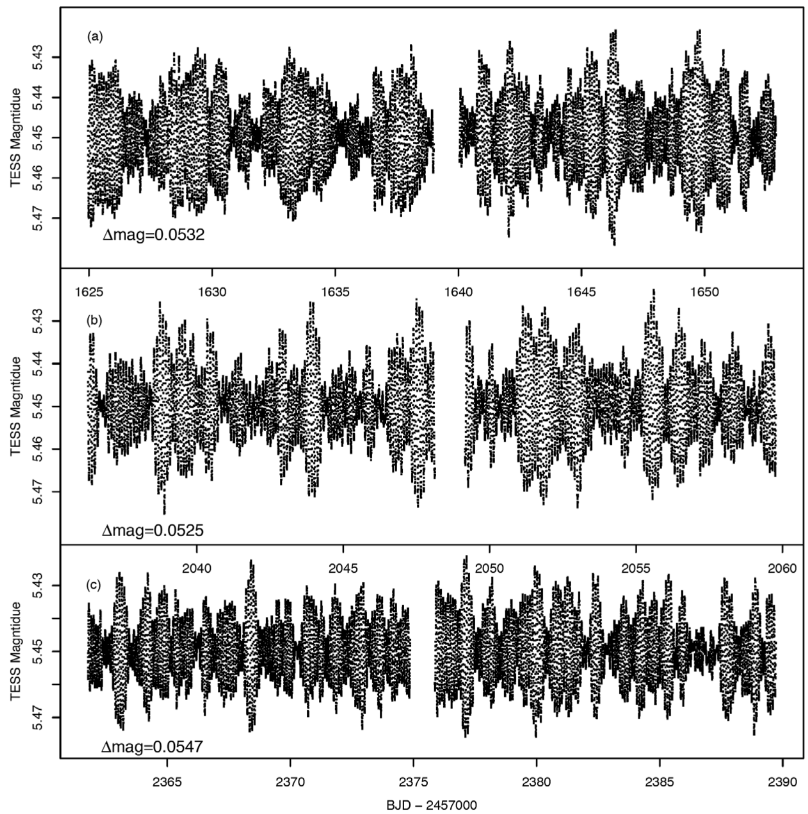

Figure 1. The full light curves for three sectors of TESS data for σ Oct/HD 177482. Panel (a) is Sector 12, panel (b) is Sector 27, and panel (c) is Sector 39. Δ mag is the range between highest and lowest magnitudes in that Sector's observations.

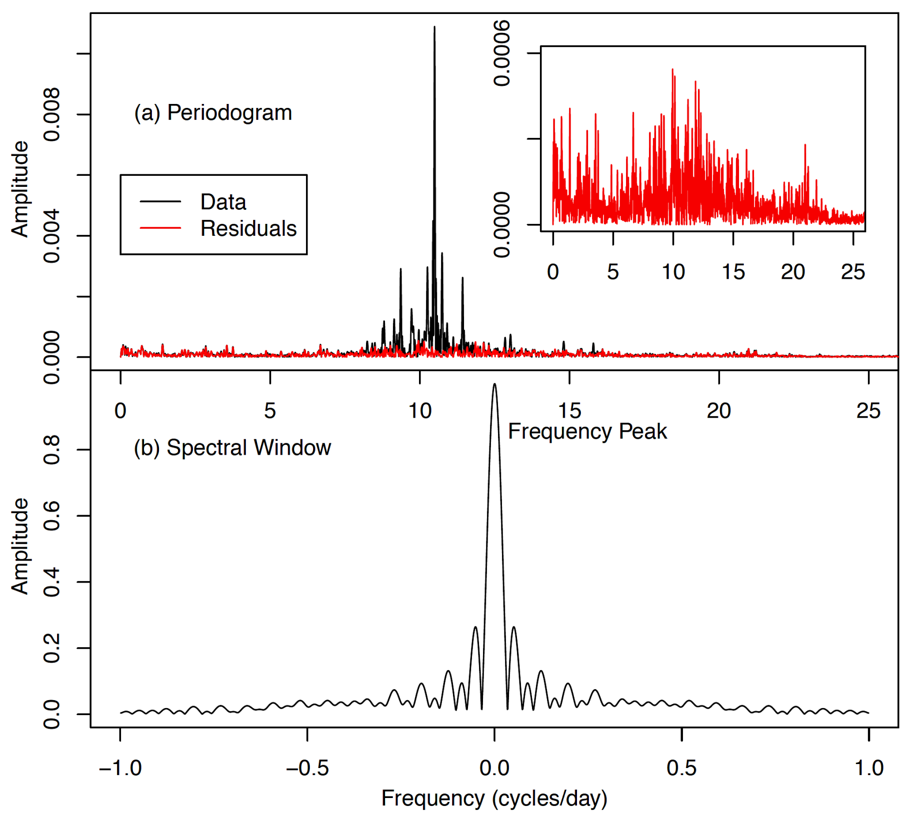

Figure 2. Panel (a) is the periodogram of the Sector 12 data in black while the red is the periodogram of the residuals after all the stiatistically signicant frequencies identied by FAMIAS were fitted. The inset graph in panel (a) is an expanded view of the periodogram of the residuals. Panel (b) is the spectral window from the same Sector.

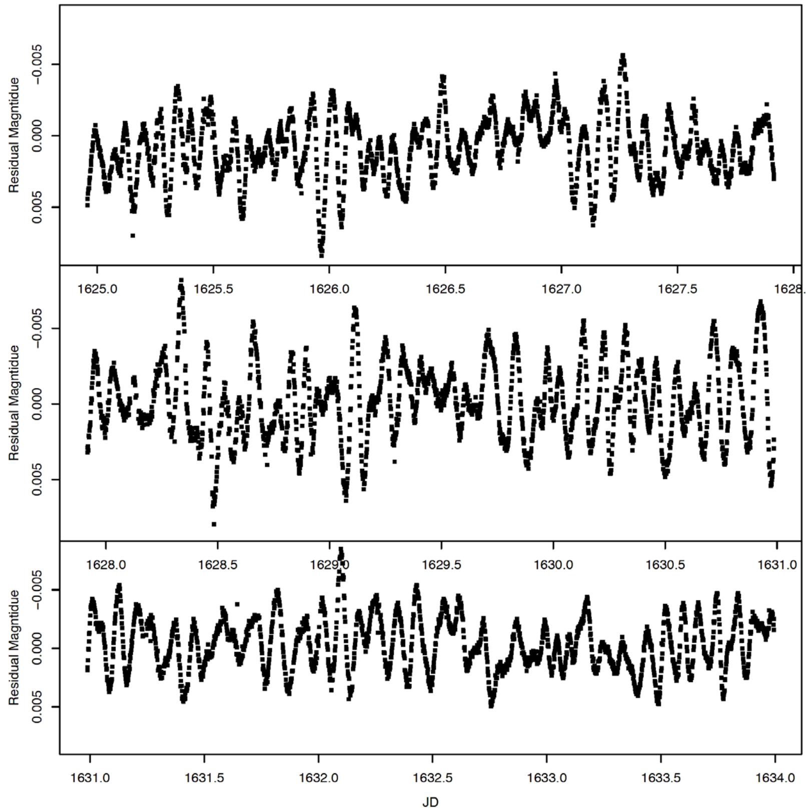

Figure 3. A plot of the residuals after all the statistically signicant frequencies were fitted to the Sector 12 data. The light curve covers an approximately nine day period rather than the full observing run in order to show the structure of the residuals more clearly.

They are frequencies D1 (10.49), D3 (9.36), D7 (9.72), and D10 (8.80). Each of these frequencies also underwent changes in amplitude in the Crouzet *et al.* (2018) data. Other frequencies were stable for both sets of data. For example, the amplitude of D2 (10.74) was stable across the four seasons of the Crouzet *et al.* (2018) data and the three Sectors of the TESS data. However, the amplitudes reported by Crouzet *et al.* (2018), about 2.77 mmag (amplitude for the combined data), were lower than each of the three TESS Sectors. To determine if this frequency undergoes amplitude modulation would require observations on a much longer time baseline than the approximately 27-day sectors of the TESS observation mode.

While frequency analysis was carried out using SigSpec (Reegen 2011), little is reported here because the presence of large numbers of spurious frequencies. For example, of the 483 δ Sct frequencies reported by SigSpec for the Sector 12 data, 138 of these were higher than 22 cycles d^{-1} and clearly did not correspond to any feature in the periodogram because the periodogram was featureless above this level. The first frequency reported in this featureless region was frequency number 179, meaning that the data had been through 178 cycles of prewhitening at this point in the analysis. As Balona (2014) pointed out, each cycle of prewhitening introduces a new frequency into the data, making it impossible to distinguish between real low amplitude frequencies and spurious frequencies. In fact, Balona (2014) writes: "Thus, it is not possible to count the number of individual modes with any degree of certainty below a certain amplitude level." As far as the author is aware, no statistical test has yet been implemented which can give guidance to the researcher that the "certain amplitude level" has been reached. This leaves anyone working on δ Sct stars in the unsatisfactory position where the decision on which frequencies to report as real and which to disregard as spurious is a subjective one.

Although restricted range analysis, reported in Table 4, did result in a useful reduction in the number of significant frequencies, there were still very large numbers of frequencies reported, the majority of which could not be identified with any feature in the relevant periodogram.

In the γ Dor range, active frequencies were reported in only two of the three sectors (see Table 6) with a maximum SNR of 5.86 which, qualitatively, is only weakly significant. While the 3.55 cycles d^{-1} frequency is included in this Table it is above the usual cutoff point for γ Dor frequencies so perhaps should be in Table 5. Only two of the remaining four frequencies were also reported by Crouzet *et al.* (2018) in their data. The 3-σ confidence interval was sufficiently large that it was not possible to analyze the data for amplitude modulation between sectors. The G3 frequency in the Table had a similar amplitude to that reported by Crouzet *et al.* (2018). While the G4 frequency appears to have a lower amplitude in the TESS data compared to the Crouzet *et al.* (2018) data, the large confidence interval made it impossible to reach a conclusion.

5. Conclusions

This analysis of the TESS data on σ Oct confirms Crouzet *et al.* (2018) that σ Oct pulsates in δ Sct mode but the evidence for γ Dor pulsation modes as reported by them was weak in the TESS data. In two of the three Sectors' data a frequency in the γ Dor range exceeded an SNR of 5, with the maximum significance of 5.86. In the other Sector no γ Dor reached statistical significance, that is, no frequencies were reported with a SNR exceeding four.

The low amplitudes of the γ Dor frequencies made assessing whether they also undergo amplitude modulation difficult. The limited evidence suggests that they do because only two of the significant frequencies reported here were also reported by Crouzet *et al.* (2018), and two other γ Dor frequencies reported by Crouzet *et al.* (2018) were not detected in the TESS data. However, to resolve this question will require observations with longer time baselines than the approximately 27-days Sectors of the TESS mission.

The TESS data also confirm Crouzet *et al.* (2018) and, more generally, Bowman *et al.* (2016), that some of the δ Sct frequencies active in σ Oct undergo statistically significant amplitude modulation, including in the dominant 10.49 cycles d^{-1} frequency.

6. Acknowledgements

The author would like to thank NASA for making the data from its Transiting Exoplanet Search Satellite freely available and the TESS Asteroseismic Science Operations Center for operating their particular database (TASOC) of TESS photometry data.

The author would like to thank The American Association of Variable Star Observers for maintaining and making freely available the International Variable Star Index (VSX).

This research has made use of the SIMBAD database, operated at CDS, Strasbourg, France.

The author would like to thank an anonymous referee and editor Morrison for their constructive comments which helped improve the paper.

References

Balona, L. A. 2014, *Mon. Not. Roy. Astron. Soc.*, **439**, 3453.

Balona, L. A., Hearnshaw, J. B., Koen, C., Collier, A., Machi, I., Mkhosi, M., and Steenberg, C. 1994, *Mon. Not. Roy. Astron. Soc.*, **267**, 103.

Bedding, T. R., *et al.* 2020, *Nature* **581**, 147.

Bowman, D. M., Kurtz, D. W., Breger, M., Murphy, S. J., and Holdsworth, D. L. 2016, *Mon. Not. Roy. Astron. Soc.*, **460**, 1970.

Breger, M., and Beichbuchner, F. 1996, *Astron. Astrophys.*, **313**, 851.

Campbell, W. W., and Wright, W. H. 1900, *Astrophys. J.*, **12**, 254.

Catelan, M., and Smith, H. A. 2015, *Pulsating Stars*, Wiley-VCH, Berlin.

Centre de Donnees astronomiques de Strasbourg. 2007, SIMBAD Astronomical Database (http://simbad.u-strasbg.fr/simbad/).

Coates, D. W., Halprin, L., Moon, T. T., and Thompson, K. 1981, *Inf. Bull. Var. Stars*, No. 2047, 1.

Crouzet, N., *et al.* 2018, *Astron. Astrophys.*, **619A**, 116.

Eggen, O. 1956, *Publ. Astron. Soc. Pacific*, **68**, 238.

Gaia Collaboration. 2020, VizieR Online Data Catalog: Gaia EDR3 (Gaia Collaboration, 2020), VizieR On-line Data Catalog: I/350 (doi: 10.5270/esa-1ug).

Grigahcène, A., *et al.* 2010, *Astrophys. J., Lett.*, **713L**, 192.

Kafka, S. 2022, variable star observations from the AAVSO International Database (https://www.aavso.org/aavso-international-database-aid).

Krisciunas, K. 1993, *Bull. Amer. Astron. Soc.*, **25**, 1422.

Lenz, P., and Breger, M. 2005, *Commun. Asteroseismology*, **146**, 53.

McInally, C. J., and Austin, R. 1978, *Mon. Not. Roy. Astron. Soc.*, **184**, 885.

R Core Team. 2019, R: A Language and Environment for Statistical Computing, R Foundation for Statistical Computing, Vienna, Austria (https://www.R-project.org).

Rea, B. 2022a, *J. Amer. Assoc. Var. Star Obs.*, **50**, 8.

Rea, B. 2022b, *J. Amer. Assoc. Var. Star Obs.*, **50**, 107.

Rea, W. 2019, *Asteroseismology of HD 177482*, Technical Report, University of Canterbury, Department of Physical Sciences.

Reegen, P. 2007, *Astron. Astrophys.*, **467**, 1353.

Reegen, P. 2011, *Commun. Asteroseismology*, **163**, 3.

Ricker, G. R., *et al.* 2014, *Proc. SPIE, 9143*, id. 914320 (doi: 10.1117/12.2063489).

Sprott, J. C. 2003, *Choas and Time-Series Analysis*, Oxford Univ. Press, Oxford, UK.

TESS Asteroseismic Science Operations Center (TASOC). 2023, TESS Data for Asteroseismology (https://tasoc.dk/).

Tsvetkov, Ts. G. 1982, *Inf. Bull. Var. Stars*, No. 2084, 1.

Watson, C., Henden, A. A., and Price, C. A. 2014, AAVSO International Variable Star Index VSX (Watson+, 2006–2014; https://www.aavso.org/vsx).

Zima, W. 2008, *Commun. Asteroseismology*, **155**, 17.

Light Curve Modeling and Secular Analyses of the Totally Eclipsing Overcontact Binary System V514 Draconis

Kevin B. Alton
UnderOak Observatory, 70 Summit Avenue, Cedar Knolls, NJ 07927; kbalton@optonline.net

Franz-Josef Hambsch
Oude Bleken 12, Mol, 2400, Belgium; hambsch@telenet.be

Received December 13, 2022; revised March 7, 2023; accepted March 18, 2023

Abstract Precise time-series CCD-derived photometric data (BVR_c) were acquired from V514 Dra at Astrokolhoz Observatory in 2010 and Desert Blooms Observatory in 2022. An updated linear ephemeris was calculated from nine new times of minimum (ToM) produced from this study along with eight other values from the literature. Based on a quadratic fit of residuals from observed and predicted minimum times, secular analyses suggested the orbital period of V514 Dra may be slowly increasing at the rate of $0.0061 \pm 0.0011\ s \cdot y^{-1}$. In addition, simultaneous modeling of new multi-bandpass (BVR_c) light curve data was accomplished using the Wilson-Devinney (WD) code, revealing that V514 Dra is likely a W-subtype overcontact binary (OCB). Since a total eclipse is observed, a photometrically derived value for the mass ratio (q_{ptm}) with acceptable uncertainty could be determined which consequently provided preliminary estimates for selected physical and geometric elements of V514 Dra.

1. Introduction

Sparsely sampled monochromatic photometric data from V514 Dra (= NSVS 1090740) were first captured during the ROTSE-I survey between 1999 and 2000 (Akerlof *et al.* 2000; Wozniak *et al.* 2004). Hoffman *et al.* (2008) initially identified V514 Dra as a new β Lyrae system from the ROTSE-I survey but later (Hoffman *et al.* 2009) re-classified this system as a W UMa-type variable. Lewandowski *et al.* (2009) mis-classified V514 Dra as an Algol-type variable in a study involving 66 other new variable stars discovered by Niedzielski *et al.* (2003). Other sources of photometric data from this eclipsing binary include the sparsely-sampled All-Sky Automated Survey for SuperNovae (ASAS-SN: Shappee *et al.* 2014; Jayasinghe *et al.* 2018) and the Catalina Sky Survey (CSS: Drake *et al.* 2014). Legacy unpublished light curve data (V and I_c) were also obtained from WD30, an AAVSOnet instrument operated at Astrokolhoz Observatory (AO: Cloudcroft, New Mexico, 32.979 N, 105.7334 W) in 2010. Since these light curves were incomplete, they were only used to generate additional times of minimum. Lastly, Korda *et al.* (2017) conducted a photometric investigation (V, R_c, and I_c) of V514 Dra along with 13 other low-mass binaries which included light curve modeling with the Wilson-Devinney (WD) code (Wilson and Devinney 1971; Wilson 1979, 1990). Multi-bandpass (BVR_c) light curves captured from V514 Dra at DBO in 2022 were synthesized using the same Roche-lobe modeling code.

2. Observations and data reduction

Precise time-series photometric observations were obtained in 2022 at Desert Blooms Observatory (DBO, USA, 31.941 N, 110.257 W) using a QSI 683 wsg-8 CCD camera mounted at the Cassegrain focus of an 0.4-m Schmidt-Cassegrain telescope. This focal-reduced (f/7.2) instrument produces an image scale of 0.76 arcsec/pixel (bin = 2 × 2) and a field of view (FOV) of 15.9 × 21.1 arcmin. The CCD camera was equipped with photometric B, V, and R_c filters manufactured to match the Johnson-Cousins Bessell specification. Image (science, darks, and flats) acquisition software (TheSkyX Pro Edition 10.5.0; Software Bisque 2019) controlled the main and off-axis guide cameras. Image acquisition at AO was accomplished using MaxIm DL 5.07 (Diffraction Limited. 2012) to control an SBIG ST-9 CCD detector (V and I_c passbands) that was mounted at the Cassegrain focus of an LX-200 (12") optical tube assembly. Dark subtraction, flat correction, and registration of all images were performed prior to any analysis. Instrumental readings were reduced to catalog-based magnitudes using APASS DR9 values (Henden *et al.* 2009, 2010, 2011; Smith *et al.* 2011) built into MPO Canopus v 10.7.12.9 (Minor Planet Observer 2010). Light curve data acquired at AO were similarly reduced to APASS DR9 values using LesvePhotometry V1.2.0.137 (de Ponthière 2010).

Magnitude values for photometric data were produced from two comparison stars (DBO: GSC 4421-0175 and GSC 4421-0197; AO: GSC 4421-0175 and GSC 4421-0399) which on average remained constant throughout every imaging session. The identity, J2000 coordinates, and color indices (B–V) for these stars are provided in Table 1. An AAVSO finder chart annotated with the location of the target (T) and comparison stars (1–3) is reproduced in Figure 1. Only data acquired above 30° altitude (airmass < 2.0) were evaluated; considering the close proximity of all program stars, differential atmospheric extinction was ignored. All photometric data acquired by co-author Hambsch from V514 Dra at AO (2010) and co-author Alton at DBO (2022) can be retrieved from the AAVSO International Database (Kafka 2021).

3. Results and discussion

Results and a detailed discussion about the determination of linear and quadratic ephemerides are provided in this section.

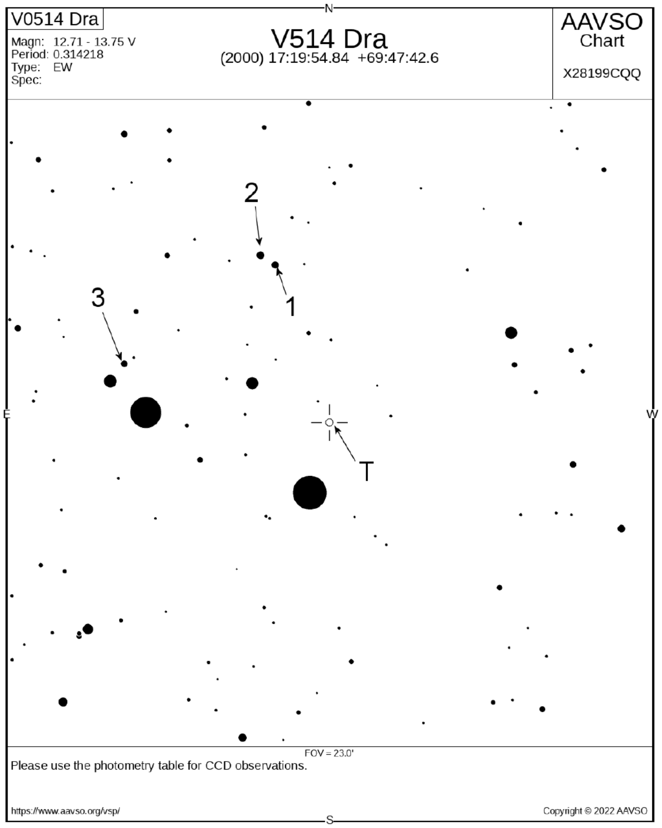

Figure 1. Finder chart for V514 Dra (T) also showing the comparison stars (1–3) used for aperture-derived photometery and generation of APASS DR9-derived magnitude estimates.

Table 1. Astrometric coordinates, V-magnitudes, and color indices (B–V) for V514 Dra, and the corresponding comparison stars (Figure 1) used in this photometric study.

Star Identification	*R.A. (J2000)*[a] *h m s*	*Dec. (J2000)*[a] *° ′ ″*	*V-mag*[b]	*(B–V)*[b]
(1) GSC 4421-0175[c,d]	17 20 23.2704	+69 53 39.228	12.074	0.472
(2) GSC 4421-0197[c]	17 20 17.1648	+69 53 18.852	12.455	0.385
(3) GSC 4421-0399[d]	17 21 19.3656	+69 49 46.740	12.711	0.535
(T) V514 Dra	17 19 54.8279	+69 47 42.649	12.976	0.662

[a] *R.A. and Dec. from Gaia EDR3 (Gaia Collab.* et al. *2021)*
[b] *V-mag and (B–V) for comparison stars derived from APASS DR9 database described by Henden* et al. *(2009, 2010, 2011) and Smith* et al. *(2011).*
[c] *Comparison stars used for DBO data.*
[d] *Comparison stars used for AO data.*

Thereafter, a multi-source approach for estimating the effective temperature of V514 Dra along with Roche-lobe modeling with the WD code are examined. Finally, preliminary estimates for mass ($M_\odot$) and radius ($R_\odot$) along with corresponding calculations for luminosity ($L_\odot$), surface gravity (log (g)), semi-major axis (a), and bolometric magnitude (M_{bol}) are derived.

3.1. Photometry and ephemerides

A total of 274 photometric values in B, 309 in V, and 300 in R_c passbands were acquired from V514 Dra at DBO between 2022 March 3 and 2022 March 27. Photometric uncertainty, which typically remained within ±0.005, was calculated according to the so-called "CCD Equation" (Mortara and Fowler 1981; Howell 2006). The 2010 imaging campaign (2010 April 4–2010 April 25) at AO provided an additional 446 values in V and 149 readings in I_c bandpass which were only used to supplement ToM values needed for secular analysis of the orbital period. ToM values and associated errors from data acquired at DBO and AO were calculated according to Andrych and Andronov (2019) and Andrych *et al.* (2020) using the program MAVKA (Andrych *et al.* 2020). Simulations of extrema were automatically optimized by finding the most precise degree (α) and best fit algebraic polynomial expressions. ToM differences (ETD) vs. epoch were fit using scaled Levenberg-Marquardt algorithms (QtiPlot 0.9.9-rc9; IONDEV SRL 2021).

Table 2. V514 Dra times-of-minimum (HJD: 2006 March 23–2022 March 27), cycle number, and eclipse timing difference (ETD) between observed and predicted times derived from the updated linear ephemeris (Equation 1).

HJD = 2400000+	*HJD Error*	*Cycle No.*	*ETD*	*Ref.*
53817.7773	0.0000	–18611	0.0004	1
54210.8662	0.0010	–17360	0.0019	2
55291.9336	0.0002	–13919.5	0.0007	3
55293.9766	0.0002	–13913	0.0012	3
55311.8869	0.0002	–13856	0.0011	3
55721.7832	0.0005	–12551.5	–0.0006	4
57089.4184	0.0003	–8199	–0.0014	5
57126.4962	0.0008	–8081	–0.0013	5
57126.6532	0.0009	–8080.5	–0.0015	5
57142.3643	0.0002	–8030.5	–0.0013	5
57147.3919	0.0005	–8014.5	–0.0012	5
57177.3994	0.0004	–7919	–0.0016	5
57890.0472	0.0010	–5651	–0.0013	6
59644.0178	0.0002	–69	0.0017	7
59663.8129	0.0002	–6	0.0011	7
59663.9703	0.0002	–5.5	0.0013	7
59665.8551	0.0002	0.5	0.0008	7

References: (1) Lewandowski et al. *(2009); (2) CSS (Drake* et al. *2014); (3) AO: this study; (4) Diethelm (2011); (5) Korda* et al. *(2017); (6) ASAS-SN (Shappee* et al. *2014; Jayasinghe* et al. *2018); (7) DBO: this study.*

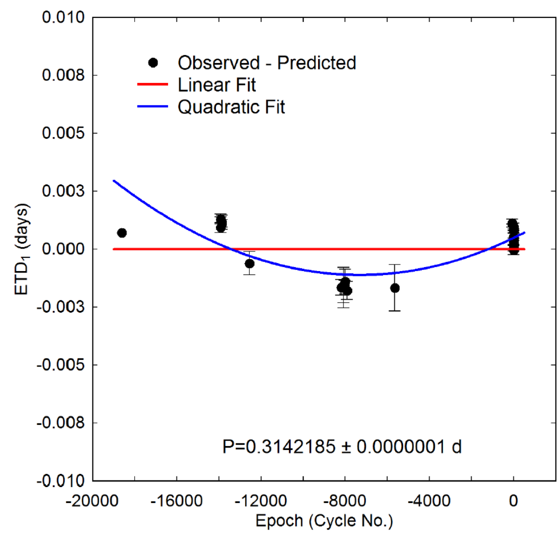

Figure 2. Linear and quadratic fit of ToM differences (ETD_1) vs. epoch for V514 Dra calculated using the new linear ephemeris (Equation 1). Measurement uncertainty is denoted by the error bars.

Seven new ToM values were derived from photometric data acquired at DBO and AO. An additional ToM value was extrapolated from the ASAS-SN and Catalina Sky surveys along with eight other observations gathered from the literature (Table 2). A new linear ephemeris (HJD) based on near-term (2017–2022) results was determined as follows:

$$\text{Min. I(HJD)} = 2459665.6978(4) + 0.314219(1)\,E\,. \quad (1)$$

The difference (ETD) between observed eclipse times (Figure 2) and those predicted by the linear ephemeris against epoch (cycle number) reveals what appears to be a quadratic relationship where:

$$\text{ETD} = 1.0668 \pm 0.3903 \cdot 10^{-3} + 5.0325 \pm 0.98205 \cdot 10^{-7}E + 3.0179 \pm 0.5552 \cdot 10^{-11}E^2\,. \quad (2)$$

Given that the quadratic term coefficient ($Q=3.0179\pm0.5552$) is positive, this result would suggest that the orbital period has been increasing at the rate ($dP/dt=2Q/P$) of $0.0061\pm0.0011\ \mathrm{s\cdot y^{-1}}$. This rate, albeit slow, falls within those reported from many other overcontact systems in the literature (Latković *et al.* 2021). Period change over time that can be described by a parabolic expression is often attributed to mass transfer or by angular momentum loss (AML) due to magnetic stellar wind (Qian 2001, 2003; Li *et al.* 2019). Ideally the net effect is a decreasing orbital period when AML dominates. When conservative mass transfer from the more massive to its less massive binary partner prevails, then the orbital period can also decrease. Separation increases when conservative mass transfer from the less massive to its more massive cohort occurs or when spherically symmetric mass loss from either body (e.g. a wind but not magnetized) takes place. In mixed situations (e.g. mass transfer from less massive star, together with AML) the orbit evolution depends on which process dominates.

3.2. Effective temperature estimation

The primary star is herein defined as the more massive, and therefore more luminous component. In the absence of a published medium to high resolution UV-vis spectrum, $T_{\rm eff1}$ was derived from a composite (USNO-A2, 2MASS, APASS, UCAC4) of photometric determinations that were as appropriate transformed to (B–V)[1,2]. Interstellar extinction ($A_V=0.1026\pm0.0016$) and reddening ($E(B–V)=A_V/3.1$) were estimated according to a galactic dust map model derived by Schlafly and Finkbeiner (2011). Additional sources used to establish a mean value for $T_{\rm eff1}$ included the Gaia DR2 release of stellar parameters (Andrae *et al.* 2018) and an empirical relationship (Houdashelt *et al.* 2000) based on intrinsic color, $(B–V)_0$. The mean result ($T_{\rm eff1}=5390\pm239$ K) was adopted for WD modeling of light curves from V514 Dra (Table 3).

3.3. Light curve modeling with the Wilson-Devinney Code

Roche-lobe modeling of light curve data (Figure 3) acquired in 2022 (DBO) was initially performed with PHOEBE 0.31a (Prša and Zwitter 2005) and then refined using WDwint56a (Nelson 2009). Both programs feature a graphical interface to the Wilson-Devinney WD2003 code (Wilson and Devinney 1971; Wilson 1979, 1990). WDwint56a incorporates Kurucz's atmosphere models (Kurucz 2002) that are integrated over BVR_c passbands. Most commonly, W-subtype OCBs (Binnendijk 1970) have been shown to have a relatively cool effective temperature (late G to early K spectral class) and an orbital period less than 0.4 d. Based on this assumption, Roche-lobe modeling of the DBO (Figure 3) light curves initially proceeded using Mode 3 for an overcontact binary; other modes (detached and semi-detached) never improved light curve simulation as defined by the model residual mean square errors. Since the effective temperature of the primary was estimated to be 5390 K, internal energy transfer to the stellar surface is driven

Table 3. Estimation of the primary star effective temperature ($T_{\rm eff1}$) for V514 Dra.

Parameter	*Value*
DBO $(B–V)_0$[a]	0.608 ± 0.033
Mean combined $(B–V)_0$[a]	0.727 ± 0.135
Galactic reddening E(B–V)[b]	0.0331 ± 0.0005
Survey $T_{\rm eff1}$[c] (K)	5506 ± 391
Gaia $T_{\rm eff1}$[d] (K)	5165^{-144}_{+366}
Houdashelt $T_{\rm eff1}$[e] (K)	5495 ± 477
Mean $T_{\rm eff1}$ (K)	5390 ± 239
Spectral Class[f].	G8V-G9V

[a] *DBO and mean combined intrinsic $(B–V)_0$ determined using reddening value (E(B–V)).*
[b] *https://irsa.ipac.caltech.edu/applications/DUST/*
[c] *$T_{\rm eff1}$ interpolated from mean combined $(B–V)_0$ using Table 4 in Pecaut and Mamajek (2013).*
[d] *Values from Gaia DR2 (Gaia Collab. 2016, 2018; http://vizier.u-strasbg.fr/viz-bin/VizieR?- source=I/345/gaia2).*
[e] *Values calculated with Houdashelt* et al. *(2000) empirical relationship.*
[f] *Spectral class estimated from Pecaut and Mamajek (2013) based on mean $T_{\rm eff}$*

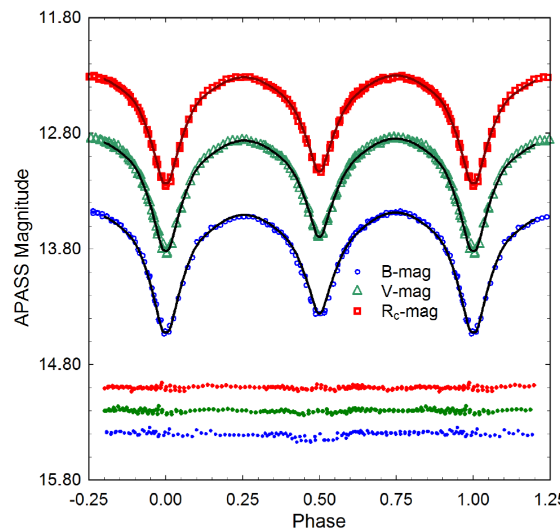

Figure 3. Period-folded (0.3142189 ± 0.0000001 d) CCD-derived light curves for V514 Dra produced from photometric data collected at DBO between 2022 March 3 and 2022 March 27. The top (R_c), middle (V), and bottom curves (B) were transformed to magnitudes based on APASS DR9-derived catalog values from comparison stars. In this case, the model assumed a W-subtype overcontact binary with a cool spot on the primary star; residuals from the model fits are offset at the bottom of the plot to compress the y-axis.

[1] http://www.aerith.net/astro/color_conversion.html
[2] http://brucegary.net/dummies/method0.html

by convective (< 7200 K) rather than by radiative processes (Bradstreet and Steelman 2004). Therefore, bolometric albedo ($A_{1,2} = 0.5$) was assigned according to Ruciński (1969), while the gravity darkening coefficient ($g_{1,2} = 0.32$) was adopted from Lucy (1967). Logarithmic limb darkening coefficients (x_1, x_2, y_1, y_2) were interpolated (Van Hamme 1993) following any change in effective temperature during model fit optimization by differential corrections (DC). All but the temperature of the more massive star (T_{eff1}), $A_{1,2}$, and $g_{1,2}$ were allowed to vary during DC iterations. In general, the best fits for T_{eff2}, i, q, and Roche potentials ($\Omega_1 = \Omega_2$) were collectively refined (method of multiple subsets) by DC using the multi-bandpass light curve data until a simultaneous solution was found. Light curve data acquired at DBO in 2022 (Figure 3) showed an obvious asymmetry during quadrature (Max I < Max II). This so-called "O'Connell effect" (O'Connell 1951) assumes some sort of surface inhomogeneity often associated with star spots. In this case the addition of a single cool spot positioned on the primary star provided the best fit light curve models. Furthermore, V514 Dra did not require any third light correction ($l_3 = 0$) to improve WD model fits.

3.4. Wilson-Devinney modeling results

It is generally not possible to unambiguously determine the mass ratio or total mass of an eclipsing binary system without spectroscopic radial velocity (RV) data. In this case, an obvious flattened bottom during minimum light that is usually indicative of a total eclipse was not observed. Nonetheless, a total eclipse is still possible when two similarly sized binary stars are viewed edge on ($i \approx 90°$). With totality, degeneracy between the radii and inclination is broken (Terrell and Wilson 2005; Terrell 2022) such that a mass ratio can be determined with very small (< 1%) relative error (Liu 2021). To address this potential concern, an exhaustive "q-search" analysis was conducted in which values of the mass ratio ranging between 0.55 and 1.15 were fixed during WD modeling in order to find the best fit (χ^2) using differential corrections while changing i, $\Omega_{1,2}$, and T_{eff2}. As can be seen in Figure 4, mean model residuals using the MAO light curve data (B, V, and R_c) reach a minimum when $q \approx 0.75$.

Standard errors reported in Table 4 are computed from the DC covariance matrix and only reflect the model fit to the observations which assume exact values for any fixed parameter. These formal errors are generally regarded as unrealistically small, considering the estimated uncertainties associated with the mean adopted T_{eff1} values along with basic assumptions about $A_{1,2}$, $g_{1,2}$, the influence of spots added to the WD model, and immeasurable total experimental error. Normally, the value for T_{eff1} is fixed with no error during modeling with the WD code. When T_{eff1} is varied by as much as ± 10%, investigations with other OCBs including A- (Alton 2019; Alton *et al.* 2020) and W-subtypes (Alton and Nelson 2018) have shown that uncertainty estimates for i, q, or $\Omega_{1,2}$ were not appreciably (< 2.5%) affected. Assuming that the actual T_{eff1} value falls within ± 10% of the adopted values used for WD modeling (not unreasonable based on T_{eff1} data provided in Table 3), then uncertainty estimates for i, q, or $\Omega_{1,2}$ along with spot size, temperature, and location would likely not exceed this amount.

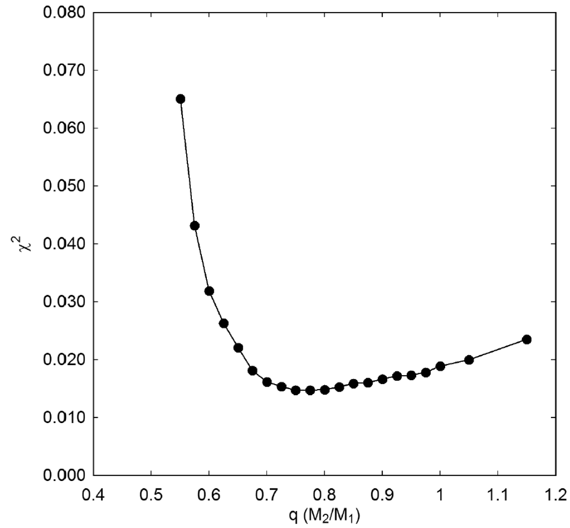

Figure 4. A "q-search" assessment using PHOEBE v0.31a during which the best Roche-lobe model fit was determined using differential corrections after fixing a value for the mass ratio (q) between 0.55 and 1.15 and then varying i, $\Omega_{1,2}$, and T_{eff2}.

Table 4. Light curve parameters evaluated by WD modeling and the geometric elements derived for V514 Dra assuming it is a W-type W UMa variable.

Parameter[a]	*DBO No Spot*	*DBO Spotted*
T_{eff1} (K)[b]	5390 (239)	5390 (239)
T_{eff2} (K)	5598 (248)	5597 (248)
q (m_2/m_1)	0.76 (1)	0.75 (1)
A[b]	0.50	0.50
g[b]	0.32	0.32
$\Omega_1 - \Omega_2$	3.28 (1)	3.26 (1)
i°	88.9 (19)	89.6 (7)
$A_P = T_S/T_\star$[c]	—	0.89 (1)
Θ_P (spot co-latitude)[c]	—	101 (5)
φ_P (spot longitude)[c]	—	119 (3)
r_P (angular radius)[c]	—	15 (3)
$L_1/(L_1+L_2)_B$[d]	0.503 (1)	0.504 (1)
$L_1/(L_1+L_2)_V$	0.518 (1)	0.519 (1)
$L_1/(L_1+L_2)_{Rc}$	0.526 (1)	0.526 (1)
r_1 (pole)	0.389 (1)	0.390 (1)
r_1 (side)	0.412 (1)	0.414 (1)
r_1 (back)	0.446 (1)	0.449 (1)
r_2 (pole)	0.343 (2)	0.343 (2)
r_2 (side)	0.360 (2)	0.361 (2)
r_2 (back)	0.398 (3)	0.399 (4)
Fill-out factor (%)	15.2	17.0
RMS (B)[e]	0.01601	0.01362
RMS (V)	0.01048	0.00871
RMS (R_c)	0.00853	0.00838

[a] *All uncertainty estimates for q, $\Omega_{1,2}$, i, $r_{1,2}$, and L_1 from WDwint56a (Nelson 2009).*
[b] *Fixed with no error during DC.*
[c] *Primary star spot parameters in degrees (Θ_P, φ_P, and r_P); A_P equals the spot temperature (T_S) divided by star temperature, $T_\star$.*
[d] *L_1 and L_2 refer to scaled luminosities of the primary and secondary stars, respectively.*
[e] *Monochromatic residual mean square error from observed values.*

The fill-out parameter (f) which corresponds to the outer surface shared by each star was calculated according to Kallrath and Malone (2009) and Bradstreet (2005) where:

$$f = (\Omega_{inner} - \Omega_{1,2}) / (\Omega_{inner} - \Omega_{outer}), \quad (3)$$

wherein Ω_{outer} is the outer critical Roche equipotential, Ω_{inner} is the value for the inner critical Roche equipotential, and $\Omega = \Omega_{1,2}$ denotes the common envelope surface potential for the binary system. In this case V514 Dra is considered overcontact since $0 < f < 1$.

Spatial renderings (Figure 5) were produced with Binary Maker 3 (BM3: Bradstreet and Steelman 2004) using the final WDwint56a modeling (BVR_c) results from 2022. The smaller secondary is shown to fully transit across the primary face during Min II ($\varphi = 0.5$), thereby confirming that the secondary star is totally eclipsed at Min I.

An earlier (2015–2016) multi-bandpass (VR_cI_c) CCD study on V514 Dra (Korda *et al.* 2017) produced modeling results that were quite disparate from those generated herein. Aside from a large difference in the adopted T_{eff} (4750 vs. 5390 K) for the primary star, estimates for the mass ratio (1 vs. 0.75) and related parameters ($R_\odot$, $L_\odot$, M_{bol}, and Log (g)) suggested that both stars are nearly identical in size and temperature. This is in contrast to the corresponding estimates summarized in Table 5 which indicate that both stars are distinctly different. Obviously a radial velocity (RV) study could reconcile which light curve solution is closest to the true fit.

3.5. Preliminary stellar parameters

Mean physical characteristics were estimated for V514 Dra (Table 5) using results from the best fit (spotted) light curve simulations from 2022. Without the benefit of RV data which define the orbital motion, mass ratio, and total mass of the binary pair, these results should be considered "relative" rather than "absolute" parameters and regarded as preliminary. Nonetheless, since the photometric mass ratio (q_{ptm}) is derived from a totally eclipsing OCB, there is a reasonable expectation that DC optimization with the WD2003 code would have arrived at a solution with acceptable uncertainty for q (Terrell and Wilson 2005; Liu 2021; Terrell 2022).

Calculations are described below for estimating the solar mass and size, semi-major axis, solar luminosity, bolometric V-mag, and surface gravity of each component. Four empirically derived mass-period relationships (M-PR) for W UMa-type binaries were used to estimate the primary star mass. The first M-PR was reported by Qian (2003), others followed from Gazeas and Stępień (2008), Gazeas (2009), and more recently Latković *et al.* (2021). According to Qian (2003), when the primary star is less than $1.35\,M_\odot$ or the system is W-type its mass can be determined from:

$$M_1 = 0.391(59) + 1.96(17) \cdot P, \quad (4)$$

where P is the orbital period in days. This leads to $M_1 = 1.007 \pm 0.080\,M_\odot$ for the primary.

The M-PR derived by Gazeas and Stępień (2008):

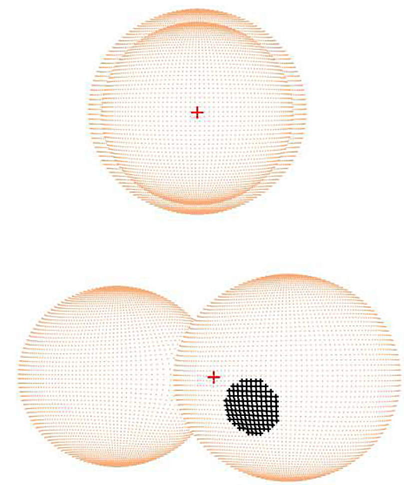

Figure 5. A spatial model of V514 Dra observed at DBO during 2022 illustrating (bottom) location of the cool (black) spot on the primary star and (top) the secondary star transit across the primary star face at Min II ($\varphi = 0.5$).

Table 5. Fundamental stellar parameters for V514 Dra using the photometric mass ratio ($q_{ptm} = m_2/m_1$) from the spotted WD model fits of light curve data (DBO) and the estimated primary star mass based on four empirically derived M-PRs for overcontact binary systems.

Parameter	*Primary*	*Secondary*
Mass ($M_\odot$)	1.05 ± 0.04	0.79 ± 0.03
Radius ($R_\odot$)	0.96 ± 0.01	0.85 ± 0.01
a ($R_\odot$)	2.38 ± 0.02	2.38 ± 0.02
Luminosity ($L_\odot$)	0.70 ± 0.13	0.63 ± 0.11
M_{bol}	5.13 ± 0.02	5.25 ± 0.19
Log (g)	4.49 ± 0.02	4.48 ± 0.02

$$\log(M_1) = 0.755(59) \cdot \log(P) + 0.416(24), \quad (5)$$

corresponds to an OCB system where $M_1 = 1.087 \pm 0.096\,M_\odot$.

Gazeas (2009) reported another empirical relationship for the more massive (M_1) star of a contact binary such that:

$$\log(M_1) = 0.725(59) \cdot \log(P) - 0.076(32) \cdot \log(q) + 0.365(32). \quad (6)$$

from which $M_1 = 1.023 \pm 0.062\,M_\odot$.

Finally, Latković *et al.* (2021) conducted an exhaustive analysis from nearly 700 W UMa stars in which they established mass-period, radius-period, and luminosity-period relationships for the primary and secondary stars. Accordingly, the M-PR:

$$M_1 = (2.94 \pm 0.21 \cdot P) + (0.16 \pm 0.08). \quad (7)$$

leads to a primary star mass of $1.084 \pm 0.104\,M_\odot$.

The mean result from these four values ($M_1 = 1.05 \pm 0.04\,M_\odot$) was used for subsequent determinations of M_2, semi-major axis a, volume-radii r_L, and bolometric magnitudes (M_{bol}) using the formal errors calculated by WDwint56a (Nelson 2009). The secondary mass ($0.79 \pm 0.03\,M_\odot$) and total mass ($1.84 \pm 0.05\,M_\odot$) were determined using the photometric mass ratio ($q_{ptm} = 0.75 \pm 0.01$) derived from the best fit (spotted) model obtained from the DBO light curves.

The semi-major axis, $a(R_\odot) = 2.38 \pm 0.02$, was calculated from Newton's version of Kepler's third law where:

$$a^3 = (G \cdot P^2 (M_1 + M_2)) / (4\pi^2). \quad (8)$$

The effective radius of each Roche lobe (r_L) can be calculated over the entire range of mass ratios ($0 < q < \infty$) according to an expression derived by Eggleton (1983):

$$r_L = (0.49q^{2/3}) / (0.6q^{2/3} + \ln(1 + q^{1/3})), \quad (9)$$

from which values for r_1 (0.4037 ± 0.0004) and r_2 (0.3546 ± 0.0004) were determined for the primary and secondary stars, respectively. The radii in solar units for both binary components can be calculated such that $R_1 = a \cdot r_1 = 0.96 \pm 0.01\, R_\odot$ and $R_2 = a \cdot r_2 = 0.85 \pm 0.01\, R_\odot$.

Luminosity in solar units ($L_\odot$) for the primary (L_1) and secondary stars (L_2) was calculated from the well-known relationship derived from the Stefan-Boltzmann law where:

$$L_{1,2} = (R_{1,2} / R_\odot)^2 (T_{1,2} / T_\odot)^4. \quad (10)$$

Assuming that $T_{eff1} = 5390\,K$, $T_{eff2} = 5597\,K$, and $T_\odot = 5772\,K$, then the solar luminosities ($L_\odot$) for the primary and secondary are $L_1 = 0.70 \pm 0.13$ and $L_2 = 0.63 \pm 0.11$, respectively.

4. Conclusions

This investigation of V514 Dra has expanded the list of totally eclipsing W UMa-type variables that have been provisionally characterized using a photometrically derived mass ratio. Like many other W-subtype OCBs, V514 Dra is comprised of two relatively cool (late spectral class G) stars with an orbiting period less than 0.4 d. Seven new ToM values were determined from light curves acquired at AO in 2010 and DBO in 2022. These values were supplemented with a single value extrapolated from both the ASAS-SN (2017) and CSS (2007) surveys along with eight others reported in the literature. Based on a quadratic fit of residuals from observed and predicted minimum times, secular analyses suggested the orbital period of V514 Dra may be slowly increasing at the rate of 0.0061 ± 0.0011 $s \cdot y^{-1}$. The photometric mass ratio ($q_{ptm} = 0.75 \pm 0.01$) determined by WD modeling is expected to compare favorably with a mass ratio (q_{sp}) derived from RV data. Nevertheless, spectroscopic studies (RV and high resolution classification spectra) will be required to unequivocally determine a total mass and spectral class for this binary system. Consequently, all parameter values and corresponding uncertainties reported herein should be considered preliminary.

5. Acknowledgements

This research has made use of the SIMBAD database operated at Centre de Données astronomiques de Strasbourg, France. In addition, the All-Sky Automated Survey for Supernovae (https://asas-sn.osu.edu/variables), Catalina Sky Survey (http://nesssi.cacr.caltech.edu/DataRelease/), and the AAVSO International Variable Star Index (Watson *et al.* 2014) were mined for essential information. This work also presents results from the European Space Agency (ESA) space mission Gaia. Gaia data are being processed by the Gaia Data Processing and Analysis Consortium (DPAC). Funding for the DPAC is provided by national institutions, in particular the institutions participating in the Gaia MultiLateral Agreement (MLA). The Gaia mission website is https://www.cosmos.esa.int/gaia. The Gaia archive website is https://archives.esac.esa.int/gaia. This research was made possible through use of the AAVSO Photometric All-Sky Survey (APASS), funded by the Robert Martin Ayers Sciences Fund.

Many thanks to the anonymous referee and Editor Morrison, both of whom provided valuable commentary along with corrections.

References

Akerlof, C., *et al.* 2000, *Astron. J.*, **119**, 1901.
Alton, K. B. 2019, *J. Amer. Assoc. Var. Star Obs.*, **47**, 7.
Alton, K. B., and Nelson, R. H. 2018, *Mon. Not. Roy. Astron. Soc.*, **479**, 3197.
Alton, K. B., Nelson, R. H., and Stępień, K. 2020, *J. Astrophys. Astron.*, **41**, 26.
Andrae, R., *et al.* 2018, *Astron. Astrophys.*, **616A**, 8.
Andrych, K. D., and Andronov, I. L. 2019, *Open Eur. J. Var. Stars*, **197**, 65.
Andrych, K. D., Andronov, I. L., and Chinarova, L. L. 2020, *J. Phys. Stud.*, **24**, 1902 (https://uavso.org.ua/mavka/).
Binnendijk, L. 1970, *Vistas Astron.*, **12**, 217.
Bradstreet, D. H., and Steelman, D. P. 2004, Binary Maker 3, Contact Software (http://www.binarymaker.com).
Bradstreet, D. H. 2005, in *The Society for Astronomical Sciences 24th Annual Symposium on Telescope Science*, Society for Astronomical Sciences, Rancho Cucamonga, CA, 23.
de Ponthière, P. 2010, LesvePhotometry, automatic photometry software (http://www.dppobservatory.net).
Diethelm, R. 2011, *Inf. Bull. Var. Stars*, No. 5992, 1.
Diffraction Limited. 2023, MaxIm DL image processing software (http://www.cyanogen.com).
Drake, A. J., *et al.* 2014, *Astrophys. J., Suppl. Ser.*, **213**, 9.
Eggleton, P. P. 1983, *Astrophys. J.,* **268**, 368.
Gaia Collaboration, *et al.* 2016, *Astron. Astrophys.*, **595A**, 1.
Gaia Collaboration, *et al.* 2018, *Astron. Astrophys.*, **616A**, 1.
Gaia Collaboration, *et al.* 2021, *Astron. Astrophys.*, **649A**, 1.
Gazeas, K. D. 2009, *Commun. Asteroseismology*, **159**, 129.
Gazeas, K., and Stępień, K. 2008, *Mon. Not. Roy. Astron. Soc.*, **390**, 1577.
Henden, A. A., Levine, S. E., Terrell, D., Smith, T. C., and Welch, D. L. 2011, *Bull. Amer. Astron. Soc.*, **43**.
Henden, A. A., Terrell, D., Welch, D. and Smith, T. C. 2010, *Bull. Amer. Astron. Soc.*, **42**, 515.
Henden, A. A., Welch, D. L., Terrell, D., and Levine, S. E. 2009, *Bull. Amer. Astron. Soc.*, **41**, 669.
Hoffman, D. I., Harrison, T. E., Coughlin, J. L., McNamara, B. J., Holtzman, J. A., Taylor, G. E., and Vestrand, W. T. 2008, *Astron. J.*, **136**, 1067.
Hoffman, D. I., Harrison, T. E., and McNamara, B. J. 2009, *Astron. J.*, **138**, 466.

Houdashelt, M. L., Bell, R. A., and Sweigart, A. V. 2000, *Astron. J.*, **119**, 1448.

Howell, S. B. 2006, *Handbook of CCD Astronomy*, 2nd ed., Cambridge Univ. Press, Cambridge.

IONDEV SRL. 2021, QtiPlot—Data Analysis and Scientific Visualisation (https://www.qtiplot.com/).

Jayasinghe, T., *et al.* 2018, *Mon. Not. Roy. Astron. Soc.*, **477**, 3145.

Kafka, S. 2021, Observations from the AAVSO International Database (https://www.aavso.org/data-download).

Kallrath, J., and Milone, E. F. 2009, *Eclipsing Binary Stars: Modeling and Analysis*, Springer-Verlag, New York.

Korda, D., Zasche, P., Wolf, M., Kučáková, H., Hoňková, K., and Vraštil, J. 2017, *Astron. J.*, **154**, 30.

Kurucz, R. L. 2002, *Baltic Astron.*, **11**, 101.

Latković, O., Čeki, A., and Lazarević, S. 2021, *Astrophys. J., Suppl. Ser.*, **254**, 10.

Lewandowski, M., Gorecka, M., Maciejewski, G., and Niedzielski, A. 2009, *Open Eur. J. Var. Stars*, **104**, 1.

Li, K., *et al.* 2019, *Res. Astron. Astrophys.*, **19**, 147.

Liu, L. 2021, *Publ. Astron. Soc. Pacific*, **133**, 084202.

Lucy, L. B. 1967, *Z. Astrophys.*, **65**, 89.

Mortara, L., and Fowler, A. 1981, in *Solid State Imagers for Astronomy*, eds. J. C. Geary, D. W. Latham, SPIE, Bellingham, WA, 28.

Minor Planet Observer. 2010, MPO Software Suite (https://minplanobs.org/BdwPub/php/displayhome.php), BDW Publishing, Colorado Springs.

Nelson, R. H. 2009, WDwint56a: Astronomy Software by Bob Nelson[3]

Niedzielski, A., Maciejewski, G., and Czart, K. 2003, *Acta Astron.*, **53**, 281.

O'Connell, D. J. K. 1951, *Publ. Riverview Coll. Obs.*, **2**, 85.

Pecaut, M. J., and Mamajek, E. E. 2013, *Astrophys. J., Suppl. Ser.*, **208**, 9.

Prša, A., and Zwitter, T. 2005, *Astrophys. J.*, **628**, 426.

Qian, S. 2001, *Mon. Not. Roy. Astron. Soc.*, **328**, 635.

Qian, S. 2003, *Mon. Not. Roy. Astron. Soc.*, **342**, 1260.

Ruciński, S. M. 1969, *Acta Astron.*, **19**, 245.

Schlafly, E. F., and Finkbeiner, D. P. 2011, *Astrophys. J.*, **737**, 103.

Shappee, B. J., *et al.* 2014, *Astrophys. J.*, **788**, 48.

Smith, T. C., Henden, A. A., and Starkey, D. R. 2011, in *The Society for Astronomical Sciences 30th Annual Symposium on Telescope Science*, Society for Astronomical Sciences, Rancho Cucamonga, CA, 121.

Software Bisque. 2019, TheSkyX professional edition 10.5.0 (https://www.bisque.com/product/theskyx-pro/).

Terrell, D. 2022, *Galaxies*, **10**, 8.

Terrell, D., and Wilson, R. E. 2005, *Astrophys. Space Sci.*, **296**, 221.

van Hamme, W. 1993, *Astron. J.*, **106**, 2096.

Watson, C., Henden, A. A., and Price, C. A. 2014, AAVSO International Variable Star Index VSX (Watson+, 2006–2014; https://www.aavso.org/vsx).

Wilson, R. E. 1979, *Astrophys. J.*, **234**, 1054.

Wilson, R. E. 1990, *Astrophys. J.*, **356**, 613.

Wilson, R. E., and Devinney, E. J. 1971, *Astrophys. J.*, **166**, 605.

Woźniak, P. R., *et al.* 2004, *Astrophys. J.*, **127**, 2436.

[3] Nelson (2009); https://www.variablestarssouth.org/resources/bob-nelsons-software-tools/software-by-bob-nelson

Precision Photometric Observations and Analysis of the Totally Eclipsing, Solar-Type Binary WISE J051352.5-170113

Ronald G. Samec
Pisgah Astronomical Research Institute, 318 Monti Drive, Anderson, SC 29625; ronaldsamec@gmail.com

Walter Van Hamme
Department of Physics, Florida International University, Miami, FL 33199; vanhamme@fiu.edu

Daniel Caton
Dark Sky Observatory, Department of Physics and Astronomy, Appalachian State University, 525 Rivers Street, Boone, NC 28608-2106; catondb@appstate.edu

Danny Faulkner
AIG, Johnson Observatory, 1414 Bur Oak Court, Hebron, KY 41048; dfaulkner@answersingenesis.org

Received December 28, 2022; revised March 7, 2023; accepted March 18, 2023

Abstract CCD BVRI light curves of WISE J051352.5-170113 (GSC 5906 0087 = ASASSN-V J051352.59-170113.6) were taken on 21, 22, and 26, 27 January and 04 February 2021 at the Cerro Tololo InterAmerican Observatory, Chile, with the 0.6-m reflector, remotely. It is classified as a contact variable with a mean V magnitude of 11.77 and amplitude of V ~ 0.4. Five times of minimum light were determined, with one from the literature, along with 7 times of low light. From our present observations, and one primary eclipse and four secondary eclipses, we determined linear and quadratic ephemerides. From our 20-year period study, the period is found to be increasing. This might be due to mass transfer to the more massive, primary component making the mass ratio more extreme ($q = M_2 / M_1$). A Wilson-Devinney Program analysis reveals that the system is a A-type (more massive component is the hottest) W UMa binary with a fairly extreme mass ratio, $q = 0.2987 \pm 0.0007$, $1/q = M_1 / M_2 = 3.35$). Its Roche Lobe fill-out is ~18.9%. One hot spot was needed in the solution. The temperature difference of the components is only ~32 K, making the system in good thermal contact. The inclination is high, 80°, resulting in a brief total secondary eclipse lasting about 15 minutes.

1. History and background

The variable star WISE J051352.5-170113 (GSC 5906 0087 = ASASSN-V J051352.59-170113.6) is found online in the ASAS-SN Catalog of Variable Stars: V. The ASAS-SN low precision light curve is given as Figure 1.

The information given in the catalog includes the alternate name WISE J051352.5-170113, Mean VMag 11.57, APASS Vmag = 11.656, Amplitude VMag = 0.54, and an ephemeris:

$$\mathrm{HJD} = 2457767.55404\,\mathrm{d} + 0.3418393 * E, \quad (1)$$

a J–K: 0.415, and parallax, 4.2518 mas., giving a distance of 235.2 pc. Gezer and Bozkurt (2016) solved the low precision ASASSN-V V light curve (Figure 1) with the PHOEBE software (Prša and Zwitter 2005). This single curve has a precision of $\Delta V \sim 0.03$ mag. We simultaneously solved four light curves (B, V, R, I) with a much higher precision of ~0.004 mag. Their one color, low precision "solution" is given as Table 1; this, of course, bears little resemblance to our BVRI synthetic light curve solution. For instance, their inclination is 70.3° whereas our light curve solution gives $80.2 \pm 0.2°$, with a short total eclipse in the secondary. Such low precision light curves do not avail themselves of useful or accurate solutions.

From the ASAS curves (ASASSN-V J051352.59-170113.6) we were able to phase the data with Equation 1 and perform parabola fits to the primary and secondary minima to locate

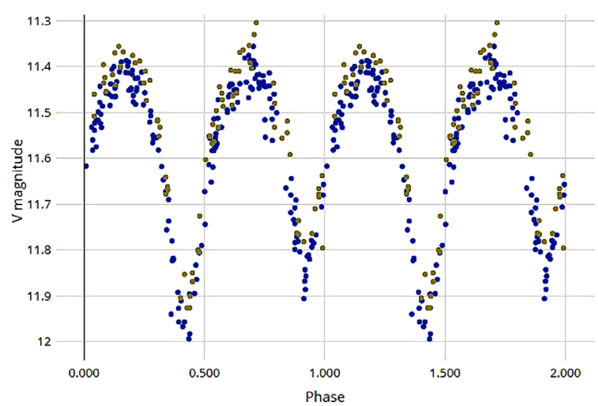

Figure 1. ASASSN-V J051352.59-170113.6, (low resolution) light curves (Pojmański 2002).

Table 1. Low Precision ASAS-SN Light Curve "Solution."

Parameter	*Prša Software Value*
I (°)	70.3
q (mass ratio)	0.52
T_1, T_2 (K)	5419, 5086
Ω (potential)	2.81
f (fill-out, %)	34
$L_{1v} / (L_{1v} + L_{2v})$	0.71
r_1 / a, r_2 / a	0.71. 0.46
HJD (T_o)	2,451,914.6192
Period (d)	0.34183617

seven times of "low light" within 0.001 phase of each minimum. We also included the ASAS HJD Min I in our period study.

This system was observed as a part of our professional collaborative studies of interacting binaries at Pisgah Astronomical Research Institute using data taken from CTIO observations.

The observations were taken by Caton. Reduction and analyses were done by Samec.

The 2020 BVRI light curves were taken at Cerro Tololo InterAmerican Observatory, on 21, 22, 26, 27 January, 3 and 4 February 2021 with a thermoelectrically cooled (–25° C) 1KX1K FLI camera and Bessell BVRI filters.

Individual observations included 179 in B, 180 in V, 188 in R, and 180 in I. The probable error of a single observation was 4 mmag in B, V, and R, and 3 mmag in I. The nightly C–K values stayed constant throughout the observing run, with a precision of about 1%. Exposure times varied from 45 s in B, to 20 s in V, and 15 s in R and I. To produce these images, nightly images were calibrated with 25 bias frames, at least five flat frames in each filter, and ten 300-second dark frames. A sample of the observations are given in Table 3 (The full table is available through the AAVSO ftp site as noted in the table).

2. Target stars

Figure 2 shows the variable (V), comparison (C), and check (K) stars. Details regarding these stars are given in Table 2.

3. Period determination

Five mean times (from BVRI data) of minimum light were calculated from our present observations, one primary and four secondary eclipses:

HJD I = 2459240.54968 ±0.00040

HJD II = 2459235.59483 ± 0.00042; 2459236.62057 ± 0.00079; 2459240.7216 ± 0.0015; 2459249.61244 ± 0.00086.

These minima were weighted as 1.0 in the period study. Another minimum was obtained from Gezer and Bozkurt (2016). In addition, seven times of minimum light were calculated

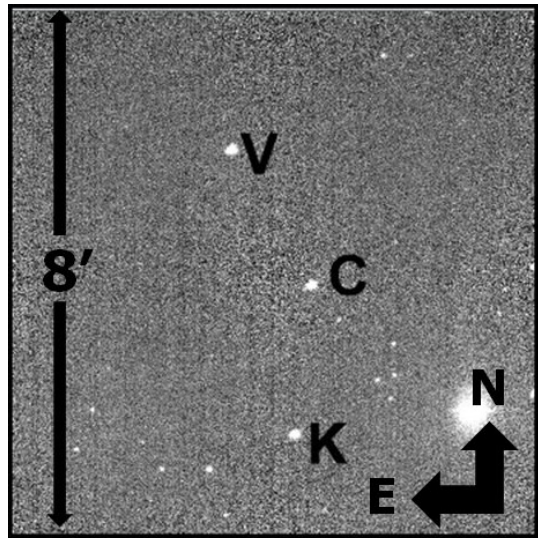

Figure 2. V magnitude finding chart, showing the variable star (V), comparison star (C), and check star (K).

from ASAS data and were weighted 0.1. These 13 minima gave us a period study with an interval of ~20.1 years. From these timings, two ephemerides have been calculated, a linear and a quadratic one:

$$\text{JD Hel Min I} = 2459240.55065 \pm 0.00066\,\text{d} + 0.341838117 \pm 0.000000078 \times E \quad (2)$$

$$\text{JD Hel Min I} = 2459240.55147 \pm 0.00030\,\text{d} + 0.34184041 \pm 0.00000023 \times E + 0.000000000108 \pm 0.000000000011 \times E2. \quad (3)$$

The initial ephemeris used to start the period study was:

$$\text{JD Hel Min I} = 2459240.54968 + 0.3418393 \times E. \quad (4)$$

The residuals of the period study are given in Table 4.

The current study covers a time interval of 20.1 years. It shows an orbital period that is increasing as shown in the O–C curve. This might be due to mass transfer to the more massive, primary component making the mass ratio more extreme.

Table 2. Photometric targets.

Star	*Name*	*R.A. (2000)* h m s	*Dec. (2000)* ° ′ ″	*V*	*J–K*	*Type*[2]
V (Variable) distance: 235.2 pc parallax: 4.2518 mas proper motion: α –22.76(4), δ –46.25(5)	WISE J051352.5-170113 GSC 5906 0087 2MASS J05135261-1701128 ASAS J051353-1701.2 Gaia DR2 2982692166728058880	05 13 52.6098618119[1]	–17 01 13.018190520[1]	11.359	0.415 ± 0.041	G7.5
C (Comparison)	GSC 5906 0601 3UC146-016767	05 13 46.0730[2]	–17 03 53.47[2]	12.25	0.36 ± 0.046	G2V
K (Check)	GSC 5906 0211 3UC255-052413	05 13 47.4780[2]	–17 06 49.807[2]	12.26	0.380 ± 0.046	G4V

[1] *ICRS (IAU 2013).* [2] *UCAC3 (Zacharias, N.,* et al. *2010).*

Table 3. Sample of first ten WISE J051352.5-170113 *B, V, R, I* observations.

ΔB	*HJD 2459200+*	ΔV	*HJD 2459200+*	ΔR	*HJD 2459200+*	ΔI	*HJD 2459200+*
–0.7010	35.5232	–0.8360	35.5184	–0.8680	35.5336	–0.9410	35.5221
–0.6730	35.5290	–0.7900	35.5246	–0.7660	35.5545	–0.9320	35.5268
–0.6490	35.5372	–0.8040	35.5319	–0.6650	35.5683	–0.8970	35.5349
–0.4810	35.5639	–0.7370	35.5394	–0.6180	35.5737	–0.8020	35.5592
–0.4110	35.5713	–0.6040	35.5670	–0.5740	35.5778	–0.7150	35.5696
–0.3630	35.5756	–0.5270	35.5728	–0.5320	35.5818	–0.6640	35.5744
–0.2690	35.5836	–0.4930	35.5770	–0.4940	35.5858	–0.6250	35.5784
–0.2430	35.5875	–0.4520	35.5810	–0.4750	35.5897	–0.5890	35.5824
–0.2060	35.5915	–0.4140	35.5849	–0.4580	35.5937	–0.5530	35.5863
–0.1890	35.5955	–0.3780	35.5889	–0.4590	35.5977	–0.5420	35.5903

Note: First ten data points of WISE J051352.5-170113 *B, V, R, I observations. The complete table is available through the AAVSO ftp site at ftp://ftp.aavso.org/public/datasets/3871-Samec-511-wisej051.txt (if necessary, copy and paste link into the address bar of a web browser).*

Table 4. Period study residuals, WISE J051352.5-170113.

	Epoch +2400000	*Cycle*	*Initial Residuals*	*Linear Residuals*	*Quadratic Residuals*	*Wt.*	*Ref.*
1	51914.6192	–21431.0	0.0276	0.0013	0.0000	1.0	2
2	56978.943	–6616.0	0.0021	–0.0067	0.0030	0.1	1
3	57004.919	–6540.0	–0.0017	–0.0104	–0.0008	0.1	1
4	57599.890	–4799.5	–0.0020	–0.0086	–0.0009	0.1	1
5	57724.662	–4434.5	–0.0013	–0.0075	–0.0003	0.1	1
6	57745.684	–4373.0	–0.0024	–0.0086	–0.0014	0.1	1
7	58010.781	–3597.5	–0.0018	–0.0070	–0.0010	0.1	1
8	58035.737	–3524.5	–0.0001	–0.0052	0.0007	0.1	1
9	59235.5949	–14.5	0.0019	0.0009	0.0001	1.0	3
10	59236.6206	–11.5	0.0020	0.0011	0.0003	1.0	3
11	59240.5497	0.0	0.0000	–0.0010	–0.0018	1.0	3
12	59240.7216	0.5	0.0010	0.0001	–0.0008	1.0	3
13	59249.6124	26.5	0.0040	0.0031	0.0022	1.0	3

References: (1) Shappee et al. *(2014), Kochanek* et al. *(2017); (2) Gezer and Bozkurt (2016); (3) present observations.*

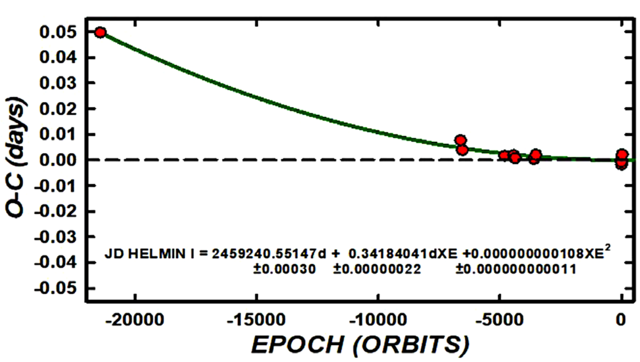

Figure 3. Quadratic period residuals, Equation 2.

The quadratic ephemeris yields a $dP/dt = 2.31 \times 10^{-7}$ d/yr, or a mass exchange rate of $dM/dt = 9.86 \times 10^{-8} M_{\odot}/d$, in a conservative scenario (the primary component is the gainer.) The phased light curves from Equation 2 are given in Figures 4 and 5.

4. Light curve characteristics

The curves are of good precision, averaging about 1% over the run. This variability is probably due to coronal action in this solar-type binary over the fourteen nights. The amplitude of the light curve varies from 0.581 to 0.506 mag. B to I. The O'Connell effect, an indicator of spot activity, was 0.017–0.040 mag, B to I, indicating some magnetic activity. The variation of the maximum in the primary maximum of the R and I curves is the effect of this activity. The difference in minima, 0.062 to 0.046 B to I, indicates overcontact light curves in good thermal contact. A time of zero secondary component flux in our BVRI light curve solutions reveals an eclipse that lasts 15 minutes. The phased light curve characteristics are given in Table 5.

5. Light curve solution

5.1. Temperature

The 2MASS, $J–K = 0.415 \pm 0.033$ for the binary star corresponds to ~G7.5 ± 0.5, which yields a temperature of ~5750 ± 250 K. Fast rotating binary stars of this type are noted for having strong magnetic activity, so the binary is of solar type with a convective atmosphere.

The BVRI curves were pre-modeled with Binary Maker 3.0 (Bradstreet and Steelman 2002), and fits were determined in all filter bands which were very stable. The solution was that of an overcontact eclipsing binary. The parameters were

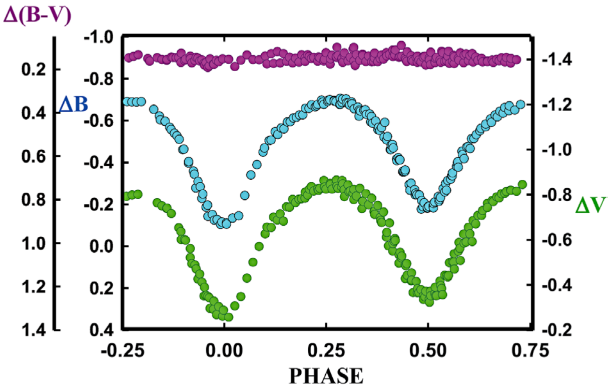

Figure 4. B, V mag light curves phased with Equation 2.

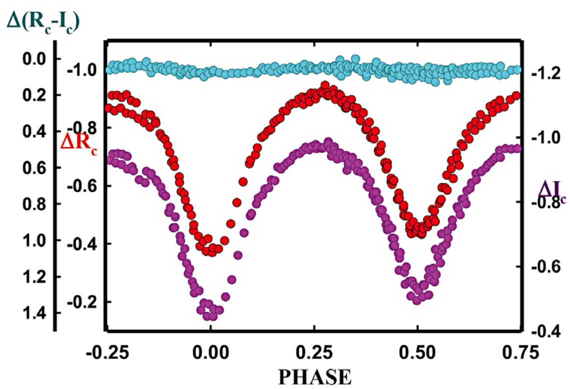

Figure 5. R, I mag light curves phased with Equation 2.

Table 5. Light Curve Characteristics, WISE J051352.5-170113.

Filter	*Phase Mag. Min I*	*±σ*	*Phase Mag. Max I*	*±σ*
	0.000		0.25	
B	–0.107	0.006	–0.693	0.004
V	–0.284	0.018	–0.842	0.015
R	–0.391	0.021	–0.918	0.005
I	–0.465	0.020	–0.968	0.003

Filter	*Phase Mag. Min II*	*±σ*	*Phase Mag. Max II*	*±σ*
	0.50	0.75		
B	–0.194	0.014	–0.688	0.004
V	–0.348	0.017	–0.796	0.015
R	–0.443	0.010	–0.911	0.005
I	–0.523	0.021	–0.945	0.003

Filter	*Min I– Max I*	*±σ*	*Max II– Max I*	*±σ*	*Min I– Min II*	*±σ*
B	0.586	0.010	0.005	0.005	0.087	0.020
V	0.558	0.033	0.046	0.046	0.063	0.035
R	0.527	0.026	0.007	0.007	0.053	0.031
I	0.503	0.023	0.023	0.023	0.057	0.041

Filter	*Min II– Max I*	*±σ*	*Min I– Max II*	*±σ*	*Min II– Max II*	*±σ*
B	0.499	0.018	0.581	0.010	0.494	0.018
V	0.495	0.032	0.512	0.033	0.449	0.032
R	0.475	0.015	0.520	0.026	0.468	0.015
I	0.446	0.023	0.480	0.023	0.423	0.023

Table 6. Synthetic Light Curve Solution of WISE J051352.5-170113.

Parameters	*Values*
$\lambda_B,\lambda_V,\lambda_R,\lambda_I$ (nm)	440, 550, 640, 790
g_1, g_2	0.32
A_1, A_2	0.5
Inclination (∞)	80.2±0.2[1]
T_1, T_2 (K)	5500, 5468±36
$\Omega_1=\Omega_2$	2.42820±0.00228
$q(m_1/m_2)$	0.29868±0.00074
Fill-outs: f(%)	18.9±0.2
$L_1/(L_1+L_2)_I$	0.7509±0.0102
$L_1/(L_1+L_2)_R$	0.7489±0.0098
$L_1/(L_1+L_2)_V$	0.7523±0.0133
$L_1/(L_1+L_2)_B$	0.7538±0.0085
JDo (days)	2459240.55082±0.00009
Period (days)	0. 341896±0.000008
Dimensions:	
r_1/a, r_2/a (pole)	0.463±0.002, 0.268±0.001
r_1/a, r_2/a (side)	0.5004±0.0024, 0.281±0.001
r_1/a, r_2/a (back)	0.528±0.003, 0.320±0.008
Spot, Primary Component	*Hot Spot Region*
Colatitude (°)	80.1±0.2
Longitude (°)	209.6±0.3
Radius (°)	12.57±0.20
T-Factor	1.119±0.003

[1] *Note on Wilson (WD) program errors: The WD uncertainties are computed from the covariance matrix of the normal equations in the standard way. They are 1-σ uncertainties, which may strike some persons as too small, but they are standard error estimates—not peculiar to WD.*

Table 7. Roche Lobe Dimensions.[1]

Radii	*Star 1*	*Star 2*
R_1, R_2 (pole, $R_\odot$)	1.0234±0.0039	0.5931±0.0027
R_1, R_2 (side, $R_\odot$)	1.1046±0.0027	0.6200±0.0006
R_1, R_2 (back, $R_\odot$)	1.1656±0.0050	0.7063±0.0005

[1] *Using light curve solution units, a = 1, R's output of Wilson program, a is calculated for the Wilson program, the semi-major axis, using a = 2.20762 $R_\odot$ from Kepler's law.*

Table 8. WISEJ051352.5-170113 estimated system parameters (totally eclipsing).[1]

Parameter	*Star 1*	*Star 2*
Mean Radius ($R_\odot$)	1.098±0.004	0.640±0.0013
Mean density	1.020	1.556
Mass ($M_\odot$)	0.958	0.289
Log g	4.34	4.29

[1] *The densities are in g/cm³ BINARY MAKER, using calculated density from Roche Lobes by Bradstreet and Steelman (2002).*

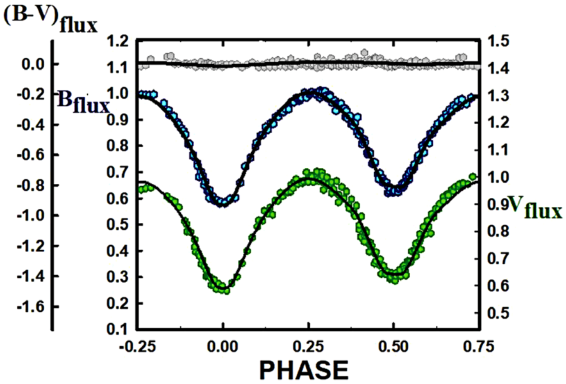

Figure 6. Figure 6. B, V light curve solution overlaying normalized flux light curves.

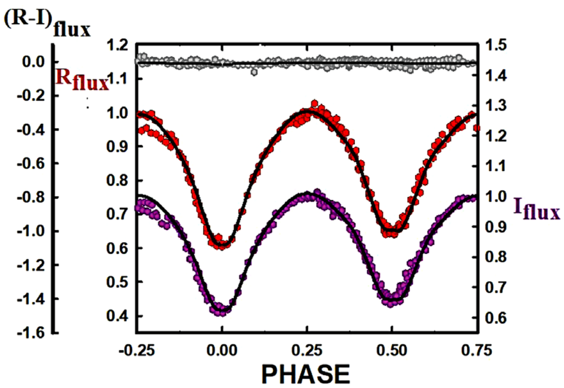

Figure 7. Figure 7. R, I light curve solution overlaying normalized flux light curves. The variability of the R and I light curves are probably due to magnetic activity.

then averaged (q = 0.30, fill-out = 30%, i = 80.5°, T_1 = 5750, with one 10° hot spot, T-FACT = 1.18) and input into a four-color simultaneous light curve calculation using the Wilson-Devinney Program (WD; Wilson and Devinney 1971; Wilson 1990, 1994, 2004; Van Hamme and Wilson 1998). The solution was computed in Mode 3 and converged to a solution. Convective parameters, g = 0.32, A = 0.5 were used. An eclipse duration of ~15 minutes was determined for the secondary eclipse from the light curve solution. The more massive component is the hottest one, making the system an A-type W UMa overcontact binary. We tried third light but that did not solve any fitting issues. The solution parameters are given in Table 6.

The estimated and absolute system parameters follow in Tables 7 and 8.

The surface geometry at quarter phases of the orbit is shown in Figure 8.

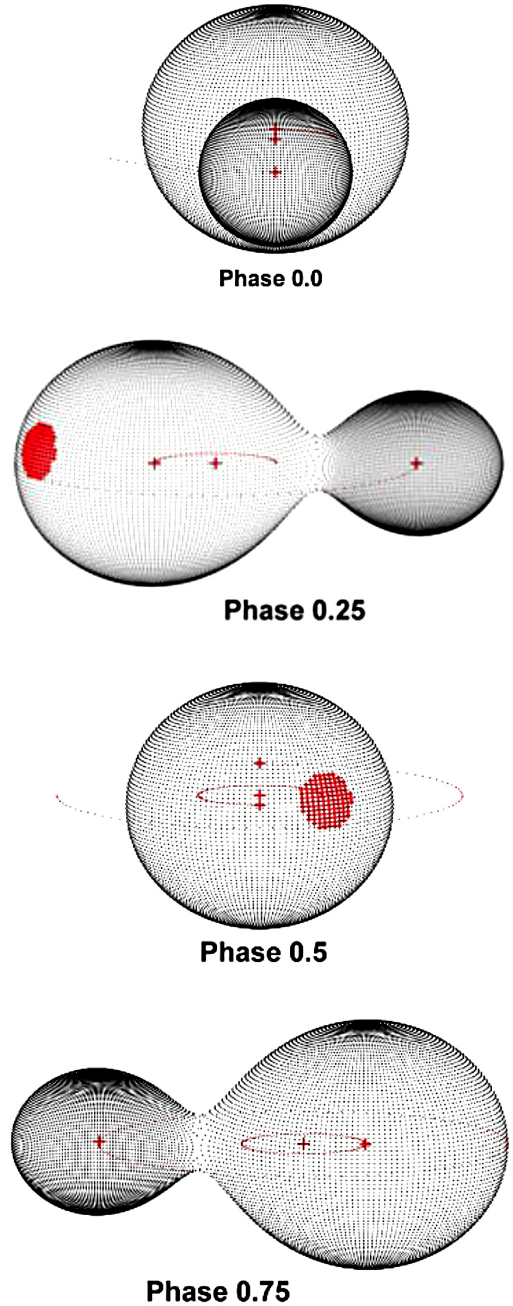

Figure 8. The surface geometry at quarter phases of the orbit

6. Discussion and conclusion

WISE J051352.5-170113 is a A-type, W UMa binary. Since the eclipses are total, the mass ratio, q = 0.30, is well determined with a fill-out of ~19%. The system has a component temperature difference of only ~32 K, and is in good thermal contact. One spot was needed in the final modeling. The inclination of ~80.2 degrees resulted in a time of constant light in the primary eclipse. Its photometric spectral type indicates a surface temperature of ~5500 K for the primary component, making it a solar-type binary. Such a main sequence star would have a mass of ~0.96 $M_\odot$ (G7.5V) and the secondary (from the solution's mass ratio) would have a mass of ~0.29 $M_\odot$, making it under-massive for its size. The temperature of the secondary component (~5468 K) of a main sequence star would make it of type G7.5V instead of M3.5V as indicated by its mass. This is probably due to substantial energy transfer between them. The period study of this binary indicates that it is increasing. This could be due to mass exchange with the flow toward the more massive component making the mass ratio more extreme.

7. Future work

Radial velocity curves are needed to obtain absolute (not relative) system parameters.

References

Bradstreet, D. H., and Steelman, D. P. 2002, *Bull. Amer. Astron. Soc.*, **34**, 1224.

Gezer, I., and Bozkurt, Z. 2016, *New Astron.*, **44**, 40.

International Astronomical Union. 2013, International Earth Rotation and Reference Systems Service, International Celestial Reference System (ICRS; https://www.iers.org/IERS/EN/Science/ICRS/ICRS.html).

Kochanek, C. S., *et al.* 2017, *Publ. Astron. Soc. Pacific*, **129**, 104502.

Pojmański, G. 2002, *Acta Astron.*, **52**, 397.

Prša, A., and Zwitter, T. 2005, *Astrophys. J.*, **628**, 426.

Shappee, B. J., *et al.* 2014, *Astrophys. J.*, **788**, 48.

Van Hamme, W., and Wilson, R. E. 1998, *Bull. Amer. Astron. Soc.*, **30**, 1402.

Wilson, R. E. 1990, *Astrophys. J.*, **356**, 613.

Wilson, R. E. 1994, *Publ. Astron. Soc. Pacific*, **106**, 921.

Wilson, R. E. 2004, *New Astron. Rev.*, **48**, 695.

Wilson, R. E., and Devinney, E. J. 1971, *Astrophys. J.*, **166**, 605.

Zacharias, N., *et al.* 2010, *Astron. J.*, **139**, 2184.

A Photometric Study of the Contact Binaries CD Sextantis, V365 Sagittae, V1148 Herculis, and NSVS 9027851

Edward J. Michaels
Waffelow Creek Observatory, 10780 FM1878, Nacogdoches, TX 75961; astroed@ejmj.net

Received January 16, 2023; revised February 22, 2023; accepted February 22, 2023

Abstract Multi-band photometric observations were acquired for the eclipsing binary stars CD Sex, V365 Sge, V1148 Her, and NSVS 9027851. These binaries have orbital periods less than 0.37 day, stellar surface temperatures less than solar, and total eclipses at primary minimum. New ephemerides were computed using minima timings from the observations, combined with other timings located in the literature. A period analysis found possible long-term orbital period changes for V1148 Her and V365 Sge. In addition, sinusoidal variations in the O–C residuals of V365 Sge indicate a possible low mass circumbinary companion. Photometric solutions using the Wilson-Devinney (WD) program confirmed that each system is a W-subtype contact binary with fill-outs that range from 15 to 22%. The total eclipses provided reliable solution mass ratios for estimating the absolute parameters of the component stars. All the light curves displayed asymmetries with obvious differences in the brightness of Max I and Max II (O'Connell effect). The asymmetries were attributed to magnetic activity and were modeled as hot and cool spots on the stellar surfaces.

1. Introduction

1.1. Background

Over the past 20 years a number of surveys have identified numerous new contact eclipsing binaries (ASAS, Pojmański 2002; NSVS, Woźniak *et al.* 2004; Hoffman *et al.* 2009; CRTS, Drake *et al.* 2014; ATLAS, Tonry *et al.* 2018). The stars in this study, CD Sex, V365 Sge, V1148 Her, and NSVS 9027851, were classified as W UMa contact binaries in one or more of these surveys. Presented in this paper are new multi-band photometric observations of each star at a higher precision and cadence than provided by the survey data. A brief history of each system is given in the next subsection, with the photometric observations presented in section 2. New minima times, ephemerides, observed properties, and WD light curve analyses are presented in section 3. Discussions of the results are presented in section 4 and conclusions in section 5.

1.2. Notes on individual stars

1.2.1. CD Sex

The variability of CD Sex (GSC 00253-00870, 2MASS J10392274+0135355) was first discovered in the Northern Sky Variability Survey (NSVS; Woźniak *et al.* 2004). Automated variable star classification techniques using NSVS, and All-Sky Automated Survey (ASAS; Pojmański, G. 2002) observations classified it as a W UMa binary (Hoffman *et al.* 2009; Richards *et al.* 2012). The All-Sky Automated Survey for Supernovae (ASAS-SN) catalog also classified the star as a W UMa system with an orbital period of P = 0.2688689 day (Shappee *et al.* 2014; Jayasinghe *et al.* 2018). The Catalina Sky Survey (CRTS) gives a visual magnitude of V = 13.1 with a 0.63-amplitude eclipse (Drake *et al.* 2014). There were six times of minima found in the literature. The Gaia-DR3 parallax gives a distance to this system of d = 288 ± 2 pc (Gaia Collaboration 2022).

1.2.2. V365 Sge

The variability of V365 Sge (GSC 01621-02192, 2MASS J20075538+1731161) was first recognized by Richmond (2002) while observing an outburst of WZ Sge in the same field. He later obtained BVI_c observations of this star and found a maximum visual magnitude of V = 12.5 and a primary eclipse depth of 0.7 magnitude, and classified it as a W UMa contact binary with a period of 0.3690 day. V365 Sge was also given this classification using NSVS observations (Hoffman *et al.* 2009) and from Terrell *et al.*'s (2012) BVR_cI_c photometry. A literature search located eight minima timings for this star. The Gaia-DR3 parallax gives a distance of d = 471 ± 4 pc.

1.2.3. V1148 Her

The variability of V1148 Her (GSC 03494-01097, 2MASS J16012197+4829378) was first reported in the NSVS Skydot catalog (Woźniak *et al.* 2004). An automated classification of NSVS variables identified this star as a W UMa eclipsing binary with an orbital period of P = 0.28229 day (Hoffman *et al.* 2009). The same classification was assigned in the ASAS-SN catalog of variable stars (Jayasinghe *et al.* 2018). A catalog of bright contact binary stars gives a maximum visual magnitude of V = 12.421 and an eclipse amplitude of 0.683 magnitude (Gettel *et al.* 2006). Only two times of minima were located for this star and the Gaia-DR3 parallax gives a distance of d = 288 ± 1 pc.

1.2.4. NSVS 9027851

NSVS 9027851 (2MASS J23231590+3018226, GSC 02752-01272, ASASSN-V J232315.88+301822.9) is located in the constellation Pegasus. It should be noted that a search in the SIMBAD database gives this star's designation as NSVS 6222255, which is not recognized in The International Variable Star Index (VSX; Watson *et al.* 2014). The variability of this star was first discovered in NSVS observations (Woźniak *et al.* 2004). Both the NSVS and ASAS-SN catalogs classified this star as a W UMa eclipsing binary with an orbital period of P = 0.3626625 day, a visual magnitude of V = 13.13, and an eclipse amplitude of 0.57 magnitude (Hoffman *et al.* 2009; Jayasinghe *et al.* 2018). This star has a distance of d = 430 ± 4 pc according to the Gaia-DR3. A literature search did not locate any minima times for this star.

2. Photometric observations

Photometric observations of the close binaries in this study were acquired with a SBIG-STXL CCD camera attached to the 0.36-m Ritchey-Chrétien robotic telescope at the Waffelow Creek Observatory (https://obs.ejmj.net/index.php). The telescope and camera have an image scale of 0.66 arcsec / pixel and a 33.7' × 22.5' field of view. Each star was imaged in four passbands, Johnson V and Sloan g', r', and i'. In addition, V365 Sge and NSVS 9027851 were also imaged in the Johnson B passband. The observation log in Table 1 gives the observation season, the number of nights each star was observed, and the number of images acquired in each passband. The finder charts in Figure 1 show the locations of the comparison and check stars in each field. Table 2 gives the GSC designation, coordinates, and standard magnitudes for all stars used in this study. The standard magnitudes were taken from the AAVSO Photometric All-Sky Survey database (APASS; Henden *et al.* 2015). MIRA software was used for image calibration (bias, dark, and flat correction) and to perform the ensemble aperture photometry of the light images (Mirametrics 2015). The instrumental magnitudes of the variable stars were converted to standard magnitudes. The Heliocentric Julian Date of each observation was converted to orbital phase (φ) using the new linear epochs and orbital periods given in Table 5. Figure 2 shows the folded light curves plotted from orbital phase -0.6 to 0.6, with negative phase defined as φ – 1. The check star magnitudes were plotted below the light curves, which showed no significant variability. The standard error of a single observation ranged from 4 to 10 mmag. The light curve properties are given in Table 3 (Min I, Min II, Max I, Max II, Δm, and total eclipse duration). All the observations can be accessed from the AAVSO International Database (Kafka 2017).

3. Analysis

3.1. Ephemerides

As previously discussed, literature searches located the minima timings available for each star. The primary and secondary minima from the new observations were determined using the Kwee and van Woerden (1956) method. Several additional minima times were derived using observations with sufficient nightly cadence from the AAVSO and SuperWASP databases. All the minima times and errors are compiled in Table 4. This table also shows the cycle numbers and the difference between the observed and predicted minima times (O–C). The predicted minima times were calculated using the reference epochs and orbital periods given in Table 5. New linear light elements were computed by least-squares solution using the O–C residuals. The regression results and residuals are shown in the O–C diagrams in Figure 3 and the new linear light elements in Table 5.

The residuals from the regression analysis of V365 Sge indicate the orbital period of this binary may be undergoing a long-term linear and possibly a cyclic period change (see Figure 3). A long-term period change reveals itself as a parabolic trend in the O–C residuals and a cyclic change as a sinusoidal trend. A long-term period change is frequently attributed to mass transfer between the component stars or loss of angular momentum from the system. An apparent cyclic period change can result from a light-time effect (LITE) caused by a circumbinary companion. It is not uncommon for contact binaries to have a third star orbiting around them (Liao and Qian 2010; Qian *et al.* 2013; Pribulla and Ruciński 2006). The sinusoidal variation in the residuals appears symmetrical, which indicates a circular orbit for a tertiary component (see bottom panel in Figure 4). To describe the general trend of the O–C residuals, the following equation was used to investigate the parabolic and sinusoidal variations in the orbital period:

$$\text{HJD Min I} = \text{HJD}_0 + PE + QE^2 + A \sin(\omega E + \varphi). \qquad (1)$$

The first three terms ($\text{HJD}_0 + PE + QE^2$) is the quadratic ephemeris where Q measures the long-term period change, and the fourth term is the time difference resulting from the orbital motion of the binary about the barycenter of a tertiary system. For the regression analysis the following weights were assigned to individual minima times: w = 1 for times derived from visual observations and w = 10 for CCD observations. The parameter values HJD_0, P, Q, A, ω, and φ were determined using the Levenberg-Marquardt algorithm, which gives the following ephemeris:

$$\begin{aligned}\text{HJD Min I} = {} & 2459767.6180(1) + 0.3691265(5)\,E \\ & -2.889(2) \times 10^{-10}\,E^2 \\ & + 0.001887(2) \sin(0.0005278(4)\,E + 0.494(5)). \qquad (2)\end{aligned}$$

The negative quadratic coefficient in Equation 2 suggests a slowly decreasing orbital period with a rate of $-1.055(2) \times 10^{-7}\,\text{d} \cdot \text{yr}^{-1}$, or about 1 second per century. The top panel of Figure 4 shows the O–C diagram where the solid line represents Equation 2, a combination of the long-term period change and the cyclic LITE variation caused by the proposed tertiary component. The dashed line is the quadratic component in this equation. The middle panel shows the residuals after removing the downward parabolic change and the cyclic variation. In the bottom panel only the quadratic term of Equation 2 is subtracted to show the periodic variation more clearly. The results of this period analysis will be discussed further in section 5.

The residuals from the linear regression analysis of V1148 Her also has a parabolic shape which indicates a possible long-term linear period change (see Figure 3). A second least-squares solution of the O–C residuals in Table 4 gives the following quadratic ephemeris:

$$\begin{aligned}\text{HJD Min I} = {} & 2459771.794(3) + 0.2822539(1)\,E \\ & + 1.28(3) \times 10^{-11}\,E^2. \qquad (3)\end{aligned}$$

The positive sign of the quadratic coefficient indicates the period is increasing at a rate of $dP/dt = 3.31(9) \times 10^{-8}\,\text{d} \cdot \text{yr}^{-1}$. This slow period change should be considered preliminary since it was determined from a relatively small number of minima timings. The dashed line in the O–C diagram of Figure 5 (top panel) represents Equation 3 with the residuals in the bottom panel.

Table 1. Observation Log.

System	Dates	No. Nights	Images Acquired B	V	g′	r′	i′
CD Sex	2022 Mar	13	--	457	711	620	625
V365 Sge	2020 Aug	24	771	665	531	523	510
V1148 Her	2020 Jun/Jul	14	--	1375	637	701	448
NSVS 9027851	2022 Sep	13	747	861	685	729	881

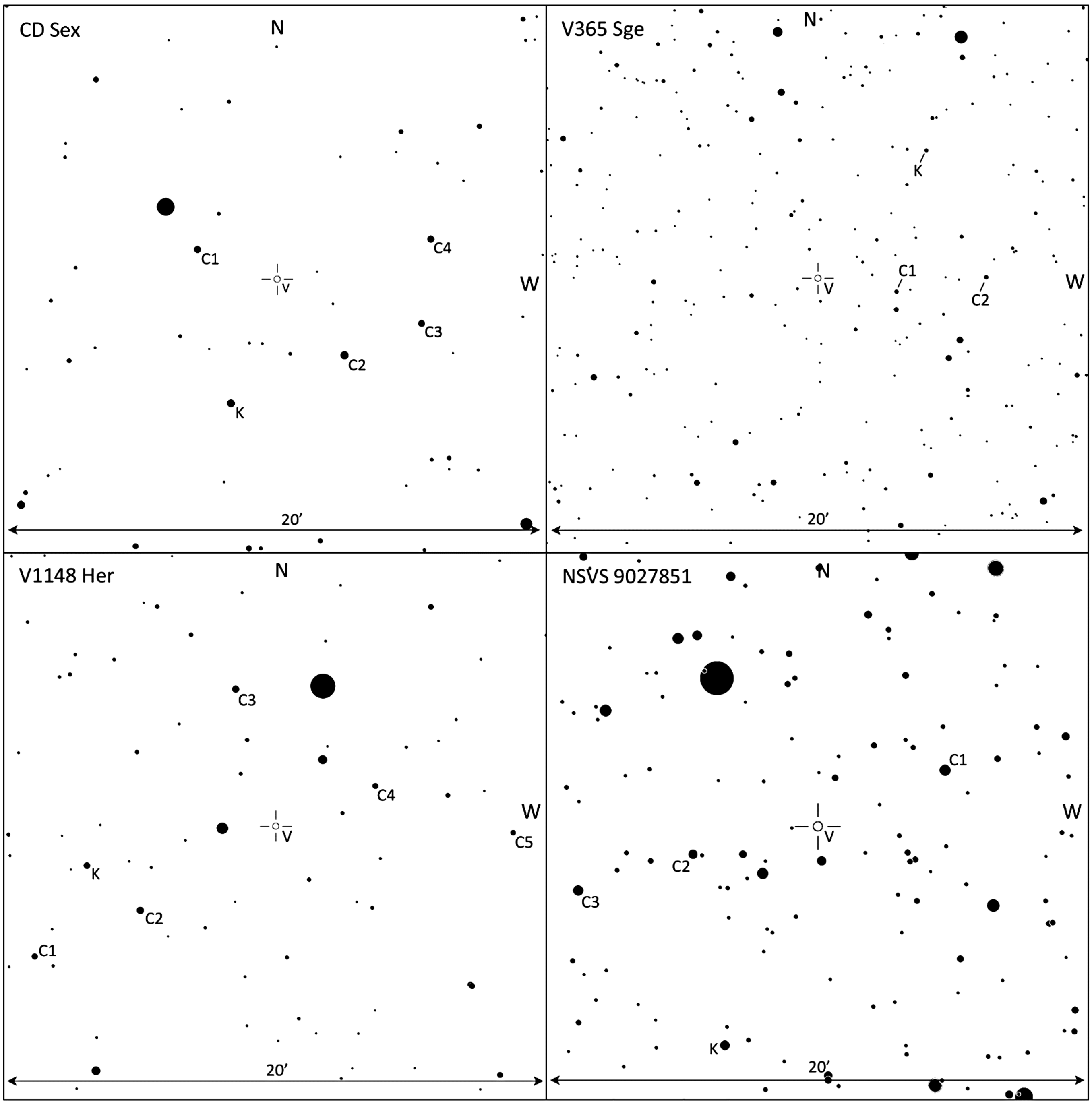

Figure 1. Finder charts showing the locations of the binary (V), comparison (C1–C6), and check (K) stars for each system. The comparison star designations correspond to the values in Table 2.

Table 2. APASS (Henden *et al.* 2015) Comparison and Check Star Magnitudes.

System	R.A. (2000) h	Dec. (2000) °	B	V	g′	r′	i′
CD Sex	10.65631	+1.59310					
GSC 00253-00725 (C1)	10.65950	+1.61099	—	12.735	12.966	12.590	12.460
GSC 00253-00688 (C2)	10.65361	+1.54740	—	12.286	12.611	12.057	11.849
GSC 00253-01037 (C3)	10.65053	+1.56658	—	12.831	13.045	12.717	12.585
GSC 00253-00243 (C4)	10.65016	+1.61724	—	12.702	12.903	12.599	12.494
GSC 00253-00964 (K)	10.65816	+1.51859	—	12.427	12.587	12.340	12.255
Standard deviation of observed K-star magnitudes			—	± 0.004	± 0.004	± 0.004	± 0.006
V365 Sge	20.13205	+17.52113					
GSC 01621-02177 (C1)	20.12876	+17.51321	13.901	12.820	13.253	12.396	11.826
GSC 01621-02205 (C2)	20.12499	+17.52172	12.764	12.472	12.511	12.361	12.244
GSC 01621-01948 (K)	20.12750	+17.59833	14.094	13.131	13.506	12.777	12.358
Standard deviation of observed K-star magnitudes			± 0.015	± 0.008	± 0.010	± 0.006	± 0.008
V1148 Her	16.02276	+48.49413					
GSC 03494-01301 (C1)	16.03723	+48.41505	—	13.289	13.478	13.149	13.000
GSC 03494-00204 (C2)	16.03090	+48.44308	—	12.848	13.312	12.501	12.202
GSC 03494-00893 (C3)	16.02518	+48.57641	—	12.862	13.227	12.580	12.291
GSC 03494-00980 (C4)	16.01677	+48.51808	—	13.399	13.670	13.213	13.025
GSC 03494-00963 (C5)	16.00849	+48.48968	—	13.674	13.995	13.460	13.235
GSC 03494-00516 (K)	16.03412	+48.46998	—	13.096	13.302	12.940	12.770
Standard deviation of observed K-star magnitudes			—	± 0.010	± 0.007	± 0.007	± 0.008
NSVS 9027851	23.38775	+30.30626					
GSC 02752-01546 (C1)	23.38169	+30.34064	13.224	12.455	12.792	12.226	11.992
GSC 02752-01892 (C2)	23.39369	+30.28903	13.879	13.099	13.441	12.841	12.591
GSC 02752-01924 (C3)	23.39915	+30.26692	13.680	12.846	13.214	12.588	12.318
GSC 02752-01240 (K)	23.39217	+30.17197	13.857	13.023	13.388	12.743	12.461
Standard deviation of observed K-star magnitudes			± 0.012	± 0.006	± 0.006	± 0.005	± 0.006

Table 3. Light curve properties.

	Min I Mag.	Min II Mag.	Max I Mag.	Max II Mag.	Delta Mag. Max II - Min I	Total Eclipse Duration (minutes)
CD Sex						
V	13.943 ± 0.014	13.850 ± 0.007	13.153 ± 0.005	13.127 ± 0.010	0.816 ± 0.008	≈ 12
g'	14.365 ± 0.013	14.279 ± 0.013	13.563 ± 0.011	13.526 ± 0.005	0.839 ± 0.027	≈ 12
r'	13.610 ± 0.009	13.522 ± 0.003	12.860 ± 0.004	12.820 ± 0.006	0.791 ± 0.002	≈ 12
i'	13.278 ± 0.013	13.200 ± 0.014	12.546 ± 0.008	12.525 ± 0.008	0.753 ± 0.012	≈ 11
V365 Sge						
B	14.042 ± 0.010	13.906 ± 0.012	13.253 ± 0.007	13.263 ± 0.004	0.779 ± 0.011	≈ 27
V	13.381 ± 0.006	13.283 ± 0.010	12.652 ± 0.007	12.680 ± 0.007	0.701 ± 0.017	≈ 27
g'	13.597 ± 0.019	13.485 ± 0.012	12.844 ± 0.005	12.866 ± 0.006	0.732 ± 0.056	≈ 27
r'	13.119 ± 0.012	13.014 ± 0.004	12.411 ± 0.004	12.432 ± 0.007	0.688 ± 0.038	≈ 27
i'	12.795 ± 0.007	12.702 ± 0.007	12.122 ± 0.001	12.137 ± 0.005	0.658 ± 0.049	≈ 27
V1148 Her						
V	13.135 ± 0.012	13.086 ± 0.013	12.465 ± 0.006	12.526 ± 0.005	0.609 ± 0.008	≈ 20
g'	13.427 ± 0.008	13.380 ± 0.010	12.745 ± 0.006	12.818 ± 0.009	0.610 ± 0.046	≈ 20
r'	12.910 ± 0.003	12.859 ± 0.003	12.262 ± 0.003	12.318 ± 0.003	0.593 ± 0.004	≈ 21
i'	12.648 ± 0.008	12.605 ± 0.007	12.024 ± 0.005	12.072 ± 0.002	0.576 ± 0.011	≈ 20
NSVS 9027851						
B	14.410 ± 0.014	14.352 ± 0.013	13.758 ± 0.017	13.818 ± 0.009	0.592 ± 0.017	≈ 32
V	13.527 ± 0.005	13.477 ± 0.010	12.916 ± 0.006	12.963 ± 0.007	0.564 ± 0.023	≈ 31
g'	13.926 ± 0.011	13.862 ± 0.004	13.295 ± 0.005	13.334 ± 0.007	0.592 ± 0.030	≈ 31
r'	13.244 ± 0.003	13.200 ± 0.008	12.657 ± 0.004	12.683 ± 0.005	0.561 ± 0.037	≈ 31
i'	12.956 ± 0.009	12.907 ± 0.007	12.381 ± 0.004	12.413 ± 0.006	0.543 ± 0.010	≈ 30

Table 4. Times of minima and O–C residuals.

Epoch HJD 2400000+	*Error*	*Cycle*	*O–C*	*Ref.*
CD Sex				
55259.9227	0.00010	0.0	0.00000	5
55591.8422	0.00020	1234.5	–0.00052	6
55591.9765	0.00010	1235.0	–0.00065	6
55671.6958	0.00080	1531.5	–0.00130	6
55959.9224	0.00050	2603.5	–0.00334	8
56015.7154	0.00020	2811.0	–0.00087	8
57530.7919	—	8446.0	–0.00678	2
59638.7252	0.00007	16286.0	–0.01436	19
59638.8592	0.00006	16286.5	–0.01476	19
59648.8072	0.00010	16323.5	–0.01499	19
59649.6135	0.00009	16326.5	–0.01526	19
59650.8240	0.00011	16331.0	–0.01462	19
59669.6453	0.00012	16401.0	–0.01426	19
59669.7785	0.00012	16401.5	–0.01554	19
59670.7205	0.00012	16405.0	–0.01451	19
V365 Sge				
[a] 52122.660	0.002	0.0	0.00000	17
[a] 52526.304	0.005	1093.5	0.00089	3
[a] 52526.486	0.003	1094.0	–0.00167	3
[a] 52530.363	0.004	1104.5	–0.00053	3
[a] 52533.496	0.003	1113.0	–0.00513	3
[a] 52574.298	0.006	1223.5	0.00806	3
[a] 52576.322	0.004	1229.0	0.00184	3
[a] 52708.658	0.003	1587.5	0.00492	3
[a] 52764.582	0.003	1739.0	0.00580	3
[a] 52791.525	0.006	1812.0	0.00235	3
[a] 52813.489	0.004	1871.5	0.00314	3
[a] 52814.411	0.004	1874.0	0.00232	3
[a] 52829.536	0.003	1915.0	–0.00699	4
[a] 52839.512	0.004	1942.0	0.00251	4
[a] 52877.532	0.005	2045.0	0.00217	4
[a] 52886.393	0.004	2069.0	0.00406	4
[a] 52903.364	0.004	2115.0	–0.00489	4
[a] 52945.261	0.003	2228.5	–0.00409	4
[a] 52967.232	0.003	2288.0	0.00370	4
[a] 53003.224	0.004	2385.5	0.00558	4
[a] 53094.578	0.003	2633.0	0.00003	4
[a] 53121.532	0.004	2706.0	0.00757	4
[a] 53214.545	0.006	2958.0	–0.00006	18
[a] 53233.366	0.004	3009.0	–0.00467	18
[a] 53257.355	0.002	3074.0	–0.00908	18
[a] 53267.319	0.002	3101.0	–0.01158	18
55028.4226	0.0004	7872.0	–0.02482	14
55067.3656	0.0014	7977.5	–0.02499	14
55352.5146	0.0009	8750.0	–0.02853	13
55362.8485	0.0002	8778.0	–0.03025	5
55389.4280	0.0011	8850.0	–0.02808	9
55828.6892	0.0006	10040.0	–0.03098	7
56094.4591	0.0012	10760.0	–0.03432	12
56539.4421	0.0016	11965.5	–0.03693	11
[b] 57254.6208	0.0002	13903.0	–0.04663	1
[b] 57262.5553	0.0005	13924.5	–0.04846	1
[b] 57976.8135	0.0001	15859.5	–0.05577	1
[b] 57977.9204	0.0001	15862.5	–0.05626	1
[b] 57980.8738	0.0001	15870.5	–0.05588	1
[b] 57981.7959	0.0001	15873.0	–0.05665	1
[b] 57992.8697	0.0001	15903.0	–0.05669	1
[b] 58002.8360	0.0001	15930.0	–0.05692	1
59068.6818	0.0002	18817.5	–0.07252	19
59068.8653	0.0001	18818.0	–0.07364	19
59069.7889	0.0002	18820.5	–0.07284	19
59070.7109	0.0002	18823.0	–0.07368	19
59072.7422	0.0001	18828.5	–0.07261	19
59073.6639	0.0001	18831.0	–0.07370	19
59073.8495	0.0001	18831.5	–0.07267	19
59074.7712	0.00022	18834.0	–0.07381	19
59075.6951	0.00027	18836.5	–0.07274	19
59076.8025	0.00010	18839.5	–0.07273	19
59077.7242	0.00009	18842.0	–0.07387	19
59080.6773	0.00009	18850.0	–0.07380	19
59082.7087	0.00011	18855.5	–0.07264	19
59767.8015	0.00008	20711.5	–0.08411	19
V1148 Her				
51399.8490	—	0.0	0.00000	15
[c] 54297.4693	0.0001	10266.0	–0.00955	16
57100.5368	0.0006	20197.0	–0.01643	10
[b] 58999.8269	0.0001	26926.0	–0.02028	1
59012.8109	0.0001	26972.0	–0.01995	19
59013.6578	0.0000	26975.0	–0.01986	19
59014.7869	0.0001	26979.0	–0.01976	19
59016.7628	0.0001	26986.0	–0.01966	19
59020.7143	0.0001	27000.0	–0.01974	19
59021.8435	0.0001	27004.0	–0.01951	19
59771.6531	0.0001	29660.5	–0.02036	19
59771.7939	0.0001	29661.0	–0.02062	19
NSVS 9027851				
[c] 53180.6946	0.0007	0.0	0.00000	16
[c] 53184.6853	0.0006	11.0	0.00136	16
[c] 53192.6637	0.0008	33.0	0.00122	16
[c] 53196.6534	0.0025	44.0	0.00161	16
[c] 53200.6437	0.0025	55.0	0.00259	16
[c] 53204.6315	0.0028	66.0	0.00113	16
[c] 53220.5873	0.0031	110.0	–0.00019	16
[c] 53240.5364	0.0030	165.0	0.00243	16
[c] 53252.5020	0.0025	198.0	0.00016	16
[c] 53270.6353	0.0034	248.0	0.00034	16
[c] 53938.6604	0.0020	2090.0	0.00115	16
[c] 53942.6472	0.0023	2101.0	–0.00134	16
[c] 53950.6283	0.0026	2123.0	0.00116	16
[c] 53970.5737	0.0031	2178.0	0.00010	16
[c] 54001.3994	0.0024	2263.0	–0.00050	16
[c] 54022.4339	0.0030	2321.0	–0.00038	16
[c] 54050.3609	0.0020	2398.0	0.00158	16
59839.8957	0.0001	18362.0	–0.00776	19
59841.7085	0.0001	18367.0	–0.00824	19
59846.7853	0.0001	18381.0	–0.00873	19
59848.5989	0.0002	18386.0	–0.00843	19
59849.6867	0.0002	18389.0	–0.00863	19

(a) Visual Minima (all other minima in this table were derived from CCD observations).
(b) Minima derived from AAVSO data.
(c) Minima derived from SuperWASP data.

References: (1) AAVSO (Kafka 2017); (2) ASAS-SN (Shappee, et al. *2014; Jayasinghe,* et al. *2019); (3) Diethelm (2003); (4) Diethelm (2004); (5) Diethelm (2010); (6) Diethelm (2011); (7) Diethelm (2012a); (8) Diethelm (2012b); (9) Hübscher (2011); (10) Hübscher (2016); (11) Hübscher (2014); (12) Hübscher and Lehmann (2013); (13) Hübscher and Monninger (2011); (14) Hübscher* et al. *(2010); (15) Khruslov (2006); (16) SuperWASP (Masaryk Univ. 2022); (17) Richmond (2002); (18) Locher (2005); (19) this paper.*

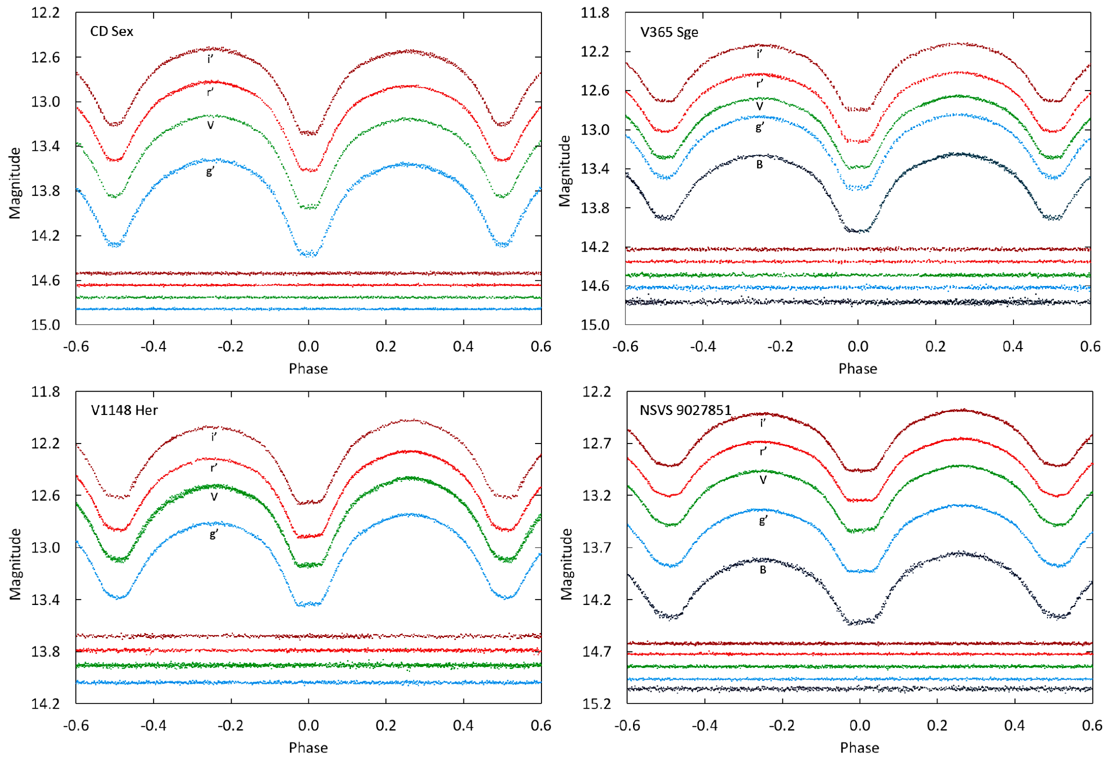

Figure 2. The folded light curves in standard magnitudes. From top to bottom the passbands are i', r', V, and g' for the stars CD Sex and V1148 Her, and i', r', V, g', and B for V365 Sge and NSVS 9027851. The bottom curves in each panel are the offset check star magnitudes in the same passband order as the light curves. Error bars were omitted from the plotted points for clarity.

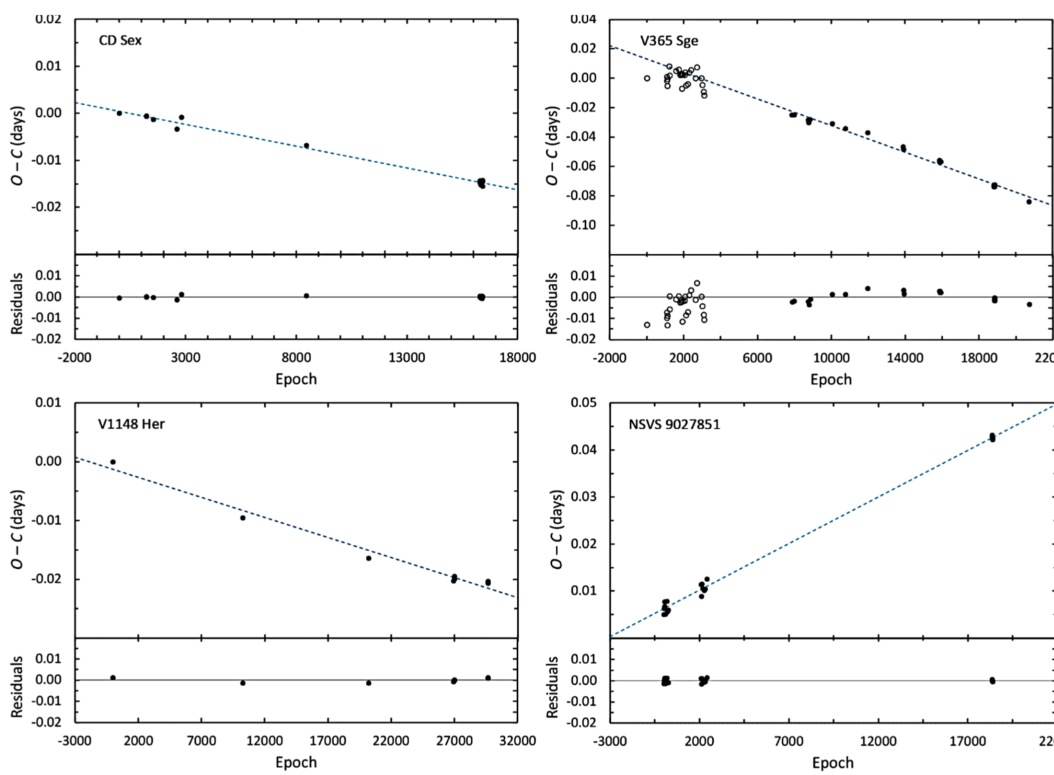

Figure 3. The top panel shows the O–C residuals that were calculated from the reference ephemeris for each star (see Table 5). The open circles are visually determined minima and the filled circles CCD minima. The dashed lines are the linear fits to the residuals. The bottom panel of each diagram shows the residuals from each fit.

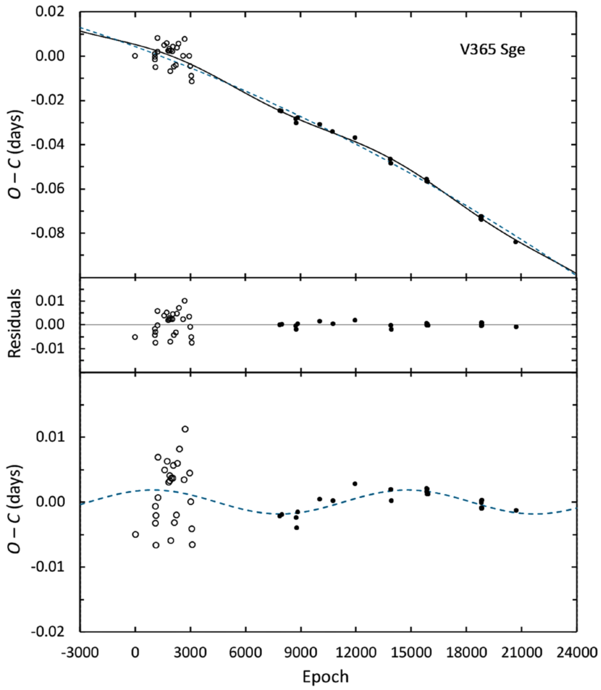

Figure 4. The top panel shows the O–C residuals that were calculated from the reference ephemeris for V365 Sge (see Table 5). The open circles are the visually determined minima and the filled circles the CCD minima. The solid line corresponds to Equation 2, which shows the fit for a circular orbit (e = 0) of a supposed third body. The dashed line refers to the quadratic term in this equation. The middle panel shows the residuals after removing the downward parabolic change and the cyclic variation. In the bottom panel the quadratic term of Equation 2 is subtracted to show the periodic variation more clearly.

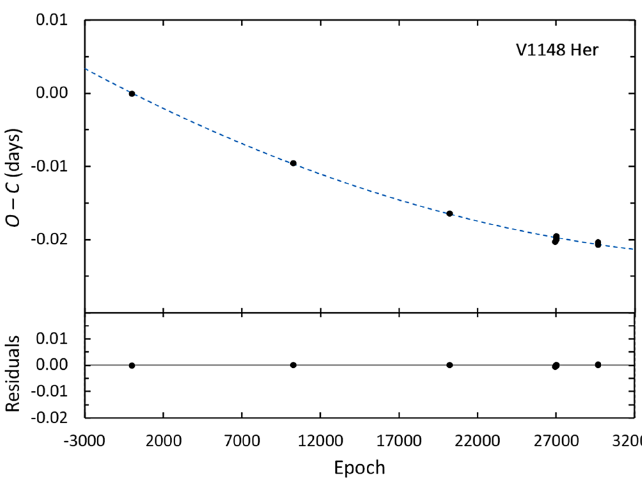

Figure 5. The O–C residuals (filled-circles) were calculated from the reference ephemeris for V1148 Her (see Table 5). The dashed line is the quadratic fit to the residuals. The bottom panel shows the residuals after removing the upward parabolic change.

3.2. Color, temperature, spectral type, absolute magnitude, luminosity

The averaged observed color of each system was determined by binning the phase and magnitude of the B and V observations with a phase width of 0.01. The phases and magnitudes in each bin interval were averaged. The binned V magnitudes were subtracted from the linearly interpolated B magnitudes, resulting in an observed (B–V) color at each phase point. Since B observations were not available for CD Sex and V1148 Her, the binning process used the g' and r' observations to give the (g'– r') colors for these two stars. The (g'– r') colors were converted to (B–V) colors using the transformation equation of Jester et. al (2005):

$$(B-V) = 0.98(g' - r') + 0.22. \quad (4)$$

The observed colors were corrected using color excess values from three-dimensional dust maps based on Pan-STARRS 1 and 2MASS photometry and Gaia parallaxes (Green *et al.* 2019). The V passband apparent magnitudes were corrected for interstellar extinction (A_V), using the extinction to reddening ratio of $A_V / E(B-V) = 3.1$. The absolute visual magnitude (M_V) of each star was computed using the following equation:

$$M_V = V - A_V - 5 \log (d / 10), \quad (5)$$

where V is the apparent magnitude at the brightest quadrature (see Table 3), A_V is the extinction, and d the Gias-DR3 distance in parsecs (Gaia Collaboration 2022). The visual luminosity of each system in solar units was calculated from the following equation:

$$M_V = M_{V\odot} - 2.5 \log (L / L_\odot), \quad (6)$$

Where $M_{V\odot} = 4.81$ is the absolute visual magnitude of the sun (Willmer 2018). The effective temperatures were computed using the corrected colors in the empirically derived equation of Eker *et al.* (2020):

$$\log T_{eff} = 0.07569(0.012) \times (B-V)_0^2 \\ -0.38786(0.01368) \times (B-V)_0 + 3.96617(0.00338). \quad (7)$$

For each binary, the color excess, visual extinction, the average dereddened color, Gaia-DR3 distance, extinction-corrected visual magnitude, absolute visual magnitude, and visual luminosity are shown in Table 6. Compiled in Table 7 are the effective temperatures derived from the corrected color and the estimated spectral type of each system. For comparison with the color derived temperatures, this table also contains values collected from three surveys using the VizieR Online Data Catalog—LAMOST, Gaia-DR3, and 2MASS. The temperatures from these surveys compared reasonably well with dereddened color temperatures having differences of less than 300 K. The one outlier was the 2MASS temperature for V365 Sge; it was 479 K greater than the color derived temperature.

3.3. Light curve modeling

W UMa-type contact binaries are characterized by continuous brightness variations and nearly equal light curve minima, as is certainly the case for the stars in this study. In addition, the light curves of each system reveal total eclipses at their deepest minima ($\varphi = 0$) and asymmetries likely resulting from spotting caused by their magnetically active dwarf stars. This light curve morphology indicates these systems are W-subtype contact binaries with the larger and cooler primary star eclipsing the hotter secondary star at primary minima. Given that each system displays a total primary eclipse, photometric light curve solutions should provide for well-determined mass ratios, $q = m_2 / m_1$, where the subscripts 1 and 2 refer to the more massive primary star and the less massive secondary component, respectively (Wilson 1978; Terrell and Wilson 2005; Hambálek and Pribulla 2013).

Photometric light curve solutions for each binary were obtained using the 2015 version of the Wilson-Devinney (WD) program (Wilson and Devinney 1971; van Hamme and Wilson 1998). The simultaneous solutions utilized four passbands, Johnson V and Sloan g', r', and i'. The input data for each color consisted of 100 binned points formed from the observed standard magnitudes (see section 3.2). These points were converted to normalized flux, with each point weighted by the number of observations forming that point. The WD program was configured for overcontact binaries (Mode 3), the Kurucz (2002) stellar atmosphere model was applied, and the logarithmic limb darkening coefficients were calculated by the method of van Hamme (1993). For CD Sex, V1148 Her, and NSVS 9027851, the effective temperature (T_1) of the primary star was fixed at the LAMOST values in Table 7. Since a spectroscopically-determined temperature was not available for V365 Sge, its effective temperature was fixed at the value determined from the observed color corrected for reddening. All the stellar effective temperatures were well below 7200 K; therefore, standard convective parameters for gravity brightening and bolometric albedo were fixed at $g_1 = g_2 = 0.32$ and $A_1 = A_2 = 0.5$, respectively (Lucy 1968; Ruciński 1969). The adjustable parameters include the inclination (i), mass ratio ($q = m_2 / m_1$), potential ($\Omega_1 = \Omega_2$), temperature of the secondary star (T_2), the band-specific luminosity for each wavelength (L), and third light (l_3). To address the light curve asymmetries, star spots were included in each system's model. The following parameters were adjustable for each spot modeled: colatitude, longitude, spot radius, and temperature factor (T_{spot} / T_{eff}). Before attempting WD solution iterations, a preliminary fit to the light curves was made using the BINARY MAKER 3.0 program (BM3; Bradstreet and Steelman 2002). The parameters resulting from the BM3 model fits were used as the inputs for the WD simultaneous four-color light curve solutions. The Method of Multiple Subsets (MMS; Wilson and Biermann 1976) was employed to minimize strong correlations of the parameters. Throughout the solution iteration process, the third-light corrections for each system were negligibly small (or negative). This indicates that if any stellar third-bodies are orbiting the binaries or if there are unresolved field stars, the contribution of these sources to the total system light is small. The final best-fit solution parameters for each system are shown in Table 8.

The filling-factors were computed using the method of Lucy and Wilson (1979):

$$f = (\Omega_{inner} - \Omega) / (\Omega_{inner} - \Omega_{outer}), \qquad (8)$$

where Ω_{inner} and Ω_{outer} are the inner and outer critical equipotential surfaces and Ω is the equipotential that describes the common envelope stellar surface. Figures 6 and 7 display the normalized light curves overlaid by the synthetic solution curves (solid lines) with the residuals shown in the bottom panels. A BM3 graphical representation of each system solution is shown in Figure 8 (Bradstreet and Steelman 2002).

4. Discussion

The light curve solutions confirmed that each system belongs to the W-type subclass of W UMa systems, where the less massive hotter component is eclipsed at primary minimum. The high inclinations ($i > 86°$) and the smaller secondary stars resulted in total eclipses at primary minimum. Each system is in an overcontact configuration but not excessively so with the degree of fill-out ranging from 15 to 23%. A large majority of totally eclipsing W UMa systems with well determined parameters have mass ratios that range from 0.1 to 0.5 (Latković and Lazarević 2021). The mass ratios of the stars in this study fall within that range, 0.33–0.50. The primary stars were all cooler than the sun, with spectral types from K3 to G7. The temperature differences between the component stars ($\Delta T = T_2 - T_1$) ranged from 233 K for CD Sex to 381K for V365 Sge. During modeling, hot or cool spots were necessary to fit the light curve asymmetries. This stellar dynamo magnetic activity was not unexpected, given the convective envelopes and rapid rotation of the stars. It should be noted that the solution spot parameters are not definitive; other spot configurations may give equal or better results (Terrell 2022).

Radial velocity observations were not available for the stars in this study, but provisional absolute stellar parameters can be calculated with the binary's mass ratio and an estimate of the primary star's mass. The photometric solutions provided the mass ratios and the primary stars' masses were calculated using Latković *et al*'s (2021) period-mass relation for W UMa binaries:

$$M_1 = (2.94 \pm 0.21)\, P + (0.16 \pm 0.08). \qquad (9)$$

The secondary star masses (M_2) were computed from the solution mass ratio. The distance between the mass centers of the two stars was calculated using Kepler's Third Law. Using this distance as an input parameter, the volume radii were calculated by the WD light curve program (LC). The bolometric magnitudes of each star were calculated using the following equation:

$$M_{bol} = -10 \log (T / T_{\odot}) - 5 \log (R / R_{\odot}) + M_{bol,\odot}, \qquad (10)$$

and the luminosities in solar units using the Stefan-Boltzmann law:

Table 5. Ephemeris elements for HJD Min I.

System	Reference Elements Epoch 2400000+	Reference Elements P_{orb} (days)	New Linear Elements Epoch 2400000+	New Linear Elements P_{orb} (days)
CD Sex	155259.9227	10.268870	59670.7203 (1)	0.26886907 (1)
V365 Sge	255028.4226	30.3691295	59767.6202 (4)	0.36912494 (2)
V1148 Her	451399.849	40.282255	59771.793 (1)	0.2822543 (1)
NSVS 9027851	553180.695	60.36266	59849.687 (1)	0.362662 (1)

References: (1) Diethelm 2010; (2) Hübscher 2010; (3) ASAS-SN (Shappee, et al. *2014; Jayasinghe,* et al. *2019); (4) Khruslov 2006; (5) SuperWASP (Masaryk Univ. 2022); (6) Watson* et al. *2014.*

Table 6. Color excess, visual extinction, dereddened color, Gaia-DR3 distance, extinction corrected apparent visual magnitude at quadrature, calculated absolute visual magnitude and visual luminosity.

	CD Sex	*V365 Sge*	*V1148 Her*	*NSVS 9027851*
E(B–V)	0.021 ± 0.016	0.018 ± 0.016	0.027 ± 0.008	0.150 ± 0.009
A_V	0.066 ± 0.013	0.055 ± 0.095	0.082 ± 0.023	0.464 ± 0.027
$(B–V)_0$	0.903 ± 0.013	0.643 ± 0.020	0.682 ± 0.013	0.711 ± 0.014
Dist. (pc)	288 ± 2	471 ± 4	288 ± 1	430 ± 4
V	13.06 ± 0.02	12.60 ± 0.10	12.38 ± 0.02	12.45 ± 0.03
M_V	5.76 ± 0.02	4.23 ± 0.10	5.08 ± 0.03	4.28 ± 0.03
$L_{V\odot}$	0.42 ± 0.01	1.70 ± 0.15	0.78 ± 0.02	1.63 ± 0.05

Table 7. Effective temperatures from dereddened $(B–V)_0$ colors compared with other surveys and approximate spectral class.

System	*$(B-V)_0$ $T_{eff}(K)$*	*LAMOST $T_{eff}(K)$*	*Gaia-DR3 $T_{eff}(K)$*	*2Mass $T_{eff}(K)$*	*Spectral Class*
CD Sex	4762 ± 267	4865 ± 64	5088 ± 8	4948 ± 160	K2–K3
V365 Sge	5598 ± 261	—	5855 ± 12	6077 ± 175	F9–G7
V1148 Her	5457 ± 202	5161 ± 64	5437 ± 10	5391 ± 139	K1–G8
NSVS 9027851	5352 ± 209	5533 ± 88	5620 ± 26	5515 ± 149	G9–G6

$$L / L_\odot = (R / R_\odot)^2 \, (T / T_\odot)^4. \qquad (11)$$

Compiled in Table 9 are the estimated absolute stellar parameters: the masses (M_1, M_2), distance between the mass centers (a), volume radii (R_1, R_2), bolometric magnitudes ($M_{bol,1}$, $M_{bol,2}$), luminosities (L_1, L_2), and surface gravities (g_1, g_2).

The distance modulus ($V – M_V$) was used to estimate the distance to each system. The apparent magnitude V in this estimation utilized the observed magnitude at the brightest quadrature (corrected for extinction). The system absolute magnitudes (M_V) were computed using the bolometric magnitudes and the bolometric corrections for each star. The bolometric corrections were interpolated from the tables of Pecaut and Mamajek (2013) according to the effective temperatures of the component stars. By combining the visual luminosities of the component stars, the system absolute magnitude M_V was derived for each binary. The estimated distances of each system could then be compared to the Gaia-DR3 distances (see section 5).

The period analysis of V365 Sge revealed a possible circumbinary companion. The orbital period of the proposed third body was computed using the relation $P_3 = 2\pi P / \omega$, where $\omega = 5.278(4) \times 10^{-4}$ is the angular frequency from Equation 2 and P is the orbital period of V365 Sge. This gives an estimated period of $P_3 = 12.032 \pm 0.009$ yr of the tertiary companion. Assuming a circular orbit (e = 0), the projected orbital radius of the binary about the barycenter was calculated from this relation, $a_{12} \sin i_3 = A_3 \times c$, where Equation 2 gives the amplitude of the cyclic variation, $A_3 = 1.887(3) \times 10^{-3}$ days, and c is the speed of light. For a coplanar orbit with the binary, the mass and orbital radius of the third body were computed using the mass function and the provisional masses of the binary components (see Table 9). The mass function was determined using the following well-known equation:

$$f(m) = \frac{4\pi 2}{GP_3^2} (a_{12} \sin l_3) = \frac{(M_3 \sin l_3)^3}{(M_1 + M_2 + M_3)^2} . \qquad (12)$$

where G is the gravitational constant. The third body's mass, calculated by the iteration method and its orbital radius using Kepler's Third Law, gives the following values: $M_3 = 0.094 \pm 0.004 \, M_\odot$ and $a_3 = 6.1 \pm 0.1$ AU. This low mass suggests a very dim red dwarf star with a luminosity of $0.0007 \, L_\odot$ (Pecaut and Mamajek 2013). The contribution to the total system light would only amount to about 0.0003%, which would not have produced a noticeable third light (l_3) in the WD solution. Table 10 gives the tertiary component parameters, including computed masses and orbital radii for inclinations of 30°, 60°, and 90°. The presence of a third star in this system was based upon the sinusoidal component of the O–C residuals, which only covers about one orbital cycle.

Table 8. Results derived from light curve modeling.

Parameter	CD Sex	V365 Sge	V1148 Her	NSVS 9027851
Filling factor	15%	20%	20%	22%
i (°)	87.7 ± 0.8	89.1 ± 0.5	88 ± 1	86.7 ± 0.7
T_1 (K)	[1]4865	15598	15161	15533
T_2 (K)	5098 ± 3	5980 ± 8	5403 ± 6	15779 ± 7
$\Omega_1 = \Omega_2$	2.836 ± 0.010	2.657 ± 0.004	2.570 ± 0.006	2.483 ± 0.007
$q(m_2 / m_1)$	0.502 ± 0.006	0.415 ± 0.003	0.370 ± 0.004	0.328 ± 0.004
$L_1 / (L_1 + L_2)$ (V)	0.584 ± 0.007	0.619 ± 0.005	0.654 ± 0.007	0.685 ± 0.007
$L_1 / (L_1 + L_2)$ (g')	0.573 ± 0.007	0.605 ± 0.005	0.645 ± 0.007	0.677 ± 0.008
$L_1 / (L_1 + L_2)$ (r')	0.595 ± 0.007	0.628 ± 0.005	0.662 ± 0.007	0.692 ± 0.007
$L_1 / (L_1 + L_2)$ (i')	0.604 ± 0.007	0.637 ± 0.004	0.670 ± 0.007	0.697 ± 0.007
r_1 side	0.4451 ± 0.0008	0.4701 ± 0.0006	0.4807 ± 0.0007	0.4949 ± 0.0010
r_2 side	0.3392 ± 0.0050	0.3068 ± 0.0024	0.2966 ± 0.0039	0.2819 ± 0.0052
Spot Parameters				
Spot 1	$Star_1$	$Star_1$	$Star_1$	$Star_1$
Colatitude (°)	51 ± 13	128 ± 21	51 ± 16	67 ± 19
Longitude (°)	102 ± 2	244 ± 2	260 ± 3	264 ± 2
Spot radius (°)	17 ± 4	15 ± 5	22 ± 5	17 ± 5
Temp. factor	0.83 ± 0.05	0.85 ± 0.09	0.83 ± 0.04	0.88 ± 0.06
Spot 2	—	$Star_1$	$Star_1$	$Star_1$
Colatitude (°)	—	108 ± 1	100 ± 15	70 ± 8
Longitude (°)	—	9 ± 1	336 ± 4	33 ± 7
Spot radius (°)	—	10 ± 1	10 ± 2	10 ± 3
Temp. factor	—	1.18 ± 0.03	0.83 ± 0.05	1.11 ± 0.06

[1]*Assumed.*
The subscripts 1 and 2 refer to the star being eclipsed at secondary and primary minimum, respectively.
Note: The errors in the stellar parameters result from the least-squares fit to the model. The actual uncertainties are considerably larger.

Table 9. Provisional absolute parameters.

Parameter	Symbol	CD Sex	V365 Sge	V1148 Her	NSVS 9027851
Stellar mass	M_1 ($M_\odot$)	0.95 ± 0.10	1.25 ± 0.11	0.99 ± 0.10	1.23 ± 0.11
	M_2 ($M_\odot$)	0.48 ± 0.05	0.52 ± 0.05	0.37 ± 0.04	0.40 ± 0.04
Semi-major axis	a ($R_\odot$)	1.97 ± 0.05	2.61 ± 0.05	2.00 ± 0.05	2.52 ± 0.05
Mean stellar radius	R_1 ($R_\odot$)	0.89 ± 0.02	1.23 ± 0.03	0.94 ± 0.02	1.24 ± 0.03
	R_2 ($R_\odot$)	0.66 ± 0.02	0.84 ± 0.02	0.60 ± 0.02	0.76 ± 0.02
Bolometric magnitude	$M_{bol,1}$	5.75 ± 0.09	4.4 ± 0.2	5.39 ± 0.08	4.47 ± 0.09
	$M_{bol,2}$	6.21 ± 0.12	5.0 ± 0.3	6.17 ± 0.10	5.35 ± 0.11
Stellar luminosity	L_1 ($L_\odot$)	0.40 ± 0.03	1.3 ± 0.3	0.56 ± 0.04	1.30 ± 0.10
	L_2 ($L_\odot$)	0.26 ± 0.03	0.8 ± 0.2	0.27 ± 0.03	0.58 ± 0.06
Surface gravity	log g_1 (cgs)	4.51 ± 0.05	4.35 ± 0.04	4.46 ± 0.05	4.34 ± 0.04
	log g_2 (cgs)	4.48 ± 0.05	4.31 ± 0.04	4.42 ± 0.05	4.28 ± 0.04

Note: The calculated values in this table are provisional. Radial velocity observations are necessary for direct determination of M1, M2 and a.

Table 10. Parameters of the V365 Sge tertiary component.

Parameter	Value	Units
P_3	12.032 ± 0.009	years
A_3	0.001887 ± 0.000002	days
e	*0.0	
$a_{12} \sin i_3$	0.3267 ± 0.0003	AU
f(m)	0.0002408 ± 0.0000008	$M_\odot$
M_3 (i_3 = 90°)	0.094 ± 0.004	$M_\odot$
M_3 (i_3 = 60°)	0.109 ± 0.005	$M_\odot$
M_3 (i_3 = 30°)	0.194 ± 0.011	$M_\odot$
a_3 (i_3 = 90°)	6.13 ± 0.14	AU
a_3 (i_3 = 60°)	6.09 ± 0.14	AU
a_3 (i_3 = 30°)	5.92 ± 0.13	AU

**Assumed*

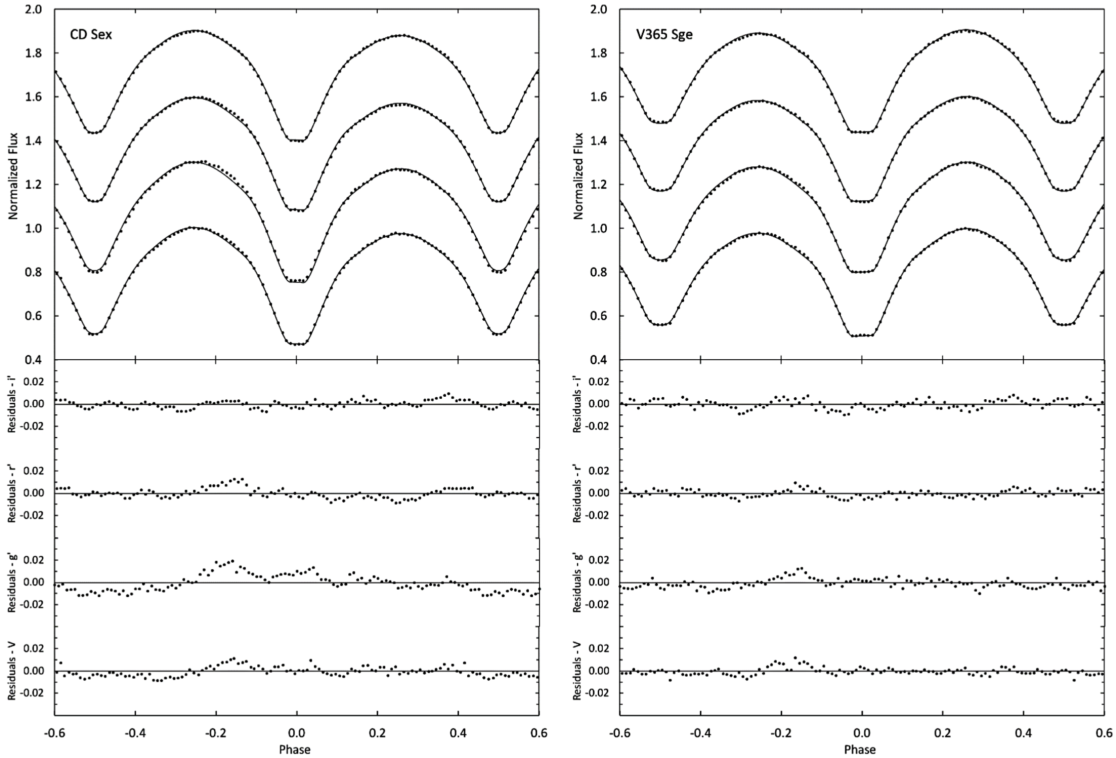

Figure 6. Comparison between the WD model fits (solid curve) and the observed normalized flux curves for CD Sex and V365 Sge. From top to bottom the passbands are i', r', g', and V. Each curve is offset by 0.3 for this combined plot. The residuals for the best-fit model are shown in the bottom panel. Error bars are omitted from the points for clarity.

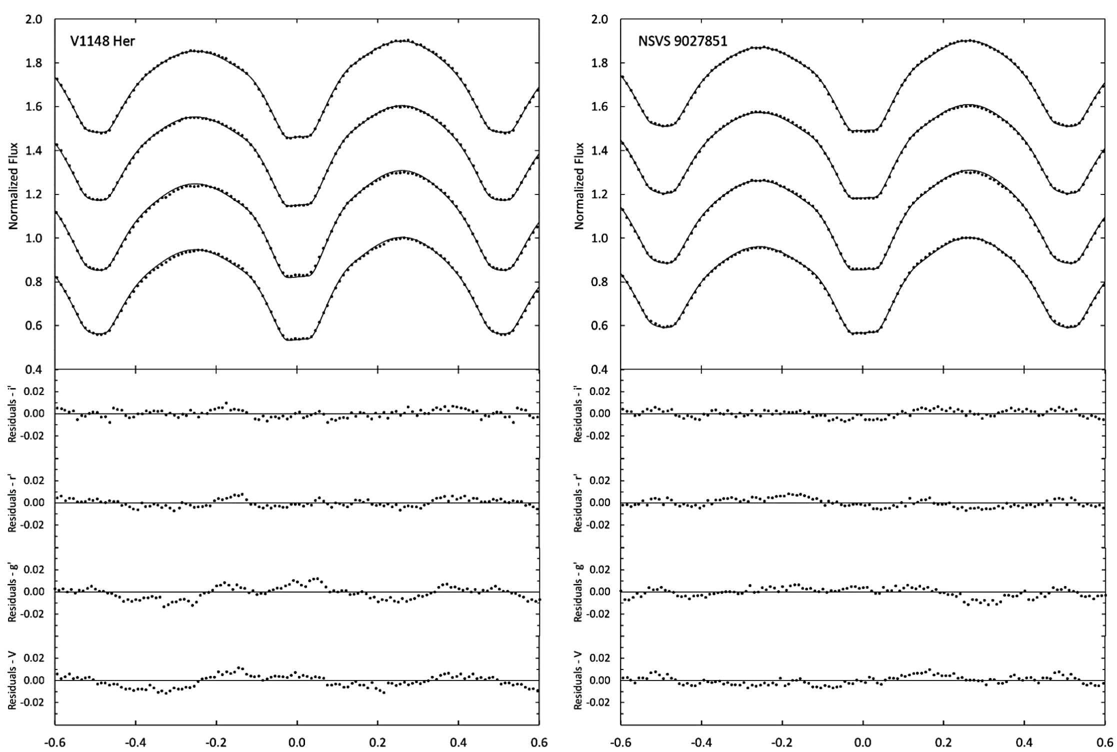

Figure 7. Comparison between the WD model fits (solid curve) and the observed normalized flux curves for V1148 Her and NSVS 9027851. From top to bottom the passbands are i', r', g', and V. Each curve is offset by 0.3 for this combined plot. The residuals for the best-fit model are shown in the bottom panel. Error bars are omitted from the points for clarity.

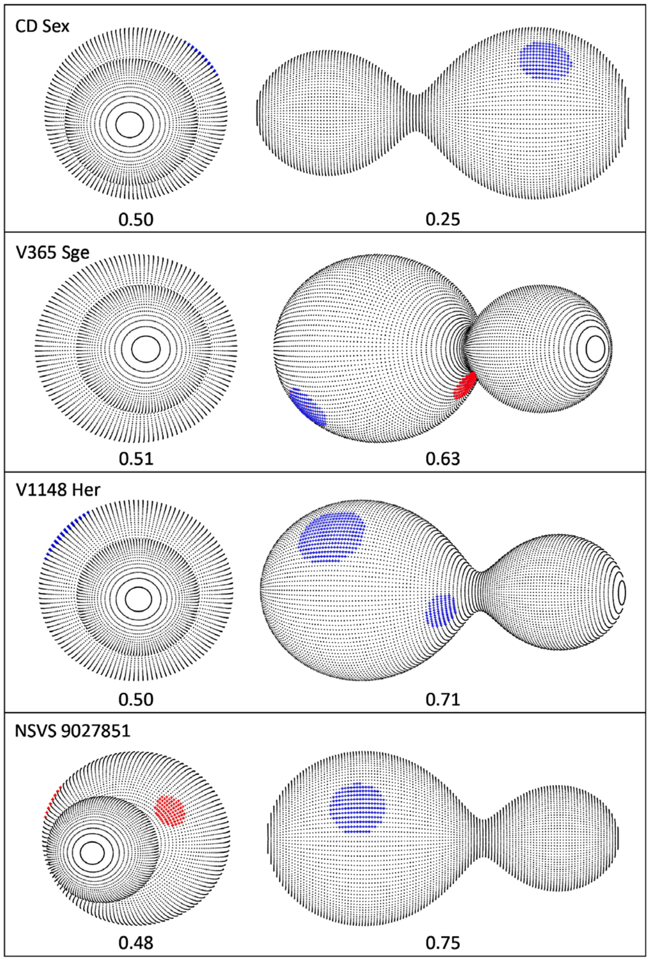

Figure 8. Roche Lobe surfaces of the best-fit WD spot model showing spot locations. The orbital phase is shown below each diagram.

Eclipse minima timings covering another cycle or two (12–24 years) will be necessary to confirm this tertiary star and revise the orbital parameters.

5. Conclusions

New high cadence multi-band photometric observations resulted in precision light curves and new minima timings for each star in this study. Light curve modeling with the WD program found a contact configuration for each system with the stars overfilling their critical Roche lobe. The solution mass ratios (q) should be well determined, given the light curves displayed total eclipses. Spot modeling was required to fit the light curve asymmetries, indicating magnetically active stars. The linear ephemerides of each system were updated using all available minima timings. The large mass differences and nearly equal temperatures of each system's component stars indicates a significant energy exchange between the stars.

The CD Sextantis system is a short period (P = 0.2688 d) contact binary. The orbital period of its K stars appears constant, though this conclusion is not certain given the large gaps in the few minima timings currently available (see Figure 3). The photometric solution gives an inclination of i = 87.7°, and a temperature difference of 233 K between the component stars. This system has a fill-out of 15% and its mass ratio, q = 0.502, is at the high end of the range when compared to the majority of observed totally eclipsing systems (Latković *et al.* 2021). The O'Connell (1951) effect is evident in the light curves, with Max II 0.026 magnitude brighter than Max I in the V passband. A single cool spot was modeled on the larger primary star to address this asymmetry. There is a small difference between the solution derived distance, 322 ± 12 pc, and the Gaia-DR3 distance of 288 ± 2 pc. This indicates the system's total luminosity is possibly overestimated in the model.

V365 Sagittae is a W-type contact binary that exceeds its critical lobe with a fill-out of 20%. This system has a mass ratio of q = 0.415, a temperature difference of 382 K between its component stars, and an orbital inclination nearly perpendicular to the sky (i = 89.1°). The light curves show Max I is brighter than Max II by 0.028 magnitude in the V passband. Minimizing the light curve asymmetries required the addition of both a hot and a cool star spot to the WD model. Both spots were located on the larger and cooler primary star. The solution derived distance, d = 520 ± 48 pc, when compared to the Gaia value, d = 471 ± 4 pc, is within the margin of errors. The period analysis of this system indicates the orbital period of the binary is slowly decreasing at a rate of $-1.055(2) \times 10^{-7}$ d · yr^{-1} and that there is a possible low mass tertiary component with a 12-year orbital period.

The photometric solution of V1148 Herculis gives an inclination of i = 88° and indicates an overcontact configuration with a fill-out of 20%. The component stars have a mass ratio of q = 0.370 and a temperature difference of 242 K. The larger cooler primary star has a spectral type of K1 and G9 for the smaller secondary star. The O'Connell effect is very apparent in the light curves, with Max I brighter than Max II by 0.061 magnitude in the V passband. The light curve asymmetries were modeled by adding two cool spots to the primary star. The derived system distance and the Gaia value are in good agreement, d = 288 ± 10 pc and d = 288 ± 1 pc, respectively. The period analysis, using the few minima times available, indicates a possible slowly decreasing orbital period.

NSVS 9027851 is a contact binary whose G stars orbit each other in 0.3627 day. There are too few minima times available to assess whether the orbital period is constant. The WD solution gives a fill-out of 22%, a mass ratio of q = 0.328, and a temperature difference of 246 K between its component stars. The O'Connell effect is quite noticeable in the light curves, with Max I 0.047 magnitude brighter than Max II in the V passband. A good fit between the observed and synthetic light curves was obtained by modeling both a cool and a hot spot on the primary star. The derived system distance is in good agreement with the Gaia value, d = 450 ± 16 pc and d = 430 ± 4 pc, respectively.

6. Acknowledgements

This research was made possible through the use of the AAVSO Photometric All-Sky Survey (APASS), funded by the Robert Martin Ayers Sciences Fund. This research has made use of the SIMBAD database and the VizieR catalogue access tool, operated at CDS, Strasbourg, France. This work has made use of data from the European Space Agency (ESA) mission Gaia (https://www.cosmos.esa.int/gaia), processed by the Gaia Data Processing and Analysis Consortium (DPAC, https://www.cosmos.esa.int/web/gaia/dpac/consortium). Funding for the DPAC has been provided by national institutions, in particular the institutions participating in the Gaia Multilateral Agreement. Data from the Guo Shou Jing Telescope (the Large Sky Area Multi-Object Fiber Spectroscopic Telescope, LAMOST) were also used in this study. This telescope is a National Major Scientific Project built by the Chinese Academy of Sciences. Funding for the project has been provided by the National Development and Reform Commission. LAMOST is operated and managed by National Astronomical Observatories, Chinese Academy of Sciences. The author greatly appreciated the comments and suggestions of the anonymous referee.

References

Bradstreet, D. H., and Steelman, D. P. 2002, *Bull. Amer. Astron. Soc.*, **34**, 1224.
Diethelm, R. 2003, *Inf. Bull. Var. Stars*, No. 5438, 1.
Diethelm, R. 2004, *Inf. Bull. Var. Stars*, No. 5543, 1.
Diethelm, R. 2010, *Inf. Bull. Var. Stars*, No. 5945, 1.
Diethelm, R. 2011, *Inf. Bull. Var. Stars*, No. 5992, 1.
Diethelm, R. 2012a, *Inf. Bull. Var. Stars*, No. 6011, 1.
Diethelm, R. 2012b, *Inf. Bull. Var. Stars*, No. 6029, 1.
Drake, A. J., *et al.* 2014, *Astrophys. J., Suppl. Ser.*, **213**, 9.
Eker, Z., *et al.* 2020, *Mon. Not. Roy. Astron. Soc.*, **496**, 3887.
Gaia Collaboration. 2022, VizieR Online Data Catalog: Gaia DR3 Part 1, I/355 (*Astron. Astrophys.*, in prep.).
Gettel, S. J., Geske, M. T., and McKay, T. A. 2006, *Astron. J.*, **131**, 621.
Green, G. M., Schlafly, E., Zucker, C., Speagle, J. S., and Finkbeiner, D. 2019, *Astrophys. J.*, **887**, 93.
Hambálek, Ľ., and Pribulla, T. 2013, *Contrib. Astron. Obs. Skalnaté Pleso*, **43**, 27.
Henden, A. A., *et al.* 2015, AAVSO Photometric All-Sky Survey, data release 9 (https://www.aavso.org/apass).
Hoffman, D. I., Harrison, T. E., and McNamara, B. J. 2009, *Astron. J.*, **138**, 466.
Hübscher, J. 2011, *Inf. Bull. Var. Stars*, No. 5984, 1.
Hübscher, J. 2014, *Inf. Bull. Var. Stars*, No. 6118, 1.
Hübscher, J. 2016, *Inf. Bull. Var. Stars*, No. 6157, 1.
Hübscher, J., and Lehmann, P. B. 2013, *Inf. Bull. Var. Stars*, No. 6070, 1.
Hübscher, J., and Monninger, G. 2011, *Inf. Bull. Var. Stars*, No. 5959, 1.
Hubscher, J., Lehmann, P. B., Monninger, G., Steinbach, H.-M., and Walter, F. 2010, *Inf. Bull. Var. Stars*, No. 5941, 1.
Jayasinghe, T., *et al.* 2018, *Mon. Not. Roy. Astron. Soc.*, **477**, 3145.
Jester, S., *et al.* 2005, *Astron. J.*, **130**, 873.
Kafka, S. 2017, variable star observations from the AAVSO International Database (https://www.aavso.org/aavso-international-database).
Khruslov, A. V. 2006, *Perem. Zvezdy Prilozh.*, **6**, 16 (http://www.astronet.ru/db/varstars/msg/eid/PZP-06-0016).
Kurucz, R. L. 2002, *Baltic Astron.*, **11**, 101.
Kwee, K. K., and van Woerden, H. 1956, *Bull. Astron. Inst. Netherlands*, **12**, 327.
Latković, O., Čeki, A., and Lazarević, S. 2021, *Astrophys. J., Suppl. Ser.*, **254**, 10.
Liao, W.-P., and Qian, S.-B. 2010, *Mon. Not. R. Astron. Soc.*, **405**, 1930.
Locher, K. 2005, *Open Eur. J. Var. Stars*, **3**, 1 (http://var.astro.cz/oejv/oejv.php?oejv=3).
Lucy, L. B. 1968, *Astrophys. J.*, **151**, 1123.
Lucy, L. B., and Wilson, R. E. 1979, *Astrophys. J.*, **231**, 502.
Masaryk University, Brno. 2022, SuperWASP Wide Angle Search for Planets database (https://wasp.cerit-sc.cz/form).
Mirametrics. 2015, Image Processing, Visualization, Data Analysis, (https://www.mirametrics.com).
O'Connell, D. J. K. 1951, *Publ. Riverview Coll. Obs.*, **2**, 85.
Pecaut, M. J., and Mamajek, E. E. 2013, *Astrophys. J., Suppl. Ser.*, **208**, 9.[1]
Pojmański, G. 2002, *Acta Astron.*, **52**, 397.
Pribulla, T., and Rucinski, S. M. 2006, *Astron. J.*, **131**, 2986.
Qian, S.-B., Liu, N.-P., Liao, W.-P., He, J.-J., Liu, L., Zhu, L.-Y., Wang, J.-J., and Zhao, E.-G. 2013, *Astron. J.*, **146**, 38.
Richards, J. W., Starr, D. L., Miller, A. A., Bloom, J. S., Butler, N. R., Brink, H., and Crellin-Quick, A. 2012, *Astrophys. J., Suppl. Ser.*, **203**, 32.
Richmond, M. W. 2002, *Inf. Bull. Var. Stars*, No. 5221, 1.
Ruciński, S. M. 1969, *Acta Astron.*, **19**, 245.
Shappee, B. J., *et al.* 2014, *Astrophys. J.*, **788**, 48 (ASAS-SN Catalog of Variable Stars: II, https://asas-sn.osu.edu/).
Terrell, D. 2022, *Galaxies*, **10**, 8.
Terrell, D., and Wilson, R. E., 2005, *Astrophys. Space Sci.*, **296**, 221.
Terrell, D., Gross, J., and Cooney, W. R. 2012, *Astron. J.*, **143**, 99.
Tonry, J., *et al.* 2018, *Astrophys, J.*, **867**, 105.
van Hamme, W. 1993, *Astron. J.*, **106**, 2096.
van Hamme, W., and Wilson, R. E. 1998, *Bull. Amer. Astron. Soc.*, **30**, 1402.
Watson, C., Henden, A. A., and Price, C. A. 2014, AAVSO International Variable Star Index VSX (Watson+, 2006–2014; https://www.aavso.org/vsx).
Willmer, C. N. A. 2018, *Astrophys. J., Suppl. Ser.*, **236**, 47.
Wilson, R. E., 1978, *Astrophys. J.*, **224**, 885.
Wilson, R. E., and Biermann, P. 1976, *Astron. Astrophys.*, **48**, 349.
Wilson, R. E., and Devinney, E. J. 1971, *Astrophys. J.*, **166**, 605.
Woźniak, P. R., *et al.* 2004, *Astron. J.*, **127**, 2436.

[1] Pecaut, M. J., and Mamajek, E. E. (2013): http://www.pas.rochester.edu/~emamajek/EEM_dwarf_UBVIJHK_colors_Teff.txt

Spectroscopic and Photometric Study of the Eclipsing Binary Star σ Aquilae

Ulisse Quadri
Luca Strabla
IAU station 565, Bassano Bresciano Astronomical Observatory, Brescia, Italy; info@ulisse.bs.it; *lucapietro.strabla@fastwebnet.it*

Lorenzo Franco
IAU station A81, Balzaretto Observatory, Rome, Italy; lor_franco@libero.it

Received January 22, 2023; revised March 31, 2023; accepted March 31, 2023

Abstract We report on spectroscopic and photometric observations of the eclipsing binary star σ Aquilae (44 Aql). Archival TESS and Hipparcos data are used to confirm the orbital period of 1.95028 ± 0.00002 days, consistent with previous measurements. Doppler shifts of the He I line at 4922 Angstroms from high-resolution spectroscopic data were used to model the system's orbital motion. From this we were able to determine a mass ratio of the two stars of M2 / M1 = 0.79, an inclination angle of the orbital plane of i = 72 degrees, masses of M1 = 5.8 $M_{\odot}$ and M2 = 4.6 $M_{\odot}$, and radii of 3.7 and 3.3 solar radii, respectively. The mass ratio is consistent with previous results, but we note that our derived masses are lower by approximately 5–10% with respect to most of the previous studies.

1. History

Many studies have been conducted on the variable σ Aquilae in the modern age of astronomy; below, we report the most significant for the purposes of our study. The star is cataloged as an eclipsing binary star in the GCVS (Samus *et al.* 2017) with B3V+B3V type star components. The variable radial velocity of σ Aql was discovered at Mount Wilson in 1912, and the spectroscopic orbit was published by Jordan (1916) with a period of 1.95022 d, circular orbit (e = 0), K1 = 163.52 km, K2 = 199 km, m1 $\sin^3(i) = 5.3\,M_{\odot}$, and m2 $\sin^3(i) = 4.4\,M_{\odot}$. The first photoelectric light curve was obtained by Wylie (1922) with a period of 1.95026 d. Spectroscopic observations by Luyten *et al.* (1939) showed an orbital period of 1.950272 d, while Koch *et al.* (1965) found the spectral types B3+B4 for the components of this binary system with an orbital inclination sin i = 0.949 (71.6°). Cester *et al.* (1978) reported an orbital period of 1.9503 d, orbital inclination of 72.2°, q ratio of 0.79 with masses of 6.8, 5.4 $M_{\odot}$, radii of 4.22, 3.05 solar radii, spectral types B3+B3, and a T = 18950 K for the hotter component. Brancewicz and Dworak (1980), using an iterative numerical method and data collected from several sources, determined a q ratio of 0.86 and a mass of 5.70 $M_{\odot}$ for the more massive star. The radii determined are 3.75 and 3.32 solar radii for each star Brancewicz and Dworak 1980). Hoffleit and Jaschek (1991) reported in the *Bright Star Catalogue* that the spectral type of the two component stars is B3V+B3V. Pan *et al.* (1998) calculated a perfectly circular orbit (e = 0).

2. Instrumentation and methodology

Observations were made near the Bassano Bresciano Astronomical Observatory (45° 19' 32" N, 10° 07' 49" E) (WGS84[1]) with a home-made 0.4-m Schmidt telescope operating at an effective focal ratio of f/10. Both the telescope and the home-made dome were operated remotely to make the observations presented here; Figure 1 shows the telescope, with its horseshoe equatorial mount, and the dome.

The telescope is controlled using custom software written in C++ and called Polypus 2.0. It controls the operations of the telescope and instrumentation, including pointing, tracking, and taking exposures.

Spectra were secured with the ATHOS spectrograph that was made for high-resolution spectroscopy (Figure 2). It is a Littrow-type spectrograph operating at the same focal ratio as the telescope. The effective focal length of the acromat doublet of the spectrograph is 180 mm with a diameter of 25 mm. The spectrograph is equipped with 12 slits of 10, 20, 30, 40, 50, 70, 100, 150, 200, 300, 500, and 700 uM width. The diffraction grating has 2400 lines per mm and the images are secured with a StarlightXpress Trius-SX9 CCD camera, which has a sensor area of 1392 × 1040 pixels (pixels are 6.45 uM square).

Slit width used for the observations is 20 uM and, in order to maximize the signal-to-noise ratio, we have used the CCD binned 2 × 2. With this configuration the spectral resolution is about R = 10000 in the range 4822–4980 Å and a dispersion of 0.18 Å / pixel. For calibration purpose the spectrograph is equipped by a RELCO starter lamp placed in front of the slit.

Sources were targeted only above 30° elevation, both so that nearby trees would not get in the way and because atmospheric extinction and refraction significantly degrade the images at and above airmass values of about 2. Three types of images were secured for each observing run: images of the target were made at exposure times of 300 s to ensure good signal-to-noise in the final spectra, dark frames were taken at the same exposure time after each night of observing, and flat field images were secured using an external halogen lamp shining on a white panel that is attached to the inside of the dome.

The software package ISIS version 6.1.1 (Buil 2021) was used to reduce the data and extract the stellar spectra in an automated way. The software package Peranso 3 (Paunzen

[1] WGS84—World Geodetic System 1984 (also known as EPSG:4326) is a worldwide geodetic geographic coordinate system based on a reference ellipsoid developed in 1984.

Figure 1. Observations were obtained using home-made 0.4-m Schmidt telescope operating at an effective focal ratio of f/10, equipped with Starlight Xpress Trius-SX9 CCD.

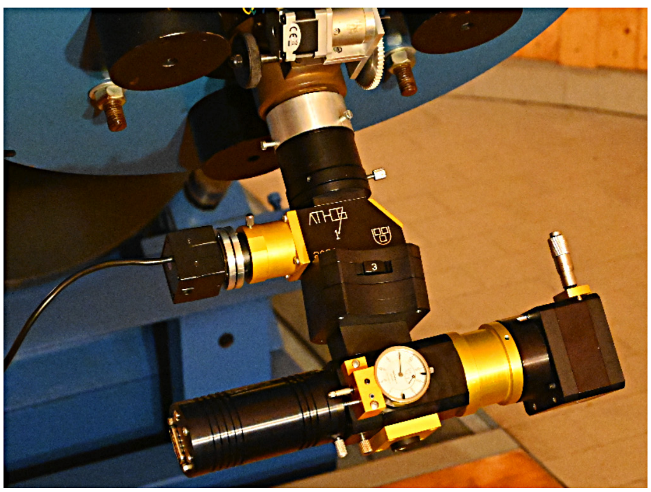

Figure 2. ATHOS is a home-made spectrograph equipped with a 2400-line grating and rotating slits.

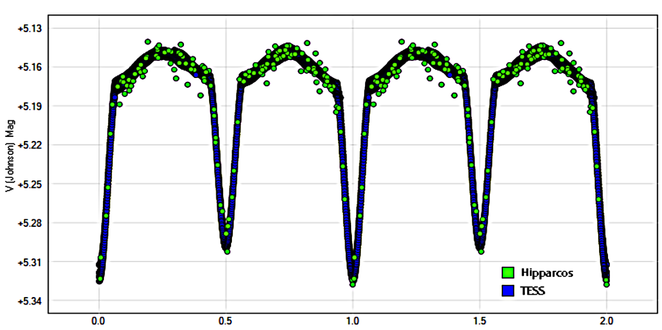

Figure 3. Light curve of σ Aql derived from Hipparcos and TESS data, folded with a period of 1.95028 d.

Table 1. Time of minima for σ Aquilae from TESS data.

Time of Minima	*Eclipse Type*
2459770.1410 ± 0.0013	primary
2459771.1148 ± 0.0012	secondary
2459772.0901 ± 0.0010	primary
2459773.0644 ± 0.0013	secondary
2459774.0397 ± 0.0010	primary
2459783.7929 ± 0.0010	primary
2459784.7668 ± 0.0010	secondary
2459785.7419 ± 0.0014	primary
2459786.7165 ± 0.0012	secondary
2459787.6908 ± 0.0009	primary
2459788.6667 ± 0.0011	secondary
2459789.6418 ± 0.0013	primary
2459795.4935 ± 0.0014	primary

and Vanmunster 2016) was used to create the photometric light curve and determine the period of variability.

3. Photometric data

We used Hipparcos (Perryman *et al.* 1997) and TESS (TASC 2023) data, via the "Internet light curve plotting" function implemented in Peranso. For all imported data the HJD correction was applied. To the TESS data an appropriate offset was applied to the magnitudes in order to minimize the differences in relation to the Hipparcos data. The period analysis was carried out with ANOVA algorithm, implemented in Peranso, on all imported data, for a more precise period determination. The resulting period is 1.95028 ± 0.00002 d, accepted by the VSX, in place of the previous period of 1.950269 d. From TESS data we obtained eight primary minima and five secondary minima measurements (Table 1). The center of eclipses and the Epoch (2459787.6908 HJD) was determined by a fifth-degree polynomial using Peranso. Figure 3 shows the light curve obtained from Hipparcos and TESS data folded with a period of 1.95028 days.

4. Spectroscopic data

We observed σ Aql spectroscopically for 24 nights, from 2022 Aug 19 to 2022 Sep 22, obtaining a set of 45 spectra, each stacking seven raw images of 300 s in order to improve the signal and to minimize errors. Before stacking each raw image was calibrated with dark and flat frames. For each set of seven spectra a relative calibration lamp image was obtained. All spectra were corrected for heliocentric velocity before wavelength measurements were made.

Since σ Aql is a blue star, we performed the measurements in λ using the He I line (λ 4922 Å) which presents a clear doubling due to the Doppler-Fizeau effect (see Figure 4).

The radial velocities were derived from the λ measurement (Å) performed with Peranso software and a fifth degree polynomial fit on both halves of the double-line He I of each spectrum, obtaining a total of 59 (41+18) λ values for the two stars. From the λ measurements we calculated the radial velocities using the following formula:

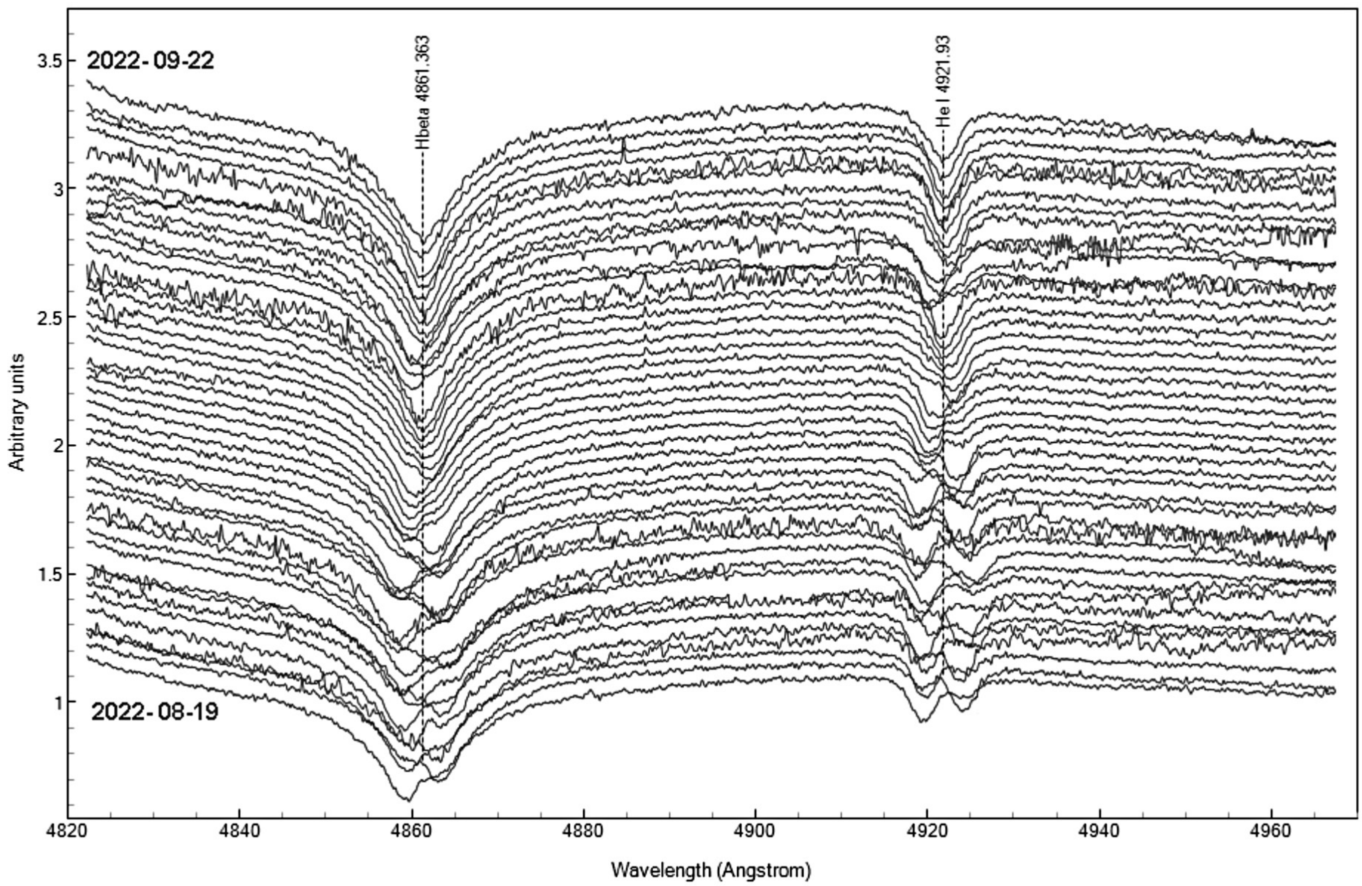

Figure 4. The spectra acquired from 2022 08 19 to 2022 09 22 show the evolution of the double-peaked Hβ and He I absorption lines. This last was used for the radial velocity measurements.

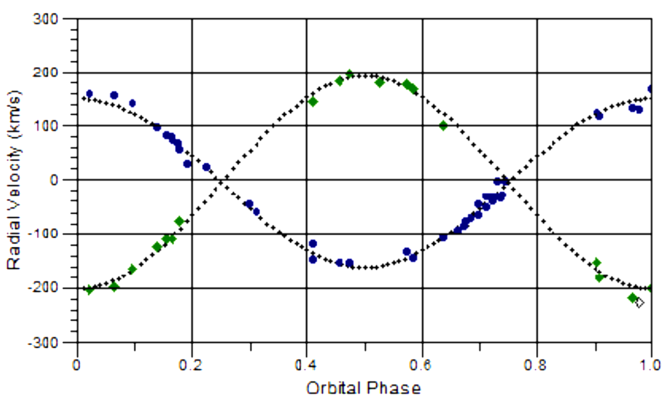

Figure 5. Orbital phase for σ Aql obtained from radial velocity data and plotted with SBS software.

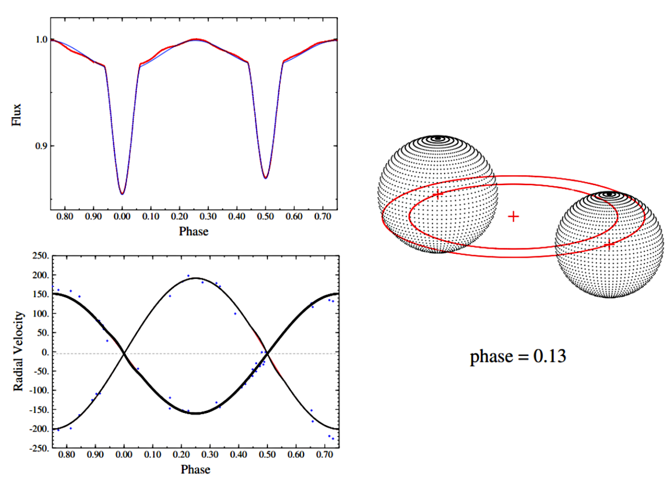

Figure 6. Model of the σ Aql system obtained with Binary Maker 3.

$$\mathrm{RV(km/s)} = \frac{\Delta\lambda}{\lambda 0}\, c, \qquad (1)$$

where $\Delta\lambda$ is the measured shift in wavelength of a given spectral line, $\lambda 0$ is the rest wavelength of a spectral line, and c is the speed of light in a vacuum (299792.458 km/s).

The Spectroscopic Binary Solver (SBS) software version 1.4 (Johnson 2004) was used to estimate the relevant orbital parameters of the binary system σ Aql.

For more detailed information about the use of SBS software see the user manual installed with the software and references therein. All derived radial velocities were arranged into a text file, according to the SBS-required file format for double-line observation data.

A typical SBS session performs in succession the functions: Read File, Period, Solve, and Error Est. The period was fixed to 1.95028 d (from photometric data) and a circular orbit was assumed (e = 0). By means of the function Solve the software automatically solves for the orbital parameters via the Downhill Simplex method implemented into the SBS software. Once the orbital parameters were obtained, the Error Est. function made it possible to obtain the estimate of the uncertainties. The summary of parameters produced is shown in Table 2.

5. Modelling

To model the σ Aql binary system, the software Binary Maker 3 (Bradstreet and Steelman 2002) was used with a subset of TESS photometric data. Assuming the mass ratio of the system as the ratio of the two radial velocity semi-amplitudes, the value derived from SBS analysis was q = K1/K2 = M2/M1 = 0.794171. The primary star temperature has been assumed as T = 19050 K, on the basis of the spectral type B3V from log T_{eff} = 4.280 (Pickles 1998). The eccentricity was assumed to be circular (e = 0), on the basis of previous studies reported in section 1.

The model parameters have been derived using an iterative approach, changing the fractional radii of the two components and the inclination of the binary system towards the Earth observer's line of sight, in order to minimize the sum square of the residual of the model fit. The final parameters used for the model are shown in Table 3.

From the orbital elements and inclination we can derive the absolute masses of the components, the semi-major axis of the orbit, and the stellar radii, which are shown in Table 4.

6. Discussion

We report in Table 5 the current findings on σ Aql, comparing them with the previously published results. The T_{eff} of the hotter component used for our model is close to the one published by Cester *et al.* (1978). The orbital period falls within 0.001% of the other results and the orbital inclination is close to the other published values within 0.5%. In general, the masses and radii we have found are a little smaller than those reported in most of the previous studies. However, it should be noted that there is an excellent correspondence with the values found by Brancewicz and Dworak (1980), which used a computational method on existing data, except for the q ratio with respect to which we note a difference of –8%, caused by the lower mass of the secondary star. This circumstance could imply the need to review the spectral classification of the components of the binary system.

We must also consider that the high precision of the TESS light curve implies constraints on transit/occultation times that lead us to exclude the ratios of the radii k = 1.0 and k = 0.72 reported respectively by Wylie (1922), Luyten *et al.* (1939), and Cester *et al.* (1978). The fit of the TESS light curve remains very good, with a ratio of the radii k = 0.90, as in the model we have adopted.

7. Conclusions

We present updated physical parameters for the eclipsing binary star σ Aql using archival photometric data and high-resolution spectroscopy secured at Osservatorio Astronomico Bassano Bresciano. The mass ratio determined for this system is consistent with previous results. Our masses are a little lower than most previously published results, but close to the results obtained by Brancewicz and Dworak (1980). We have an exception for the mass of the secondary star which may indicate

Table 2. Parameter summary of the orbital elements derived by SBS fsoftware for the binary system σ Aquilae.

Parameter	*Summary*
Semi-Amplitude K(1)	156.192 ± 2.880 km/s
Semi-Amplitude K(2)	196.673 ± 3.126 km/s
Systemic Velocity	–4.8323 ± 1.4679 km/s
Mass ratio	0.79
Orbital Period	1.95028 days
Time of Periastron	2459809.62504 ± 0.00399 HJD
a1 sin (i)	4.1888e+06 ± 7.72e+04 km
a2 sin (i)	5.2744e+06 ± 8.38e+04 km
m1 $\sin^3$ (i)	4.9484e+00 ± 7.87e-02 $M_\odot$
m2 $\sin^3$ (i)	3.9298e+00 ± 7.25e-02 $M_\odot$

Table 3. Final parameters used for modeling the binary system σ Aquilae with Binary Maker 3.

Parameter	*Value*
q (mass ratio)	0.79
i (inclination angle, deg)	71.97
r1 (relative radius [back])	0.257
r2 (relative radius [back])	0.231
T1 (K)	19050
T2 (K)	17860

Table 4. Absolute masses, semi-major axis of the orbit, and stellar radii of σ Aql.

Parameter
M1 = 4.9484 / $\sin^3$(i) = 5.8 ± 0.1 solar masses
M2 = 3.9298 / $\sin^3$(i) = 4.6 ± 0.1 solar masses
a = (74.5 * P2 * (M1+M2))$^{1/3}$ = 14.3 ± 0.1 solar radii
(P is the orbital period in days)
R1 = 0.257 * a = 3.7 solar radii
R2 = 0.231 * a = 3.3 solar radii

Table 5. Summary of the principal elements of σ Aquilae as reported in different studies.

	Jordan (1916) *Wylie (1922)*	*Luyten* et al. (1939)	*Koch* et al. (1965)	*Cester* et al. (1978)	*Brancewicz* et al. (1980)	*This Study*
Spectral type	B8+B8	—	B3+B4	B3+B3	B3V+B3V	B3V+B3V
T_{eff} primary (K)	—	—	—	18950	16840	19050
Period (days)	1.95026	1.950272	1.95	1.9503	1.950260	1.95028
i (°)	71.7	—	71.6	72.2	—	71.97
e	0	0	—	—	—	0
q (M2/M1)	0.83	0.79	—	0.79	0.86	0.79
M1 ($M_\odot$)	6.19	6.8	—	6.8	5.70	5.8
M2 ($M_\odot$)	5.14	5.4	—	5.4	4.90	4.6
k (R2/R1)	1.0	1.00	—	0.72	0.89	0.90
R1 ($R_\odot$)	3.9	3.66	—	4.22	3.75	3.7
R2 ($R_\odot$)	3.9	3.66	—	3.05	3.32	3.3
a ($R_\odot$)	14.7	15.1	—	—	14.43	14.3

the need to revise the spectral class so, we recommend follow-up observations to clarify this point. The constraints on light curve fit led us to exclude the ratios of the radii very different from k = 0.90, which we have adopted for our model. This work was a major test of the data taken at Bassano Bresciano using the ATHOS spectrograph: they show us that it is possible to present results that are of scientific quality using home-made equipment that will be useful to the wider astronomical community.

References

Bradstreet, D. H., and Steelman, D. P. 2002, *Bull. Amer. Astron. Soc.*, **34**, 1224.

Brancewicz, H. K., and Dworak, T. Z. 1980, *Acta Astron.*, **30**, 501.

Buil, C. 2021, ISIS: Integrated Spectropgraphic Innovative Software (http://www.astrosurf.com/buil/isis-software.html).

Cester, B., Fedel, B., Giuricin, G., Mardirossian, F., and Mezzetti, M. 1978, *Astron. Astrophys., Suppl. Ser.*, **33**, 91.

Hoffleit, D., and Jaschek, C. 1991, *The Bright Star Catalogue*, 5th rev. ed., Yale Univ. Observatory, New Haven, CT.

Johnson D. O. 2004, *J. Astron. Data*, **10**, 3.

Jordan F. C. 1916, *Publ. Allegheny Obs. Univ. Pittsburgh*, **3**, 189.

Koch R. H., Olson E. C., and Yoss K. M. 1965, *Astrophys. J.*, **141**, 955.

Luyten W. J., Struve O., and Morgan W. W. 1939, *Publ. Yerkes Obs.*, **7**, 251.

Pan, K., Tan, H., and Shan, H. 1998, *Astron. Astrophys.*, **335**, 179.

Paunzen, E., and Vanmunster, T. 2016, *Astron. Nachr.*, **337**, 239.

Pickles, A. J. 1998, *Publ. Astron. Soc. Pacific*, **110**, 863.

Samus N. N., Kazarovets E. V., Durlevich O. V., Kireeva N. N., and Pastukhova E. N. 2017, *Astron. Rep.*, **61**, 80 (*General Catalogue of Variable Stars*: Version GCVS 5.1; http://www.sai.msu.su/groups/cluster/gcvs/gcvs).

Wylie, C. C. 1922, *Astrophys. J.*, **56**, 232.

Studies of R CrB Star Pulsation Using ASAS-SN Photometry

John R. Percy
Department of Astronomy and Astrophysics, and Dunlap Institute of Astronomy and Astrophysics, University of Toronto, 50 St. George Street, Toronto ON M5S 3H4, Canada; john.percy@utoronto.ca

Received January 27, 2023; revised March 27, 2023; accepted March 28, 2023

Abstract R Coronae Borealis (RCB) stars are low-mass, carbon-rich, hydrogen-poor stars which suddenly and unpredictably fade by up to eight magnitudes or more in visual brightness, then slowly return to maximum. They may also undergo small-amplitude variations, on time scales of weeks, due to pulsation. The present study uses data from the All-Sky Automated Search for Supernovae (ASAS-SN), along with light curve analysis and time-series analysis, to study pulsational variations in 23 stars which were classed as RCB stars in both the *ASAS-SN Variable Star Catalog* and the *General Catalogue of Variable Stars*. All show irregular or semiregular variability on time scales of 20 to 100+ days, with semi-amplitudes of 0.05 to 0.3 magnitudes. For 14, some estimate of the period could be derived; the periods cluster between 30 and 50 days and are, on average, about half those of low-mass yellow supergiants with similar luminosity but more normal composition.

1. Introduction

R Coronae Borealis (RCB) stars are rare, low-mass yellow supergiant stars with bizarre chemical compositions. They can spend years or decades at normal maximum brightness, then suddenly and unpredictably fade by up to eight magnitudes or more in the course of a few days or weeks, then slowly return to maximum. See Clayton (2012) for an excellent review.

Unlike "normal" stars which are about 3/4 hydrogen, 1/4 helium, and 2 percent everything else, by mass, RCB stars are about 9/10 helium, 1/10 carbon, and less than one percent hydrogen, by mass. There are two main models for the formation of these stars, neither of which is entirely satisfactory—the merger of two white dwarfs, or a final helium flash.

The fadings are due to the obscuring effect of clouds of carbon-rich dust ("soot"), ejected randomly from the star in time and direction. If the cloud lies between the observer and the photosphere of the star, then a fading is seen. The cloud, being warm, can be detected at infra-red wavelengths. As the dust disperses, the star slowly returns to normal maximum brightness.

Some and perhaps all RCB stars show another form of variability—pulsation. This is not surprising; normal low-mass yellow supergiants pulsate as RV Tauri or SRd variables. In the RCB stars, this pulsation may have some role in ejecting matter from the star, perhaps leading to a fading. A very comprehensive study of the pulsation of RCB stars was carried out by Lawson *et al.* (1990). Percy *et al.* (2004) carried out self-correlation time-series analysis of the Lawson *et al.* data and of other data. The results, for the stars in the present sample, are included in Table 1.

The brightest RCB stars are RY Sgr and R CrB itself. RY Sgr has a normal visual magnitude of 6.5 and a pulsation period of 38.6 days, and a range of 0.5 in V. R CrB has a normal visual magnitude of 5.8 and a pulsation period of about 41 days and a range of 0.1 or more, but its pulsational variability is semiregular at best; some observers have suggested that it also has a 67-day period, and is bimodal. Figure 1 shows recent AAVSO V observations of R CrB as it came out of a deep minimum (Kafka 2022). In the first half of the dataset, a 42-day variability can be clearly seen. The variability then becomes semiregular. The 42-day signal reappears at the end.

There is evidence that, in a few stars, the onset of fadings may be linked to the phase in the pulsation cycle (Pugach 1977; Lawson *et al.* 1992; Crause *et al.* 2007; Percy and Dembski 2018), but the sample sizes were not large enough to tell whether this link is statistically significant.

The photometric observations in the All-Sky Automated Survey for Supernovae (ASAS-SN) database are a potentially useful tool for studying RCB star pulsation. That is the purpose of the present paper.

2. Data and analysis

The ASAS-SN variable star website and catalog (Shappee *et al.* 2014; Jayasinghe *et al.* 2018, 2019), contains 93 stars which the catalog classifies as RCB stars. For many of these, there was no evidence of a fading in the ASAS-SN data.

Table 1. Period and amplitude analysis of ASAS-SN observations of RCB stars.

Name	*GCVS Range*	*P(d) / A (mag)*	*Other Periods*
UX And	8.2–9.9	54/0.03	—
U Aqr	10.6–15.9	30/0.22	40,80 L, 40 PY
V943 Ara	10.8–17.2	55/0.05:	—
UW Cen	8.89–17.9	41:/0.05, 68:/0.05	42.8 L
DY Cen	12.0–<16.4	18:/0.02	—
V742 Lyr	11.5–<17.5	48.6/0.16	—
W Men	13.4–<18.3	32/0.03, 47/0.03	—
Y Mus	10.5–12.1	38/0.05	107, 227 L, 100 ± PY
RT Nor	10.6–16.3	40/0.07, 60/0.07	43 L, 50 ± 6 PY
RZ Nor	10.63–<13.	50:/0.05:	—
V409 Nor	11.8–19.	49.9/0.05, 70/0.07	—
VZ Sgr	10.8–15.0	126/0.06	40–50 L
GU Sgr	11.33–15.0	—	37.8 L
V3795 Sgr	11.5–<15.5	35	—
FH Sct	13.4–16.8	47/0.08	—
RS Tel	9.0–15.34	100/0.07	40 L, 40 ± 6 PY

Note: In the last column of other period determinations, L denotes Lawson et al. *(1990), and PY denotes Percy* et al. *(2004).*

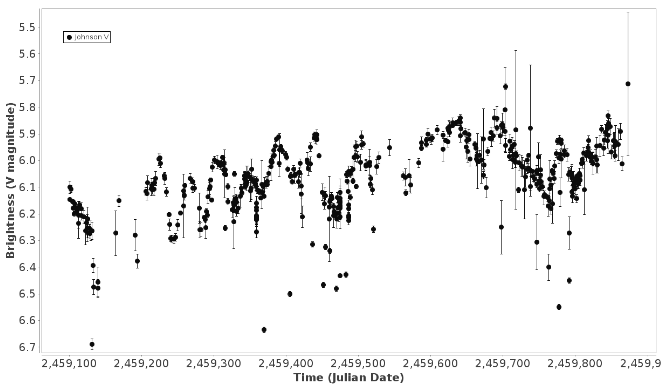

Figure 1. A 1000-day light curve of R CrB, based on AAVSO V photometry, showing the semiregular variability due to pulsation.

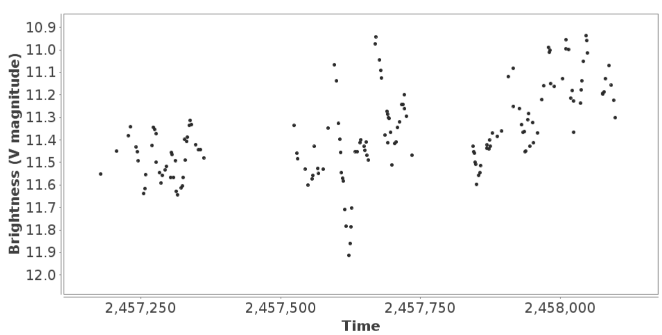

Figure 2. The light curve of U Aqr, based on ASAS-SN V photometry, showing short-term semiregular variability due to pulsation.

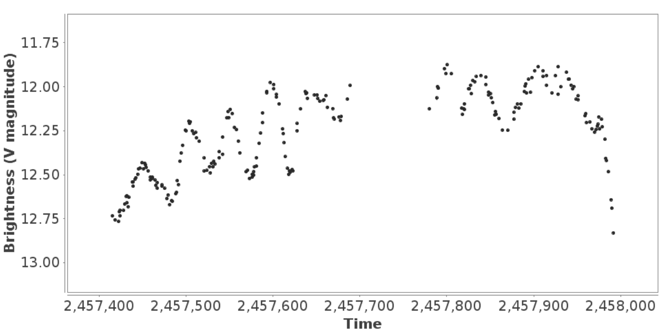

Figure 3. The light curve of V742 Lyr, based on ASAS-SN V photometry, showing relatively regular 48.6-day variability due to pulsation.

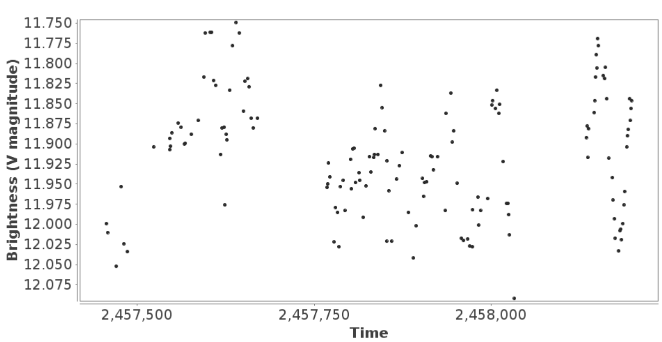

Figure 4. The light curve of V409 Nor, based on ASAS-SN V photometry, showing 49.9-day variability due to pulsation.

The present study included only stars which are also classified as RCB stars in the *General Catalogue of Variable Stars* (Samus *et al.* 2017). Some of these stars were in the process of entering or leaving a fading, and were unsuited for study of the small-amplitude pulsation. A few others were either too bright or too faint for study. In the end, the present study included the 16 stars in Table 1, plus those seven mentioned at the end of section 3.

The ASAS-SN data and light curves are freely available online (asas-sn.osu.edu/variables). The error bars on the ASAS-SN observations are 0.02 mag, and this is also the noise level in our Fourier analyses.

In addition to very careful analysis of the light curves, the Fourier analysis routine in the American Association of Variable Star Observers (AAVSO) time-series package VStar (Benn 2013) was used. Note that the amplitudes which are given in this paper, including in the tables, are actually semi-amplitudes—the coefficient of the sine curve with the given period—and not the full amplitude or range.

3. Results

The results are summarized in Table 1, which includes the range as given in the *General Catalogue of Variable Stars*, as well as the period(s) and amplitude(s), and comparisons with other determinations. A colon (:) denotes uncertainty. Notes on individual stars are given below. A few typical light curves are shown.

UX Ant A 54 ± 4-day period is clearly visible in the light curve though, in the wavelet analysis, it is possible that there are separate 47- and 57-day periods. The amplitude seems to decrease as a fading approaches.

U Aqr There is a strong signal, with a period of 30 ± 3 days and an amplitude of 0.22, but reaching as high as 0.5 (!). There is an even stronger 80-day period in the last 3/4 of the dataset, as the star begins a fading (Figure 2).

V943 Ara The light curve is dominated by fading and recovery, but there is a strong 50–60-day period in one season of the light curve.

UW Cen There is very weak evidence for periods of about 41 and 68 days; the amplitude is less than 0.05 and the periodicity is not convincing.

DY Cen There is a very weak signal at a period of 18 days.

V742 Lyr There is a very strong (amplitude 0.16) signal at a period of 48.6 days in the data between two fadings; it is also visible before the first of the two fadings (Figure 3). The light curve shows some degree of regularity.

W Men The pulsation amplitude seems to increase as a fading approaches, and is greatest at the end of the dataset. The dominant period switches from 32 to 47 days.

Y Mus There is a 38-day signal which, though weak, becomes more noticeable as a fading approaches at the end of the dataset.

RT Nor There are strong semiregular variations with periods of 40 and 60 days, with amplitudes of 0.07. There is also a signal in the Fourier spectrum at 180 days, with amplitude 0.09, but it is not visible in the light curve.

RZ Nor The light curve is dominated by recovery from a fading, but there is a hint of a 50-day period in one season of the light curve.

V409 Nor There is a period of 49.9 days, with an amplitude of 0.05, and a slightly weaker signal at 70 days. The amplitude of the 49.9-day period increases to 0.10 or more at the end of the dataset (Figure 4).

VZ Sgr There are large, irregular variations on time scales greater than 100 days. A period of 126 days (amplitude 0.06) is present in the Fourier spectrum.

GU Sgr Although there are no signals in the Fourier spectrum with amplitude greater than 0.03, there is one very large cycle with amplitude of 0.3 just before the fading at the end of the dataset.

V3795 Sgr There are complex variations in the period range of 30-40 days, which are clearly visible in the light curve.

FH Sct There is a strong 47 ± 10-day signal, with an amplitude of 0.08, including just before a fading.

RS Tel There is a strong 100-day period, with amplitude 0.07, which is visible especially in the last 2/3 of the dataset.

For the following stars, there was small-amplitude, short-term variability, but no obvious period in the Fourier spectrum or in the light curve: S Aps, UV Cas, V854 Cen, V2552 Oph, MV Sgr, SV Sge, V482 Cyg. RY Sgr and R CrB are normally too bright for ASAS-SN photometry.

4. Discussion

All of the stars in Table 1 show small-amplitude (typically 0.05 to 0.30) variations on time scales of 20 to 100 days (but clustering between 30 and 50 days), presumably due to pulsation.

Determining precise periods and amplitudes is a challenge. In some stars, the amplitude is only slightly larger than the nominal error in the data, namely 0.02 magnitude. There are seasonal gaps in the data, which may introduce alias periods in the Fourier spectra. In some stars, the pulsations are superimposed on slow variations due to changes in dust obscuration. The variations are semiregular at best. This can be seen in the figures, including Figure 1. Only V742 Lyr (Figure 3) showed reasonable regularity. Some stars may be bimodal.

It is known that low-mass yellow supergiants with normal composition show semiregular pulsation. For instance, Percy (2022) examined a sample of yellow semiregular (SRd) variables, and found that 34/38 were semiregular primarily because their pulsation amplitudes varied by factors of up to 10 on time scales of 20–30 pulsation periods. This may be because the mode lifetimes are only 20–30 pulsation periods, unless the modes are continuously driven. Other causes of semiregularity were long secondary periods, multiple pulsation periods, period switch, or "wandering."

This is one possible reason why the periods, determined in this study, differ in some cases from those in the literature (Table 1, last column). The length, distribution, and accuracy of the ASAS-SN data differ from those of the photoelectric data, which were used by both Lawson *et al.* (1990) and Percy *et al.* (2004). Different modes may dominate at different times. In Figure 1, for instance, the behavior of R CrB changes between the first half of the data and the second half. Also, Percy *et al.* 2004) used a different method of time-series analysis—self-correlation—than Lawson *et al.* 1990). This method tends to identify a single dominant period in the data, rather than multiple periods.

There are six stars for which absolute visual magnitudes M_V can be crudely estimated from their mean normal V magnitude, because their GAIA distances (taken from the ASAS-SN catalogue) are reasonably accurate, and their interstellar reddening and extinction are small. They are: UX Ant, –2.92; U Aqr, –4.08; V742 Lyr, –5.08; RS Tel, –4.71; R CrB, –4.31; and RY Sgr, –5.50. These are consistent with previous estimates of the M_V of RCB stars, namely –3 to –5 (Clayton 2012). There is no obvious period-luminosity relation in these six stars.

The pulsation periods of RCB stars are generally 20 to 100 days, but clustering between 30 and 50 days. Comparing the M_V and log P values with the period-luminosity relation for RV Tauri stars—which are also low-mass yellow supergiants, but of normal composition—indicates that their periods are about half what would be expected from the RV Tauri P–L relation (Bodi and Kiss 2019). This could indicate that the periods are high overtones, but it is more likely because the composition, structure, and previous evolution of the RCB stars are much different from those of the RV Tauri stars.

In section 3.1, a few stars have been noted as having a pulsation amplitude which seems to increase before a fading, but the sample size is too small to tell whether this trend is significant.

5. Conclusions

This study strengthens the conclusion that most, if not all, RCB stars vary semiregularly or irregularly on a time scale of weeks, with small amplitude, due to pulsation. The periods cluster between 30 and 50 days, and are about half those of normal low-mass yellow supergiants of similar luminosity.

6. Acknowledgements

This paper made use of ASAS-SN photometric data. The author thanks: the ASAS-SN project team for their remarkable contribution to stellar astronomy, and for making the data freely available on-line; and the AAVSO for creating and making available the VStar time-series analysis package. The Dunlap Institute is funded through an endowment established by the David Dunlap Family and the University of Toronto.

References

Benn, D. 2013, VStar data analysis software (https://www.aavso.org/vstar-overview).

Bódi, A., and Kiss, L. L. 2019, *Astrophys. J.*, **872**, 60.

Clayton, G. C. 2012, *J. Amer. Assoc. Var. Star Obs.*, **40**, 539.

Crause, L. A., Lawson, W. A., and Henden, A. A. 2007, *Mon. Not. Roy. Astron. Soc.*, **375**. 301.

Jayasinghe, T., *et al.* 2018, *Mon. Not. Roy. Astron. Soc.*, **477**, 3145.

Jayasinghe, T., *et al.* 2019, *Mon. Not. Roy. Astron. Soc.*, **486**, 1907.

Kafka, S. 2022, variable star observations from the AAVSO International Database (https://www.aavso.org/aavso-international-database-aid).

Lawson, W.A., Cottrell, P. L., Gilmore, A. C., and Kilmartin, P. M. 1992, *Mon. Not. Roy. Astron. Soc.*, **256**, 339.

Lawson, W.A., Cottrelll, P. L., Kilmartin, P. M., and Gilmore, A. C. 1990, *Mon. Not. Roy. Astron. Soc.*, **247**, 91.

Percy, J. R. 2022, *J. Amer. Assoc. Var. Star Obs.*, **50**, 96.

Percy, J. R., and Dembski, K. H. 2018, *J. Amer. Assoc. Var. Star Obs.*, **46**, 127.

Percy, J. R., Bandara, K., Fernie, J. D., Cottrell, P. L., and Skuljan, L. 2004, *J. Amer. Assoc. Var. Star Obs.*, **33**, 27.

Pugach, A. F. 1977, *Inf. Bull, Var. Stars*, No. 1277, 1.

Samus, N. N., Kazarovets, E. V., Durlevich, O. V., Kireeva, N. N., and Pastukhova, E. N. 2017, *Astron. Rep.*, **61**, 80.

Shappee, B. J., *et al.* 2014, *Astrophys. J.*, **788**, 48.

13 New Light Curves and Updated Mid-Transit Time and Period for Hot Jupiter WASP-104 b with EXOTIC

Heather B. Hewitt
School of Earth and Space Exploration, Arizona State University, 781 E Terrace Mall, Tempe, AZ 85287-6004; hbhewittt@asu.edu

Federico Noguer
Suber Corley
James Ball
Claudia Chastain
Richard Cochran-White
Kendall Collins
Kris Ganzel
Kimberly Merriam Gray
Mike Logan
Steve Marquez-Perez
Chyna Merchant
Matthew Pedone
Gina Plumey
Matthew Rice
Zachary Ruybal
School of Earth and Space Exploration, Arizona State University, 781 E Terrace Mall, Tempe, AZ 85287-6004

Molly N. Simon
School of Earth and Space Exploration, Arizona State University, 781 E Terrace Mall, Tempe, AZ 85287-6004

Isabela Huckabee
School of Earth and Space Exploration, Arizona State University, 781 E Terrace Mall, Tempe, AZ 85287-6004 and Jet Propulsion Laboratory, California Institute of Technology, 4800 Oak Grove Drive, Pasadena, CA 91109

Robert T. Zellem
Jet Propulsion Laboratory, California Institute of Technology, 4800 Oak Grove Drive, Pasadena, CA 91109

Kyle A. Pearson
Jet Propulsion Laboratory, California Institute of Technology, 4800 Oak Grove Drive, Pasadena, CA 91109

Received February 2, 2023; revised May 31, 2023, June 6, 2023; accepted June 6, 2023

Abstract Using the EXOplanet Transit Interpretation Code (EXOTIC), we reduced 52 sets of images of WASP-104 b, a Hot Jupiter-class exoplanet orbiting WASP-104, in order to obtain an updated mid-transit time (ephemeris) and orbital period for the planet. We performed this reduction on images taken with a 6-inch telescope of the Center for Astrophysics | Harvard & Smithsonian MicroObservatory. Of the reduced light curves, 13 were of sufficient accuracy to be used in updating the ephemerides for WASP-104 b, meeting or exceeding the three-sigma standard for determining a significant detection. Our final mid-transit value was 2457805.170208 ± 0.000036 BJD_TBD and the final period value was 1.75540644 ± 0.00000016 days. The true significance of our results is in their derivation from image sets gathered over time by a small, ground-based telescope as part of the Exoplanet Watch citizen science initiative, and their competitive results to an ephemeris generated from data gathered by the TESS telescope. We use these results to further show how such techniques can be employed by amateur astronomers and citizen scientists to maximize the efficacy of larger telescopes by reducing the use of expensive observation time. The work done in the paper was accomplished as part of the first fully online Course-Based Undergraduate Research Experience (CURE) for astronomy majors in the only online Bachelor of Science program in Astronomical and Planetary Sciences.

1. Introduction

The study of exoplanets is a popular and fast-growing subject in astronomy. By studying the variety of extrasolar planets and planetary systems that have been discovered, researchers gain a deeper understanding of how planetary formation and evolution occur and gain valuable insights into the composition of other distant worlds. Currently, over 5,000 exoplanets have been confirmed, up from 32 in 2000. Historically, opportunities for research on exoplanets have been limited for amateur astronomers and those without professional backgrounds in astronomy. High costs and technical expertise are some of the obstacles to building, operating, or maintaining appropriate observational equipment. However, citizen science projects, including Exoplanet Watch, aim to expand the usefulness of direct observations of transiting exoplanets with a network of small Earth-based telescopes (Zellem *et al.* 2020). Similarly, Exoplanet Watch and others increase the efficiency of exoplanet studies conducted by large telescopes by reducing uncertainty about the predicted timing of transit events (Zellem *et al.* 2020).

Improving the potentially stale ephemerides of known exoplanet transits is now an established method of reducing observational costs for space telescopes (e.g. Zellem *et al.* 2020; Kokori *et al.* 2022b; Yeung *et al.* 2022). The work done in this paper contributes to the network of small telescope observations that funnel improved ephemerides to established repositories for use by scientists conducting large space- and ground-based telescope observation missions. Given the large cost of using space-based telescopes, these improvements represent thousands of dollars in cost savings by improving efficiency (Drier 2021). The work that amateur astronomers and citizen scientists do when working with teams such as Exoplanet Watch ensures that future use of expensive time on telescopes is used efficiently. This project partnered with Exoplanet Watch to examine previously unreviewed astronomical data for the planet WASP-104 b. WASP-104 b is a characteristic Hot Jupiter with a mass of about 1.272 Jupiter masses, a period of about 1.75 days, and orbits at a distance of 0.029 AU from its host star, WASP-104 (Smith *et al.* 2014). WASP-104 is a G-type star.

The work done in the paper was accomplished as part of the first fully online Course-Based Undergraduate Research Experience (CURE) for astronomy majors. Fifteen students participated in the 15-week online course, Exoplanet Research Experience, at Arizona State University (ASU). This course was developed to enhance the only completely online Bachelor of Science program in Astronomical and Planetary Sciences (APS). The APS degree program was developed to mirror the existing in-person Astrophysics degree program at ASU, but at the time this course was developed, there was no opportunity for the online students to participate in authentic research experiences. This is a common disparity between online and in-person degree programs that we aimed to address with the development of this CURE.

2. Observatory

We obtained our data from the MicroObservatory Robotic Telescope Network, which is operated by the Harvard Smithsonian Center for Astrophysics (Sadler *et al.* 2001). The MicroObservatory uses a network of robotic 6-inch telescopes. Our observations were taken using Cecilia. Cecilia is part of the MicroObservatory network and is located on Mount Hopkins, Arizona, at the Whipple Observatory. It is a custom-built Maksutov-Newtonian with an aperture of 152 mm and a focal length of 560 mm. It is equipped with a KAF-1402ME camera and produces 0.94 × 0.72 degree images; the images are binned 2 × 2.

3. Weather

Observations by ground-based telescopes have two main environmental factors with which they have to contend to produce favorable data: atmospheric turbulence and weather phenomena. Any combination of environmental and technical issues can hamper ground-based observations, which is a hindrance when compared to orbital telescopes. However, a ground-based telescope can make up for this deficit by the sheer volume of observations. Table 1 includes the date of each observation, and the average quality of the weather as estimated by Cecilia in the FITS header. The bolded dates in Table 1 indicate a significant detection. The weather is rated on a scale of 0 to 100. A 0 score represents a completely cloudy night, whereas a score of 100 represents a completely clear night. It's important to note that the MicroObservatory weather ratings were not available between 2018 and 2020; therefore, the weather ratings listed in Table 1 from 2018-02-23 to 2020-01-13 are not accurate (Sienkiewicz 2022). Additionally, we were able to remove some images with significant cloud cover from the data sets with low weather rankings to still obtain a significant detection in some cases. These weather ratings are used as a guide; they are estimated from NOAA weather satellites and do not always accurately reflect the local weather conditions. A further analysis of the data is required to determine the quality for each night of data.

Table 1. Weather quality estimates by average WEATHER value in Cecilia data: (Bold lines indicate a significant detection).

Date	*Weather Quality*	*Date*	*Weather Quality*
2015-02-07	**98.74**	2017-03-09	99.01
2015-02-14	39.09	2017-03-31	98.95
2015-02-21	22.83	**2017-05-13**	**99.78**
2015-02-22	14.43	2018-01-04	0.00
2015-02-28	**84.10**	2018-02-23	4.00
2015-03-22	91.93	2018-03-03	4.00
2015-04-05	**79.37**	2018-03-10	4.00
2015-05-12	**38.64**	2018-03-17	4.00
2015-05-26	**99.27**	2018-03-18	4.00
2015-06-02	99.82	2018-03-24	4.00
2016-01-03	73.88	2018-03-25	4.00
2016-01-10	36.47	**2018-04-01**	**4.00**
2016-01-17	10.22	2018-04-22	4.00
2016-02-22	98.66	2018-05-06	4.00
2016-02-29	**98.33**	2018-11-23	4.00
2016-03-07	3.54	2018-11-29	4.00
2016-03-23	98.68	2019-01-19	4.00
2016-04-06	0.20	2019-02-17	4.00
2016-04-13	**98.83**	2019-02-24	4.00
2016-04-21	**99.00**	2019-03-18	4.00
2016-11-28	55.62	2020-01-06	4.00
2016-12-05	87.03	**2020-01-13**	**4.00**
2017-01-17	68.51	2020-01-28	96.72
2017-02-22	**98.38**	**2020-02-25**	**96.53**
2017-02-23	98.55	2020-03-11	0.00
2017-03-01	96.25	2020-03-18	59.76

4. Data reduction

Our team utilized NASA Jet Propulsion Laboratory's software, EXOTIC (EXOplanet Transit Interpretation Code), to analyze our photometric data and reduce the light curves for our 52 nights of data (Zellem *et al.* 2020). EXOTIC reduces raw ".fits" files into a light curve and calculates target parameters by tracking the target throughout the observation. EXOTIC is a PYTHON 3 pipeline that can be run locally or on Google Colab. We chose to run EXOTIC in the Google Colab Cloud, which supports the sharing of files among team members. In the Google Colab, we mounted our data and installed EXOTIC onto a virtual machine. Priors for the target are obtained from the NASA Exoplanet Archive by searching the target's name. Then, an image is displayed, and users are prompted to locate the target and up to ten comparison stars. To determine the flux of the target, an optimal aperture size is determined and all the pixel values within the aperture are summed. The background light is subtracted from each pixel value to isolate the flux from the star itself. To ensure the star's brightness is changing due to a transit and not to atmospheric interference, EXOTIC compares the star's brightness to the brightness of nearby comparison

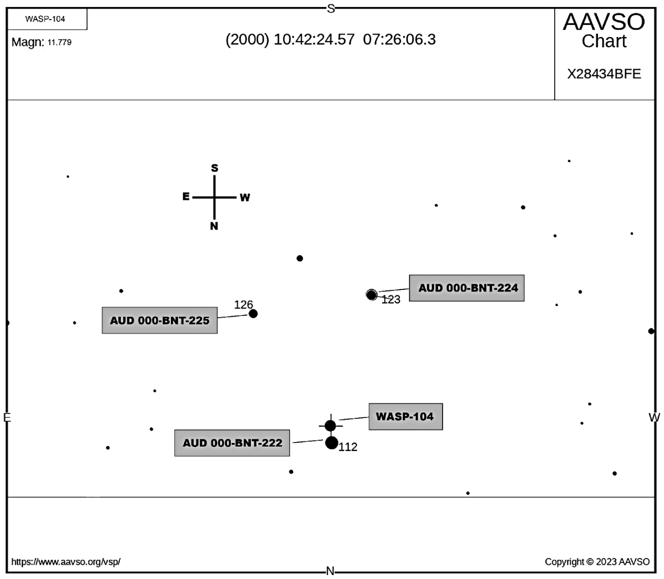

Figure 1. AAVSO VSP Chart for WASP-104 b with comparison stars labeled. Original field of view of AAVSO VSP Chart was 18.5 arc minutes. The image was magnified for easier viewing.

Table 2. Calculated mid-transit times and transit depths for WASP-104 b.

Date	*Transi Depth (%)*	*Transit Depth Uncertainty*	*Mid-transit (BJD_TBD)*	*Mid-transit Uncertainty (d)*
2015-02-07	2.30	0.51	2457060.8809	0.0026
2015-02-28	2.29	0.44	2457081.9381	0.0028
2015-04-05	2.30	0.3	2457118.8094	0.0025
2015-05-12	2.29	0.53	2457155.6699	0.0032
2015-05-26	2.30	0.16	2457169.7162	0.0029
2016-03-01	2.26	0.68	2457448.8305	0.0042
2016-04-14	2.30	0.41	2457492.7111	0.0032
2016-04-21	2.30	0.45	2457499.7262	0.0041
2017-02-22	2.30	0.18	2457806.9359	0.0023
2017-05-13	2.30	0.47	2457887.6848	0.0035
2018-04-01	2.30	0.16	2458210.6607	0.0039
2020-01-13	2.27	0.27	2458861.9278	0.0024
2020-02-25	2.06	0.22	2458905.8001	0.0035

stars (Zellem *et al.* 2020). EXOTIC's output includes a light curve, the mid-transit time, ratio of planet to stellar radius, transit depth, ratio of semi-major axis to stellar radius, scatter in residuals, and transit duration.

In order to confirm which data sets we intended to use, our research team used an agreed-upon control method to ensure that a uniform process was followed before we finalized our list of significant detections. This agreed-upon method of analyzing the data included defining which images are candidates for deletion and identifying the best comparison stars to use for every data set. First, we cleaned the images up by removing "bad" images, defined as having clouds, an unacceptable level of visual noise, or the target missing from the field of view. This assessment was conducted using astronomical image-viewing programs SAOImage DS9, AstroImageJ, or JS9. Then, using the American Association of Variable Star Observer (AAVSO) Variable Star Plotter (VSP; AAVSO 2023), we selected three comparison stars to use in our reduction process: AUD 000-BNT-222, AUD 000-BNT-224, and AUD 000-BNT-225. Our chart (Chart ID X27938O) is shown in Figure 1 with our comparison stars labeled.

With our agreed-upon selection process, we re-analyzed the 16 possibly significant detections of the original 52 observations and produced 13 confirmed significant detections. We determined a detection as significant when the detection significance was greater than 3σ using Equation (1):

$$\frac{\text{Transit Depth}}{\text{Transit Depth Uncertainty}} \geq 3 \qquad (1)$$

5. Data

From 52 nights worth of data and images, we reduced 13 significant light curves using EXOTIC's reduction process on the target hot Jupiter, WASP-104 b, as shown in Table 2. A sample light curve is shown in Figure 2 and all the light curves are presented in Appendix A, Figure A1.

We created an observed-calculated (O–C) plot to calculate our updated mid-transit time (ephemeris) and period. We also used a posterior distribution to analyze our parameters statistically. A secondary tool in Colab[1] was used that fit the ephemeris of our observations to previously published observations in the Exoplanet Archive. In the O–C plot, shown in Figure 3, we included the mid-transit times from our 13 significant detections along with two of the mid-transit times on the NASA Exoplanet Archive: Smith *et al.* (2014) and the most recent, Ivshina and Winn (2022). For consistency, we chose only to include previously published mid-transit times derived from a measured light curve. As such, we excluded the Bonomo *et al.* (2017) and Kokori *et al.* (2022a) values from the O–C plot. The values used from the NASA Exoplanet Archive are shown in Table 3. We used the most recently published mid-transit time (2457805.170205 ± 0.000037) and period (1.75540569 ± 0.00000011) as our priors (Ivshina and Winn 2022). The ephemeris fitter calculated our updated mid-transit time to be 2457805.170208 ± 0.000036 BJD_TDB and our updated period to be 1.75540644 ± 0.00000016 days. The posterior plot distribution for our new mid-transit time and period are shown in Figure 4.

6. Results

Over time, the uncertainties of mid-transit times become stale, so, in order to accurately compare our mid-transit uncertainties to those published previously, it was necessary to forward-propagate the previously published mid-transit times to our newly updated mid-transit time. In order to do this, we used Equation (2) from Zellem *et al.* (2020):

$$\Delta T_{mid} = (n_{orbit}^2 \cdot \Delta P^2 + 2n_{orbit} \cdot \Delta P \Delta T_0 + \Delta T_0^2)^{1/2} \qquad (2)$$

Following Zellem *et al.* (2020), we dropped the second term of Equation 2 because none of the previous publications report their covariance term. This leads the propagated mid-transit uncertainties to be slightly underestimated. After forward-

[1] The ephemeris fitter can be found at https://colab.research.google.com/drive/1T5VT2gZ-ip6K6T9IXqMzQdSiEaf-UbJn?usp=sharing

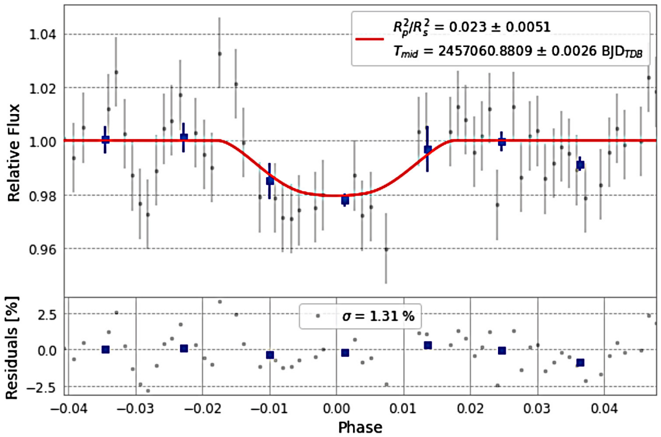

Figure 2. Sample light curve that was reduced from data taken on 2015-02-07. The gray points represent data from each image in the data set. The blue points represent the average of a set of binned data points, used to fit the light curve.

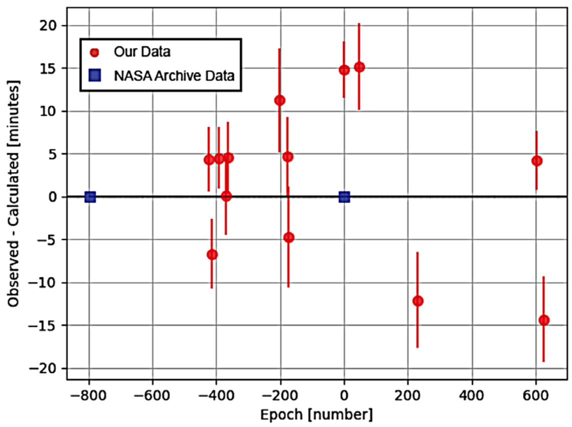

Figure 3. O–C plot for WASP-104 b using t_0 = 2457805.170205 BJD_TDB and P = 1.75540569 days.

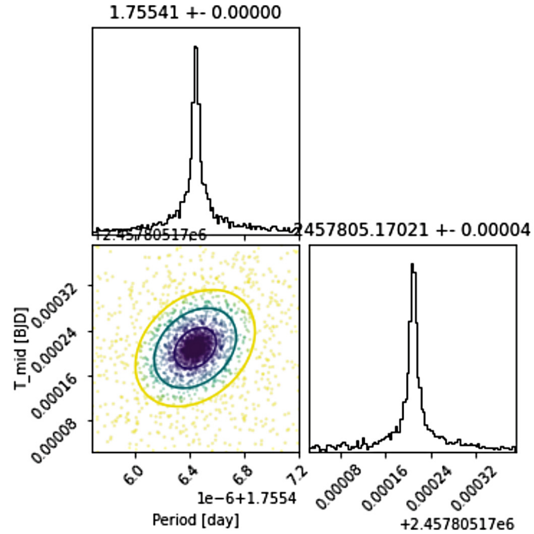

Figure 4. Posterior plot distribution of our new mid-transit time and period. The data points are color-coded to the likelihood of each fit, with darker colors indicating a higher likelihood.

Table 3. Values from the NASA Exoplanet Archive used in the creation of the O–C plot.

Citation	*Mid-transit (BJD_TBD)*	*Mid-transit Uncertainty (d)*
Smith *et al.* (2014)	2456406.11126	0.00012
Ivshina and Winn (2022)	2457805.170205	0.000037

Table 4. Updated Ephemerides.

Citation	*Mid-transit (BJD_TBD)*	*Mid-transit Uncertainty (d)*	*Propagated Mid-transit Uncertainty (d)*	*Period (d)*	*Period Uncertainty (d)*
Our data	2457805.170208	0.000036	N/A	1.75540644	0.00000016
Smith *et al.* (2014)	2456406.11126	0.00012	0.0014	1.7554137	+0.0000018 −0.0000036
Kokori *et al.* (2022a)	2457048.59061	0.00016	0.00021	1.7554060	0.0000003
Ivshina and Winn (2022)	2457805.170205	0.000037	0.000037	1.75540569	0.00000011

propagating the mid-transit times published by Smith *et al.* (2014), Kokori *et al.* (2022a), and Ivshina and Winn (2022), we found the new times to be 2456406.11126 ± 0.0014, 2457048.59061 ± 0.00021, and 2457805.170205 ± 0.000037, respectively. The Ivshina and Winn (2022) mid-transit uncertainty remains unchanged due to how recently it was calculated. Our updated mid-transit time, mid-transit uncertainty, period, and period uncertainty for WASP-104 b are presented in Table 4 along with the original mid-transit times and mid-transit uncertainty values from Smith *et al.* (2014), Kokori *et al.* (2022a), and Ivshina and Winn (2022) and their respective propagated mid-transit uncertainties. Comparing these propagated mid-transit times to our updated mid-transit time, we have decreased the mid-transit uncertainty by 97.4% since the discovery paper (Smith *et al.* 2014). We also decreased the Kokori *et al.* (2022) mid-transit uncertainty by 82.9% and nearly matched the results from Ivshina and Winn (2022), slightly decreasing the mid-transit uncertainty by 2.7%. We also compared the uncertainty in our reported period to that reported by Smith *et al.* (2014), Kokori *et al.* (2022a), and Ivshina and Winn (2022). We decreased the period uncertainty from Smith *et al.* (2014) by 91% in the positive direction and 95.6% in the negative direction, decreased the period uncertainty from Kokori *et al.* (2022a) by 46.7%, and produced a slightly increased period uncertainty from Ivshina and Winn (2022) (by 45.5%).

Out of 52 data sets from Cecilia, we were able to reduce 13 light curves with an accuracy meeting or exceeding the three-sigma standard for a successful detection. In so doing, we managed to calculate mid-transit and period values for WASP-104 b with improved precision over previous results on the NASA Exoplanet Archive and rivaling those more recent results that relied on data from the orbital TESS telescope. We calculated our updated mid-transit time to be $2457805.170208 \pm 0.000036$ BJD_TDB and our updated period to be $1.75540644 \pm 0.00000016$ days.

The results achieved in the work done by the first-ever fully online research experience course that is documented here substantiate that the Exoplanet Watch model of using small-format terrestrial telescopes to gather observations and to process them through the EXOTIC pipeline is a cost-effective alternative to observations with large terrestrial and space telescopes. The changes in the ephemerides of WASP-104 b over the past few years illustrate the need to regularly refresh them, and the use of a low-cost solution for the required observations, as shown here, is a logical path to achieving this goal.

In addition to the value of the data, the results of this study imply the value for small ground-based telescope photometry by citizen and amateur astronomers. Within a short amount of time, amateur astronomers around the world are able to reduce light curves, analyze the data, and present findings that are a benefit to the science community. The updating of ephemerides is a key part of future observations by large telescopes. Space-based telescopes like the NASA Transiting Exoplanet Survey Satellite (TESS) can update the ephemerides of many planets with higher precision. With the number of current and future scientists studying exoplanets on the rise, we need a reliable process to accomplish these updates. Our method can be continued regardless of current space missions, budget, and availability of observing time.

The network of amateur astronomers participating with Exoplanet Watch and using EXOTIC have grown substantially, and it is a powerful tool for the study of extrasolar planets. Furthermore, Exoplanet Watch's network has the ability to be fluid and quickly coordinate observations and data reduction without long waits during the process of applying for a space-based or a large ground-based telescope's time. There are planets whose transit time is longer than observing time from any location. With the coordination of Exoplanet Watch's network around the world, an entire transit can be observed with such planets as shown (Zellem *et al.* 2020).

7. Conclusion

With 52 nights of observation from the MicroObservatory, collected with a 6-inch ground-based robotic telescope and using the reduction tool EXOTIC, we present 13 significant light curves as well as an updated mid-transit time and period for WASP-104 b. We were able to decrease the uncertainties in the mid-transit time and period compared to those published previously this year (Kokori *et al.* 2022) as well as achieve nearly identical mid-transit time and period uncertainties as those obtained using data from TESS (Ivshina and Winn 2022). The comparison of our updated ephemerides to recently published results demonstrates the importance of citizen science groups like Exoplanet Watch and the capabilities of small ground-based telescopes.

The work done in this paper was performed in the first fully online CURE for astronomy majors. Online course and degree programs make higher education accessible to a more diverse learner population (e.g. women, veterans, parents, persons with disabilities, students with full-time jobs, and students of color). The success of the first offering of Arizona State University's Exoplanet Research Experience demonstrates the importance of undergraduate research experiences. The educational benefits and affective outcomes of participation in this online CURE will be addressed in a future paper.

This project validated several paradigms in exoplanet astronomy and astronomy education and, in the process, confirmed the conjunction of these paradigms. This included (1) the use of the small terrestrial telescopes in the Exoplanet Watch network, (2) the use of EXOTIC as a reduction pipeline for exoplanet transit data, and (3) a large-scale collaborative approach to learning the concepts and tools that are used in the identification and ephemerides refreshment of exoplanets.

8. Acknowledgements

These observations were conducted with MicroObservatory, a robotic telescope network maintained and operated as an educational service by the Center for Astrophysics | Harvard & Smithsonian. MicroObservatory is supported by NASA's Universe of Learning under NASA award number NNX16AC65A to the Space Telescope Science Institute.

This publication makes use of data products from Exoplanet Watch, a citizen science project managed by NASA's Jet Propulsion Laboratory on behalf of NASA's Universe of Learning. This work is supported by NASA under award number NNX16AC65A to the Space Telescope Science Institute, in partnership with Caltech/IPAC, Center for Astrophysics|Harvard & Smithsonian, and NASA Jet Propulsion Laboratory.

This research has made use of the NASA Exoplanet Archive, which is operated by the California Institute of Technology, under contract with the National Aeronautics and Space Administration under the Exoplanet Exploration Program.

This work is supported by the National Science Foundation (NSF) under grant #IUSE 2121225

Part of the research was carried out at the Jet Propulsion Laboratory, California Institute of Technology, under contract with the National Aeronautics and Space Administration.

References

AAVSO. 2023, Variable Star Plotter
(VSP; https://www.aavso.org/apps/vsp/).

Bonomo, A. S., *et al.* 2017, *Astron. Astrophys.*, **602A**, 107.

Drier, C. 2021, Planetary.org
(https://www.planetary.org/articles/cost-of-the-jwst).

Ivshina, E. S., and Winn, J. N. 2022, *Astrophys. J., Suppl. Ser.*, **259**, 62.

Kokori, A., Tsiaras, A., Edwards, B., *et al.* 2022a, *Astrophys. J., Suppl. Ser.*, **258**, 40.

Kokori, A., *et al.* 2022b, *Exp. Astron.,* **53**, 547.

Sadler, P. M., *et al.* 2001, *J. Sci. Education Technol.*, **10**, 39.

Sienkiewicz, F. 2022, private communication (August 6, 2022).

Smith, A. M., *et al.* 2014, *Astron. Astrophys.*, **570A**, 64.

Yeung, P., Perian, Q., Robertson, P., Fitzgerald, M., Fowler, M., and Sienkiewicz, F. 2022. *J. Korean Astron. Soc.*, **55**, 111.

Zellem, R., *et al.* 2020, *Publ. Astron. Soc. Pacific*, **132**, 054401.

Appendix A: Significant detections of WASP-104 b

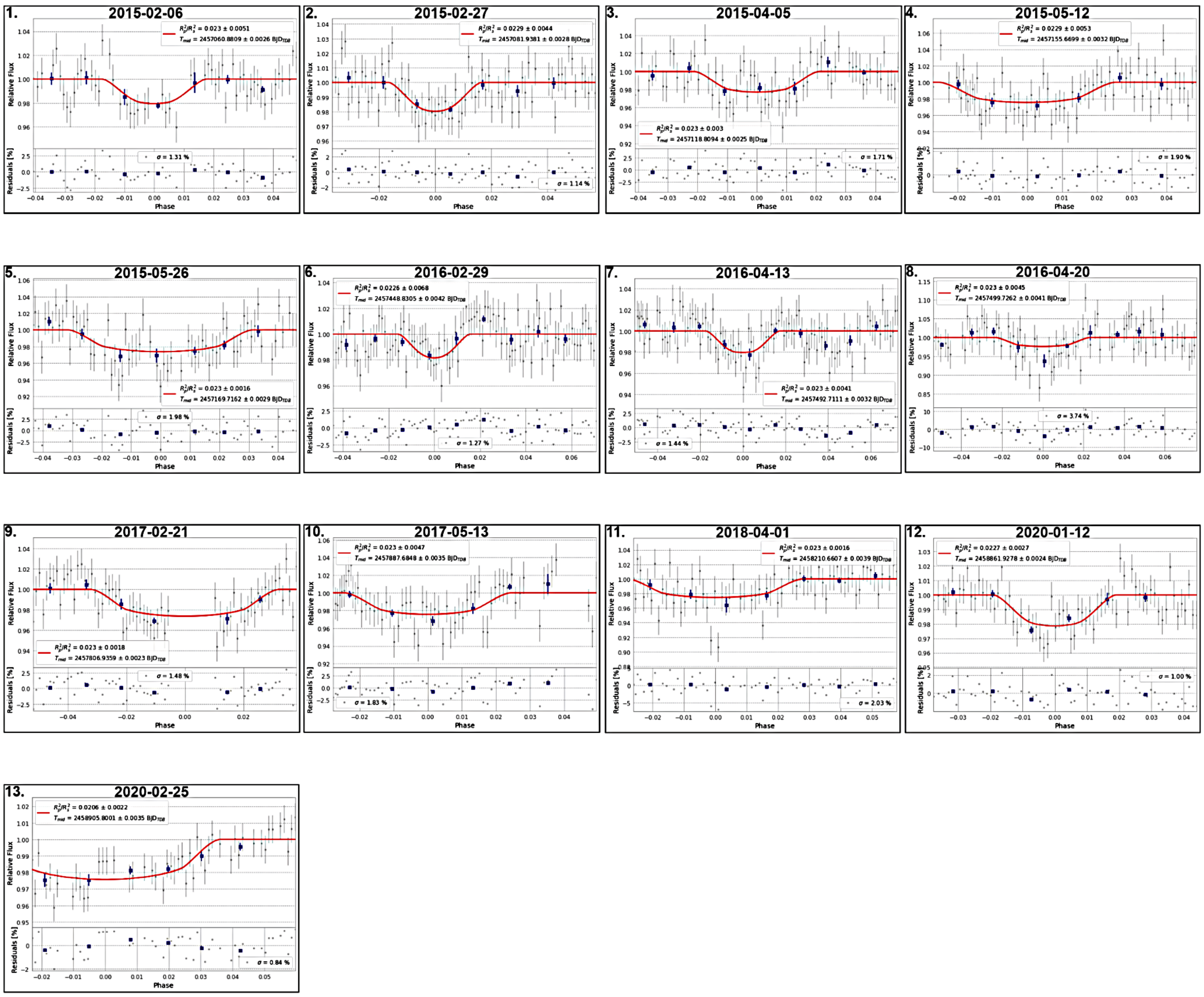

Figure A1. Light curves from this study.

Long-term Study of Changes in the Orbital Periods of 18 Eclipsing SW Sextantis Stars

David Boyd
West Challow Observatory, OX12 9TX, UK; davidboyd@orion.me.uk

Received April 8, 2023; revised May 18, 2023; accepted May 19, 2023

Abstract SW Sex stars are an informal sub-class of eclipsing nova-like cataclysmic variables. We report 934 new eclipse times measured over the past 17 years for HS 0728+6738 (V482 Cam), SW Sex, DW UMa, HS 0129+2933 (TT Tri), V1315 Aql, PX And, HS 0455+8315, HS 0220+0603, BP Lyn, BH Lyn, LX Ser, UU Aqr, V1776 Cyg, RW Tri, 1RXS J064434.5+334451, AC Cnc, V363 Aur, and BT Mon. When combined with published eclipse times going back in some cases many decades, we show that these binary systems exhibit a range of behaviors, including increasing, decreasing, and possibly oscillating orbital periods. Nevertheless, the duration of these observations is still not long enough to be able to make reliable quantitative statements about their long term behaviors. In addition to these long term trends, we also observed rapid and unusual decreases in the orbital periods of SW Sex and RW Tri during 2017 and 2018, respectively.

1. The SW Sex phenomenon

Nova-like variables are a sub-category of cataclysmic variables (CVs) in which the transfer of hydrogen-rich material from the main sequence secondary star to the white dwarf primary via Roche lobe overflow is sustained at a high rate. This maintains the accretion disc around the primary in a bright state and inhibits the disc instability mechanism responsible for dwarf nova outbursts. The majority of nova-like variables have binary orbital periods longer than 3 hours, which places them above the period gap and in the regime where magnetic braking progressively shrinks the binary orbit and drives mass transfer. Further information on CVs can be found in Patterson (1984), Warner (1995), and Hellier (2001).

The name SW Sex stars was first introduced in Thorstensen *et al.* (1991) to characterise a range of observational properties shared by a number of eclipsing nova-like variables which displayed complex and unusual spectral variation with orbital phase. Prototypes of this informal sub-class were SW Sex, DW UMa, PX And, and V1315 Aql. Honeycutt *et al.* (1986) first noticed that SW Sex (known at the time as PG 1012-029) showed deep eclipses in its continuum but hardly at all in its emission lines, suggesting the presence of a bipolar wind emanating from the accretion disk. Several more so-called SW Sex stars were first identified as variables in the Hamburg Quasar Survey (Hagen *et al.* 1995). The observational characteristics of SW Sex stars are described in Hoard *et al.* (2003). Although initially quite narrow, the definition of SW Sex stars now encompasses most nova-like CVs above the period gap with high mass transfer rates. For a review of our knowledge of the SW Sex phenomenon see Schmidtobreick (2015) and references therein.

SW Sex stars with high orbital inclinations experience deep eclipses which provide a means to measure and monitor their orbital periods. Two motivations for this study, which began in 2006, were to produce accurate eclipse ephemerides for predicting future eclipse times and to investigate if any of the stars deviated from the linear ephemeris expected for a constant orbital period. Several of these stars had not been observed systematically for many years and by combining published data on eclipse times going back in some cases over many decades with new eclipse measurements, their ephemerides could be updated and the stability of their orbital periods investigated.

We chose 18 SW Sex stars which are deeply eclipsing, observable from the UK, and bright enough to yield accurate eclipse times with amateur-sized telescopes. These are listed in Table 1 with their mean orbital periods and the time span of available observations including new results reported here. All have orbital periods above the period gap. One member of the group, BT Mon, experienced a nova outburst in 1939 and a nova shell has since been observed (Duerbeck 1987). Nova shells have also been imaged around V1315 Aql (Sahman *et al.* 2015) and AC Cnc (Shara *et al.* 2012), evidence of nova eruptions several hundred years ago. AC Cnc and BT Mon have two of the longest orbital periods in the group.

An initial report covering the period 2006 to 2012 was published in the *Journal of the AAVSO* (Boyd 2012), hereafter referred to as Paper 1. Here we report on a continuation of this study to 2023 and present results which now cover a 17-year period.

2. Measuring new eclipse times

Predicted times of primary eclipses were obtained from the ephemerides in Paper 1 and a time-series of images of the field of each star obtained starting well before and ending well after these predicted eclipse times to allow for possible variation in orbital period. All images were made unfiltered to maximize photon statistics with either a 0.25-m or 0.35-m Schmidt-Cassegrain Telescope (SCT) and an SXV-H9 (later SXVR-H9) CCD camera located at West Challow Observatory near Oxford, UK. Image scales with these telescopes were 1.45 and 1.21 arcsec/pixel, respectively. Images were dark subtracted and flat fielded and a magnitude for the star was measured in each image using differential aperture photometry with respect to an ensemble of between three and five nearby comparison stars. Comparison star V band magnitudes with errors were obtained from AAVSO charts or from catalogues available at the start of the study. The same comparison star magnitudes and analysis procedures have been used for each star throughout the study to maintain consistency. A list of comparison stars used for each variable is given in Table 2. If we were starting the project today, we would choose comparison stars from the AAVSO Photometric All-Sky Survey (Henden *et al.* 2018). The photometry error for each star was calculated using the CCD Equation (Howell 2006). For each comparison star this error was then added in quadrature with the comparison chart magnitude error and a weighted mean magnitude zero point and error was computed for the image. This was then used to compute the magnitude and error of the variable star for that image.

A quadratic polynomial was fitted to the lower section of each eclipse in order to find the time of minimum which was expressed as a Heliocentric Julian Date (HJD). An associated analytical error in the time of minimum was derived from uncertainties in the magnitude measurements. The section of the eclipse used for the polynomial fit was normally between the points of maximum slope of the eclipse ingress and egress. Figure 1 shows examples of eclipse profiles. Uncertainties in individual magnitude measurements are generally smaller than the plotted mark. Some eclipses have rounded minima, some are V-shaped, while others exhibit random fluctuations in light output throughout the eclipse, indicating that the source of these fluctuations has not been eclipsed. Irregular eclipse profiles are more difficult to measure and this can lead to larger uncertainties in measured times of minimum. In what follows we will refer to these uncertainties as errors.

It was generally found that analytical errors from the quadratic fits underestimated the real uncertainty in eclipse times. The scatter in eclipse times for each star over a short interval during which the eclipse times were likely to have varied linearly was examined and the analytical errors scaled to make them consistent with the observed scatter about the linear trend. For stars with the smoothest eclipses, a scaling factor of 3 gave errors consistent with the scatter of eclipse times, while for eclipses with the largest fluctuations a factor of 7 was required. This scaling factor was generally found to be consistent for each star throughout the study.

A total of 898 new eclipse times for the 18 stars in this study have been observed and measured by the author. The number of new eclipse times for each star are listed in Table 1. Based on the ephemerides in Paper 1, cycle numbers were assigned to each new eclipse. Measured eclipse times with errors and corresponding cycle numbers for each of the 18 stars are listed in Tables 3.1 to 3.18. For completeness we also include here the eclipse times given in Paper 1. A further 36 eclipse times for LX Ser were measured by the author from observations of LX Ser by Cook and Dvorak in the AAVSO International Database (Kafka 2021). These are listed in Table 4.

3. Published eclipse times

Altogether 1338 eclipse times for these 18 stars were found in more than 40 published papers and in many issues of *Information Bulletin on Variable Stars* (IBVS), *Bulletin of the Variable Star Observers League in Japan* (BVSOLJ), and *Open European Journal on Variable Stars* (OEJV). The numbers of published eclipse times for each star are listed in Table 1 and the sources of published eclipse times are given in Table 5. We have not included these already published times here for reasons of space. All times of minimum were expressed in HJD for consistency, including some times originally reported in Barycentric Julian Date (BJD). In several cases errors for these eclipse times were not specified in the literature or the errors given were clearly unrealistically small given the observed spread in eclipse times. In these cases we needed to make a realistic estimate of the error in these eclipse times so they could be included in our analysis with appropriate weights. Each such data set was considered separately and the root-mean-square (rms) residual of all the times in that set calculated with respect to a locally fitted linear ephemeris. This value was then assigned as an error to all the eclipse times in that set.

We found that eclipse times derived from photographic plates generally had a large scatter compared to electronically measured times and in practice did not provide a constraint on fitting an ephemeris, so we decided not to include these in this analysis. Eclipse times for RW Tri in Smak (1995) appeared very discrepant with other times reported around the same period and therefore have not been included in this analysis.

4. O–C analysis

Each observed eclipse time of minimum was given a weight equal to the inverse square of its assigned error. A weighted linear fit of all available eclipse times vs cycle numbers was calculated for each star. This linear ephemeris was used to produce a calculated time for each eclipse. The linear term in the ephemeris is the mean binary orbital period of the star over the time interval spanned by the observations. Observed minus calculated (O–C) times for each eclipse were then plotted vs cycle number to produce an O–C diagram for each star.

An apparently linear trend in an O–C diagram is consistent with a constant orbital period, while O–C trajectories curving upward indicate the orbital period is increasing and curving downward that the orbital period is decreasing. In most cases we also calculated a weighted quadratic fit to the O–C values. This quadratic ephemeris gave a mean rate of change of orbital period. In some cases, there was a suggestion of sinusoidal variation relative to a linear ephemeris or quadratic ephemeris. In these cases, a weighted sinusoidal fit was calculated with respect to the linear or quadratic ephemeris.

Table 6 gives weighted linear ephemerides for each star computed as described above. SW Sex experienced a large change in its behavior in 2017 and two linear ephemerides are given for before and after this change. Table 7 gives weighted quadratic ephemerides and mean rates of period change for stars where these were calculated.

Our effort to make the weights used in these fits more realistic will inevitably have introduced an element of subjectivity. Therefore we do not compute a quantitative goodness of fit metric such as a reduced chi-squared for each fit as this would not be an objective basis for evaluating fit quality. This is particularly true in the case of a nonlinear model where there are recognized problems in interpreting such a metric (Andrae *et al.* 2010).

Table 1. Eclipsing SW Sex stars in this study.

Star name	*P_{orb} (hours)*	*Time span of obs. (years)*	*New eclipse times measured in this study*	*Previously published eclipse times*
HS 0728+6738 = V482 Cam	3.21	20	44	13
SW Sex = PG 1012-029	3.24	43	49	131
DW UMa = PG1030+590	3.28	39	58	596
HS 0129+2933 = TT Tri	3.35	20	42	30
V1315 Aql	3.35	38	51	80
PX And = PG0027+260	3.51	31	45	44
HS 0455+8315	3.57	21	44	9
HS 0220+0603	3.58	20	37	13
BP Lyn = PG0859+415	3.67	32	45	16
BH Lyn = PG0818+513	3.74	31	43	33
LX Ser = Stepanyan's Star	3.80	42	82 *	74
UU Aqr	3.93	37	53	53
V1776 Cyg = Lanning 90	3.95	35	58	11
RW Tri	5.57	65	58	151
1RXS J064434.5+334451	6.47	18	70	36
AC Cnc	7.21	41	49	19
V363 Aur = Lanning 10	7.71	42	62	19
BT Mon	8.01	45	44	10
Total		616	934	1338

*Note: * Includes 36 eclipse times for LX Ser measured by the author from observations of LX Ser by Cook and Dvorak in the AAVSO International Database.*

Table 2. Comparison stars used to measure the time of minimum for each star.

Star Name	*Comparison Stars Used*
HS 0728+6738 = V482 Cam	GSC 4360 0033, GSC 4124 0603
SW Sex = PG 1012-029	GSC 4907 1166, GSC 4907 0207, 2MASS J10145841-0305432
DW UMa = PG1030+590	GSC 3822 0070, GSC 3822 0983, GSC 3822 1157
HS 0129+2933 = TT Tri	GSC 1755 0855, GSC 1755 0871, GSC 1755 0942, GSC 1755 0926, GSC 1755 0982
V1315 Aql	GSC 1049 1329, GSC 1049 1288, GSC 1049 0464
PX And = PG0027+260	GSC 1734 0906, GSC 1734 1620, GSC 1734 0752
HS 0455+8315	GSC 4617 1102, GSC 4617 0542, 2MASS J05071087+8318101, 2MASS J05084059+8316305, 2MASS J 05041189+8321282
HS 0220+0603	GSC 0045 1418, GSC 0045 0338, GSC 0045 1226, GSC 0045 1400, GSC 0045 0626
BP Lyn = PG0859+415	GSC 2986 1255, GSC 2986 1258, GSC 2986 1413, GSC 2986 1427
BH Lyn = PG0818+513	GSC 3421 1055, GSC 3421 0865, GSC 3421 1015
LX Ser = Stepanyan's Star	GSC 1497 1576, GSC 1497 0962, GSC 1497 1643, [HH95] LX Ser-4, [HH95] LX Ser-8
UU Aqr	TYC 5227 0328, GSC 5227 0662, GSC 5227 0399, GSC 5227 0982
V1776 Cyg = Lanning 90	GSC 3572 1508, 2MASS J20234934+4629294, 2MASS J20234988+4632359, 2MASS J20231931+4629502, 2MASS J20233377+4634165
RW Tri	GSC 1774 0082, GSC 1178 0469, GSC 1774 0357, GSC 1774 0002
1RXS J064434.5+334451	[SGH2007] J0644-R, [SGH2007] J0644-S, [SGH2007] J0644-E, [SGH2007] J0644-G, [SGH2007] J0644-M
AC Cnc	GSC 0816 1525, GSC 0816 1021, GSC 0816 1547, GSC 0816 0998, GSC 0816 0862
V363 Aur = Lanning 10	[HH95] V363 Aur-04, [HH95] V363 Aur-19, [HH95] V363 Aur-03
BT Mon	GSC 4803 0262, 2MASS J06433904-0204189, 2MASS J06435331-0202124, 2MASS J06433839-0203003

Note: [HH95] = Henden and Honeycutt (1995), [SGH2007] = Sing et al. (2007)

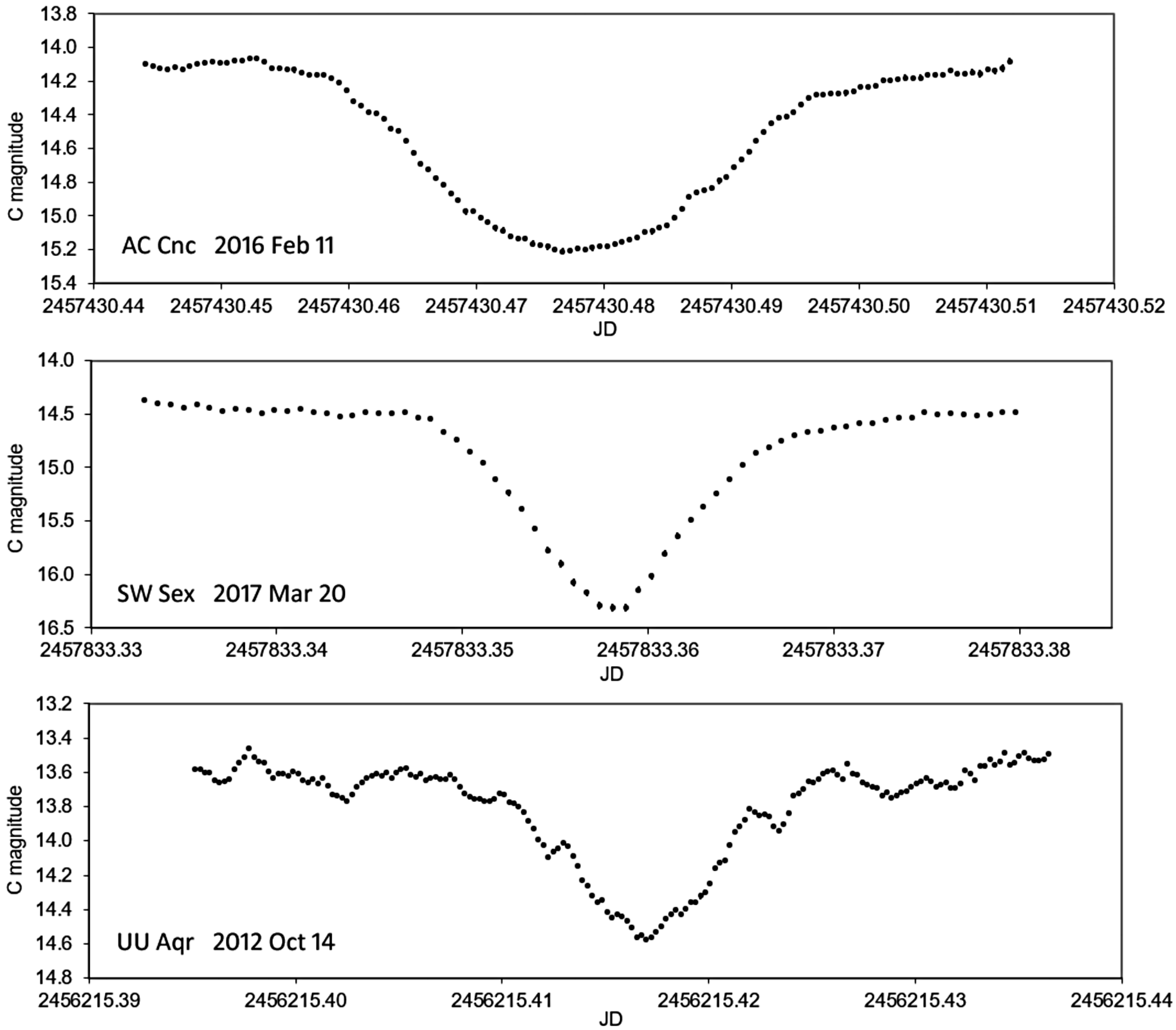

Figure 1. Examples of eclipse profiles. Uncertainties in individual magnitude measurements are generally smaller than the plotted mark.

Table 3.1. Eclipse times, errors and cycle numbers for HS 0728+6738 observed and measured by the author in this study.

Eclipse time (HJD)	*Error (d)*	*Cycle Number*
2453810.40077	0.00041	13539
2453836.45653	0.00024	13734
2453851.42254	0.00023	13846
2453853.42648	0.00013	13861
2454174.51418	0.00022	16264
2454181.32859	0.00025	16315
2454185.33706	0.00025	16345
2454186.40643	0.00024	16353
2454473.42029	0.00023	18501
2454493.33001	0.00023	18650
2454507.35967	0.00039	18755
2454835.39541	0.00032	21210
2454891.38182	0.00010	21629
2454895.39084	0.00009	21659
2454907.41644	0.00022	21749
2455188.41832	0.00021	23852
2455191.35834	0.00014	23874
2455200.31029	0.00019	23941
2455515.38459	0.00024	26299
2455520.32865	0.00038	26336
2455533.42346	0.00028	26434
2455889.38551	0.00036	29098
2455891.39036	0.00024	29113
2455893.39432	0.00019	29128
2456267.39501	0.00019	31927
2456271.40415	0.00015	31957
2456298.39531	0.00018	32159
2456725.30918	0.00035	35354
2457017.40117	0.00013	37540
2457020.34099	0.00034	37562
2457442.31106	0.00011	40720
2457443.38007	0.00017	40728
2458099.31749	0.00018	45637
2458103.45938	0.00016	45668
2458106.26552	0.00040	45689
2458444.32328	0.00034	48219
2458477.32701	0.00022	48466
2458493.36113	0.00005	48586
2458784.38450	0.00022	50764
2458806.29770	0.00031	50928
2458817.25411	0.00029	51010
2459149.43247	0.00024	53496
2459157.44964	0.00016	53556
2459159.32000	0.00023	53570

Table 3.2. Eclipse times, errors and cycle numbers for SW Sex observed and measured by the author in this study.

Eclipse time (HJD)	*Error (d)*	*Cycle Number*
2454185.43702	0.00044	72965
2454186.38145	0.00029	72972
2454553.41407	0.00048	75692
2454564.34410	0.00020	75773
2454906.41325	0.00019	78308
2454907.49269	0.00019	78316
2455260.35696	0.00018	80931
2455278.43821	0.00012	81065
2455630.35814	0.00026	83673
2455660.44910	0.00014	83896
2455662.33853	0.00028	83910
2455992.39775	0.00022	86356
2456005.48662	0.00010	86453
2456008.45550	0.00018	86475
2456343.50779	0.00012	88958
2456354.43764	0.00013	89039
2456356.46180	0.00016	89054
2456728.35219	0.00019	91810
2456739.41702	0.00013	91892
2457118.45908	0.00019	94701
2457119.40351	0.00010	94708
2457461.33764	0.00017	97242
2457462.41694	0.00015	97250
2457465.38568	0.00024	97272
2457833.36314	0.00014	99999
2457835.38696	0.00014	100014
2457836.33134	0.00026	100021
2457837.41089	0.00015	100029
2457862.37464	0.00018	100214
2458191.48919	0.00009	102653
2458212.40447	0.00013	102808
2458214.42856	0.00010	102823
2458567.42678	0.00008	105439
2458571.33929	0.00016	105468
2458575.38787	0.00011	105498
2458584.42857	0.00009	105565
2458585.37339	0.00014	105572
2458931.35406	0.00015	108136
2458932.43393	0.00010	108144
2458933.37801	0.00029	108151
2459281.38341	0.00015	110730
2459282.46286	0.00017	110738
2459291.36857	0.00011	110804
2459677.42673	0.00014	113665
2459683.36420	0.00025	113709
2459685.38844	0.00021	113724
2460052.42102	0.00008	116444
2460054.44524	0.00011	116459
2460064.43065	0.00028	116533

Table 3.3. Eclipse times, errors and cycle numbers for DW UMa observed and measured by the author in this study.

Eclipse time (HJD)	*Error (d)*	*Cycle Number*
2454181.41978	0.00019	58214
2454185.38111	0.00029	58243
2454224.45051	0.00043	58529
2454473.34780	0.00038	60351
2454564.46466	0.00020	61018
2454580.44785	0.00033	61135
2454580.58433	0.00026	61136
2454588.37104	0.00028	61193
2454588.50711	0.00019	61194
2454593.42488	0.00022	61230
2454596.43092	0.00033	61252
2454884.39723	0.00024	63360
2454892.32009	0.00025	63418
2455239.30026	0.00021	65958
2455263.34322	0.00014	66134
2455270.31000	0.00013	66185
2455278.37037	0.00017	66244
2455627.39978	0.00017	68799
2455628.35604	0.00020	68806
2455629.31205	0.00029	68813
2455991.45632	0.00028	71464
2456029.43254	0.00029	71742
2456033.39472	0.00022	71771
2456088.44663	0.00035	72174
2456382.42440	0.00027	74326
2456384.47293	0.00013	74341
2456399.36316	0.00039	74450
2456413.43361	0.00024	74553
2456728.44826	0.00015	76859
2456739.37663	0.00011	76939
2457020.37615	0.00026	78996
2457021.46907	0.00019	79004
2457075.42859	0.00021	79399
2457106.43843	0.00010	79626
2457108.35065	0.00012	79640
2457108.48716	0.00020	79641
2458174.42888	0.00017	87444
2458188.36286	0.00021	87546
2458191.36841	0.00019	87568
2458227.43235	0.00020	87832
2458231.39341	0.00016	87861
2458234.39877	0.00035	87883
2458539.44267	0.00039	90116
2458540.39817	0.00023	90123
2458541.35463	0.00015	90130
2458571.40737	0.00012	90350
2458585.34131	0.00025	90452
2458593.40129	0.00019	90511
2458855.41318	0.00034	92429
2458861.42412	0.00031	92473
2458868.39096	0.00013	92524
2458948.44193	0.00028	93110
2459258.40274	0.00058	95379
2459268.37535	0.00016	95452
2459272.33702	0.00017	95481
2459597.32418	0.00032	97860
2459599.37245	0.00018	97875
2459600.32970	0.00029	97882
2459968.34763	0.00022	100576
2459975.31458	0.00022	100627
2459989.38528	0.00017	100730

Note: The Tables 3.1 through 3.18 are available through the AAVSO ftp site at ftp://ftp.aavso.org/public/datasets/3882-Boyd-511-swsex.txt (if necessary, copy and paste link into the address bar of a web browser).

Table 3.4. Eclipse times, errors and cycle numbers for HS0129+2933 observed and measured by the author in this study.

Eclipse time (HJD)	*Error (d)*	*Cycle Number*
2454061.46332	0.00014	10892
2454081.29219	0.00016	11034
2454086.45848	0.00008	11071
2455106.37036	0.00038	18375
2455188.47729	0.00030	18963
2455191.27007	0.00019	18983
2455460.49099	0.00013	20911
2455533.38206	0.00022	21433
2455827.45860	0.00014	23539
2455835.41776	0.00016	23596
2455836.39518	0.00010	23603
2456200.43010	0.00037	26210
2456215.37178	0.00019	26317
2456237.29459	0.00022	26474
2456527.46137	0.00028	28552
2456611.38335	0.00017	29153
2456901.41023	0.00021	31230
2456904.48240	0.00024	31252
2457258.46323	0.00012	33787
2457276.47630	0.00017	33916
2457624.45255	0.00033	36408
2457631.43448	0.00018	36458
2458029.40123	0.00026	39308
2458054.39650	0.00011	39487
2458056.35143	0.00013	39501
2458362.43603	0.00029	41693
2458363.41333	0.00016	41700
2458388.40829	0.00022	41879
2458721.44286	0.00017	44264
2458741.41060	0.00012	44407
2458759.42431	0.00004	44536
2458773.38793	0.00031	44636
2458906.32283	0.00025	45588
2459105.44446	0.00018	47014
2459106.42148	0.00027	47021
2459107.39970	0.00014	47028
2459523.37876	0.00015	50007
2459526.31147	0.00011	50028
2459541.39281	0.00015	50136
2459914.36388	0.00021	52807
2459921.34628	0.00025	52857
2459928.32801	0.00018	52907

Table 3.5. Eclipse times, errors and cycle numbers for V1315 Aql observed and measured by the author in this study.

Eclipse time (HJD)	*Error (d)*	*Cycle Number*
2454272.50437	0.00018	59916
2454306.44865	0.00027	60159
2454313.43262	0.00072	60209
2454651.48330	0.00048	62629
2454670.48100	0.00046	62765
2454810.31097	0.00082	63766
2455004.47952	0.00029	65156
2455006.43480	0.00049	65170
2455038.42351	0.00055	65399
2455052.39293	0.00070	65499
2455463.36184	0.00047	68441
2455464.33978	0.00036	68448
2455490.32143	0.00026	68634
2455777.38468	0.00040	70689
2455783.39087	0.00040	70732
2455903.24546	0.00047	71590
2456131.49866	0.00042	73224
2456149.51903	0.00035	73353
2456150.49660	0.00023	73360
2456215.31256	0.00061	73824
2456446.49995	0.00064	75479
2456453.48465	0.00056	75529
2456478.48866	0.00025	75708
2456838.47024	0.00025	78285
2456845.45485	0.00023	78335
2456895.46344	0.00033	78693
2457177.49766	0.00035	80712
2457184.48150	0.00042	80762
2457203.47971	0.00026	80898
2457293.30101	0.00042	81541
2457303.35804	0.00028	81613
2457563.46136	0.00028	83475
2457587.48793	0.00021	83647
2457590.42138	0.00019	83668
2457960.46038	0.00063	86317
2457971.49598	0.00025	86396
2457978.48056	0.00023	86446
2458294.45908	0.00057	88708
2458295.43676	0.00018	88715
2458314.43516	0.00027	88851
2458655.41791	0.00044	91292
2458665.47589	0.00053	91364
2458666.45373	0.00030	91371
2459024.47947	0.00032	93934
2459025.45740	0.00032	93941
2459033.41968	0.00041	93998
2459365.46204	0.00035	96375
2459366.44091	0.00031	96382
2459379.43190	0.00044	96475
2459744.44107	0.00062	99088
2459756.45506	0.00023	99174
2459757.43293	0.00059	99181

Table 3.6. Eclipse times, errors and cycle numbers for PX And observed and measured by the author in this study.

Eclipse time (HJD)	*Error (d)*	*Cycle Number*
2454318.44729	0.00051	34708
2454319.47234	0.00046	34715
2454325.47261	0.00036	34756
2454448.40773	0.00061	35596
2454473.28943	0.00051	35766
2454503.29163	0.00022	35971
2454761.45718	0.00049	37735
2454770.38547	0.00069	37796
2455064.40680	0.00108	39805
2455066.45577	0.00069	39819
2455173.29503	0.00032	40549
2455186.32065	0.00020	40638
2455188.36884	0.00125	40652
2455191.29553	0.00055	40672
2455201.24653	0.00014	40740
2455460.43876	0.00028	42511
2455495.26963	0.00061	42749
2455515.46733	0.00025	42887
2455795.43984	0.00024	44800
2455819.44115	0.00069	44964
2455823.39248	0.00044	44991
2455901.25250	0.00064	45523
2456149.46690	0.00038	47219
2456159.41895	0.00035	47287
2456215.32501	0.00053	47669
2456512.42294	0.00048	49699
2456518.42177	0.00083	49740
2456609.45353	0.00040	50362
2456611.35720	0.00069	50375
2456908.45223	0.00028	52405
2456922.35622	0.00047	52500
2457271.40745	0.00041	54885
2457275.50498	0.00026	54913
2457615.48272	0.00042	57236
2457624.41054	0.00047	57297
2457994.38914	0.00082	59825
2457996.43794	0.00026	59839
2457997.46265	0.00064	59846
2458362.46761	0.00038	62340
2458379.44407	0.00025	62456
2458759.37448	0.00018	65052
2458806.35537	0.00021	65373
2458817.33089	0.00013	65448
2459114.42636	0.00047	67478
2459148.38126	0.00068	67710

Table 3.7. Eclipse times, errors and cycle numbers for HS 0455+8315 observed and measured by the author in this study.

Eclipse time (HJD)	*Error (d)*	*Cycle Number*
2454061.40139	0.00016	14807
2454063.48351	0.00020	14821
2454078.35643	0.00014	14921
2454112.41335	0.00017	15150
2454114.49593	0.00023	15164
2454115.38831	0.00017	15170
2454895.44552	0.00018	20415
2454906.45070	0.00013	20489
2454907.34318	0.00026	20495
2455065.43666	0.00029	21558
2455495.39753	0.00032	24449
2455519.49112	0.00017	24611
2455526.48082	0.00018	24658
2455835.38030	0.00021	26735
2455850.40114	0.00018	26836
2456271.43853	0.00015	29667
2456274.41353	0.00029	29687
2456294.34258	0.00019	29821
2456538.39879	0.00012	31462
2456903.36710	0.00014	33916
2456908.42377	0.00027	33950
2457276.36680	0.00018	36424
2457291.38805	0.00021	36525
2457594.48734	0.00024	38563
2457609.50881	0.00016	38664
2458038.42837	0.00022	41548
2458039.32057	0.00017	41554
2458042.29484	0.00019	41574
2458385.40088	0.00027	43881
2458386.44190	0.00004	43888
2458719.43614	0.00012	46127
2458721.36860	0.00023	46140
2458784.42820	0.00020	46564
2458806.43966	0.00018	46712
2458911.43828	0.00015	47418
2458925.41820	0.00014	47512
2459041.42251	0.00017	48292
2459053.46929	0.00025	48373
2459056.44407	0.00010	48393
2459110.43117	0.00022	48756
2459117.42066	0.00011	48803
2459389.43726	0.00014	50632
2459414.42257	0.00010	50800
2459415.46405	0.00014	50807

Table 3.8. Eclipse times, errors and cycle numbers for HS 0220+0603 observed and measured by the author in this study.

Eclipse time (HJD)	*Error (d)*	*Cycle Number*
2454061.32109	0.00048	10038
2454081.31479	0.00032	10172
2454081.46403	0.00018	10173
2454086.38783	0.00026	10206
2455156.35608	0.00028	17377
2455188.43603	0.00027	17592
2455200.37262	0.00034	17672
2455490.43180	0.00028	19616
2455515.34977	0.00031	19783
2455533.40410	0.00029	19904
2455867.48013	0.00024	22143
2455884.48964	0.00012	22257
2456249.45127	0.00022	24703
2456250.49598	0.00015	24710
2456266.46118	0.00022	24817
2456609.34044	0.00042	27115
2456619.33720	0.00028	27182
2456955.50247	0.00033	29435
2456985.34355	0.00024	29635
2457354.48328	0.00027	32109
2457403.27389	0.00013	32436
2457407.30240	0.00016	32463
2457684.38159	0.00023	34320
2457698.40661	0.00021	34414
2458054.41601	0.00022	36800
2458082.31770	0.00022	36987
2458477.27022	0.00022	39634
2458492.34036	0.00031	39735
2458817.46349	0.00020	41914
2458819.40361	0.00011	41927
2458822.38782	0.00018	41947
2459158.40349	0.00019	44199
2459176.45724	0.00022	44320
2459189.43843	0.00018	44407
2459584.39131	0.00034	47054
2459597.37209	0.00038	47141
2459870.42209	0.00032	48971

Table 3.9. Eclipse times, errors and cycle numbers for BP Lyn observed and measured by the author in this study.

Eclipse time (HJD)	*Error (d)*	*Cycle Number*
2454186.44462	0.00069	41257
2454891.36892	0.00095	45870
2454906.49781	0.00084	45969
2455239.32473	0.00058	48147
2455260.41122	0.00042	48285
2455263.31415	0.00049	48304
2455571.38461	0.00074	50320
2455594.30701	0.00042	50470
2455619.52087	0.00059	50635
2455914.44759	0.00041	52565
2455930.34125	0.00063	52669
2455932.32762	0.00066	52682
2455942.41314	0.00039	52748
2455991.31277	0.00055	53068
2456016.37415	0.00052	53232
2456338.34928	0.00069	55339
2456343.39349	0.00056	55372
2456355.31121	0.00039	55450
2456356.38067	0.00034	55457
2456410.47808	0.00063	55811
2456415.36759	0.00065	55843
2456684.31780	0.00044	57603
2456728.32764	0.00126	57891
2457021.42236	0.00055	59809
2457059.32139	0.00083	60057
2457062.37785	0.00044	60077
2457433.40551	0.00051	62505
2457447.31156	0.00062	62596
2457455.41132	0.00026	62649
2457758.43751	0.00046	64632
2457778.30406	0.00037	64762
2458137.41551	0.00031	67112
2458161.40539	0.00031	67269
2458162.32198	0.00042	67275
2458163.39102	0.00040	67282
2458514.40265	0.00055	69579
2458517.30581	0.00051	69598
2458526.32134	0.00072	69657
2458539.31249	0.00049	69742
2458864.34320	0.00073	71869
2458886.34755	0.00040	72013
2458925.46891	0.00045	72269
2459240.41430	0.00037	74330
2459258.44656	0.00062	74448
2459271.43627	0.00051	74533

Table 3.10. Eclipse times, errors and cycle numbers for BH Lyn observed and measured by the author in this study.

Eclipse time (HJD)	*Error (d)*	*Cycle Number*
2454181.48914	0.00029	44915
2454186.32132	0.00042	44946
2454199.41436	0.00053	45030
2454482.32954	0.00048	46845
2454834.45234	0.00046	49104
2454884.33284	0.00052	49424
2455247.36666	0.00027	51753
2455260.46000	0.00033	51837
2455267.31793	0.00059	51881
2455594.34608	0.00035	53979
2455628.32676	0.00041	54197
2455670.41251	0.00040	54467
2455675.40111	0.00031	54499
2455895.34197	0.00038	55910
2455902.35570	0.00039	55955
2455941.32605	0.00040	56205
2455992.45237	0.00076	56533
2455994.32276	0.00053	56545
2455994.47949	0.00087	56546
2456028.45927	0.00021	56764
2456298.43632	0.00040	58496
2456356.42123	0.00032	58868
2456382.45272	0.00022	59035
2456699.34816	0.00027	61068
2456707.45398	0.00027	61120
2456726.47051	0.00038	61242
2457017.33447	0.00048	63108
2457020.45224	0.00043	63128
2457021.38791	0.00056	63134
2457433.36610	0.00032	65777
2457443.34252	0.00031	65841
2457460.48838	0.00021	65951
2457721.42424	0.00040	67625
2457727.34740	0.00043	67663
2458155.38234	0.00031	70409
2458163.33224	0.00019	70460
2458172.37306	0.00035	70518
2458840.45547	0.00035	74804
2458864.30434	0.00028	74957
2458868.35774	0.00038	74983
2459221.41548	0.00019	77248
2459238.40565	0.00017	77357
2459256.33224	0.00016	77472

Table 3.11. Eclipse times, errors and cycle numbers for LX Ser observed and measured by the author in this study.

Eclipse time (HJD)	*Error (d)*	*Cycle Number*
2454316.41420	0.00032	63266
2454628.52570	0.00023	65236
2454976.44297	0.00038	67432
2454994.50414	0.00026	67546
2455001.47525	0.00033	67590
2455037.43960	0.00020	67817
2455662.45627	0.00040	71762
2455663.40637	0.00045	71768
2455672.43730	0.00041	71825
2455778.42860	0.00031	72494
2456028.43528	0.00029	74072
2456076.44023	0.00042	74375
2456088.48102	0.00025	74451
2456384.43183	0.00028	76319
2456403.44388	0.00026	76439
2456410.41513	0.00047	76483
2456412.47433	0.00021	76496
2456782.41518	0.00010	78831
2456792.39591	0.00050	78894
2456798.41635	0.00018	78932
2457134.45163	0.00014	81053
2457159.48411	0.00019	81211
2457163.44478	0.00017	81236
2457491.40048	0.00055	83306
2457496.47045	0.00039	83338
2457506.45164	0.00033	83401
2457900.47370	0.00029	85888
2457901.42457	0.00029	85894
2457939.44889	0.00027	86134
2458227.47854	0.00022	87952
2458228.42935	0.00028	87958
2458241.42094	0.00033	88040
2458246.49055	0.00023	88072
2458593.45853	0.00026	90262
2458594.40834	0.00031	90268
2458599.47913	0.00019	90300
2458603.43930	0.00015	90325
2458943.43549	0.00035	92471
2458946.44578	0.00033	92490
2458949.45551	0.00039	92509
2459341.41767	0.00021	94983
2459350.44820	0.00011	95040
2459354.40902	0.00033	95065
2459704.38657	0.00024	97274
2459713.41715	0.00044	97331
2459744.47026	0.00029	97527

Table 3.12. Eclipse times, errors and cycle numbers for UU Aqr observed and measured by the author in this study.

Eclipse time (HJD)	*Error (d)*	*Cycle Number*
2454323.44995	0.00046	48760
2454357.47405	0.00027	48968
2454365.48955	0.00036	49017
2454728.47437	0.00051	51236
2454735.34486	0.00034	51278
2454736.32601	0.00056	51284
2454789.32574	0.00032	51608
2455038.45994	0.00069	53131
2455059.39716	0.00052	53259
2455106.34585	0.00043	53546
2455469.49424	0.00052	55766
2455490.26865	0.00048	55893
2455778.49715	0.00019	57655
2455795.50952	0.00019	57759
2455893.33048	0.00019	58357
2456159.47572	0.00030	59984
2456160.45716	0.00033	59990
2456162.42044	0.00044	60002
2456215.42071	0.00018	60326
2456512.48351	0.00045	62142
2456523.44298	0.00024	62209
2456532.43936	0.00066	62264
2456611.28481	0.00045	62746
2456612.26681	0.00033	62752
2456893.46177	0.00016	64471
2456903.44070	0.00038	64532
2456904.42104	0.00036	64538
2457258.40900	0.00022	66702
2457262.49817	0.00020	66727
2457275.42161	0.00012	66806
2457609.45204	0.00021	68848
2457617.46778	0.00040	68897
2457642.49568	0.00040	69050
2457979.47132	0.00035	71110
2457989.44973	0.00043	71171
2457993.37551	0.00026	71195
2458352.43417	0.00030	73390
2458360.44924	0.00025	73439
2458362.41308	0.00018	73451
2458363.39380	0.00024	73457
2458766.45546	0.00027	75921
2458784.28619	0.00018	76030
2458799.33537	0.00016	76122
2459102.44929	0.00024	77975
2459106.37518	0.00017	77999
2459107.35642	0.00036	78005
2459476.39397	0.00025	80261
2459478.35668	0.00047	80273
2459498.31321	0.00043	80395
2459499.29486	0.00029	80401
2459799.46523	0.00030	82236
2459859.33507	0.00055	82602
2459902.35724	0.00014	82865

Table 3.13. Eclipse times, errors and cycle numbers for V1776 Cyg observed and measured by the author in this study.

Eclipse time (HJD)	*Error (d)*	*Cycle Number*
2454238.48406	0.00059	43643
2454254.46252	0.00044	43740
2454306.51977	0.00050	44056
2454314.42730	0.00053	44104
2454646.54029	0.00092	46120
2454668.44971	0.00092	46253
2454670.42804	0.00080	46265
2454770.42363	0.00115	46872
2454994.46940	0.00068	48232
2455037.46488	0.00052	48493
2455057.39969	0.00051	48614
2455176.34096	0.00062	49336
2455460.34923	0.00100	51060
2455494.45030	0.00101	51267
2455778.46040	0.00052	52991
2455849.46194	0.00052	53422
2455893.28160	0.00088	53688
2456132.48198	0.00094	55140
2456144.51030	0.00076	55213
2456150.43908	0.00044	55249
2456160.48760	0.00054	55310
2456176.46818	0.00069	55407
2456445.48448	0.00041	57040
2456446.47452	0.00053	57046
2456450.42722	0.00071	57070
2456506.43829	0.00052	57410
2456803.46380	0.00068	59213
2456834.43307	0.00149	59401
2456840.52859	0.00068	59438
2456842.50564	0.00072	59450
2456893.40936	0.00044	59759
2457172.47754	0.00064	61453
2457174.45542	0.00088	61465
2457177.42075	0.00094	61483
2457532.43120	0.00068	63638
2457533.41877	0.00098	63644
2457545.44595	0.00083	63717
2457959.43351	0.00019	66230
2457971.46058	0.00068	66303
2457976.40197	0.00062	66333
2458246.40926	0.00048	67972
2458255.46985	0.00082	68027
2458272.43802	0.00051	68130
2458284.46341	0.00060	68203
2458643.42871	0.00069	70382
2458655.45529	0.00056	70455
2458656.44378	0.00057	70461
2458667.48111	0.00045	70528
2458983.44913	0.00029	72446
2458995.47540	0.00048	72519
2458997.45364	0.00043	72531
2458998.44053	0.00048	72537
2459106.34437	0.00060	73192
2459112.43907	0.00056	73229
2459113.42785	0.00089	73235
2459366.46757	0.00082	74771
2459367.45497	0.00075	74777
2459369.43276	0.00032	74789

Table 3.14. Eclipse times, errors and cycle numbers for RW Tri observed and measured by the author in this study.

Eclipse time (HJD)	*Error (d)*	*Cycle Number*
2454392.38737	0.00024	57197
2454419.51756	0.00027	57314
2454447.34346	0.00020	57434
2454789.37226	0.00041	58909
2454810.47333	0.00064	59000
2454835.28542	0.00050	59107
2455063.45767	0.00047	60091
2455106.35664	0.00047	60276
2455172.44338	0.00026	60561
2455487.34152	0.00042	61919
2455490.35562	0.00017	61932
2455533.48590	0.00023	62118
2455822.41233	0.00026	63364
2455828.44141	0.00023	63390
2455867.39741	0.00048	63558
2455881.31079	0.00014	63618
2455889.42621	0.00028	63653
2455914.23796	0.00028	63760
2455950.41154	0.00024	63916
2455953.42610	0.00051	63929
2455957.36910	0.00018	63946
2456200.38189	0.00029	64994
2456215.45437	0.00053	65059
2456228.43987	0.00027	65115
2456609.42450	0.00022	66758
2456619.39553	0.00012	66801
2456636.32322	0.00019	66874
2456922.46690	0.00018	68108
2456933.36541	0.00036	68155
2456935.45247	0.00017	68164
2457320.37908	0.00023	69824
2457327.33548	0.00025	69854
2457403.39345	0.00023	70182
2457623.45120	0.00056	71131
2457642.46534	0.00016	71213
2457645.47976	0.00013	71226
2458054.29026	0.00041	72989
2458059.39146	0.00026	73011
2458062.40634	0.00039	73024
2458379.39042	0.00036	74391
2458398.40463	0.00018	74473
2458401.41934	0.00037	74486
2458784.48887	0.00025	76138
2458817.41674	0.00013	76280
2458822.28650	0.00020	76301
2458827.38796	0.00029	76323
2459101.47488	0.00031	77505
2459114.45966	0.00030	77561
2459157.35817	0.00028	77746
2459221.35700	0.00029	78022
2459236.42944	0.00053	78087
2459273.29920	0.00025	78246
2459521.41392	0.00024	79316
2459541.35608	0.00023	79402
2459580.31229	0.00045	79570
2459912.36734	0.00021	81002
2459921.41077	0.00022	81041
2459928.36699	0.00022	81071

Table 3.15. Eclipse times, errors and cycle numbers for 1RXS J064434.5+334451 observed and measured by the author in this study.

Eclipse time (HJD)	*Error (d)*	*Cycle Number*
2455307.42924	0.00074	7067
2455310.39210	0.00056	7078
2455313.35557	0.00049	7089
2455627.44814	0.00048	8255
2455629.33392	0.00043	8262
2455634.45149	0.00035	8281
2455655.46296	0.00045	8359
2455658.42635	0.00025	8370
2455682.39947	0.00042	8459
2455685.36351	0.00051	8470
2455850.48993	0.00045	9083
2455854.53082	0.00023	9098
2455891.43482	0.00015	9235
2455905.44214	0.00063	9287
2455914.33106	0.00043	9320
2455924.29847	0.00046	9357
2455932.37955	0.00032	9387
2455949.35041	0.00027	9450
2455953.38926	0.00037	9465
2455957.43085	0.00052	9480
2455959.31737	0.00024	9487
2455960.39430	0.00028	9491
2455991.37304	0.00060	9606
2455998.37693	0.00019	9632
2456006.45817	0.00040	9662
2456012.38313	0.00029	9684
2456013.46042	0.00017	9688
2456029.35457	0.00024	9747
2456267.47943	0.00039	10631
2456274.48380	0.00059	10657
2456294.41725	0.00019	10731
2456338.32439	0.00028	10894
2456341.28762	0.00025	10905
2456343.44229	0.00024	10913
2456382.50149	0.00026	11058
2456384.38677	0.00037	11065
2456398.39477	0.00022	11117
2456655.37919	0.00015	12071
2456662.38307	0.00019	12097
2456677.46827	0.00025	12153
2456994.52257	0.00036	13330
2457000.44891	0.00030	13352
2457016.34157	0.00023	13411
2457042.47208	0.00021	13508
2457045.43393	0.00030	13519
2457047.31894	0.00015	13526
2457104.42741	0.00020	13738
2457402.35525	0.00028	14844
2457407.47333	0.00029	14863
2457408.28185	0.00047	14866
2457702.43865	0.00050	15958
2457723.45002	0.00031	16036
2457726.41335	0.00022	16047
2458074.44349	0.00019	17339
2458085.48724	0.00047	17380
2458161.45098	0.00026	17662
2458477.42648	0.00035	18835
2458493.31897	0.00048	18894
2458498.43788	0.00023	18913
2458827.34416	0.00065	20134
2458855.35853	0.00026	20238
2458866.40335	0.00025	20279
2459189.38307	0.00018	21478

Table 3.15 continued on next page.

Table 3.15. Eclipse times, errors and cycle numbers for 1RXS J064434.5+334451 observed and measured by the author in this study, cont.

Eclipse time (HJD)	*Error (d)*	*Cycle Number*
2459196.38696	0.00029	21504
2459203.39060	0.00036	21530
2459592.36698	0.00064	22974
2459593.44501	0.00024	22978
2459596.40755	0.00022	22989
2459995.35223	0.00017	24470
2460002.35630	0.00027	24496

Table 3.16. Eclipse times, errors and cycle numbers for AC Cnc observed and measured by the author in this study.

Eclipse time (HJD)	*Error (d)*	*Cycle Number*
2454199.45197	0.00026	32978
2454507.44198	0.00021	34003
2454891.45161	0.00036	35281
2454892.35306	0.00032	35284
2455260.43835	0.00023	36509
2455270.35440	0.00042	36542
2455619.50814	0.00082	37704
2455630.32565	0.00024	37740
2455675.39674	0.00047	37890
2455949.43118	0.00029	38802
2455959.34723	0.00034	38835
2455983.38539	0.00020	38915
2455994.50332	0.00107	38952
2455998.41002	0.00037	38965
2456001.41362	0.00048	38975
2456308.50261	0.00049	39997
2456330.43727	0.00025	40070
2456342.45628	0.00030	40110
2456680.49280	0.00037	41235
2456684.39897	0.00051	41248
2456699.42304	0.00065	41298
2457047.37473	0.00043	42456
2457059.39437	0.00051	42496
2457080.42748	0.00020	42566
2457421.46916	0.00028	43701
2457430.48357	0.00023	43731
2457433.48793	0.00025	43741
2457763.41179	0.00053	44839
2457803.37541	0.00022	44972
2457815.39490	0.00032	45012
2457827.41406	0.00027	45052
2458125.48746	0.00048	46044
2458137.50672	0.00026	46084
2458162.44626	0.00024	46167
2458519.41331	0.00030	47355
2458537.44254	0.00024	47415
2458568.39100	0.00031	47518
2458595.43418	0.00047	47608
2458869.46939	0.00025	48520
2458910.33507	0.00062	48656
2458925.35767	0.00019	48706
2459256.48343	0.00025	49808
2459272.40883	0.00031	49861
2459281.42325	0.00020	49891
2459632.37981	0.00047	51059
2459659.42252	0.00019	51149
2459665.43239	0.00029	51169
2459989.34592	0.00057	52247
2460001.36523	0.00027	52287

Table 3.17. Eclipse times, errors and cycle numbers for V363 Aur observed and measured by the author in this study.

Eclipse time (HJD)	*Error (d)*	*Cycle Number*
2454181.39163	0.00043	29957
2454392.44674	0.00017	30614
2454447.37885	0.00024	30785
2454471.47221	0.00031	30860
2454473.39980	0.00037	30866
2454810.38137	0.00031	31915
2454827.40653	0.00042	31968
2454835.43772	0.00044	31993
2454891.33360	0.00054	32167
2454892.29747	0.00021	32170
2455188.48144	0.00054	33092
2455191.37255	0.00040	33101
2455200.36736	0.00026	33129
2455515.50429	0.00013	34110
2455516.46885	0.00021	34113
2455524.49896	0.00034	34138
2455526.42586	0.00026	34144
2455627.29626	0.00020	34458
2455634.36298	0.00020	34480
2455649.46157	0.00047	34527
2455854.41351	0.00026	35165
2455888.46463	0.00016	35271
2455891.35618	0.00021	35280
2455905.49122	0.00039	35324
2455914.48560	0.00015	35352
2455950.46438	0.00013	35464
2455954.31900	0.00028	35476
2455994.47452	0.00029	35601
2456014.39134	0.00019	35663
2456215.48745	0.00015	36289
2456262.38905	0.00051	36435
2456291.30073	0.00025	36525
2456344.30534	0.00025	36690
2456655.26652	0.00034	37658
2456662.33389	0.00019	37680
2456677.43090	0.00025	37727
2456698.31132	0.00043	37792
2456707.30608	0.00013	37820
2456952.41251	0.00024	38583
2456985.50008	0.00022	38686
2456994.49490	0.00042	38714
2457349.46509	0.00025	39819
2457377.41312	0.00026	39906
2457429.45427	0.00015	40068
2457721.46196	0.00022	40977
2457741.37878	0.00022	41039
2457846.42357	0.00028	41366
2458066.47383	0.00023	42051
2458074.50509	0.00036	42076
2458085.42672	0.00020	42110
2458441.36127	0.00025	43218
2458465.45436	0.00018	43293
2458819.46136	0.00016	44395
2458822.35212	0.00017	44404
2458868.28933	0.00028	44547
2459148.41099	0.00018	45419
2459157.40619	0.00036	45447
2459164.47295	0.00026	45469
2459273.37328	0.00021	45808
2459575.34002	0.00015	46748
2459584.33471	0.00016	46776
2459975.28343	0.00019	47993

Table 3.18. Eclipse times, errors and cycle numbers for BT Mon observed and measured by the author in this study.

Eclipse time (HJD)	*Error (d)*	*Cycle Number*
2454447.47617	0.00050	32820
2454891.44778	0.00061	34150
2454892.44988	0.00053	34153
2455238.27878	0.00058	35189
2455239.28089	0.00095	35192
2455257.30609	0.00040	35246
2455260.31093	0.00048	35255
2455277.33531	0.00079	35306
2455571.42510	0.00067	36187
2455595.46030	0.00073	36259
2455600.46698	0.00109	36274
2455619.49354	0.00056	36331
2455960.31808	0.00104	37352
2455968.33013	0.00055	37376
2455987.35688	0.00064	37433
2455992.36366	0.00082	37448
2456001.37745	0.00090	37475
2456011.39153	0.00070	37505
2456294.46579	0.00045	38353
2456330.51701	0.00047	38461
2456338.52784	0.00048	38485
2456684.35905	0.00079	39521
2456707.39142	0.00025	39590
2456725.41702	0.00037	39644
2457011.49426	0.00023	40501
2457017.50343	0.00037	40519
2457020.50843	0.00037	40528
2457395.37986	0.00051	41651
2457402.39016	0.00052	41672
2457407.39767	0.00062	41687
2457803.29994	0.00042	42873
2457815.31701	0.00067	42909
2457827.33521	0.00038	42945
2457828.33500	0.00044	42948
2458137.44694	0.00033	43874
2458151.46592	0.00045	43916
2458161.48037	0.00039	43946
2458529.34362	0.00053	45048
2458536.35358	0.00047	45069
2458537.35429	0.00056	45072
2458866.49427	0.00023	46058
2458869.49729	0.00039	46067
2459238.36139	0.00054	47172
2459249.37680	0.00034	47205

Table 4. Eclipse times, errors and cycle numbers for LX Ser measured by the author from observations by Cook and Dvorak in the AAVSO International Database.

Eclipse time (HJD)	*Error (d)*	*Cycle Number*	*Observer*	*Eclipse time (HJD)*	*Error (d)*	*Cycle Number*	*Observer*
2452777.87523	0.00050	53555	Cook	2458192.94006	0.00020	87734	Dvorak
2452778.82598	0.00056	53561	Cook	2458193.89137	0.00042	87740	Dvorak
2452779.77652	0.00072	53567	Cook	2458220.82416	0.00025	87910	Dvorak
2452779.93474	0.00057	53568	Cook	2458227.79532	0.00032	87954	Dvorak
2452780.88542	0.00044	53574	Cook	2458233.81608	0.00042	87992	Dvorak
2452781.83604	0.00049	53580	Cook	2458239.83639	0.00045	88030	Dvorak
2452782.78676	0.00050	53586	Cook	2458242.84637	0.00036	88049	Dvorak
2452782.94528	0.00051	53587	Cook	2458272.63221	0.00031	88237	Dvorak
2452786.74760	0.00036	53611	Cook	2458589.65567	0.00034	90238	Dvorak
2452786.90593	0.00022	53612	Cook	2458966.72465	0.00027	92618	Dvorak
2452787.85672	0.00041	53618	Cook	2459271.86577	0.00043	94544	Dvorak
2457882.73016	0.00052	85776	Dvorak	2459358.68647	0.00030	95092	Dvorak
2457889.70010	0.00037	85820	Dvorak	2459363.59809	0.00021	95123	Dvorak
2457899.68152	0.00027	85883	Dvorak	2459364.70675	0.00017	95130	Dvorak
2458167.90800	0.00032	87576	Dvorak	2459375.63919	0.00029	95199	Dvorak
2458181.85027	0.00035	87664	Dvorak	2459624.85361	0.00032	96772	Dvorak
2458187.87047	0.00021	87702	Dvorak	2459625.96292	0.00050	96779	Dvorak
2458191.83129	0.00031	87727	Dvorak	2459744.47026	0.00029	97527	Dvorak

Table 5. Sources of published eclipse times.

Star Name	*Sources of published eclipse times*
HS 0728+6738 = V482 Cam	Rodriguez-Gil *et al.* (2004)
SW Sex = PG 1012-029	Penning *et al.* (1984), Ashoka *et al.* (1994), Dhillon *et al.* (1997), Groot *et al.* (2001), Fang *et al.* (2020), one issue of BVSOLJ
DW UMa = PG1030+590	Shafter *et al.* (1988), Dhillon *et al.* (1994), Bíró (2000), Stanishev *et al.* (2004), Dhillon *et al.* (2013), Boyd *et al.* (2017) (including observations from contributors to the Centre for Backyard Astrophysics), several issues of IBVS, BVSOLJ, OEJV
HS 0129+2933 = TT Tri	Warren *et al.* (2006), Rodriguez-Gil *et al.* (2007), Han *et al.* (2018)
V1315 Aql	Downes *et al.* (1986), Dhillon *et al.* (1991), Rutten *et al.* (1992), Hellier (1996), Papadaki *et al.* (2009), Fang and Qian (2021), a series of eclipse times by Cook published in *Observed Minima Times of Eclipsing Binaries, No 10* (Baldwin and Samolyk 2005)
PX And = PG0027+260	Hellier and Robinson (1994), Stanishev *et al.* (2002), Han *et al.* (2018), several issues of IBVS
HS 0455+8315	Rodriguez-Gil *et al.* (2007)
HS 0220+0603	Rodriguez-Gil *et al.* (2007)
BP Lyn = PG0859+415	Grauer *et al.* (1994), Still (1996), Han *et al.* (2018)
BH Lyn = PG0818+513	Dhillon *et al.* (1992), Hoard and Szkody (1997), Stanishev *et al.* (2006), several issues of OEJV
LX Ser = Stepanyan's Star	Horne (1980), Africano and Klimke (1981), Young *et al.* (1981), Rutten *et al.* (1992), Li (2017), several issues of IBVS, BVSOLJ and OEJV
UU Aqr	Baptista *et al.* (1994), Han *et al.* (2018), several issues of BVSOLJ, IBVS and OEJV
V1776 Cyg = Lanning 90	Garnavich *et al.* (1990)
RW Tri	Walker (1963), Africano *et al.* (1978), Robinson *et al.* (1991), Rutten *et al.* (1992), Smak (1995), Subebikova (2020), several issues of IBVS, OEJV and BVSOLJ
1RXS J064434.5+334451	Sing *et al.* (2007), Green (2008), Hernandez Santisteban (2017), Shafter and Bautista (2021)
AC Cnc	Yamasaki *et al.* (1983), Schlegel *et al.* (1984), Zhang *et al.* (1987), Thoroughgood *et al.* (2004), Qian *et al.* (2007), Bruch (2022), several issues of OEJV and IBVS
V363 Aur = Lanning 10	Horne *et al.* (1982), Schlegel *et al.* (1986), Rutten *et al.* (1992), Thoroughgood *et al.* (2004), one issue of BVSOLJ
BT Mon	Robinson *et al.* (1982), Seitter (1984), Smith *et al.* (1998)

IBVS = Information Bulletin on Variable Stars: https://konkoly.hu/ibvs/; BVSOLJ = Bulletin of the Variable Star Observers League in Japan: http://vsolj.cetus-net.org/; OEJV = Open European Journal on Variable Stars: https://oejv.physics.muni.cz/

Table 6. Weighted linear ephemerides for each star computed with all available data except in the case of SW Sex where there was a large change around 2017 and separate ephemerides are given for before and after this change. E is the cycle number.

Star Name	*Weighted Linear Ephemeris*
HS 0728+6738 = V482 Cam	2452001.32754(8) + 0.133619431(2) * E
SW Sex = PG 1012-029 (up to 2017)	2444339.6502(2) + 0.134938480(2) * E
SW Sex = PG 1012-029 (after 2017)	2444339.689(2) + 0.13493809(2) * E
DW UMa = PG1030+590	2446229.00633(8) + 0.136606541(1) * E
HS 0129+2933 = TT Tri	2452540.5335(2) + 0.139637390(7) * E
V1315 Aql	2445902.8387(2) + 0.139689996(2) * E
PX And = PG0027+260	2449238.8368(2) + 0.146352742(4) * E
HS 0455+8315	2451859.2458(2) + 0.148723946(5) * E
HS 0220+0603	2452563.57441(9) + 0.149207655(3) * E
BP Lyn = PG0859+415	2447881.8572(4) + 0.152812554(7) * E
BH Lyn = PG0818+513	2447180.3343(2) + 0.155875642(3) * E
LX Ser = Stepanyan's Star	2444293.0227(2) + 0.158432503(2) * E
UU Aqr	2446347.2670(2) + 0.163580423(3) * E
V1776 Cyg = Lanning 90	2447048.7932(3) + 0.164738652(5) * E
RW Tri	2441129.3634(4) + 0.231883245(5) * E
1RXS J064434.5+334451	2453403.7611(3) + 0.26937438(2) * E
AC Cnc	2444290.3103(3) + 0.300477307(7) * E
V363 Aur = Lanning 10	2444557.981(2) + 0.32124074(6) * E
BT Mon	2443491.7225(9) + 0.33381330(2) * E

Table 7. Weighted quadratic ephemerides and mean rates of period change for stars showing evidence of either an increasing or decreasing orbital period. E is the cycle number.

Star Name	*Weighted Quadratic Ephemeris*	*Mean Rate of Period Change (msec/year)*
HS 0728+6738 = V482 Cam	2452001.3273(1) + 0.133619451(8) * E – 3(1)10^{-13} * E2	–0.16(6)
DW UMa = PG1030+590	2446229.0069(2) + 0.136606520(7) * E + 1.7(5)10^{-13} * E2	0.08(3)
HS 0129+2933 = TT Tri	2452540.5309(2) + 0.13963764(2) * E – 4.2(3)10^{-12} * E2	–1.9(2)
V1315 Aql	2445902.8408(1) + 0.139689913(4) * E + 6.8(3)10^{-13} * E2	0.31(2)
PX And = PG0027+260	2449238.8366(2) + 0.14635275(1) * E – 1(1)10^{-13} * E2	–0.06(6)
HS 0455+8315	2451859.2476(5) + 0.14872382(3) * E + 1.9(5)10^{-12} * E2	0.8(2)
HS 0220+0603	2452563.57406(7) + 0.149207716(7) * E – 1.4(2) 10^{-12} * E2	–0.58(6)
BP Lyn = PG0859+415	2447881.8584(4) + 0.15281244(2) * E + 1.5(3)10^{-12} * E2	0.6(1)
BH Lyn = PG0818+513	2447180.3331(2) + 0.155875697(3) * E – 5.51(3)10^{-13} * E2	–0.22(1)
UU Aqr	2446347.2656(1) + 0.163580565(8) * E – 1.70(9)10^{-12} * E2	–0.66(4)
V1776 Cyg = Lanning 90	2447048.7928(3) + 0.16473869(2) * E – 5(2)10^{-13} * E2	–0.19(8)
1RXS J064434.5+334451	2453403.7596(3) + 0.26937469(5) * E – 1.2(2)10^{-11} * E2	–2.8(5)
V363 Aur = Lanning 10	2444557.9493(5) + 0.32124275(2) * E – 3.05(2)10^{-11} * E2	–5.98(4)
BT Mon	2443491.7162(4) + 0.33381392(1) * E – 1.127(8)10^{-11} * E2	–2.13(2)

Table 8. Parameters of sinusoidal fits relative to a linear ephemeris.

Star Name	*Period of Sinusoidal Variation (year)*	*Half Amplitude of Sinusoidal Cariation (sec)*
SW Sex = PG 1012-029 (up to 2017)	33 (2)	46 (6)
LX Ser = Stepanyan's Star	13.5 (2)	55 (4)
RW Tri up (up to 2018)	44.3 (7)	191 (7)
AC Cnc	37.8 (7)	134 (14)

Table 9. Parameters of sinusoidal fits relative to a quadratic ephemeris.

Star Name	*Period of Sinusoidal Variation (year)*	*Half Amplitude of Sinusoidal Cariation (sec)*
DW UMa = PG1030+590	14.4 (3)	38 (1)
HS 0129+2933 = TT Tri	13.0 (4)	47 (6)
1RXS J064434.5+334451	6.2 (2)	87 (10)

5. O–C diagrams

In these O–C diagrams, data from the published literature or derived from observations in the AAVSO International Database are shown in black while eclipse times measured by the author are shown in red. Linear ephemerides are shown dotted in black, quadratic ephemerides dotted in magenta, and sinusoidal fits dotted in green. The passing years are marked above each diagram. O–C diagrams with similar apparent behavior are grouped together. To achieve a degree of consistency between these diagrams, we have used the same scale on the O–C axis except where the range of the data is significantly larger. It is worth stating explicitly that including these fits in the O–C diagrams is a subjective exercise which yields parameters that can be quantified but does not imply a physical interpretation. The O–C diagrams are described in five groups.

HS 0728+6738 = V482 Cam, PX And = PG0027+260, HS 0220+0603, BH Lyn = PG0818+513, V1776 Cyg = Lanning 90 These stars show predominantly linear behavior with weak evidence of decreasing orbital period. Their O–C diagrams with linear and quadratic ephemerides are shown in Figure 2 and parameters of the quadratic ephemerides are given in Table 7.

HS 0129+2933 = TT Tri, UU Aqr, 1RXS J064434.5+334451, V363 Aur = Lanning 10, BT Mon These stars show stronger evidence of decreasing orbital periods. Their O–C diagrams with linear and quadratic ephemerides are shown in Figure 3 and parameters of the quadratic ephemerides are given in Table 7.

DW UMa = PG1030+590, V1315 Aql, HS0455+8315, BP Lyn = PG0859+415 These stars show evidence of increasing orbital periods. Their O–C diagrams with linear and quadratic ephemerides are shown in Figure 4 and parameters of the quadratic ephemerides are given in Table 7.

SW Sex = PG 1012-029, LX Ser = Stepanyan's Star, RW Tri, AC Cnc These stars show evidence of sinusoidal variation in their orbital periods relative to a linear ephemeris. Figure 5 shows their O–C diagrams with sinusoidal fits relative to a linear ephemeris and Table 8 gives parameters of these sinusoidal fits.

Stars also showing evidence of more complex behavior In addition to their behavior described above, DW UMa, HS0129+2933 and 1RXS J064434.5+334451 also show evidence of sinusoidal variation in their orbital periods relative to a quadratic ephemeris. Figure 6 shows their O–C diagrams with sinusoidal fits relative to a quadratic ephemeris. Table 9 gives parameters of these sinusoidal fits. DW UMa now appears to be diverging from this sinusoidal pattern.

Figure 5 shows that both SW Sex and RW Tri recently experienced large decreases in their orbital periods.

Prior to 2017 (cycle ~100000) the mean orbital period of SW Sex over the previous 37 years had been 0.134938480(2) d with relatively weak sinusoidal modulation. During 2017 this reduced to 0.13493809(2) d, a decrease of 34 msec and a proportional change of -2.9×10^{-6}.

Prior to 2018 (cycle ~74000) the mean orbital period of RW Tri over the previous 15 years had been 0.231883411(6) d with relatively strong sinusoidal modulation. Within a few months this changed and the mean orbital period since 2018 has been 0.23188288(6) d, a decrease of 46 msec and a proportional change of -2.3×10^{-6}.

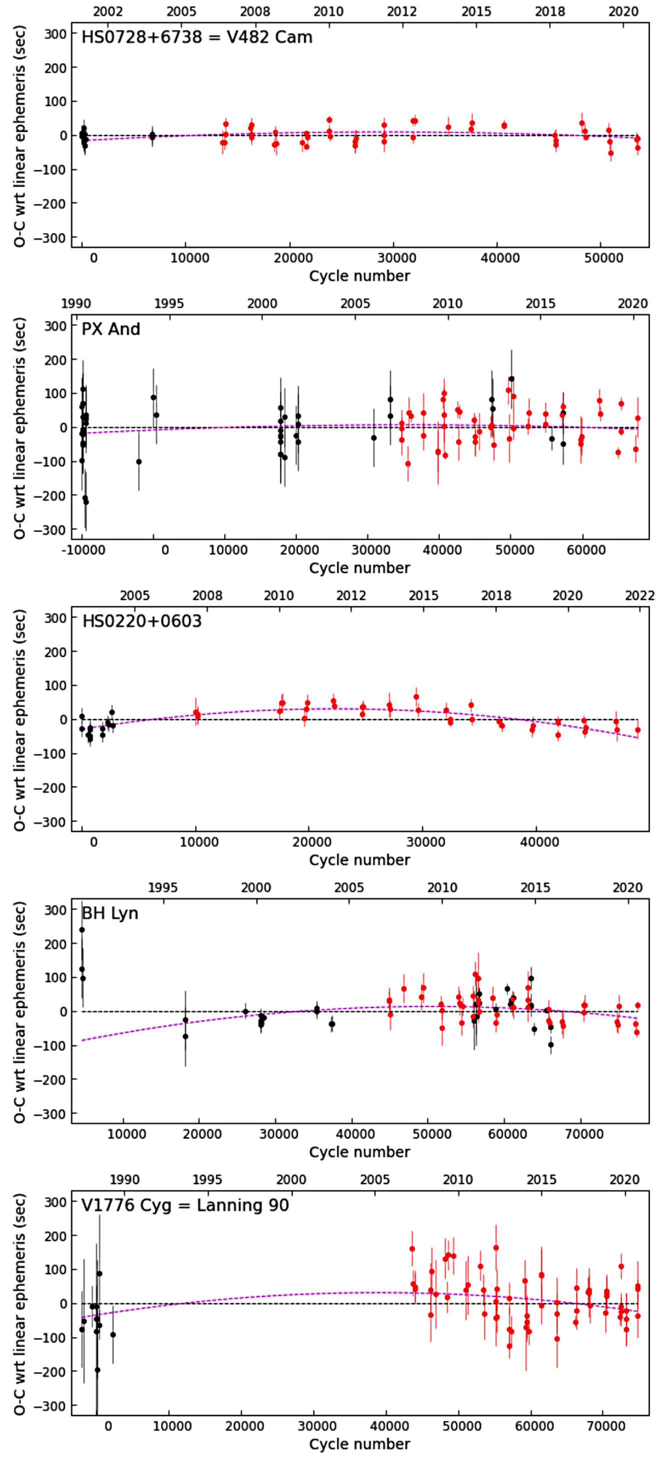

Figure 2. O–C diagrams with linear and quadratic ephemerides for stars showing weak evidence of decreasing orbital period. Data from the published literature or derived from observations in the AAVSO International Database are shown in black while eclipse times measured by the author are shown in red. Linear ephemerides are shown dotted in black, quadratic fits dotted in magenta.

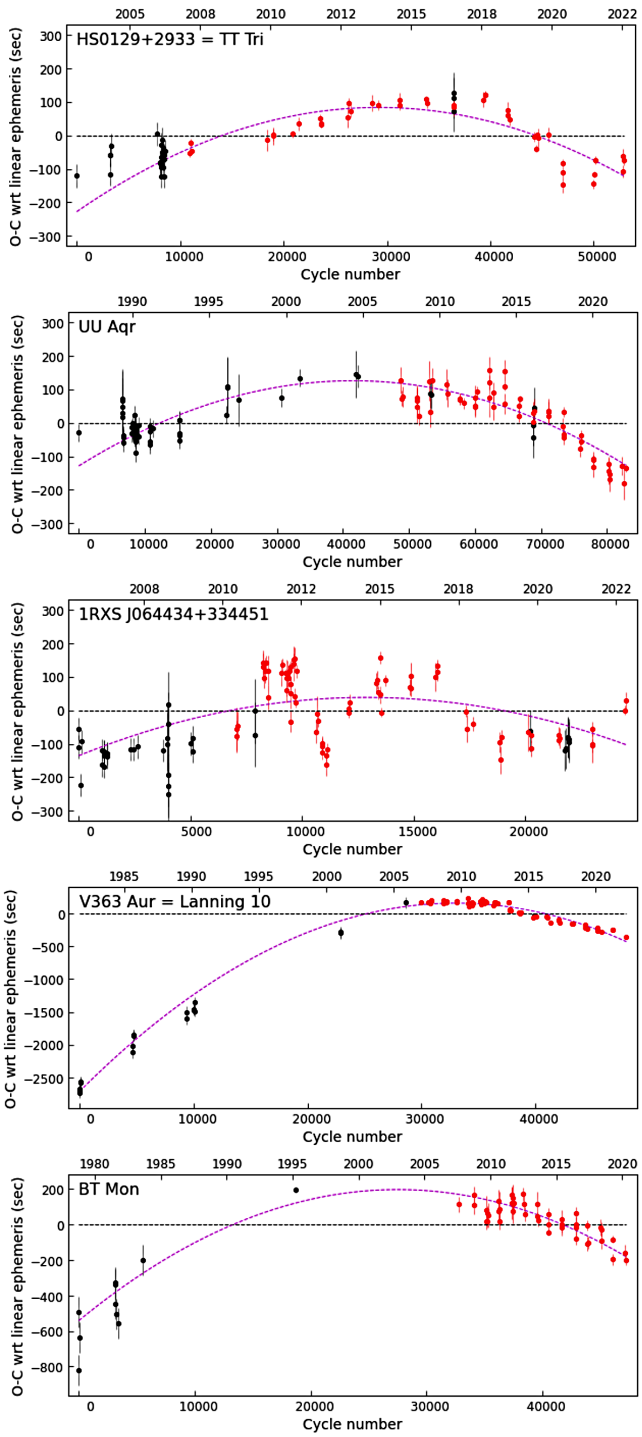

Figure 3. O–C diagrams with linear and quadratic ephemerides for stars showing stronger evidence of decreasing orbital periods. Color coding as in Figure 2.

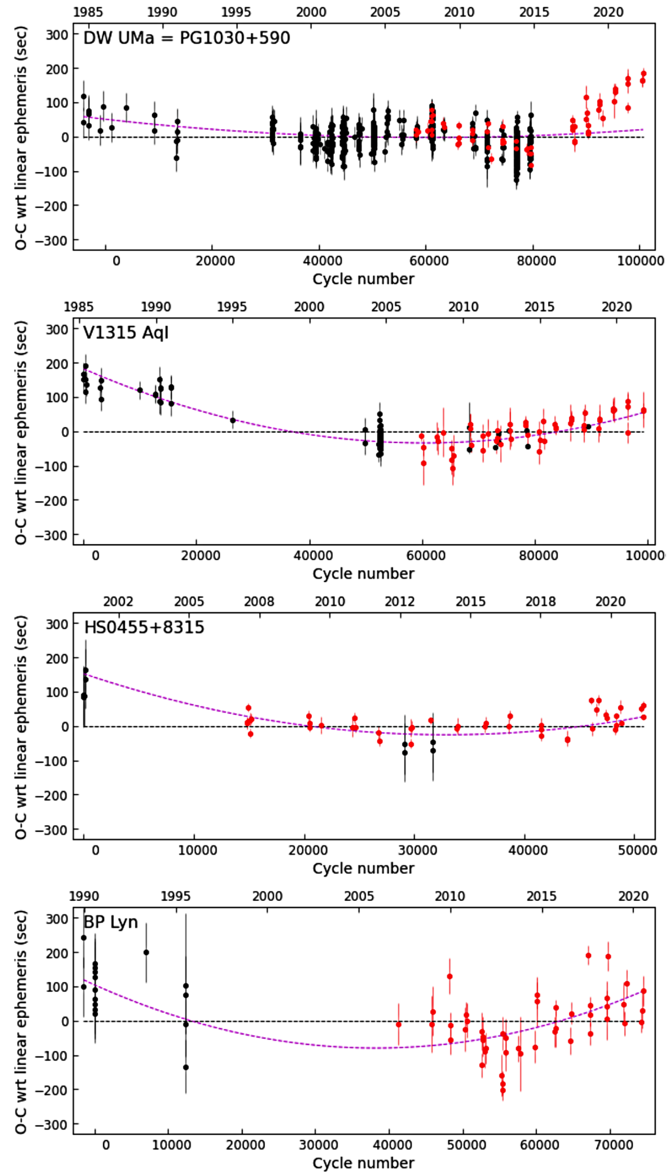

Figure 4. O–C diagrams with linear and quadratic ephemerides for stars showing evidence of increasing orbital periods. Color coding as in Figure 2.

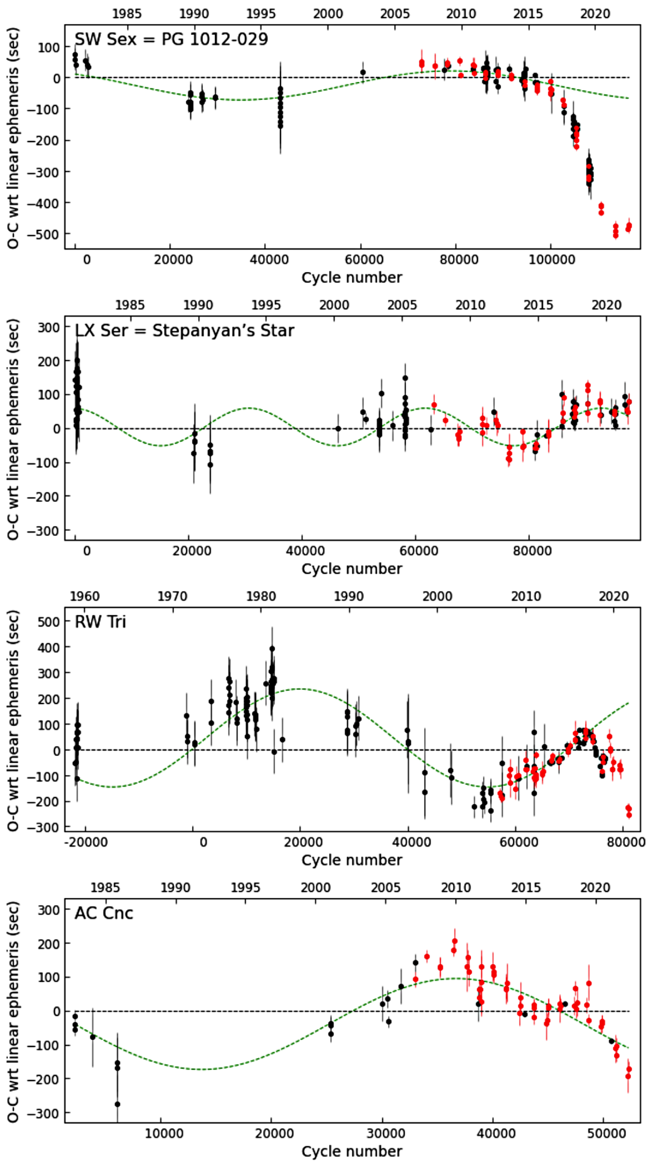

Figure 5. O–C diagrams with linear ephemerides and sinusoidal fits for stars showing evidence of sinusoidal variation in their orbital periods relative to a linear ephemeris. Color coding as in Figure 2 with sinusoidal fits dotted in green.

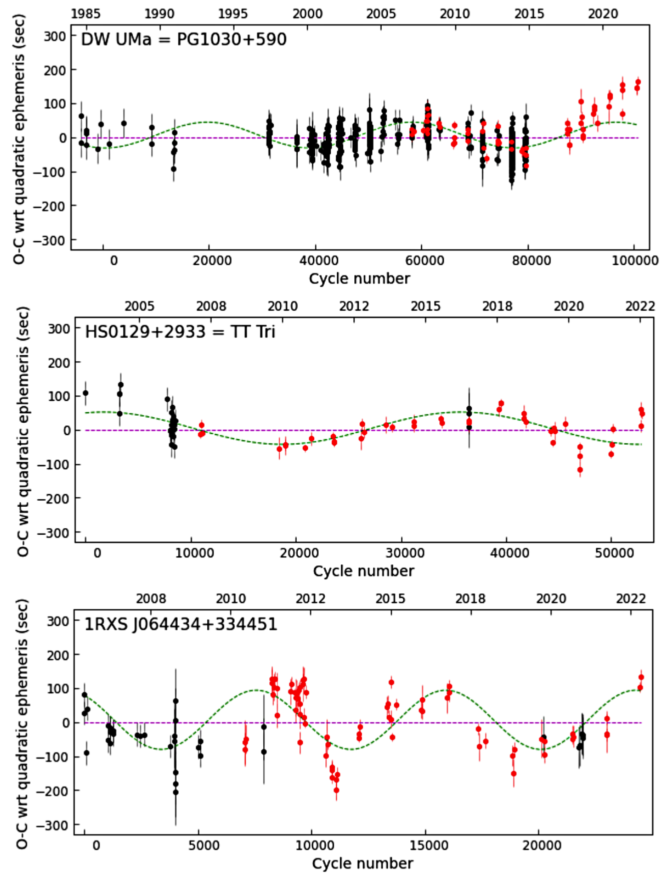

Figure 6. O–C diagrams with quadratic ephemerides and sinusoidal fits for stars showing evidence of sinusoidal variation in their orbital periods relative to a quadratic ephemeris. Color coding as in Figure 2 with sinusoidal fits dotted in green.

6. Interpretation

Several mechanisms have been proposed to explain relatively slow changes in the orbital periods of CVs above the period gap, including loss of angular momentum through magnetic braking associated with a magnetized stellar wind (Knigge *et al.* 2011), various versions of the Applegate mechanism associated with magnetically induced changes in the internal structure of the secondary star (Applegate 1992; Völschow *et al.* 2016; Lanza 2020), or a third body in the system whose presence causes a gravitationally induced oscillation of the eclipse time (Qian *et al.* 2013).

We do not believe there has been a sufficiently long period of observations to reach a firm conclusion on the long term behavior of any of the systems reported here. Whether the trends detected so far, as indicated by the fits applied to the O–C data, are maintained in the longer term only further observations will be able to determine. There have been numerous cases in the literature where attempts to assign a specific interpretation to apparently cyclical orbital behavior have failed to stand the test of time (Pulley *et al.* 2022). The dangers of interpreting observations as periodic when only two or three cycles may be present are outlined in Vaughan *et al.* (2016). We therefore do not attempt to assign physical significance to the fits shown in these O–C diagrams, but simply offer our measurements as data to anyone wishing to attempt such an interpretation in the future.

7. Summary

We report on a 17-year study to monitor the orbital periods of 18 eclipsing nova-like CVs referred to as SW Sex stars. We added 934 new eclipse times to 1338 times in the published literature and produced an O–C diagram for each star including all available data. This revealed clear trends in the behavior of most of the stars but also that many of the stars experienced deviations from these trends. We observed rapid and unusual decreases of 34 msec (a proportional change of -2.9×10^{-6}) in the orbital period of SW Sex during 2017 and of 46 msec (a proportional change of -2.3×10^{-6}) in the orbital period of RW Tri during 2018. DW UMa also appears to have recently diverged from the sinusoidal behavior it has been following for the past 30 years. It is clear from these results that observations will have to be maintained over a much longer timescale before definitive statements can be made about their long term behavior, or even whether stable long term behavior is likely for these stars. We intend to continue observing many of these stars.

8. Acknowledgements

I am grateful to the anonymous referee for a careful and helpful review. I am also grateful to Boris Gänsicke for his early encouragement to pursue this as a long-term project and to Chris Lloyd for helpful comments on an earlier draft. I acknowledge with thanks the observations of LX Ser by Cook and Dvorak in the AAVSO International Database and the use of AAVSO comparison charts and NASA's Astrophysics Data System. Software developed in the project made extensive use of the Astropy package (Astropy Collaboration 2018).

References

Africano, J. L., and Klimke, A. 1981, *Inf. Bull. Var. Stars*, No. 1969, 1.
Africano, J. L., Nather, R. E., Patterson, J., Robinson, E. L., and Warner, B. 1978, *Publ. Astron. Soc. Pacific*, **90**, 568.
Andrae, R., Schulze-Hartung, T., and Melchior, P. 2010, "Dos and don'ts of reduced chi-squared" (https://arxiv.org/pdf/1012.3754.pdf).
Applegate J. H., 1992, *Astrophys. J.*, **385**, 621.
Ashoka, B. N., Seetha, S., Marar, T. M. K., Kasturirangan, K., Rao, U. R., and Bhattcharyya, J. C. 1994, *Astron. Astrophys.*, **283**, 455.
Astropy Collaboration, *et al.* 2018, *Astron. J.*, **156**, 123.
Baldwin, M. E., and Samolyk, G. 2005, *Observed Minima Timings of Eclipsing Binaries, No. 10*, AAVSO, Cambridge, MA.
Baptista, R., Steiner, J. E., and Cieslinski, D. 1994, *Astrophys. J.*, **433**, 332.
Bíró, I. B. 2000, *Astron. Astrophys.*, **364**, 573.
Boyd, D. 2012, *J. Amer. Assoc. Var. Star Obs.*, **40**, 295.
Boyd, D., *et al.* 2017, *Mon. Not. Roy. Astron. Soc.*, **466**, 3417.
Bruch, A. 2022, *Mon. Not. Roy. Astron. Soc.*, **514**, 4718.
Dhillon, V. S., Jones, D. H. P., and Marsh, T. R. 1994, *Mon. Not. Roy. Astron. Soc.*, **266**, 859.
Dhillon, V. S., Jones, D. H. P., Marsh, T. R., and Smith, R. C. 1992, *Mon. Not. Roy. Astron. Soc.*, **258**, 225.
Dhillon, V. S., Marsh, T. R., and Jones, D. H. P. 1991, *Mon. Not. Roy. Astron. Soc.*, **252**, 342.
Dhillon, V. S., Marsh, T. R., and Jones, D. H. P. 1997, *Mon. Not. Roy. Astron. Soc.*, **291**, 694.
Dhillon, V. S., Smith, D. A., and Marsh, T. R. 2013, *Mon. Not. Roy. Astron. Soc.*, **428**, 3559.
Downes, R. A., Mateo, M., Szkody, P., Jenner, D. C., and Margon, B. 1986, *Astrophys. J.*, **301**, 240.
Duerbeck, H. W. 1987, *ESO Messenger*, **50**, 8.
Fang, X., and Qian, S. 2021, *Mon. Not. Roy. Astron. Soc.*, **501**, 3046.
Fang, X., Qian, S., Han, Z., and Wang, Q. 2020, *Astrophys. J.*, **901**, 113.
Garnavich, P. M., *et al.* 1990, *Astrophys. J.*, **365**, 696.
Grauer, A. D., Ringwald, F. A., Wegner, G., Liebert, J., Schmidt, G. D., and Green, R. F. 1994, *Astron. J.*, **108**, 214.
Green, E. M. 2008, private communication.
Groot, P. J., Rutten, R. G. M., and van Paradijs, J. 2001, *Astron. Astrophys.*, **368**, 183.
Hagen, H.-J., Groote, D., Engels, D., and Reimers, D. 1995, *Astron. Astrophys., Suppl. Ser.*, **111**, 195.
Han, X. L., Zhang, L.-Y., Shi, J.-R., Pi, Q.-F., Lu, H.-P., Zhao, L.-B., Terheide, R. K., and Jiang, L.-Y. 2018, *Res. Astron. Astrophys.*, **18**, 68.
Hellier, C. 1996, *Astrophys. J.*, **471**, 949.
Hellier, C. 2001, *Cataclysmic Variable Stars*, Springer-Verlag, Berlin.
Hellier, C., and Robinson, E. L. 1994, *Astrophys. J.*, **431**, L107.

Henden, A. A., and Honeycutt, R. K. 1995, *Publ. Astron. Soc. Pacific*, **107**, 324.
Henden, A. A., Templeton, M., Terrell, D., Smith, T. C., Levine, S., and Welch, D. 2018, VizieR Online Data Catalog: AAVSO Photometric All Sky Survey (APASS) DR10, II/336.
Hernández Santisteban, J. V., Echevarría, J., Michel, R., and Costero, R. 2017, *Mon. Not. Roy. Astron. Soc.*, **464**, 104.
Hoard, D. W., and Szkody, P. 1997, *Astrophys. J.*, **481**, 433.
Hoard, D. W., Szkody, P., Froning, C. S., Long, K. S., and Knigge, C. 2003, *Astron. J.*, **126**, 2473.
Honeycutt, R. K., Schlegel, E. M., and Kaitchuck, R. H. 1986, *Astrophys. J.*, **302**, 388.
Horne, K. 1980, *Astrophys. J.*, **242**, L167.
Horne, K., Lanning, H. H., and Gomer, R. H. 1982, *Astrophys. J.*, **252**, 681.
Howell, S. B. 2006, *Handbook of CCD Astronomy*, 2nd ed., Cambridge Univ. Press, Cambridge.
Kafka, S. 2021, Observations from the AAVSO International Database (https://www.aavso.org/data-download).
Knigge, C., Baraffe, I., and Patterson, J. 2011, *Astrophys. J., Suppl. Ser.*, **194**, 28.
Lanza, A. F. 2020, *Mon. Not. Roy. Astron. Soc.*, **491**, 1820.
Li, K. *et al.* 2017, *Publ. Astron. Soc. Japan*, **69**, 28.
Papadaki, C. *et al.* 2009, *J. Astron. Data*, **15**, 1.
Patterson, J. 1984, *Astrophys. J., Suppl. Ser.*, **54**, 443.
Penning, W. R., Ferguson, D. H., McGraw, J. T., Liebert, J., and Green, R. F. 1984, *Astrophys. J.*, **276**, 233.
Pulley, D., Sharp, I. D., Mallett, J., and von Harrach, S. 2022, *Mon. Not. Roy. Astron. Soc.*, **514**, 5725.
Qian, S.-B. *et al.* 2013, *Mon. Not. Roy. Astron. Soc.*, **436**, 1408.
Qian, S.-B., Dai, Z.-B., He, J.-J., Yuan, J. Z., Xiang, F. Y., and Zejda, M. 2007, *Astron. Astrophys.*, **466**, 589.
Robinson, E. L., Nather, R. E., and Kepler, S. O. 1982, *Astrophys. J.*, **254**, 646.
Robinson, E. L., Shetrone, M. D., and Africano, J. L. 1991, *Astron. J.*, **102**, 1176.
Rodríguez-Gil, P., Gänsicke, B. T., Barwig, H., Hagen, H.-J., and Engels, D. 2004, *Astron. Astrophys.*, **424**, 647.
Rodríguez-Gil, P., *et al.* 2007, *Mon. Not. Roy. Astron. Soc.*, **377**, 1747.
Rutten, R. G. M., van Paradijs, J., and Tinbergen, J. 1992, *Astron. Astrophys.*, **260**, 213.
Sahman, D. I., Dhillon, V. S., Knigge, C., and Marsh, T. R. 2015, *Mon. Not. Roy. Astron. Soc.*, **451**, 2863.
Schlegel, E. M., Honeycutt, R. K., and Kaitchuck, R. H. 1986, *Astrophys. J.*, **307**, 760.
Schlegel, E. M., Kaitchuck, R. H., and Honeycutt, R. K. 1984, *Astrophys. J.*, **280**, 235.
Schmidtobreick, L. 2015, in *Proceedings of The Golden Age of Cataclysmic Variables and Related Objects—III*, Palermo, Italy, https://arxiv.org/pdf/1705.09332.pdf.
Seitter, W. C. 1984, *Astrophys. Space Sci.*, **99**, 95.
Shafter, A. W., and Bautista, A., 2021, *Res. Notes AAS*, **5**, 207.
Shafter, A. W., Hessman, F. V., and Zhang, E.-H. 1988, *Astrophys. J.*, **327**, 248.
Shara, M. M., Mizusawa, T., Wehinger, P., Zurek, D., Martin, C. D., Neill, J. D., Forster, K., and Seibert, M. 2012, *Astrophys. J.*, **758**, 121.
Sing, D. K., Green, E. M., Howell, S. B., Holberg, J. B., Lopez-Morales, M., Shaw, J. S., and Schmidt, G. D. 2007, *Astron. Astrophys.*, **474**, 951.
Smak, J. 1995, *Acta Astron.*, **45**, 259.
Smith, D. A., Dhillon, V. S., and Marsh, T. R. 1998, *Mon. Not. Roy. Astron. Soc.*, **296**, 465.
Stanishev, V., Kraicheva, Z., Boffin, H. M. J., and Genkov, V. 2002, *Astron. Astrophys.*, **394**, 625.
Stanishev, V., Kraicheva, Z., Boffin, H. M. J., Genkov, V., Papadaki, C., and Carpano, S. 2004, *Astron. Astrophys.*, **416**, 1057.
Stanishev, V., Kraicheva, Z., and Genkov, V. 2006, *Astron. Astrophys.*, **455**, 223.
Still, M. D. 1996, *Mon. Not. Roy. Astron. Soc.*, **282**, 943.
Subebekova, G., Zharikov, S., Tovmassian, G., Neustroev, V., Wolf, M., Hernandez, M. -S., Kučáková, H., and Khokhlov, S. 2020, *Mon. Not. Roy. Astron. Soc.*, **497**, 1475.
Thoroughgood, T. D., Dhillon, V. S., Watson, C. A., Buckley, D. A. H., Steeghs, D., and Stevenson, M. J. 2004, *Mon. Not. Roy. Astron. Soc.*, **353**, 1135.
Thorstensen, J. R., Ringwald, F. A., Wade, R. A., Schmidt, G. D., and Norsworthy, J. E. 1991, *Astron. J.*, **102**, 272.
Vaughan, S., Uttley, P., Markowitz, A. G., Huppenkothen, D., Middleton, M. J., Alston, W. N., Scargle, J. D., and Farr, W. M. 2016, *Mon. Not. Roy. Astron. Soc.*, **461**, 3145.
Völschow, M., Schleicher, D. R. G., Perdelwitz, V., and Banerjee, R. 2016, *Astron. Astrophys.*, **587A**, 34.
Walker, M. F. 1963, *Astrophys. J.*, **137**, 485.
Warner, B. 1995, *Cataclysmic Variable Star*s, Cambridge Univ. Press, Cambridge.
Warren, S. R., Shafter, A. W., and Reed, J. K. 2006, *Publ. Astron. Soc. Pacific*, **118**, 1373.
Yamasaki, A., Okazaki, A., and Kitamura, M. 1983, *Publ. Astron. Soc. Japan*, **35**, 423.
Young, P., Schneider, D. P., and Shectman, S. A. 1981, *Astrophys. J.*, **244**, 259.
Zhang, E. 1987, *Acta Astrophys. Sinica*, **7**, 245.

Visual Photometry: Testing Hypotheses Concerning Bias and Precision

Alan B. Whiting
Department of Physics and Astronomy, University of Birmingham, Edgbaston, Birmingham BT2 5TT, UK; abw@star.sr.bham.ac.uk

Received October 28, 2022; revised May 5, 2023; accepted May 15, 2023

Abstract Visual photometry, the estimation of stellar brightness by eye, continues to provide valuable data even in this highly-instrumented era. However, the eye-brain system functions differently from electronic sensors and its products can be expected to have different characteristics. Here I characterize some aspects of the visual data set by examining ten well-observed variable stars from the AAVSO International Database. The standard deviation around a best-fit curve ranges from 0.14 to 0.34 magnitude, smaller than most previous estimates. The difference in scatter between stars is significant, but does not correlate with such things as range or quickness of variation, or even with color. Naked-eye variables, which would be expected to be more difficult to observe accurately, in fact show the smallest scatter. The difference between observers (bias) is less important than each observer's internal precision. A given observer's precision is not set but varies from star to star for unknown reasons. I note some results relevant to other citizen science projects.

1. Introduction: visual photometry

It may seem surprising that nowadays, with precision electronic instruments widespread even among amateur astronomers, visual photometry is still widely practiced and useful. But the collective database of visual observations has unmatched coverage in time. Even the All-Sky Automated Survey (ASAS) returns rather sparse coverage of any particular variable star (Mayangsari *et al.* 2014), requiring sophisticated methods to recover details of a light curve. As an alternative, visual observations may be used to fill in the gaps (Holdsworth *et al.* 2013). In any case, the visual database allows a researcher access to much history; the 87-year span of Leibowitz and Formiggini (2015), for instance, could not be matched by electronic data. In addition, the initial discovery of unexpected behavior is often visual, as in Surina *et al.* (2014).

But visual photometry is different from the instrumental sort. In a sense there are no raw visual data: they are all heavily processed by the eye-brain system before even the observer is allowed access. As one obvious example, the generally logarithmic response of the eye (as opposed to the linear behavior of a CCD) has been carried over into the magnitude system we still use. There are other effects, from the well-substantiated, conveniently collected in the AAVSO *Manual for Visual Observing of Variable Stars* (AAVSO 2013), to the anecdotal. Thus the data must be handled differently, and assumptions about their behavior can be dangerous. As an example, Pierce and Jacoby (1995) used visual data on a historical supernova in a determination of Hubble's constant; Schaefer (1996) came to a different conclusion based on a model of visual response. In reply, Jacoby and Pierce (1996) disagreed with Schaefer's method. The point is that a model and an analysis of data gave different results.

My present aim is to work out some characteristics of the visual database, taking mostly a consumer's viewpoint. The actual practice of visual photometry is relevant only as far as it suggests hypotheses to be tested. In these hypotheses I do not claim to be complete; many more aspects of the data remain to be investigated. A referee has suggested age and experience of the observer (unfortunately, difficult to test with the publicly available AAVSO data) as well as possible variation over time periods of years. No doubt others will occur to the reader as we proceed. Whiting (2012) has already considered some aspects of comparison stars.

Previous work (e.g. Stanton 1999; Collins 1999; Zissell 2003) has generally dealt with the color term, that is, on how to transform visual observations to a standard instrumental filter. Here I concentrate on internal statistics, leaving a connection to instrumental data for later studies. It seems best to have a more detailed and reliable picture of visual data before comparing them to other forms. And of course if the spread of visual data is whole magnitudes, as some authors report (Williams 1987; Price *et al.* 2007), a small color term is hardly worth applying.

In this study I look at visual data on ten well-observed variable stars from the AAVSO International Database of the American Association of Variable Star Observers (AAVSO), calculating their residuals around the best-fitting curve. My aim is to determine the size of these residuals and work out what factors affect that size. Ten is of course an inadequate sample on which to base conclusions about tens of thousands of variable *stars*. However, thousands of observations by hundreds of observers constitute quite a firm foundation for conclusions about the *data*.

One important theme is comparing differences between observers with an observer's internal variation. Here, I will use "bias" to mean the average difference between an observer's data and the best-fitting curve; "precision" to mean an observer's standard deviation about that average; and "scatter" or "accuracy" to mean the combined standard deviation about the curve.

2. Data selection and processing

2.1. The stars

We need stars with many observations, not only to produce a well-defined light curve but to populate the residuals around it. Beyond that, we would like stars with different characteristics in order to investigate possible effects of the type of variation. The final sample includes three Mira-type long period variables, five semiregular variables (three of them naked-eye stars) and two carbon stars. The selection is not intended to be exhaustive or representative, but to test certain *a priori* plausible effects (detailed below). The data on TX Piscium were sparser than those of the other stars, which probably had a minor effect on its results.

The premier source of visual photometric data for researchers is the on-line portal of the AAVSO, used for all the data in this study (Kafka 2017). Unfortunately it is not practical to list the thousands of data points individually. For each star I limited the data to a single full apparition, to avoid problems with curve-fitting over a gap. All the data were downloaded from the AAVSO web site, using only those points identified as visual. In what follows I use "days" to mean Julian Day minus 2457000.

Points identified as "fainter than" were not used. Data flagged as "magnitude uncertain" were included, since they are part of the database and indeed might have told something about it. Unfortunately, there were not enough of them (12 out of a total of 8091) to allow much of a conclusion. No other selection was performed, since the aim was to characterize the data, not to study the stars.

2.2. Fitting functions

Getting the fit right in detail is more important for this study than for other types of analysis. A curve that places the maxima and minima at the right places and times, for instance, would be sufficient for determining the period and amplitude of a Cepheid or RR Lyrae. However, if it followed the rising branch of Mira's curve (see Figure 1) with too steep or too shallow a slope, it would give systematic offsets that would change the shape of the residual dispersion and possibly throw off the answers.

A simple smoothing is the common way to deal with visual data, but would tend to flatten extrema and thus possibly distort the residuals. I tried Legendre polynomials, but as terms were added artifacts appeared (sections that obviously departed from the trend of the observations) before a good fit was obtained. The periodic Gaussian functions of Inno *et al.* (2015) looked promising, but I was unable to get them to converge on these data. In the end I fell back on a Fourier expansion plus a linear term. I used the IDL "curvefit" routine, which performed a least-squares fit.

2.3. The fit

For each star, I started with a few Fourier modes and added terms until a decent fit by eye was obtained. Initially I hoped to be able to use the residuals about each fit to decide when to stop. The process of fitting Mira is shown in Table 1. The standard deviation of the residuals around the fit is shown. Their Gaussian character was tested by running a χ^2 comparison (which gives the probability of two distributions being the same, within expected fluctuations) with the normal distribution of the same mean and standard deviation, also computing skewness and kurtosis.

As one might expect, a fourth-order fit gets the gist of the variation but doesn't follow it closely. Fifth- and sixth-order fits don't fit the rising branch very well. The seventh-order fit captures the rising branch, but has a double minimum that I reject as unphysical; only by going to tenth-order do we get a single minimum. The data and the fit are shown in Figure 1, and residuals (data minus the fit) in Figure 2.

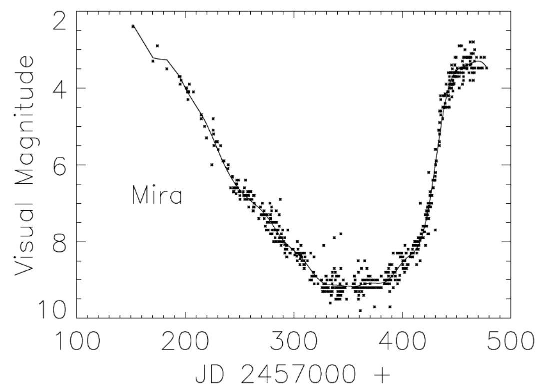

Figure 1. Visual observations of Mira, o Ceti, with the best-fitting average light curve superimposed. The most challenging task with fitting a curve proved to be following the steep rising branch without adding artifacts.

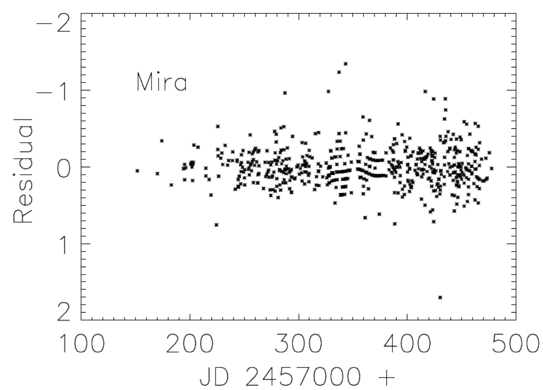

Figure 2. Residuals of the observations of Mira from the fitted light curve. The practice of most (but not all) visual observers of reporting to the nearest tenth-magnitude leads to some artifacts.

Table 1. Statistics for the best Fourier fit to the Mira visual observations.

Order	*σ*	*P(χ²)*	*Skew*	*Kurtosis*
4	0.329	0.0007	–0.129	2.47
5	0.298	0.0	–0.402	4.02
6	0.283	6×10^{-6}	–0.293	4.27
7	0.268	1.8×10^{-7}	–0.309	5.12
8	0.262	6.0×10^{-8}	–0.323	5.67
9	0.258	1.1×10^{-6}	–0.367	6.00
10	0.256	6.0×10^{-8}	–0.345	6.10

Note: From left to right: order of fit, scatter about the fit, probability of matching a normal distribution based on χ^2 (less than 10^{-8} shown as 0), skew, kurtosis.

Adding another Fourier term will *always* give a smaller scatter. The question here, as in many other situations, is whether the added term does any good; that is, does it reduce the scatter enough to make it worthwhile? For this we employ the F-ratio test on the variances, which gives the probability of the added term being useful.

Applying an F-ratio test on the Mira fits, all higher orders are significantly better fits than fifth (at the one-percent level), but order-by-order there is no preference beyond sixth and the tenth is no better than the seventh at the five-percent level. Thus, overall statistics of the residuals are no help at fitting the light curve. On the other hand (and this is important), the statistics are insensitive to details of the fit. Even a curve with obvious artifacts gives essentially the same statistics. (The F-ratio test assumes Gaussian behavior in the variance, which is not strictly true here. However, the qualitative conclusion stands: the scatter is not useful as a guide to the quality of fit.)

We want a better criterion than a by-eye fit and will need one for lower amplitude variables. To this end, consider the situation in Figure 3. Here the fit at a given order is shown by the smoother curve, while adding the next gives oscillations of a certain amplitude and wavelength around it. Focusing on one of these oscillations, evidently the average of the observations is displaced from that of the smoother curve by a certain amount. We ask: what is the probability that this happens by a chance fluctuation of residuals? The probability will be higher if there are fewer data points, if the amplitude is small, and if the standard deviation of the curve is large. Conversely, if the data points are dense and fit tightly around the curve, we will be able to detect a smaller real amplitude.

If the residuals are Gaussian with standard deviation σ, the chance of an offset by Δy over a number of observations n is related to Student's t-statistic:

$$t = \frac{\Delta y}{\sigma}\sqrt{n}. \tag{1}$$

We proceed as follows: from a previous curve of standard deviation σ, require any fluctuation to have a probability by chance of 5% or less over a number of observations $n = N/m$, where N is the total for the star and m the Fourier order. Using Equation 1 we find a threshold Δy, above which we accept the higher-order fit and below which we reject it.

This procedure should not be regarded as fully rigorous and quantitative. As noted in Table 1, the residuals are not Gaussian (this is true throughout our sample). More importantly, the amplitude of a high-order fit depends on observations outside a single oscillation (as we will see below). However, it does provide a consistent criterion for terminating the fitting procedure, and does answer the requirement that a higher density of observations is needed in order to accept higher-frequency and lower-amplitude features of the light curve (as noted by Trumpler and Weaver (1953)).

A summary of the input observations is provided in Table 2. R Andromedae, o Ceti (Mira), and R Leonis are Mira-type long period variables. U Monocerotis and R Scuti are large-amplitude semiregular variables, while α Herculis, α Orionis and μ Cephei are smaller-amplitude, naked-eye semiregular types. TX Piscium and V Aquilae are carbon stars.

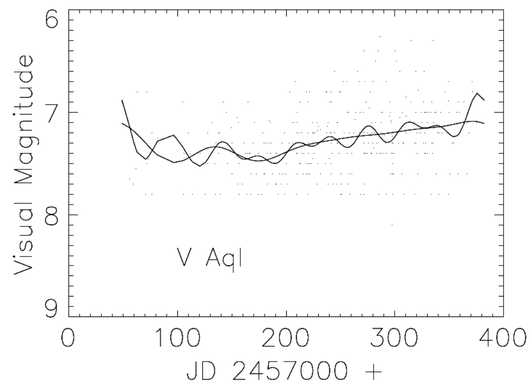

Figure 3. A step in the fitting of the light curve to V Aquilae. A lower-order fit gives the smoother curve; adding an additional order gives the more oscillatory one. Using the criterion developed in the text, the higher-order correction is rejected as noise.

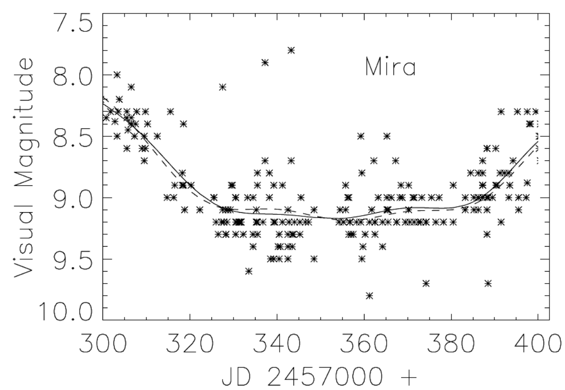

Figure 4. Observations of Mira along with the tenth-order fit (smooth curve) in the region of the minimum. Note the low-amplitude thirty-day oscillation.

Table 2. Summary of the input visual observations of ten variable stars.

Star	*Obns*	*Obsrs*	*Obsn day^{-1}*	*Order*
α Herculis	634	35	1.94	5
α Orionis	603	72	2.05	6
μ Cephei	1754	105	4.05	4
U Monocerotis	781	70	2.67	10
R Andromedae	386	62	0.99	7
R Scuti	2118	148	6.08	15
TX Piscium	124	13	0.45	2
o Ceti	594	88	1.82	10
R Leonis	745	124	2.74	6
V Aquilae	352	47	1.06	3

Note: The columns are: star designation; number of observations; number of observers; average observations per day; order of best Fourier fit.

2.4. The Full Moon effect

In the tenth-order fit for Mira there remains a stubborn oscillation of about 0.03 mag amplitude with a thirty-day period. Using the t-statistic criterion I reject it as an artifact of the data; but efforts to smooth it out proved unavailing. Looking more closely at one section of the curve, near the minimum (see Figure 4), we find that there is a thirty-day oscillation in the *number* of observations. About day 320, 350, and 380 there are few, with pulses of activity between. Following a hunch, I found that days 322, 352, and 382 were Full Moons. Clearly the amateur astronomers who followed Mira were also looking at other deep-sky objects, and preferred dark skies for their work! This pulsing of observations apparently injected a signal into the thirty-day Fourier mode.

Such a Full Moon effect is also visible in the other Miras in our sample, R Leonis and R Andromedae, though not in the other stars. The amplitude is small, and it has no effect on the overall statistics. But the implications for this and other citizen-science efforts are large: unexpected artifacts, statistically robust, can appear without warning.

3. Results and discussion

3.1. Residuals

A summary of the fits and residuals is provided in Table 3.

The first thing to notice is the size of the residuals ("Scatter" in the table). Previous work has generally given much larger figures. Williams (1987) determined a value of 0.5 magnitude from variations in field orientation alone, though that was for a single observer. Simonsen (2004) cites 1.5–2.0 mag, without giving details. Price *et al.* (2007) show a scatter ranging from 0.2 to 1.0 mag, heavily dependent on spectral type. In contrast, Whiting (2012) gives a scatter of 0.2 to 0.3 mag for visual observations of Miras.

The study of Price *et al.* (2007) is, however, problematic. They took data from the AAVSO database on 3542 stars, each with 1000 or more observations, and subtracted a tenth-order polynomial. They do not say what time span was covered, though they imply that multiple periods were included. There is no indication of how well the polynomial fit the actual light curve, or indeed that they considered the matter. It is impossible to tell what part of their results arise from a poor fit and what part is real. Their work is, therefore, not useful for the present study.

What about the data points flagged as "magnitude uncertain?" Mira has one such point, with a residual of –0.526, twice the size of the overall scatter, though not the largest residual for that star. R Andromedae has two, which at –0.143 and 0.243 are unremarkable. The well-observed μ Cephei has eight, whose standard deviation of 0.249 is greater than that of the whole dataset, though not by much. The single "uncertain" data point for V Aquilae has a residual of –0.013, much *smaller* than the run of the data. No other stars have data so flagged. From this small sample all we can conclude is that there is no reason to exclude "magnitude uncertain" data from any study, and they are included here.

The next thing to notice is that the scatter varies appreciably from star to star. There is, thus, no single figure for "the accuracy of visual photometry." Reference to Table 2 shows that it's not a matter of number or density of observations, or the Fourier order of the fit. Where else might it come from?

People are known to see what they expect to see. Perhaps a star varying swiftly, or over a great range, would be harder to follow. To test this, each star's speed of variation as well as its total range are listed in Table 3. For the speed, the slope of the fitting function was evaluated at each data point, and the standard deviation of these slopes calculated. Neither range nor speed shows a correlation with scatter, as is shown by Figures 5 and 6. Nor is predictability important: the semiregular variables show no overall tendency toward larger residuals than the more predictable Miras.

Surely color will play a part, since color perception varies widely among people. Indeed, V Aquilae, one of the reddest stars known, has the largest residuals in the sample. However, TX Piscium, the next reddest star, shows no unusual scatter. Or consider pairs of stars: TX Piscium and o Ceti differ in color more than do Betelgeuse and Rigel, and they have the same scatter. R Leonis and V Aquilae differ by even more, and again have indistinguishable accuracy. If there were a color effect it would certainly show up in these pairs, and it doesn't. A color-scatter plot is shown in Figure 7.

Table 3. Summary of the fits and residuals for the ten variable stars.

Star	*Scatter*	*B−V*	*dm/dt*	*δ m*	*Skew*	*Kurt*
α Her	0.141	1.45	3.8	0.39	1.78	5.53
α Ori	0.197	1.85	3.5	0.37	0.020	0.019
μ Ceph	0.212	1.35	2.2	0.40	0.512	0.895
U Mon	0.227	1.18	34.1	1.12	0.328	0.339
R And	0.245	1.97	55.8	8.32	–2.60	1.56
R Sct	0.249	1.47	46.4	1.80	0.053	1.12
TX Psc	0.252	2.60	3.8	0.58	–0.334	0.278
o Cet	0.256	1.10	63.1	6.82	–0.345	6.11
R Leo	0.329	1.41	31.0	4.91	–0.503	1.29
V Aql	0.337	4.19	1.7	0.50	–0.004	2.15

Note: The columns are: star designation; standard deviation of the residuals, in mag; B−V color; standard deviation of the speed of variation, in mmag day^{-1}; total amplitude of variation (minimum to maximum), mag; skew; excess kurtosis.

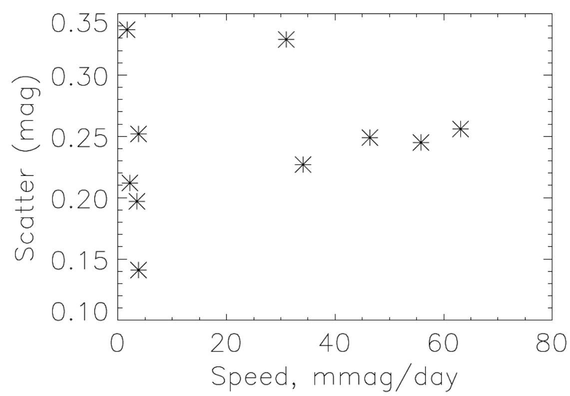

Figure 5. Scatter of the residuals of the ten stars plotted against the speed of variation (standard deviation of the slope of the fitting function, as evaluated at each data point). No correlation is evident.

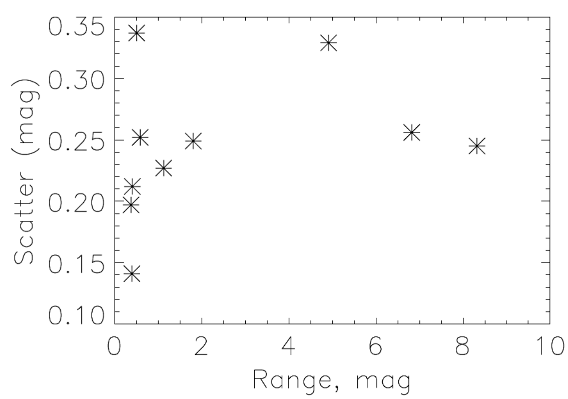

Figure 6. Scatter of the residuals of the ten stars plotted against the total range of variation. No correlation is evident.

We come to the surprising conclusion that the color of a star does not seem to affect the accuracy of its brightness estimate. This is not unprecedented, however; Whiting (2012) found that the colors of comparison stars had no effect on the scatter of visual estimates of Mira variables.

One might guess that naked-eye stars would be more difficult subjects, since comparison stars will generally be

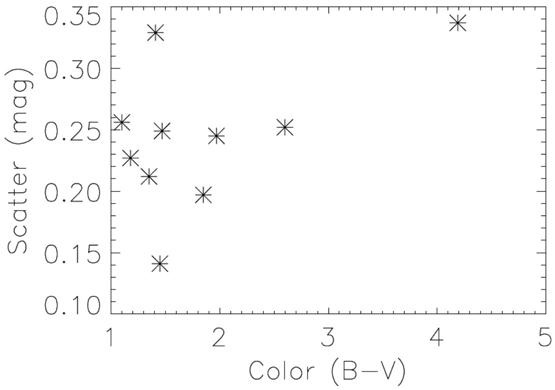

Figure 7. Scatter of the residuals of the ten stars plotted against B–V color. Note that the contrasting stars of Orion, Rigel and Betelgeuse, have a difference in B–V color of about 1.48, much less than is covered here.

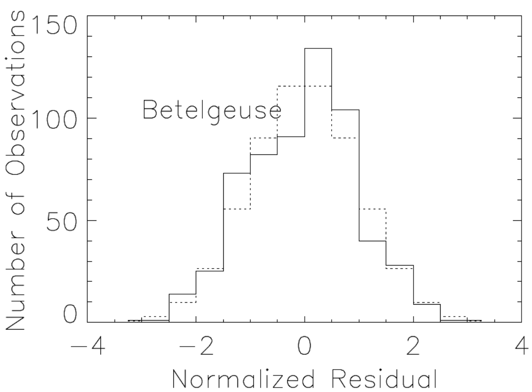

Figure 8. Residuals of observations of Betelgeuse (solid histogram) compared to a Gaussian of the same standard deviation (dotted histogram). The skew is evident. This star has the lowest excess kurtosis of the sample.

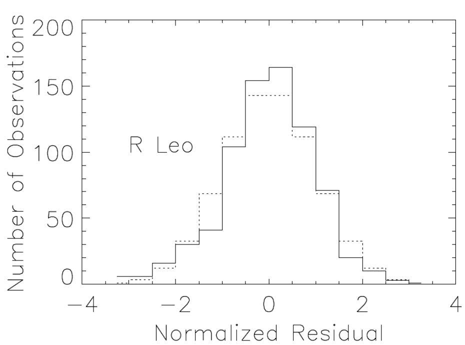

Figure 9. Residuals of observations of R Leonis (solid histogram) compared to a Gaussian of the same standard deviation (dotted histogram). Here the excess kurtosis is clear.

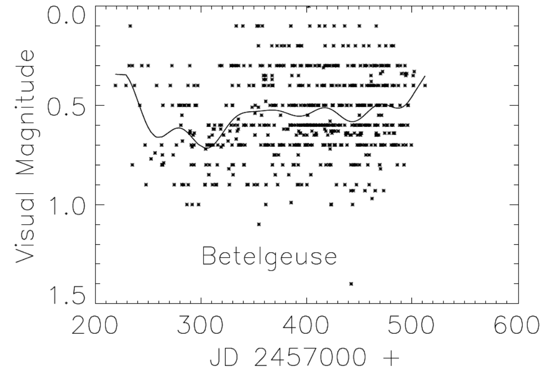

Figure 10. Visual observations of Betelgeuse, α Orionis, with the fitted light curve.

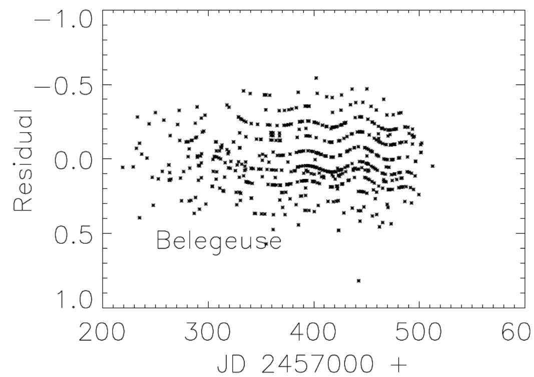

Figure 11. Residuals of the observations of Betelgeuse from the fitted light curve. The practice of most (but not all) visual observers of reporting to the nearest tenth-magnitude leads to some artifacts.

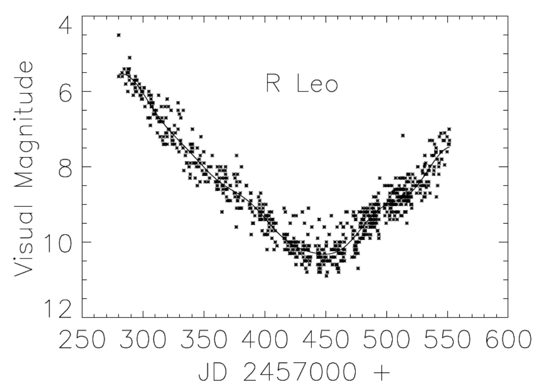

Figure 12. Visual observations of R Leonis with the fitted light curve.

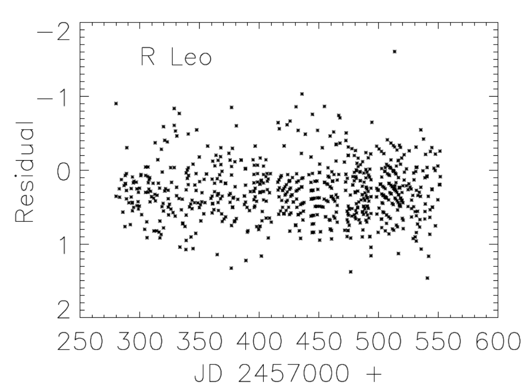

Figure 13. Residuals of the observations of R Leonis from the fitted light curve. The practice of most (but not all) visual observers of reporting to the nearest tenth-magnitude leads to some artifacts.

farther away in angular distance (and thus harder to keep in sight at the same time), and one is more likely to be distracted by other lights, to say nothing of airmass corrections. But the three naked-eye variables show the *least* scatter.

Thus, while the accuracy of visual photometry varies significantly among the stars in this sample, several plausible reasons for it do not apply.

One further feature of our sample brought out in Table 3 is the shape of the residuals. In all stars these are significantly non-Gaussian. For the most part they are not drastically different, but the departure is visible when plotted. (The exception is TX Piscium; for this star, I suggest that the observations are simply too few and sparse to rule out normality, rather than that they obey a different distribution). They all agree in having excess kurtosis (a sharper peak and more outliers than Gaussian) and significant skew, though there is no agreement on the sign of the latter. Examples of the shape of residuals compared to Gaussian are shown in Figures 8 and 9.

At this point our analysis proceeds by making eight plots for each star. It is obviously impossible to present all 80 of these within the confines of a paper. Instead, I include representatives of each type, generally R Leonis and Betelgeuse as high and low scatter stars, respectively, or others that illustrate specific results. All the plots are available in Appendix A. Fits and residuals for Betelgeuse and R Leonis are shown in Figures 10, 11, 12, and 13.

Visual observations are reported to the nearest tenth of a magnitude, a quantization obvious in the low-amplitude plots. Could this be the source of the non-Normal shape? To test this, I took the fitted curve, added random Gaussian noise, rounded to the nearest tenth-magnitude, and re-ran the fitting procedure. In each case the Gaussian character (and standard deviation) of the synthetic residuals was returned. Quantization affects neither the size nor the shape of visual residuals.

However, the re-fitted curves are not exactly the same as the originals. For most of the stars and most of the time the difference is of the order 0.03–0.04 magnitude. To see this it is necessary to zoom in on a small section of the data, for instance as in Figure 4, where the smooth curve is the original fit and the dashed curve the re-fit. However, in U Monocerotis local minima sometimes fail by a larger amount (see Figure 14). In V Aquilae, sparse observations during the beginning and end of the apparition create greater uncertainty there (Figure 15). It is beyond the scope of this paper to work out rigorously how firmly the curves are determined by the data, but these examples should give some idea.

3.2. Demographics

How much does it matter who does the observing? In particular, can the difference in residuals between stars be explained by populations of observers with greater or lesser accuracy?

As a first step in studying the demographics of visual photometry, I break down the observers by number of observations. That is, I count the number of observers who submitted one observation of a particular star, two observations, and so forth. Two representative histograms are shown in Figures 16 and 17.

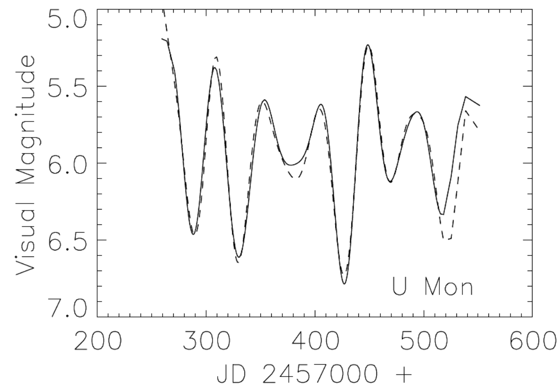

Figure 14. Original fitted light curve of U Monocerotis (solid curve) compared with one with synthetic Gaussian residuals (dashed curve). They fail to match the amplitudes in some minima.

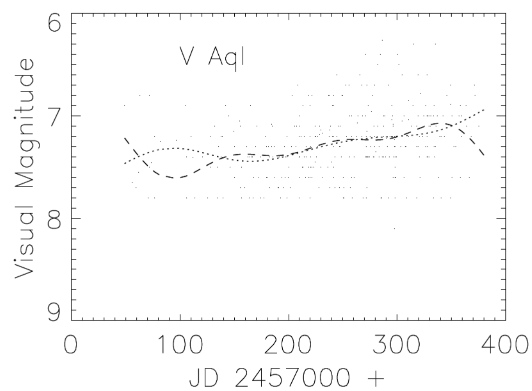

Figure 15. Original fitted light curve of V Aquilae (dashed curve) compared with one with synthetic Gaussian residuals (dotted curve). They match relatively poorly during the sparsely-observed beginning and end of the apparition.

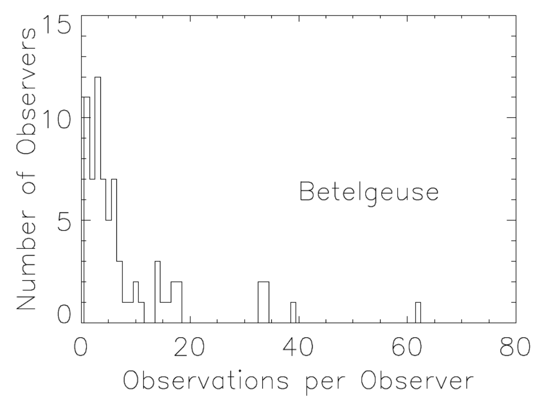

Figure 16. Number of observers of Betelgeuse compared to the number of observations each submitted. The database is dominated neither by the few-observation observers nor the handful of very active ones.

There are more observers with few observations than with many. However, counting up the contributions the mass of *observations* is not dominated by either end of the spectrum. The same holds true for all our stars (with the exception of TX Piscium, which has a relative lack of low-activity observers). The difference in residuals between stars thus cannot be attributed to observer populations of higher or lower activity. If we make the plausible assumption that low-activity observers are those with less experience, the difference is not

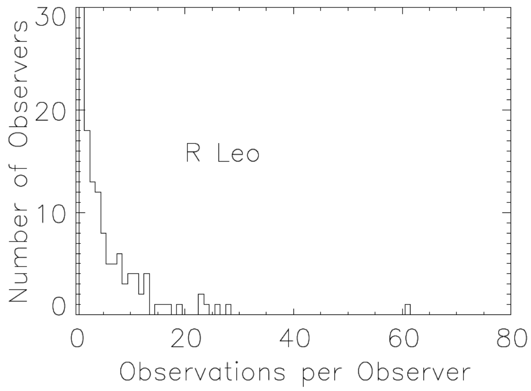

Figure 17. Number of observers versus number of observations per observer for R Leonis. Again, the mass of observations is not dominated by either end of the spectrum of activity.

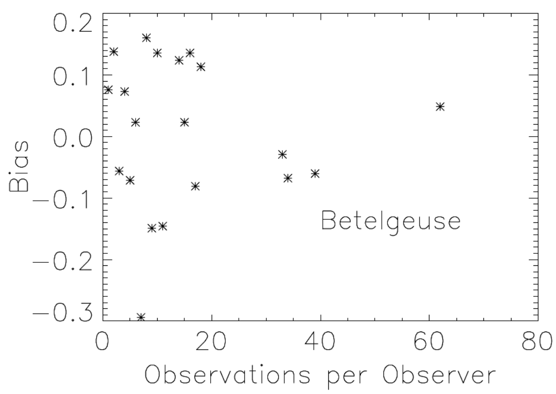

Figure 18. Bias (average residual about the fitted curve) for observations of Betelgeuse, broken down by number of observations made by the observer.

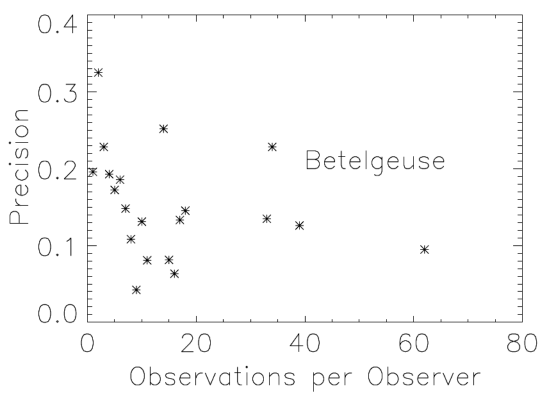

Figure 19. Precision (standard deviation of residuals) for observations of Betelgeuse, broken down by number of observations made by the observer.

due to some stars being popular with neophytes and others with veterans. (This assumption is far from certain. There are many reasons why an experienced observer might only submit a few estimates for a given star in a given season. However, it is probably true overall, and one whose observations are in the dozens certainly has gained some experience.)

Pursuing the question of observer populations further, I break down the residuals for each observer into the average (bias) and the standard deviation about that average (precision). Representative plots for bias and precision as a function of

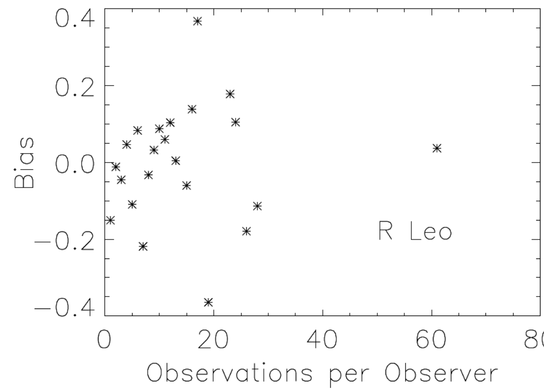

Figure 20. Bias (average residual about the fitted curve) for observations of R Leonis, broken down by number of observations made by the observer.

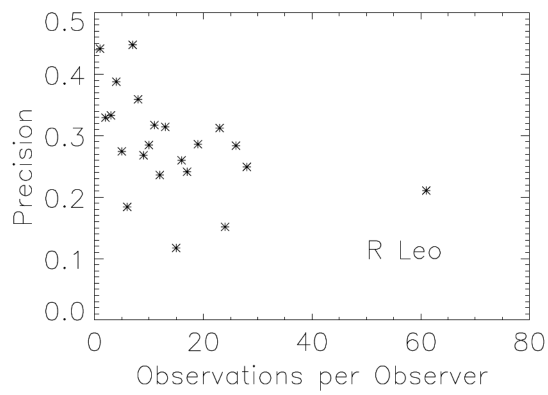

Figure 21. Precision (standard deviation of residuals) for observations of R Leonis, broken down by number of observations made by the observer.

number of observations are shown in Figures 18, 19, 20, and 21.

In each case, out to about thirty observations there is no apparent advantage to additional experience. It might appear that the points beyond are more precise or of smaller bias, but there are really too few to conclude that.

The next step is to compare the relative size of bias and precision. Plotting them against each other for each observer, something like Figures 22 and 23 results (corresponding plots appear in Appendix A). Straight lines are included to show where bias and precision are equal in magnitude, and error bars on bias produced by dividing the figure by the square root of the number of observations. (Error bars are not included for precision to avoid excessive clutter.)

There are observers more or less evenly spread over the plots, which would indicate that bias and precision contribute roughly equal amounts to residuals. For those observers inside the "funnel," bias is less important; outside, bias is more important. However, observers outside the funnel are predominantly those with large error bars and hence few observations. Most of the *observations* are inside the funnel, showing that observer-to-observer bias contributes less to the residuals than the precision of each observer's data.

A summary of the combined bias and precision for each star is given in Table 4. As shown by Figures 22 and 23, the contribution of bias to total scatter is somewhat overstated

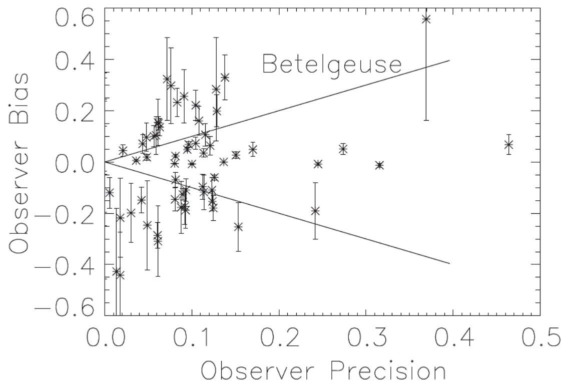

Figure 22. Bias (average of residual around the fitted curve) compared with precision (standard deviation around the average) for the observers of Betelgeuse. The straight lines show where the quantities are equal *in magnitude*. Error bars are produced by dividing the bias by the square root of the number of observations; similar bars for precision are omitted for clarity.

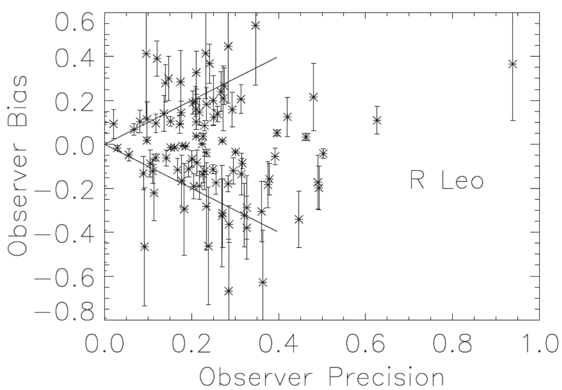

Figure 23. Bias (average of residual around the fitted curve) compared with precision (standard deviation around the average) for the observers of R Leonis. The straight lines show where the quantities are equal *in magnitude*. Error bars are produced by dividing the bias by the square root of the number of observations; similar bars for spread are omitted for clarity.

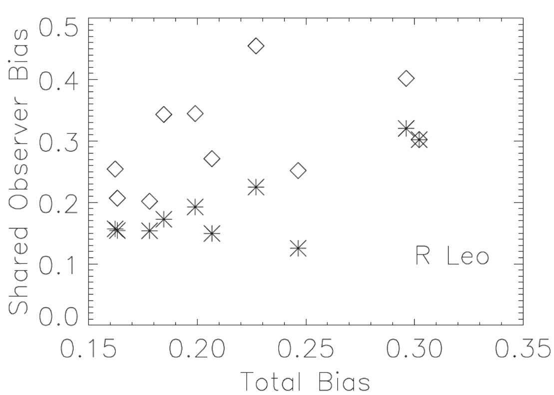

Figure 24. Comparison of the bias of sets of observers of R Leonis and another star. For each star, the standard deviation of the bias of the shared observers at R Leonis is shown by a diamond, at the other star by an asterisk; the ordinate is the standard deviation of the bias of all observers of the other star. The consistent trend is for observers to be less accurate at R Leo itself.

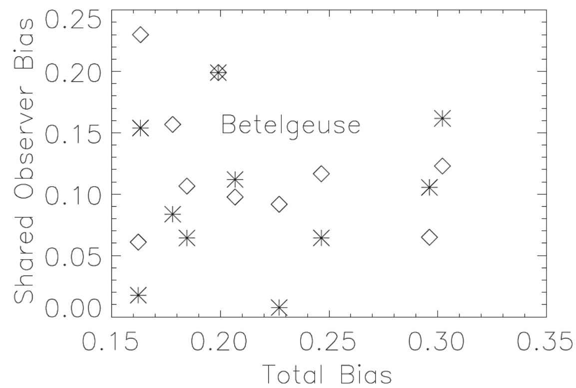

Figure 25. Comparison of the bias of sets of observers of Betelgeuse and another star. For each star, the standard deviation of the bias of the shared observers at Betelgeuse is shown by a diamond, at the other star by an asterisk; the ordinate is the standard deviation of the bias of all observers of the other star. Betelgeuse observers show higher bias at home than at low-bias stars, lower at home than high-bias stars.

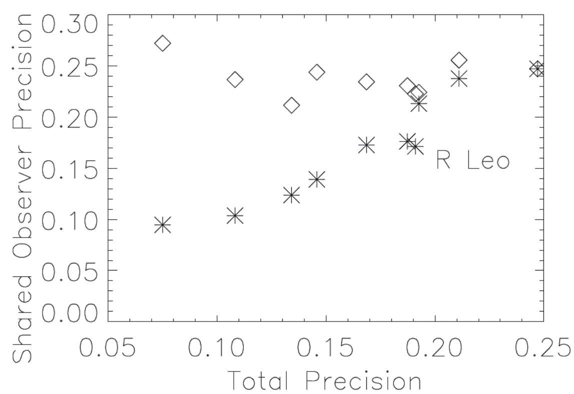

Figure 26. Comparison of the precision of sets of observers of R Leonis and another star. For each star, the average of the precision of the shared observers at R Leonis is shown by a diamond, at the other star by an asterisk; the ordinate is the average precision of all observers of the other star. The shared observers have indistinguishable precision at R Leonis, but their performance at other stars marches in step with that of all observers of that star.

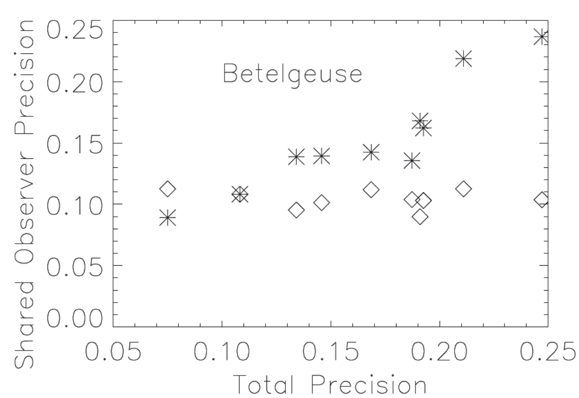

Figure 27. Comparison of the precision of sets of observers of Betelgeuse and another star. For each star, the average of the precision of the shared observers at Betelgeuse is shown by a diamond, at the other star by an asterisk; the ordinate is the average precision of all observers of the other star. The shared observers have indistinguishable precision at Betelgeuse, but their performance at other stars marches in step with that of all observers of that star.

Table 4. Contribution of bias and precision to the total scatter of the residuals of visual observations.

Star	$B-V$	Bias	Precision	Scatter
α Her	1.45	0.163	0.075	0.141
α Ori	1.85	0.199	0.108	0.197
μ Ceph	1.35	0.207	0.146	0.212
U Mon	1.18	0.162	0.169	0.227
R And	1.97	0.246	0.187	0.245
R Sct	1.47	0.184	0.211	0.249
TX Psc	2.60	0.227	0.134	0.252
o Ceti	1.10	0.178	0.192	0.256
R Leo	1.41	0.302	0.247	0.329
V Aql	4.19	0.296	0.191	0.337

Note: "Bias" is the standard deviation of the observers' biases; "Precision" is the mean of the observers' precisions; "Scatter" is the standard deviation of all the residuals of a star. (They do not add in quadrature due to the varying number of observations per observer.) The second and fifth columns are repeated from Table 3 for convenience.

by the average figure given. Note that bias for R Leonis, a star of no unusual color, is the same size as for V Aquilae, an extremely red star. This underlines the fact that a difference in color perception between observers is not an important source of scatter.

Although we have concluded that accuracy is not correlated with the activity of a given observer, the possibility remains that stars with a smaller scatter owe it to observers with smaller residuals. Indeed, there is anecdotal evidence for elite observers accurate to 0.05 mag. Under this hypothesis, the small scatter of Betelgeuse is due to a group of intrinsically more accurate observers, while the large scatter of R Leonis is due to a less accurate group. To test this, we look at observers who submitted estimates on more than one star. The nominally elite Betelgeusans should perform as well on other targets, while the Leonids should have a consistently large scatter. (The observers of, say, both R Leonis and R Scuti would not necessarily be identical with those of R Leonis and μ Cephei, so we need to look at each group's performance at each star.)

First we plot the standard deviation of their bias at the "home" star with diamonds, then at the "away" star with asterisks, using as an ordinate the standard deviation of all observers' bias at the "away" star. The resulting plots are Figures 24 and 25. It is immediately apparent that there is no consistent "observer bias" even for limited subsets of observers; the figure can vary by a factor of two or more from star to star. R Leonis observers consistently have a smaller bias at the "away" star; Betelgeuse observers are less systematic, though there is a tendency to have a larger bias at Betelgeuse for stars with smaller total bias, and a smaller bias at Betelgeuse for stars with a larger total bias. Looking only at "away" stars, R Leonis observers tend to have a larger average bias than Betelgeuse observers, but there is much overlap.

Continuing the investigation with observer precision we obtain Figures 26 and 27. The shared observers' performance at their home star is very consistent: we have not picked out unusual sets of observers. Their spread at the "away" star marches in step with that of all other observers. Indeed, comparing the performance of nominally high-precision Betelgeusans with that of nominally low-precision Leonids, we find them essentially the same. We conclude that the variation of precision is in our stars, not in ourselves.

4. Conclusions

Some of the results reported here should be encouraging both to the users and producers of visual photometry. The internal accuracy of the method is tighter than several previous works have reported. Bias, the difference between observers, is less important than precision, the spread of each observer's residuals; moreover, the precision of any set of observers at a particular star seems to be about the same. Low-activity observers have accuracy similar to more productive ones. It is unlikely, therefore, that the light curve of any particular star will suffer from bias or inaccuracy through an unlucky choice of observers.

If we identify low-activity observers with newcomers, they should be encouraged that even their first observations are useful. This is in contrast with, for example, another citizen science project, the Galaxy Zoo. As shown by Figure 2 of Willett *et al.* (2013), users who classified fewer than 100 galaxies had low scores for consistency, and consistency increased with activity up to 1000 galaxies. I suggest that the usefulness of data from new variable star observers comes from the fact that the task is simple (which is *not* the same as easy), compared with the several steps of classifying galaxy images. (Probably the extreme visual task in astronomy is measuring double stars, where a year of steady work is necessary before producing any useful data at all (Argyle 2009); for full competence, Couteau (1981) desires eight or nine years, with a year's delay if switching to another telescope.) Veteran observers should be encouraged that their work on difficult objects (like carbon stars) is, in general, no less accurate than on apparently easier targets.

On the other hand, the present work has thrown up several puzzles. Visual accuracy varies from star to star with no obvious pattern; several plausible explanations fail to fit the data. The non-Gaussian character of residuals also awaits explanation. I note in passing that the existence of two (not several) populations of observers with different means and standard deviations might produce something like this, but that is only speculation.

It is possible that the small number of subjects in this study, ten stars of three different types, have somehow biased the results. In principle, the scatter around a cataclysmic variable curve or that of a supernova could look different. But it is very hard to see how. With 8091 data points from 319 observers, the characteristics of visual photometry seem well-established.

The curve-fitting procedure adopted here is adequate for the purpose, but could be improved, in particular to eliminate sensitivity to periodic noise.

For other projects involving citizen science, note that features of the data that are expected to be present (like greater uncertainty for redder stars) might not actually be there, while unexpected effects (as from the Full Moon) can appear. Even obvious things may need checking. That is perhaps the overall lesson, when people are concerned.

5. Acknowledgements

The author wishes to express his deep appreciation for the efforts of the AAVSO and especially the observers whose work is used here:

AAP	CADA	GELB	KMY	MTON	RJOC	TCGA
AAX	CAI	GGU	KOC	MVH	RKE	TDB
ACN	CCB	GGZ	KOS	MVO	RMAF	TDG
ACO	CGF	GLG	KRAA	MXS	RMW	TFK
ADI	CJE	GLZ	KSH	MZS	RPHA	TJP
AJV	CJOB	GMD	KSP	NAO	RZM	TMAA
AMIA	CKB	GMQA	KSQ	NBMA	SAC	TOO
ARL	CKLA	GPI	KSZ	NDQ	SANF	TPS
ARN	CLEA	GRIB	KTAA	NJO	SANG	TRE
ASA	CLQ	GVD	KTHA	OCR	SAO	TSAA
ASW	CMAE	GZN	KTJA	OJEA	SBAH	UAN
ATDA	CMAG	HAB	KUC	OJMA	SBEA	VANA
ATI	CME	HBB	KVI	OJR	SDAB	VBE
BANH	CMP	HCS	LALB	ONJ	SDAV	VDE
BARM	CNOA	HDH	LCR	PARA	SDEA	VED
BBA	CNT	HGUA	LDS	PAW	SET	VFK
BBI	COV	HIVB	LHS	PDQ	SGQ	VGK
BFO	CPE	HJRA	LKR	PEG	SHA	VII
BGMB	CQP	HKAB	LMT	PEI	SHS	VNL
BGZ	CSAA	HKB	LOCA	PEX	SIV	VOL
BHA	CSM	HMQ	LZT	PGRA	SJCA	VRUB
BHAF	CWO	HMV	MAEA	PHG	SJDA	VTY
BHS	CWP	HQV	MANH	PIJ	SJEA	VUG
BJAN	CXIA	HUR	MBEA	PJAA	SJME	VWS
BJFA	DABA	ILE	MCOA	PJGA	SJQ	WAU
BLD	DAT	JDAA	MCOB	PJJ	SLUC	WBOA
BLUA	DFR	JDAC	MCPA	PJOF	SLVA	WJAA
BMAK	DMA	JGE	MDEN	PKV	SLY	WJOB
BMU	DMO	JLZ	MDP	PLA	SMAI	WKL
BNBA	DMPA	JNDB	MED	PLU	SMDB	WKM
BNW	DNO	JTP	MEGA	PMB	SPAO	WPT
BOZ	DPWA	JZO	MHH	PPL	SQN	WPX
BPSA	DRCA	KAD	MJAF	PPS	SRAB	WSHA
BRAF	DROB	KAF	MJCA	PRCA	SRBR	WTHA
BRJ	DROD	KAM	MJEF	PRVA	SSAB	WUB
BSBB	DXAA	KB	MJHA	PTFA	SSHA	WWK
BSJ	EJO	KBA	MJOE	PTT	SSU	WZIB
BSM	EPE	KGT	MMAH	PUJ	SSW	YBA
BSR	FANB	KHEA	MMAL	PVAA	STI	YIGA
BTAD	FDA	KHL	MMH	PWMA	SUS	ZBOA
BTY	FDU	KIS	MMIE	PYAB	SVAE	ZGEA
BVE	FOM	KJAF	MOW	PYG	SWV	ZMAD
BVZ	FPAA	KKAA	MPS	QYIA	SXR	ZTAA
BWW	GAA	KLO	MQA	REP	SYU	
BWX	GALB	KMA	MRGA	RFP	SZOL	
BYQ	GATH	KMIC	MTH	RJG	TACA	

References

AAVSO. 2013, *AAVSO Manual for Visual Observing of Variable Stars*, AAVSO, Cambridge, MA.

Argyle, R. 2009, personal communication.

Collins, P. L. 1999, *J. Amer. Assoc. Var. Star Obs.*, **27**, 65.

Couteau, P. 1981, *Observing Visual Double Stars*, MIT Press, Cambridge, MA, 86.

Holdsworth, D. L., Rushton, M. T., Bewsher, D., Walter, F. M., Eyres, S. P. S., Hounsell, R., and Darnley, M. J. 2013, *Mon. Not. Roy. Astron. Soc.*, **438**, 3483.

Inno, L., *et al.* 2015, *Astron. Astrophys.*, **576A**, 30.

Jacoby, G. H., and Pierce, M. J. 1996, *Astron. J.*, **112**, 723.

Kafka, S. 2017, variable star observations from the AAVSO International Database (https://www.aavso.org/aavso-international-database-aid).

Leibowitz, E. M., and Formiggini, L. 2015, *Astron. J.*, **150**, 52.

Mayangsari, L., Priyatikanto, R., and Putra, M. 2014, AIP Conf. Proc., 1589, 37.

Pierce, M. J., and Jacoby, G. H. 1995, *Astron. J.*, **110**, 2885.

Price, A., Foster, G., and Skiff, B. 2007, *The Precision of Visual Estimates of Variable Stars* (AAS Meeting, January 2007).[1]

Schaefer, B. J., 1996, *Astron. J.*, **111**, 1668.

Simonsen, M. A. 2004, *J. Amer. Assoc. Var. Star Obs.*, **33**, 65.

Stanton, R. H. 1999, *J. Amer. Assoc. Var. Star Obs.*, **27**, 97.

Surina, F., Hounsell, R. A., Bode, M. F., Darnley, M. J., Harman, D. J., and Walter, F. M. 2014, in *Stella Novae: Past and Future Decades*, eds. P. A. Woudt, V. A. R. M. Ribiero, ASP Conf. Ser. 490, 169.

Trumpler, R. J., and Weaver, H. F. 1953, *Statistical Astronomy*, Univ. California Press (Dover edition 1962), Dover Publ., New York, 157.

Whiting, A. B. 2012, *Observatory*, **132**, 148.

Willett, K. W., *et al.* 2013, *Mon. Not. Roy. Astron. Soc.*, **433**, 2835.

Williams, D. B. 1987, *J. Amer. Assoc. Var. Star Obs.*, **16**, 118.

Zissell, R. E. 2003, *J. Amer. Assoc. Var. Star Obs.*, **31**, 128.

[1] Price, Foster, G., and Skiff (2007), https://www.aavso.org/sites/default/files/publications/staff_pubs/price_visual_precision.pdf.

Appendix A: Information on the stars in this study.

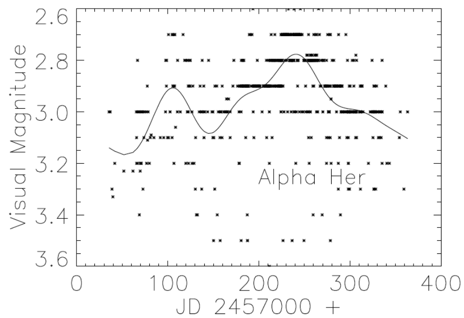

Figure A1a. Visual observations of α Herculis, with the best-fit average light curve superimposed.

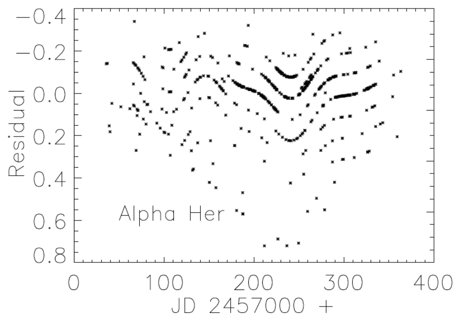

Figure A1b. Residuals of the observations of α Herculis, with the best-fit average light curve subtracted. Most (but not all) visual observers report to the nearest tenth-magnitude, leading to some artifacts.

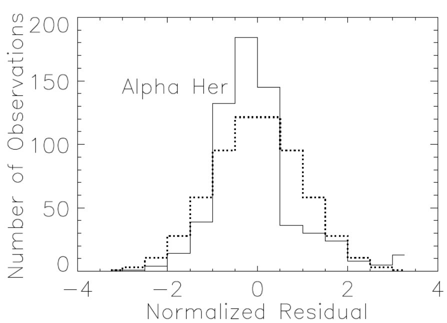

Figure A1c. Normalized residuals of α Herculis observations (solid line), with a Gaussian distribution superimposed (dotted line). The residuals are clearly non-Gaussian.

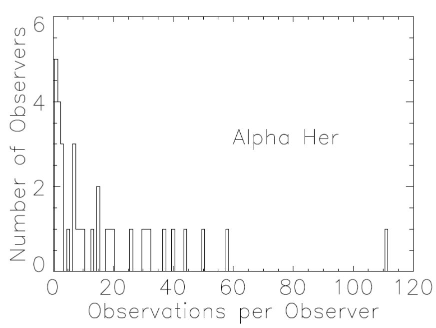

Figure A1d. The distribution of activity among observers of α Herculis. The data are not dominated by any single observer, nor by the single-digit observers.

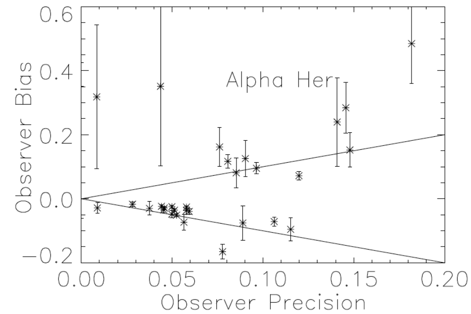

Figure A1e. Comparison of each observer's average distance from the best-fit curve (bias) with precision (the standard deviation about that average). Error bars in bias are derived by dividing the bias value by the square root of the number of observations; they are not shown for precision in order to keep the plot readable. Bias is smaller than precision for observers inside the lines drawn. Note that for most observers outside the lines, bias is not well-determined owing to few observations. Most observations fall inside the funnel.

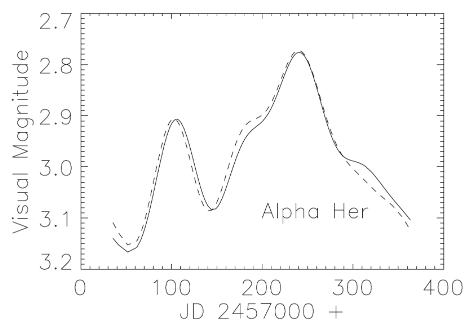

Figure A1f. The original light curve of α Herculis (solid curve) compared with the reconstructed one (dashed). The reconstructed curve was determined by imposing Gaussian residuals about the original curve, and redoing the fit.

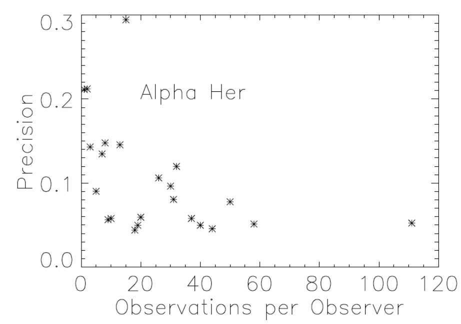

Figure A1g. The variation of observer precision with number of observations. There is some tendency for low-activity observers to have worse precision, but it depends mostly on a few outlying points.

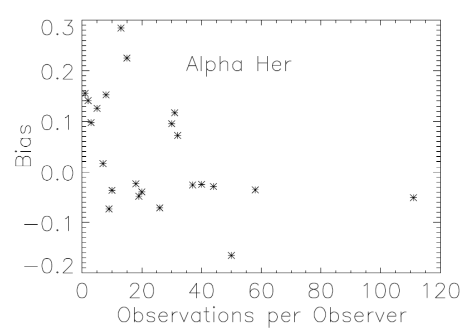

Figure A1h. The variation of observer bias with number of observations. There is no significant tendency for bias to become smaller with more activity.

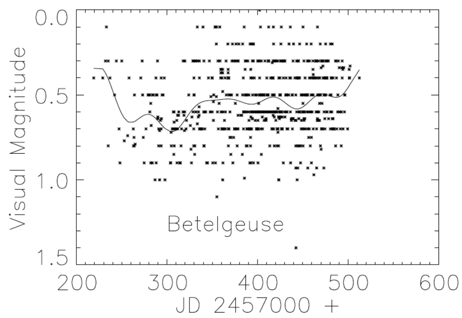

Figure A2a. Visual observations of Betelgeuse, α Ori, with the best-fit average light curve superimposed.

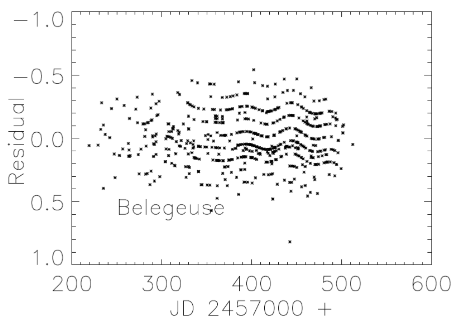

Figure A2b. Residuals of the observations of Betelgeuse, with the best-fit average light curve subtracted. Most (but not all) visual observers report to the nearest tenth-magnitude, leading to some artifacts.

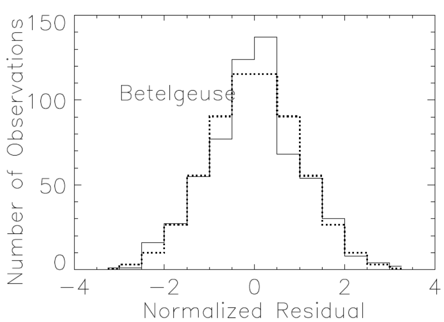

Figure A2c. Normalized residuals of Betelgeuse observations (solid line), with a Gaussian distribution superimposed (dotted line). The residuals are clearly non-Gaussian.

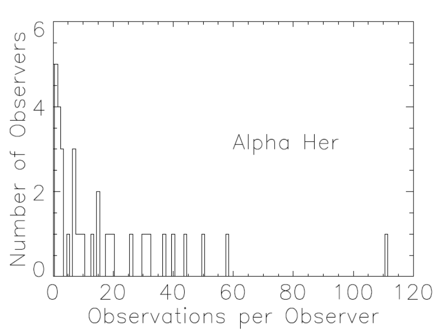

Figure A2d. The distribution of activity among observers of Betelgeuse. The data are not dominated by any single observer, nor by the single-digit observers.

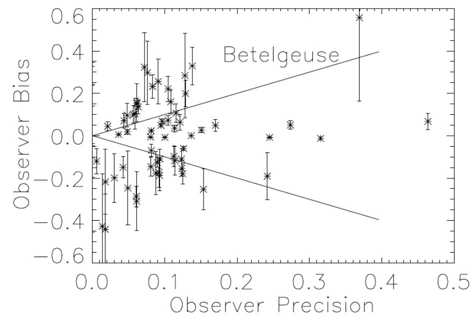

Figure A2e. Comparison of each observer's average distance from the best-fit curve (bias) with precision (the standard deviation about that average). Error bars in bias are derived by dividing the bias value by the square root of the number of observations; they are not shown for precision in order to keep the plot readable. Bias is smaller than precision for observers inside the lines drawn. Note that for many observers outside the lines, bias is not well-determined owing to few observations. Most observations fall inside the funnel.

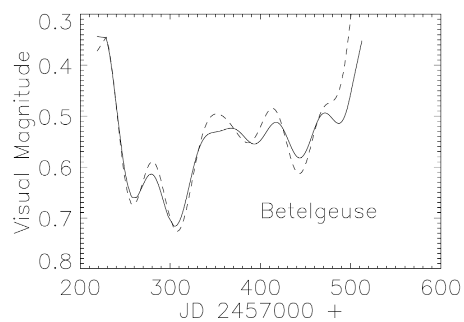

Figure A2f. The original light curve of Betelgeuse (solid curve) compared with the reconstructed one (dashed). The reconstructed curve was determined by imposing Gaussian residuals about the original curve, and redoing the fit.

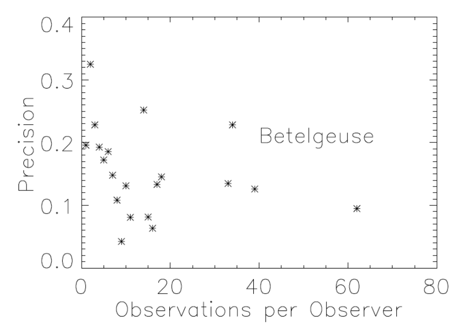

Figure A2g. The variation of observer precision with number of observations. There is no significant trend.

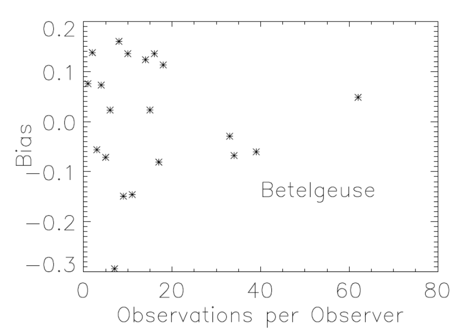

Figure A2h. The variation of observer bias with number of observations. There are too few points beyond 20 observations to reach a conclusion on overall trend; up to that point, there is certainly none.

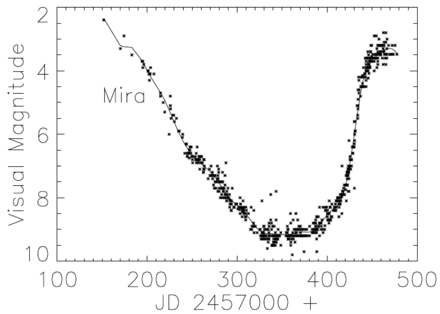

Figure A3a. Visual observations of Mira, o Ceti, with the best-fit average light curve superimposed.

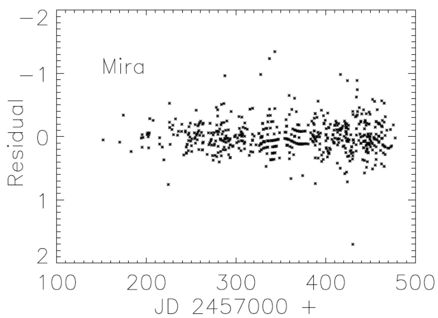

Figure A3b. Residuals of observations of Mira, with the best-fit light curve subtracted. The practice of most (but not all) observers of reporting to the nearest tenth-magnitude leads to some aritfacts.

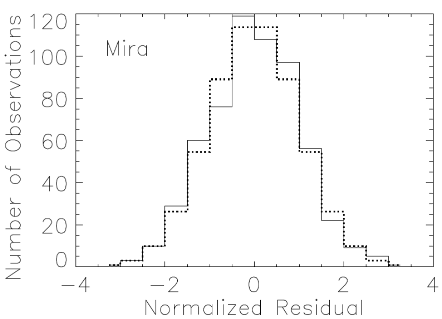

Figure A3c. Normalized residuals of Mira observations (solid line), with a Gaussian distribution superimposed (dotted line). The residuals are significantly non-Gaussian.

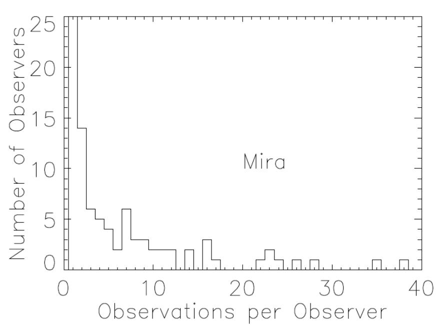

Figure A3d. The distribution of activity among observers of Mira. The data are not dominated by any single observer, nor by the single-digit observers.

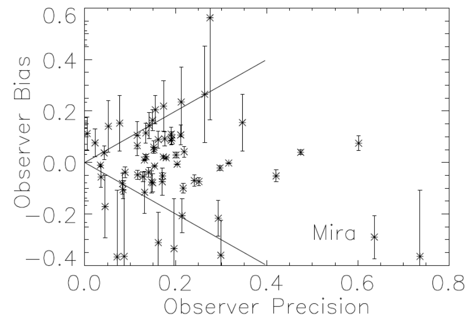

Figure A3e. Comparison of each observer's average distance from the best-fit curve (bias) with precision (the standard deviation about that average). Error bars in bias are derived by dividing the bias value by the square root of the number of observations; they are not shown for precision in order to keep the plot readable. Bias is smaller than precision for observers inside the lines drawn. Note that for most observers outside the lines, bias is not well-determined owing to few observations. Most observations fall inside the funnel.

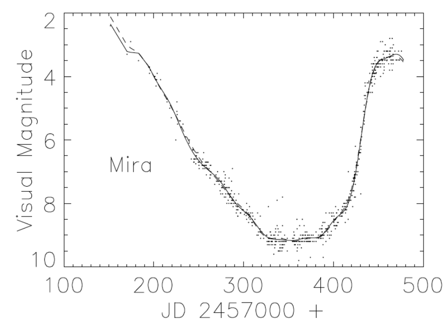

Figure A3f. Mira's original light curve (solid curve) compared with the reconstructed one (dashed). The reconstructed curve was determined by imposing Gaussian residuals about the original curve, and redoing the fit.

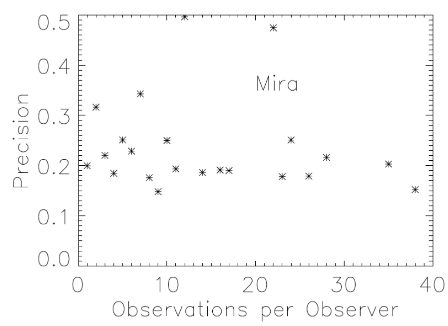

Figure A3g. The variation of observer precision with number of observations. There is no apparent trend.

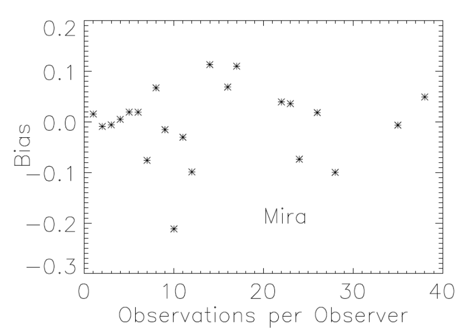

Figure A3h. The variation of observer bias with number of observations. Again, there is no apparent trend.

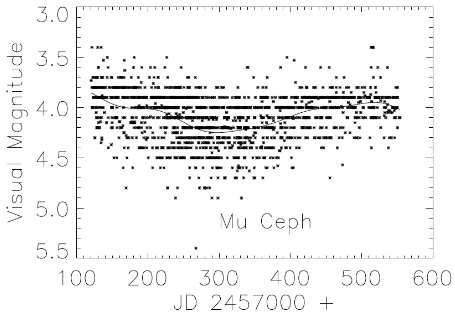

Figure A4a.Visual observations of μ Cephei, with the best-fit average light curve superimposed.

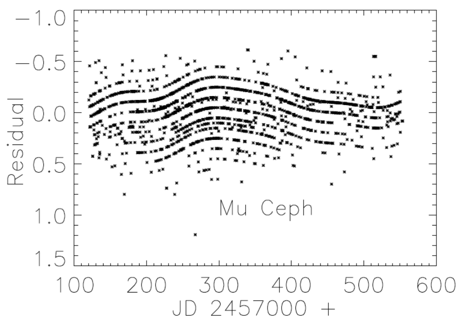

Figure A4b.Residuals of the observations of μ Cephei, with the best-fit average light curve subtracted. Most (but not all) visual observers report to the nearest tenth-magnitude, leading to some artifacts.

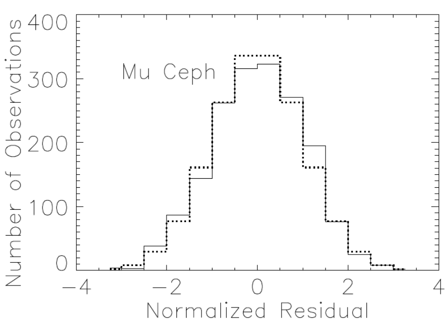

Figure A4c.Normalized residuals of μ Cephei observations (solid line), with a Gaussian distribution superimposed (dotted line). While similar, the residuals are significantly non-Gaussian.

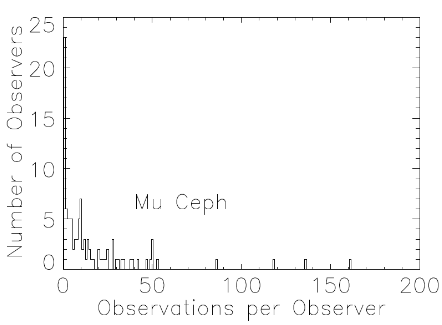

Figure A4d.The distribution of activity among observers of μ Cephei. The data are not dominated by any single observer, nor by the single-digit observers.

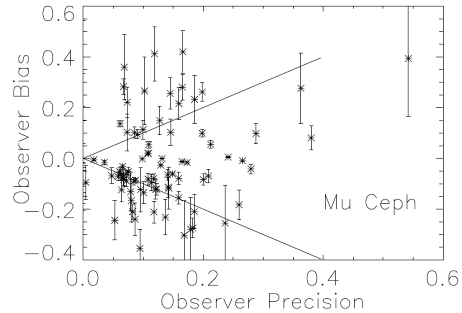

Figure A4e.Comparison of each observer's average distance from the best-fit curve (bias) with precision (the standard deviation about that average). Error bars in bias are derived by dividing the bias value by the square root of the number of observations; they are not shown for precision in order to keep the plot readable. Bias is smaller than precision for observers inside the lines drawn. Note that for many observers outside the lines, bias is not well-determined owing to few observations. Most observations fall inside the funnel.

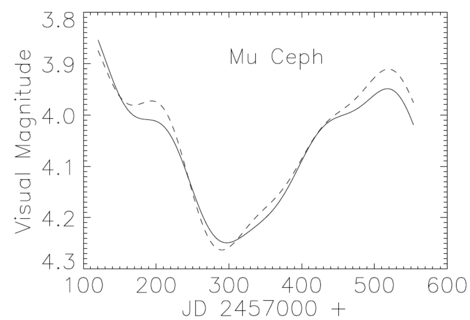

Figure A4f.The original light curve of μ Cephei (solid curve) compared with the reconstructed one (dashed). The reconstructed curve was determined by imposing Gaussian residuals about the original curve, and redoing the fit.

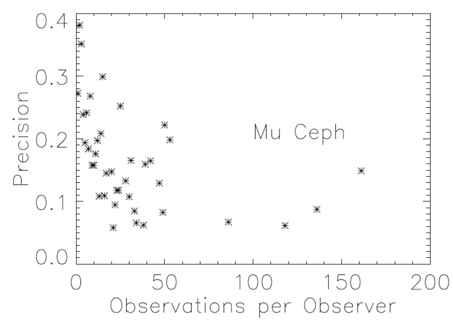

Figure A4g.The variation of observer precision with number of observations. There is no trend visible in the region below about 60 observations; above that, there are too few points to reach any conclusion.

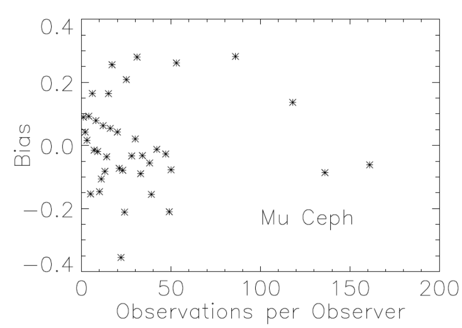

Figure A4h.The variation of observer bias with number of observations. There is no significant tendency for bias to become smaller with more activity.

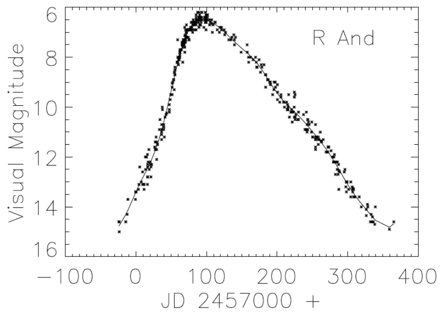

Figure A5a. Visual observations of R Andromedae, with the best-fit average light curve superimposed.

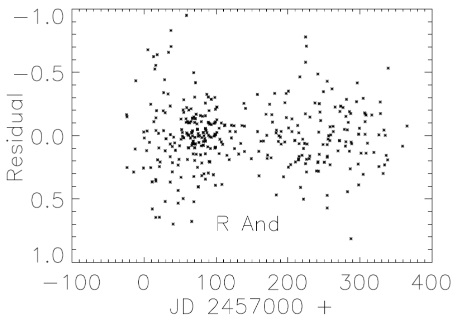

Figure A5b. Residuals of the observations of R Andromedae, with the best-fit average light curve subtracted. There is an apparent concentration of observations around maximum.

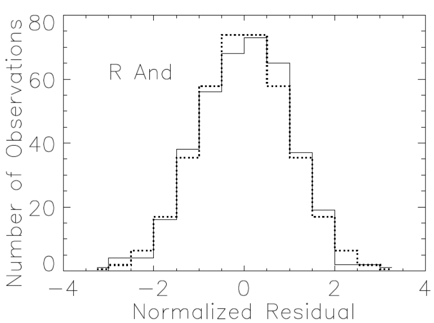

Figure A5c. Normalized residuals of R Andromedae observations (solid line), with a Gaussian distribution superimposed (dotted line). The residuals are significantly non-Gaussian.

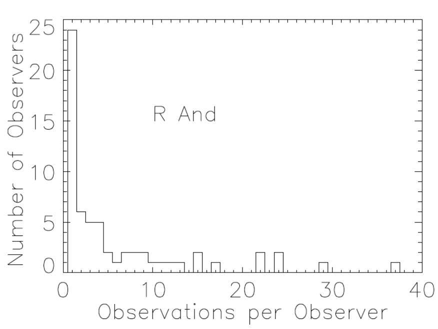

Figure A5d. The distribution of activity among observers of R Andromedae. The data are not dominated by any single observer, nor by the single-digit observers.

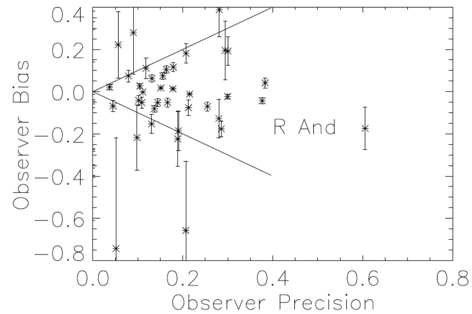

Figure A5e. Comparison of each observer's average distance from the best-fit curve (bias) with precision (the standard deviation about that average). Error bars in bias are derived by dividing the bias value by the square root of the number of observations; they are not shown for precision in order to keep the plot readable. Bias is smaller than precision for observers inside the lines drawn. Note that for most observers outside the lines, bias is not well-determined owing to few observations. Most observations fall inside the funnel.

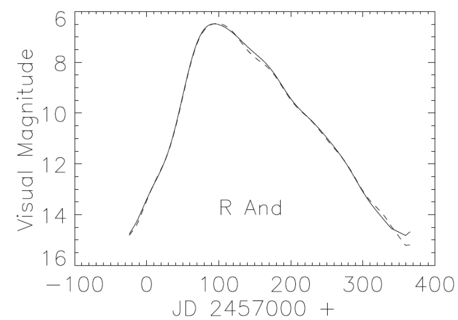

Figure A5f. The original light curve of R Andromedae (solid curve) compared with the reconstructed one (dashed). The reconstructed curve was determined by imposing Gaussian residuals about the original curve, and redoing the fit.

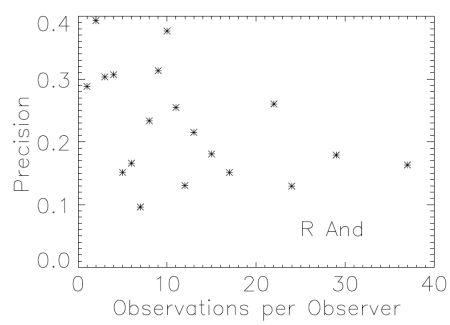

Figure A5g. The variation of observer precision with number of observations. There is some tendency for low-activity observers to have worse precision, but it depends mostly on a few outlying points.

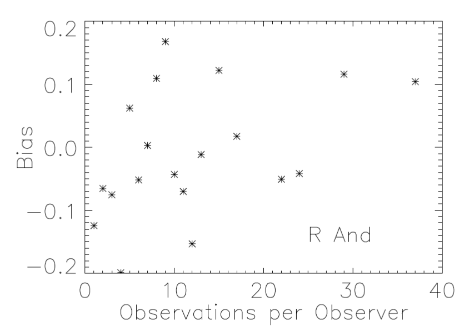

Figure A5h. The variation of observer bias with number of observations. There is no significant tendency for bias to become smaller with more activity.

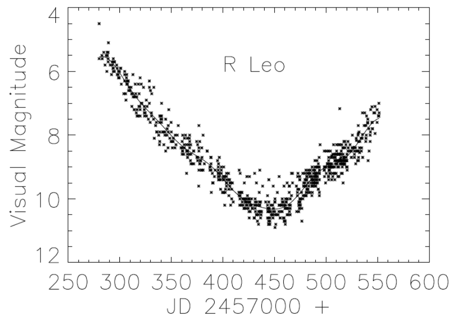

Figure A6a. Visual observations of R Leonis, with the best-fit average light curve superimposed.

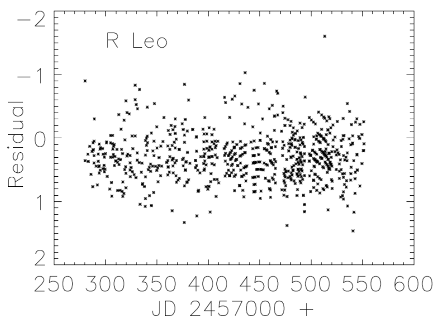

Figure A6b. Residuals of the observations of R Leonis, with the best-fit average light curve subtracted. Most (but not all) visual observers report to the nearest tenth-magnitude, leading to some artifacts.

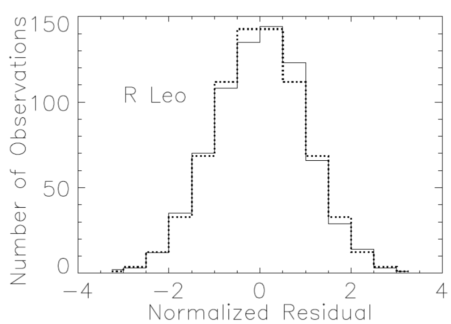

Figure A6c. Normalized residuals of R Leonis observations (solid line), with a Gaussian distribution superimposed (dotted line). The residuals are significantly non-Gaussian.

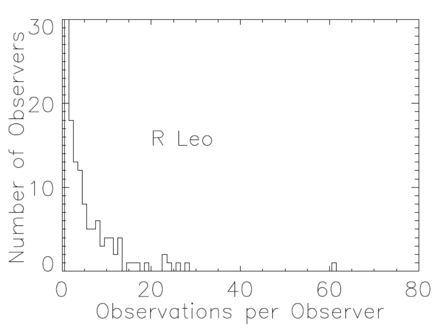

Figure A6d. The distribution of activity among observers of R Leonis. The data are not dominated by any single observer, nor by the single-digit observers.

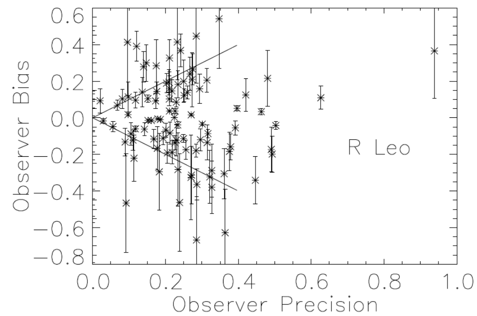

Figure A6e. Comparison of each observer's average distance from the best-fit curve (bias) with precision (the standard deviation about that average). Error bars in bias are derived by dividing the bias value by the square root of the number of observations; they are not shown for precision in order to keep the plot readable. Bias is smaller than precision for observers inside the lines drawn. Note that for most observers outside the lines, bias is not well-determined owing to few observations. Most observations fall inside the funnel.

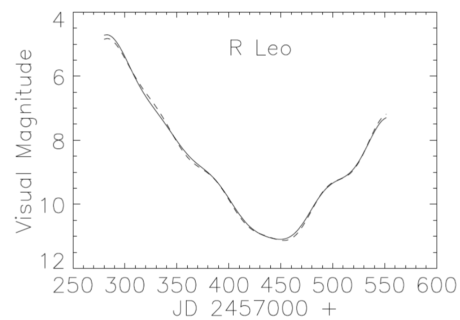

Figure A6f. The original light curve of R Leonis (solid curve) compared with the reconstructed one (dashed). The reconstructed curve was determined by imposing Gaussian residuals about the original curve, and redoing the fit.

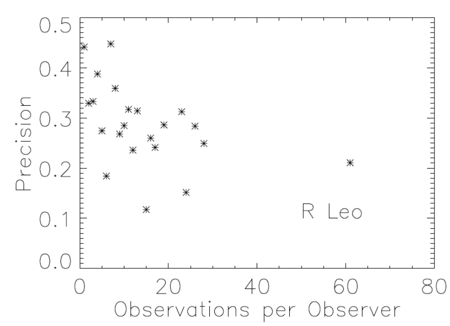

Figure A6g. The variation of observer precision with number of observations. There is a weak tendency for low-activity observers to have worse precision, but it depends mostly on a few outlying points.

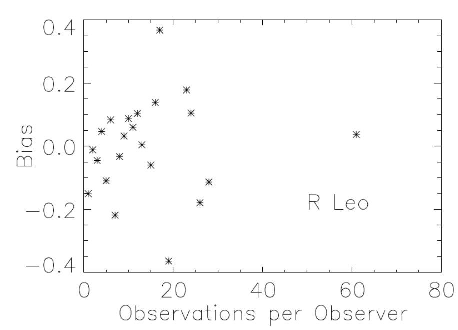

Figure A6h. The variation of observer bias with number of observations. There is no significant tendency for bias to become smaller with more activity.

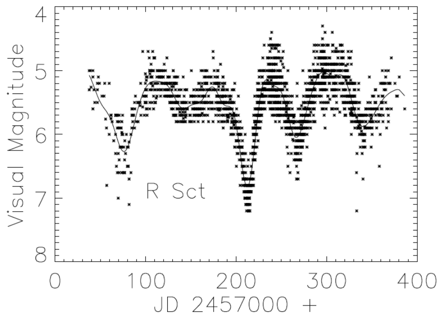

Figure A7a. Visual observations of R Scuti, with the best-fit average light curve superimposed.

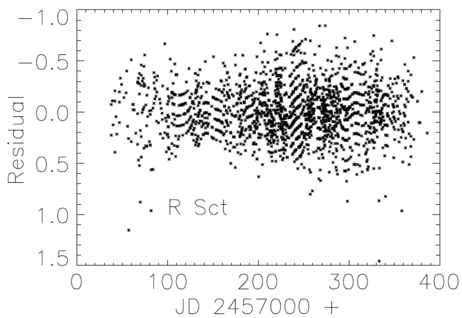

Figure A7b. Residuals of the observations of R Scuti, with the best-fit average light curve subtracted. Most (but not all) visual observers report to the nearest tenth-magnitude, leading to some artifacts.

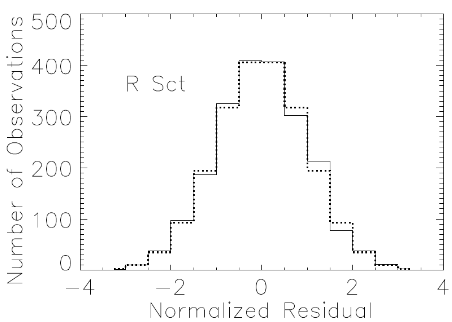

Figure A7c. Normalized residuals of R Scuti observations (solid line), with a Gaussian distribution superimposed (dotted line). The residuals are significantly non-Gaussian.

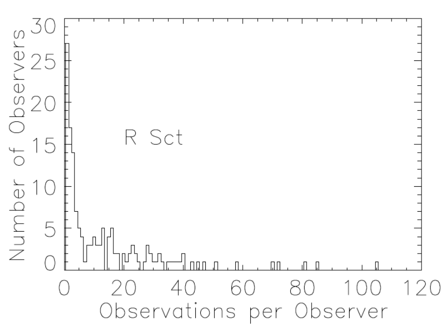

Figure A7d. The distribution of activity among observers of R Scuti. The data are not dominated by any single observer, nor by the single-digit observers.

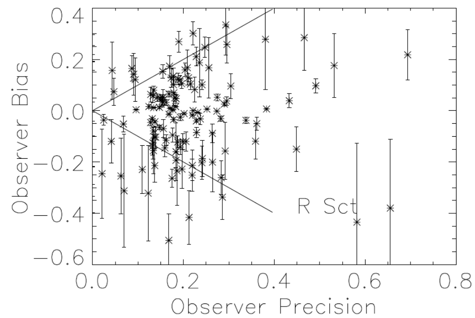

Figure A7e. Comparison of each observer's average distance from the best-fit curve (bias) with precision (the standard deviation about that average). Error bars in bias are derived by dividing the bias value by the square root of the number of observations; they are not shown for precision in order to keep the plot readable. Bias is smaller than precision for observers inside the lines drawn. Note that for most observers outside the lines, bias is not well-determined owing to few observations. Most observations fall inside the funnel.

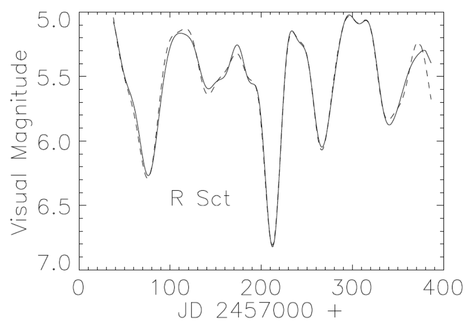

Figure A7f. The original light curve of R Scuti (solid curve) compared with the reconstructed one (dashed). The reconstructed curve was determined by imposing Gaussian residuals about the original curve, and redoing the fit.

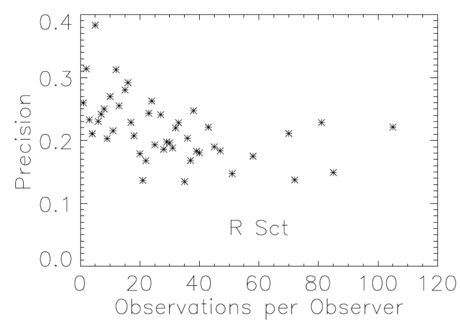

Figure A7g. The variation of observer precision with number of observations. There is some tendency for low-activity observers to have worse precision, but it depends mostly on a few outlying points.

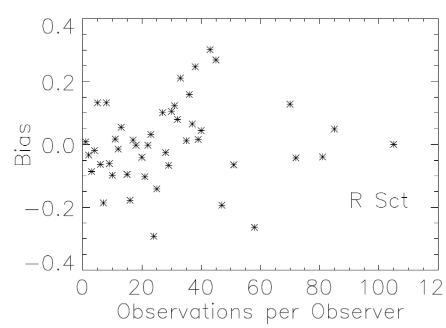

Figure A7h. The variation of observer bias with number of observations. There is no significant tendency for bias to become smaller with more activity up to about 60 observations; beyond that, there are too few points to allow a conclusion.

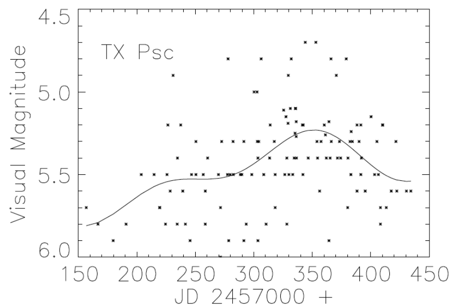

Figure A8a. Visual observations of TX Piscium, with the best-fit average light curve superimposed.

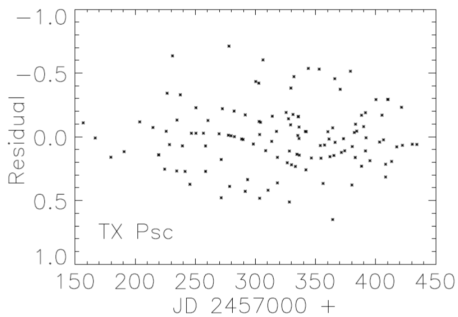

Figure A8b. Residuals of the observations of TX Piscium, with the best-fit average light curve subtracted. Most (but not all) visual observers report to the nearest tenth-magnitude, leading to some artifacts.

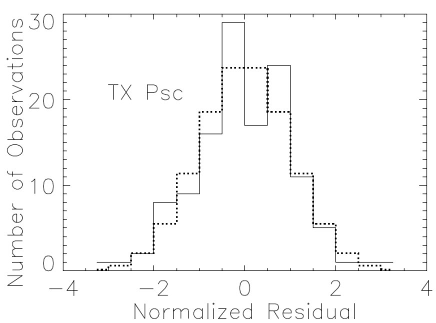

Figure A8c. Normalized residuals of TX Piscium observations (solid line), with a Gaussian distribution superimposed (dotted line). The residuals are consistent with being Gaussian.

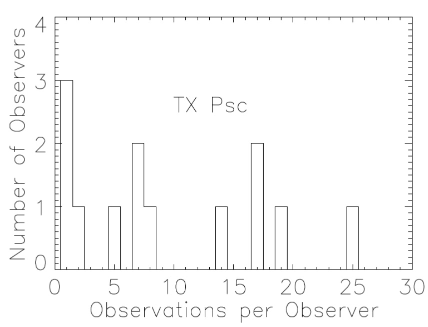

Figure A8d. The distribution of activity among observers of TX Piscium. There is a smaller proportion of low-activity observers compared with the other stars in this study.

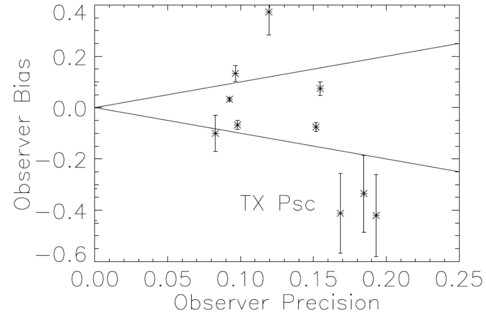

Figure A8e. Comparison of each observer's average distance from the best-fit curve (bias) with precision (the standard deviation about that average). Error bars in bias are derived by dividing the bias value by the square root of the number of observations; they are not shown for precision in order to keep the plot readable. Bias is smaller than precision for observers inside the lines drawn. Note that for most observers outside the lines, bias is not well-determined owing to few observations. Most observations fall inside the funnel.

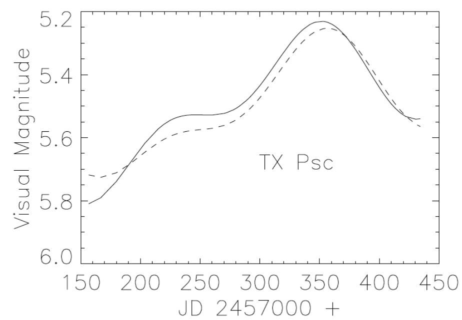

Figure A8f. The original light curve of TX Piscium (solid curve) compared with the reconstructed one (dashed). The reconstructed curve was determined by imposing Gaussian residuals about the original curve, and redoing the fit.

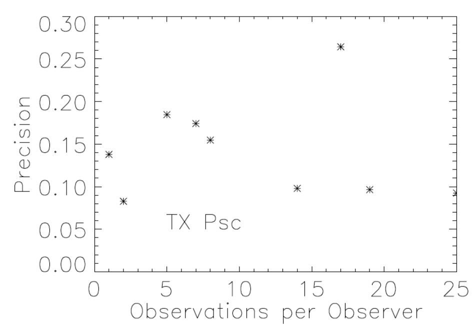

Figure A8g. The variation of observer precision with number of observations. There is no apparent trend.

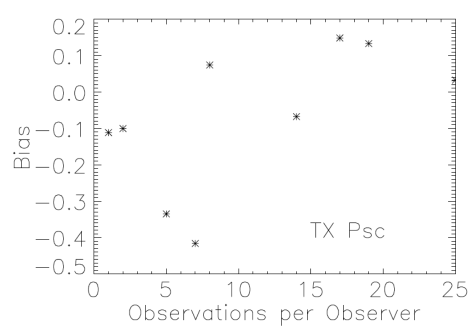

Figure A8h. The variation of observer bias with number of observations. There is no significant tendency for bias to become smaller with more activity.

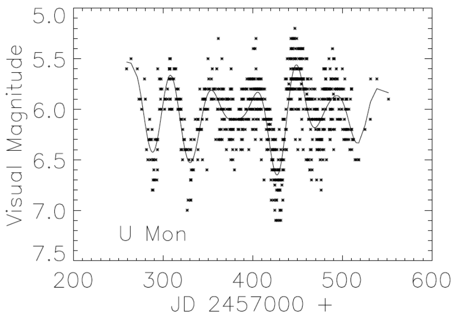

Figure A9a. Visual observations of U Monocerotis, with the best-fit average light curve superimposed.

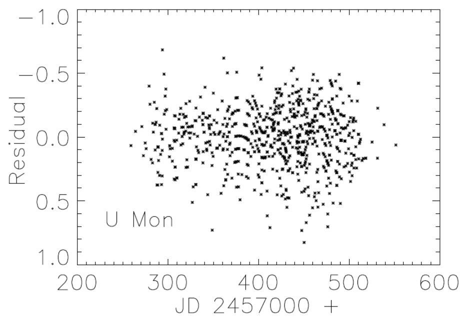

Figure A9b. Residuals of the observations of U Monocerotis, with the best-fit average light curve subtracted. Most (but not all) visual observers report to the nearest tenth-magnitude, leading to some artifacts.

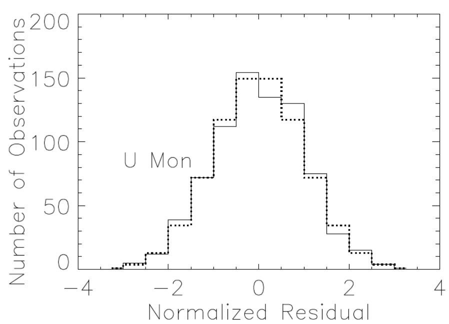

Figure A9c. Normalized residuals of U Monocerotis observations (solid line), with a Gaussian distribution superimposed (dotted line). The residuals are significantly non-Gaussian.

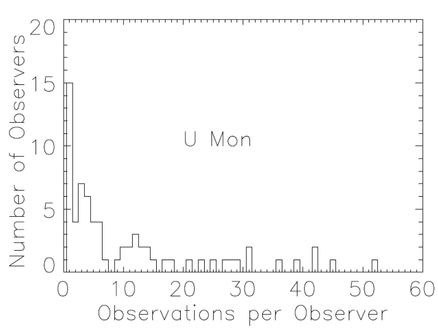

Figure A9d. The distribution of activity among observers of U Monocerotis. The data are not dominated by any single observer, nor by the single-digit observers.

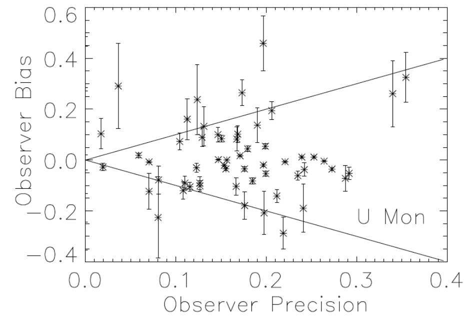

Figure A9e. Comparison of each observer's average distance from the best-fit curve (bias) with precision (the standard deviation about that average). Error bars in bias are derived by dividing the bias value by the square root of the number of observations; they are not shown for precision in order to keep the plot readable. Bias is smaller than precision for observers inside the lines drawn. Note that for most observers outside the lines, bias is not well-determined owing to few observations. Most observations fall inside the funnel.

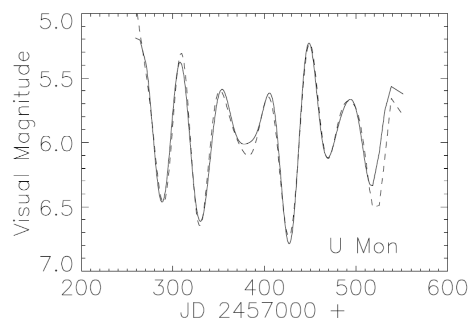

Figure A9f. The original light curve of U Monocertis (solid curve) compared with the reconstructed one (dashed). The reconstructed curve was determined by imposing Gaussian residuals about the original curve, and redoing the fit.

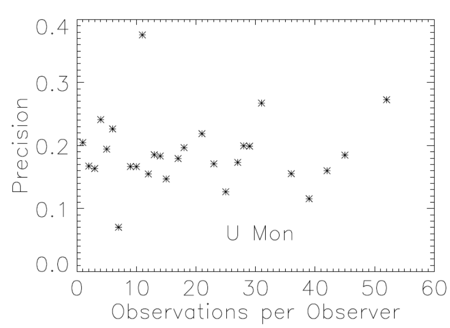

Figure A9g. The variation of observer precision with number of observations. There is no apparent trend.

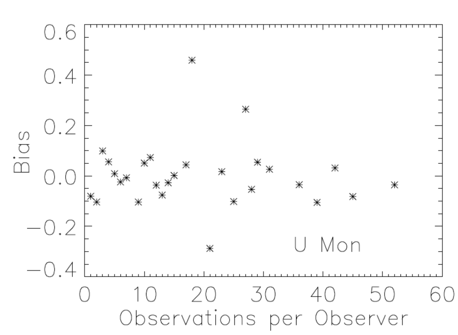

Figure A9h. The variation of observer bias with number of observations. There is no significant tendency for bias to become smaller with more activity.

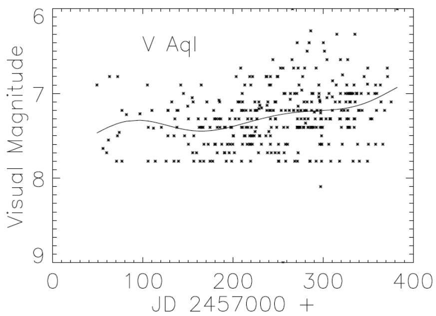

Figure A10a. Visual observations of V Aquilae, with the best-fit average light curve superimposed.

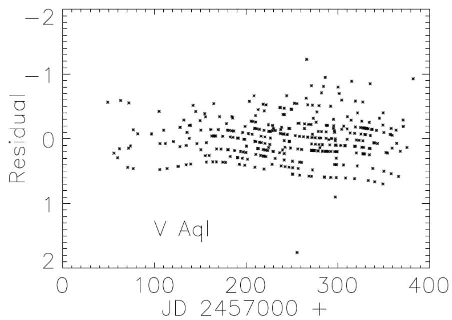

Figure A10b. Residuals of the observations of V Aquilae, with the best-fit average light curve subtracted. Most (but not all) visual observers report to the nearest tenth-magnitude, leading to some artifacts.

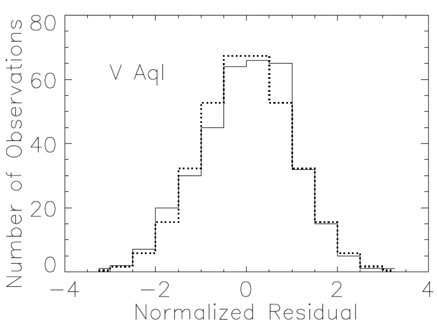

Figure A10c. Normalized residuals of V Aquilae observations (solid line), with a Gaussian distribution superimposed (dotted line). The residuals are significantly non-Gaussian.

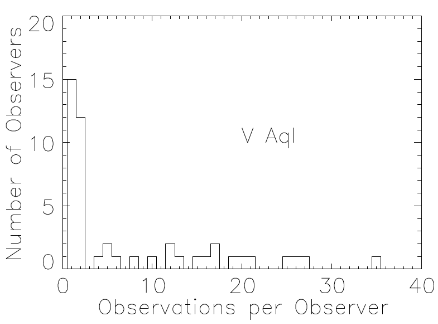

Figure A10d. The distribution of activity among observers of V Aquilae. The data are not dominated by any single observer, nor by the single-digit observers.

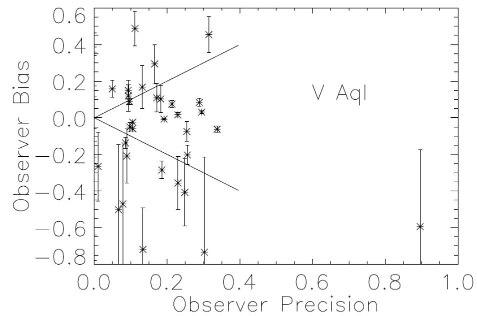

Figure A10e. Comparison of each observer's average distance from the best-fit curve (bias) with precision (the standard deviation about that average). Error bars in bias are derived by dividing the bias value by the square root of the number of observations; they are not shown for precision in order to keep the plot readable. Bias is smaller than precision for observers inside the lines drawn. Note that for most observers outside the lines, bias is not well-determined owing to few observations. Most observations fall inside the funnel.

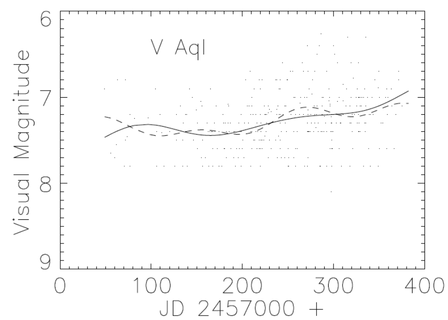

Figure A10f. The original light curve of V Aquilae (solid curve) compared with the reconstructed one (dashed). The reconstructed curve was determined by imposing Gaussian residuals about the original curve, and redoing the fit.

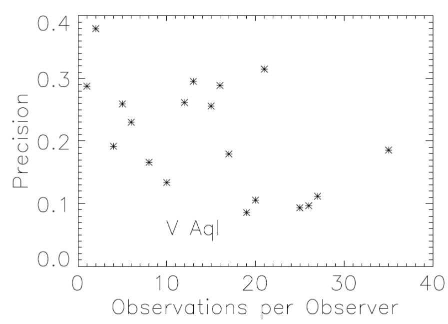

Figure A10g. The variation of observer precision with number of observations. There is no clear trend.

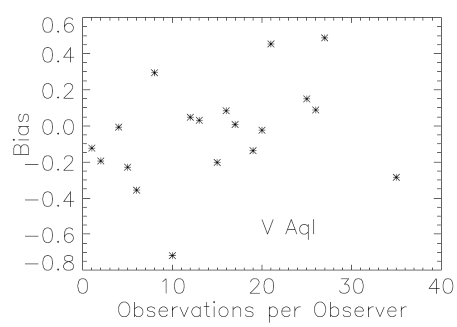

Figure A10h. The variation of observer bias with number of observations. There is no significant tendency for bias to become smaller with more activity.

Photometric Observations and Period Analysis of an SU UMa-type Dwarf Nova, MASTER OT J004527.52+503213.8

Sena A. Matsui (ORCID 0000-0003-4249-0792)
Division of Particle and Astrophysical Science, Nagoya University, Furo-cho, Chikusa-ku, Nagoya 464–8602, Japan
Department of Biosphere-Geosphere Science, Okayama University of Science, 1-1 Ridaicho, Kita-ku, Okayama 700–0005, Japan; sena.ma@nagoya-u.jp

Tsutomu T. Takeuchi (ORCID 0000-0001-8416-7673)
Division of Particle and Astrophysical Science, Nagoya University, Furo-cho, Chikusa-ku, Nagoya 464–8602, Japan
The Research Center for Statistical Machine Learning, the Institute of Statistical Mathematics, 10-3 Midori-cho, Tachikawa, Tokyo 190—8562, Japan; takeuchi.tsutomu.g8@f.mail.nagoya-u.ac.jp

Kai T. Kono
Division of Particle and Astrophysical Science, Nagoya University, Furo-cho, Chikusa-ku, Nagoya 464–8602, Japan; kono.kai@c.mbox.nagoya-u.ac.jp

Suchetha Cooray (ORCID 0000-0002-9217-1696)
Division of Particle and Astrophysical Science, Nagoya University, Furo-cho, Chikusa-ku, Nagoya 464–8602, Japan
Research Fellow of the Japan Society for the Promotion of Science (DC1); cooray@nagoya-u.jp

Received May 30, 2022; revised December 23, 2022; accepted December 24, 2022

Abstract MASTER OT J004527.52+503213.8 (hereafter MASTER J004527) is a dwarf nova discovered by the MASTER project in 2013. At 18:20 UTC on 24 October 2020, brightening of this object was reported to vsnet-alert (24843 by Denisenko). This was the second report of a superoutburst after its discovery. Photometric observations were made using the 23.5-cm Schmidt-Cassegrain telescope at Okayama University of Science observatory soon after the alert through 4 November 2020. In this work, we present the photometric data from our observation, and the analysis of the light curves of MASTER J004527 during the 2020 outburst. We propose a method to determine the period of superhumps by polynomial fitting, which can be applied to a light curve with many missing data. In addition to our own data, we incorporate other all sky survey data of the outburst to better understand the properties of the superhumps. Based on our observations, we conclude that MASTER J004527 is an SU UMa-type dwarf nova, since no early superhumps occurred.

1. Introduction

Cataclysmic variables (CVs) are close binary systems, consisting of a white dwarf primary star and a late-type secondary star. The characteristic property of CVs is their rapid increase of luminosity. Dwarf novae (DNe) are one of the subclasses of CVs. There are three types of CVs: U Gem, Z Cam, and SU UMa. SU UMa-type DNe are further classified into three subtypes: SU UMa, WZ Sge, and ER UMa. Detailed information on the DN classification can be found in, e.g., La Dous (1994) and Osaki (1996).

In the subdivision of SU UMa-type dwarf novae, the definition of the WZ Sge type is the observation of early superhumps. The early superhumps are small amplitude fluctuations of 0.1 to 0.5 magnitude that appear for about a week after the maximum magnitude. They are thought to be the result of tidal instability caused when the outer disk reaches a 3:1 resonance radius during an outburst (e.g., Osaki 1989; Hirose and Osaki 1990).

On 25 October 2020 (JST), an outburst of a DN, MASTER OT J004527.52+503213.8 (hereafter MASTER J004527), was reported on VSNET (Denisenko 2020). Denisenko *et al.* (2013) mentioned that, based on the blue color and outburst amplitude, MASTER J004527 was most likely a WZ Sge in superoutburst. Kato (2015) and AAVSO VSX labeled it as SU UMa-type.

During this outburst, reported on vsnet as a second confirmed superoutburst, MASTER J004527 increased its brightness by up to $\simeq 13$ mag. The increased brightness was sufficient to be observed by the 23.5-cm Schmidt-Cassegrain telescope at the observatory of Okayama University of Science in Japan. We conducted a photometric observation of MASTER J004527 with this telescope and obtained the light curve from 25 October through 3 November 2020 (JST).

In this study, we present the estimated parameters from the analysis of the light curve. Further, we compared our own observation data with other survey data from public databases. The data from these surveys provide information on the global characteristics of the light curve. We referred to the data obtained by the All-Sky Automated Survey for Supernovae (ASAS-SN) and the Zwicky Transient Facility Survey (ZTF). The All-Sky Automated Survey for Supernovae (here after "ASAS-SN") project surveys automatically the sky almost every night with 24 telescopes located all over the world. The Zwicky Transient Facility (here after "ZTF") is a survey of the wide field astronomy with the Samuel Oschin Telescope at Palomar Observatory in California, United States.

We present an analysis to support the classification of MASTER J004527.

This paper is organized as follows. In section 2 we introduce all the datasets we used for this study. We explained the analysis methods in section 3. Section 4 presents the observed results. We discuss some physical interpretations of the results in section 5. Section 6 is devoted to our conclusion. We explained some detailed information on the observation and data analysis in Appendix A.

2. Data

2.1. Target object

MASTER J004527 was discovered by the MASTER project in 2013 during its outburst. It had become 12.53 mag in Clear filter at the time of discovery on 17.668 September 2020 UTC, which was reported by Denisenko (2013). MASTER J004527 is located at R.A. $00^h\ 5^m\ 27.54 \pm 0.18^s$, Dec. +50° 32' 15.18 ± 0.17" (J2000). The magnitudes of MASTER J004527 in the quiescent period are presented in Table 1.

2.2. Observation and data reduction

We performed photometry of the target object MASTER J004527 during the period from 25 Oct. 2020 to 4 Nov. 2020 (JST), with one of the facilities at the Observatory of Okayama University of Science, Japan. The telescope was a Schmidt-Cassegrain, with an aperture of 235 mm and a focal length of 1480 mm. We used a cooled CCD camera, SBIG ST-9XE with 512 × 512 pixels (pixel size 20 × 20 μm). In addition, we used a Clear filter, and the exposure time was 60 s throughout this observation. The data were reduced with a standard procedure by using AstroImageJ (ver. 3.2.0) developed by Collins *et al.* (2017). Our observation log is given in Table A1, shown in Part A1 of Appendix A.

Table 1. Magnitude in the quiescent period.

Band	*Magnitude (mag)*	*Reference*
R	19.9	Monet *et al.* (2003)
B	19.7	Monet *et al.* (2003)
Gaia G[a]	18.940004 ± 0.006565	Gaia Collab. (2020)

[a] *For the definition of Gaia G-band, see https://www.cosmos.esa.int/web/gaia/edr3-passbands.*

2.3. Light curves

We present the light curve of MASTER J004527 in the whole observation period in Figure 1. Abscissa is the Julian day, subtracted with a constant so that the light curve starts from zero. Ordinate represents Δmag of MASTER J004527 compared to the standard star in the same field of view. The Δmag is defined as a relative magnitude between the comparison star TYC 3257-553-1 (denoted by C3) and a target star. Since we used a small-aperture telescope with a Clear filter, we used Δmag for the discussion on the photometry. We chose comparison stars in the

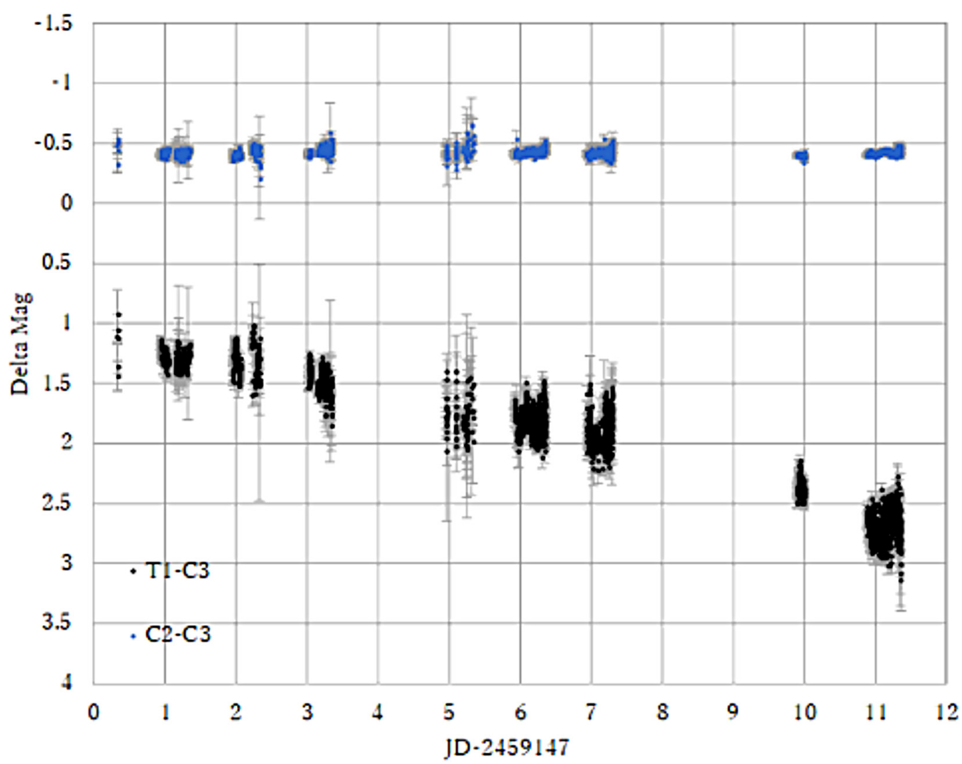

Figure 1. A light curve of MASTER OT J004527.52+503213.8 (MASTER J004527) during the whole observation period. Relative magnitude obtained by the standard star photometry is shown. The abscissa is the Julian date subtracted with a constant so that the light curve starts from zero. The ordinate represents the Δ mag, i.e., the magnitude obtained by subtracting a magnitude of the comparison star TYC 3257-553-1 (denoted by C3) from that of a target star. The black symbols are the magnitude of the target star (T1) minus the magnitude of the comparison star C3, while the blue symbols are the magnitude of comparison star TYC 3270-1038-1 (denoted by C2) minus C3. See main text for the details.

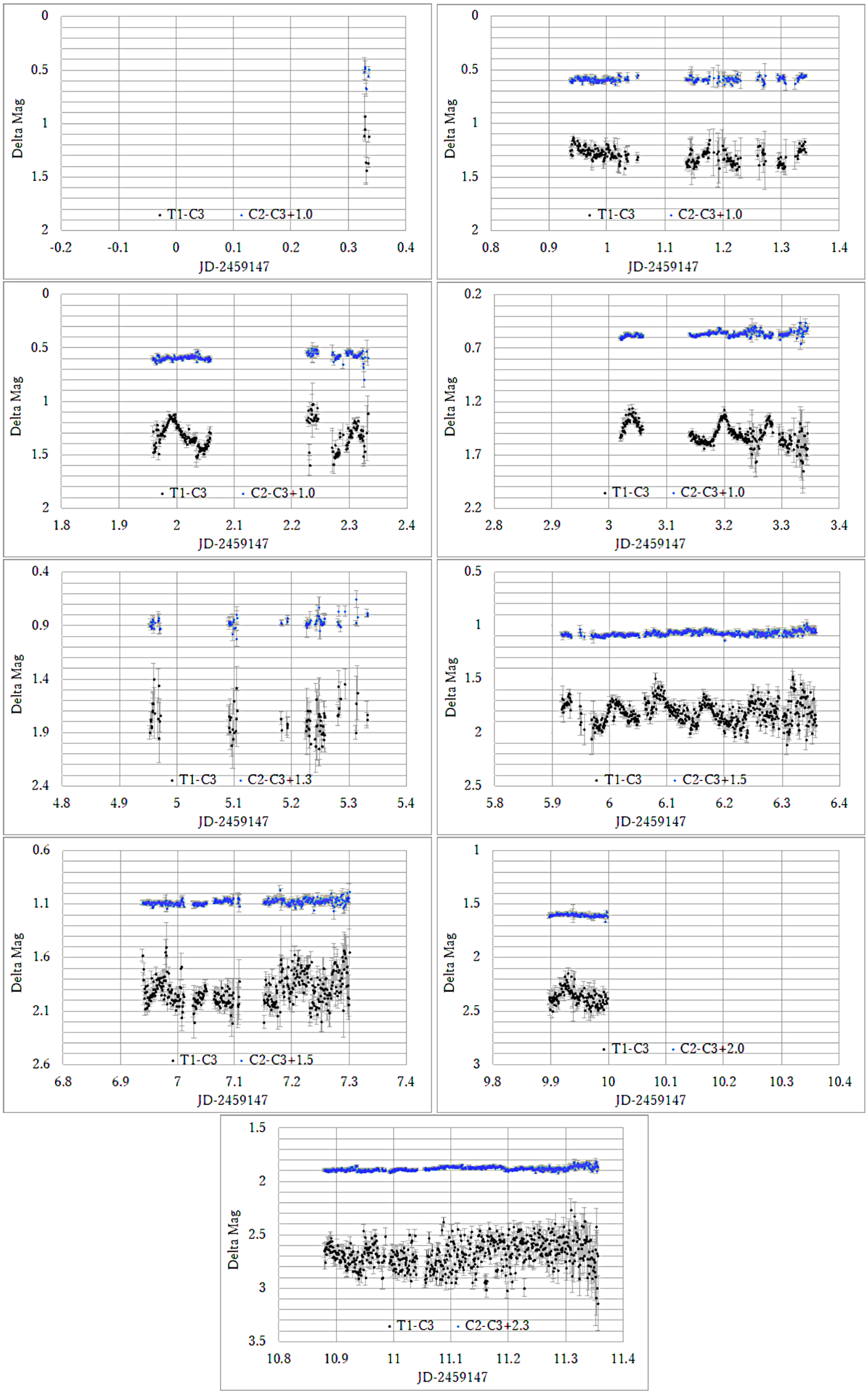

Figure 2. Detailed light curves of MASTER J004527. Symbols and format are the same as Figure 1.

neighborhood of the target MASTER J004527. We denote the magnitude of MASTER J004527 as T1. The comparison stars are TYC 3270-1038-1 located at R.A. $00^h 45^m 13.6689 \pm 0.0197^s$, Dec. +50° 30' 40.2192 ± 0.0195" (J2000) and TYC 3257-553-1 located at R.A. $00^h 44^m 52.0981 \pm 0.0135^s$, Dec. +50° 28' 11.6309 ± 0.0134" (J2000). Both stars have been confirmed that they are not variable stars. The magnitude of TYC 3270-1038-1 is 11.545754 ± 0.002761 in the Gaia G-band (Gaia Collaboration 2020) and 11.51 ± 0.09 in the V-band (Høg *et al.* 2000). The magnitude of TYC 3257-553-1 is 11.947890 ± 0.002763 in the Gaia G-band (Gaia Collaboration 2020) and 12.10 ± 0.17 in the V-band (Høg *et al* 2000). We denote the magnitudes of TYC 3270-1038-1 and TYC 3257-553-1 as C2 and C3, respectively. The relative magnitude Δmag of the target star is T1 – C3. We also estimated Δ mag of the comparison star TYC 3270-1038-1, C2 – C3, to examine the stability of the photometry. We present T1 – C3 and C2 – C3 in Figure 1.

In Figure 1, we observe a dimming of $\simeq 1.5$ mag in ten days. A light curve for each observation day is shown in Figure 2[1]. The target star is diminishing after the outburst, while the relative magnitude of the comparison star C2 – C3 stays constant. Therefore, in Figue 2, a constant is added to Δmag in each panel, to avoid C2 — C3 values to be too far from T1 — C3, to make the comparison easily. The specific values of the constant are specified in each panel. For example, the top two panels show C2 – C3 + 1.0.

3. Method

In this work, we estimated the period of superhumps by fitting polynomials to the light curve of each hump and estimating the time of extrema (peaks). We adopted this method mainly because the error is significantly large for a part of the data, and its analysis is straightforward. Fitting Errors were calculated by the standard Jackknife resampling method (Efron 1982).

We should note that the phase dispersion minimization method (PDM; Stellingwerf 1978) has been used as a standard procedure for the period analysis of CVs (e.g., Kennedy *et al.* 2016; Tanabe *et al.* 2018). However, its performance is guaranteed only for continuous data. The observed data in this study were not globally contiguous in time, and the PDM method was not suitable for this analysis. This is the reason why we adopted the polynomial fitting method for the period analysis, instead of the PDM. For comparison, we performed a PDM analysis for each continuous portion of the light curve. The results are shown in Part A3 of Appendix A.

3.1. Estimation of the time of hump maxima

3.1.1. Time of hump maxima

To estimate the timing of peaks of the superhumps, we fitted second- and third-order polynomials to each hump in the light curves. Since what we should find is only the timing of a peak, we do not have to consider higher-order polynomials. We determined which order is more appropriate to describe the hump, we evaluated the Akaike information criterion (AIC; Akaike 1974) and Bayesian information criterion (BIC; Schwarz 1978). Formulation of AIC and BIC is provided in Part A2 of Appendix A.

The fitting results are presented in Figures 3 through 5, and the obtained peak times are tabulated in Table 2. In Table 2, we summarize the information on the peaks of humps estimated by the polynomial fitting. For some humps, the AIC and BIC suggest different conclusions and we cannot determine which order is better to fit. We adopted the second-order peak in such a case, since the error of the parameter estimation is smaller. The order of the selected fitting polynomial model k is also tabulated in Table 2.

As a first step, we start from a first-order approximation that the period is constant. We estimated the period of humps from the difference between the two detected peaks. For this, we assumed the following relation

$$O = T_0 + EP, \tag{1}$$

where O is an estimated time of a peak, T_0 is the time of the first peak that occurred on 25 Oct. 2020 (JST), and P is a period temporarily determined from the average for sequential peaks observed on 27 and 30 Oct. 2020 (JST).

By rearranging Equation 1, we have

$$E = \frac{O - T_0}{P}, \tag{2}$$

where T_0 is the time of the first peak obtained by observation, and P is a tentative period averaged over the difference between two successive peaks that could be observed. In this work, we adopted $T_0 = 1.9912$ and $P = 0.08058$ to estimate the epoch E. Since E should be an integer in principle, we round off E from Equation 2. We denote the rounded E as [E]. The precise period is then estimated from a scatter plot between [E] and O. The slope of the linear fit to the [E] – O relation yields the proper estimation of the period between the humps.

Table 2. Time of the detected maxima.

Date (JST)	*Time of maxima (JD–2459147)*
26 Oct 2020	1.9912 ± 0.0004
27 Oct 2020	3.0393 ± 0.0006
	3.1996 ± 0.0008
	3.2795 ± 0.0007
30 Oct 2020	6.0110 ± 0.0005
	6.0870 ± 0.0131
	6.1679 ± 0.0005
	6.2534 ± 0.0101

[1] The machine-readable data are available from the following URL: https://drive.google.com/file/d/1Zwqui6r36J4RQmYP2dPqDIsWEewd1wsb/view?usp=sharing.

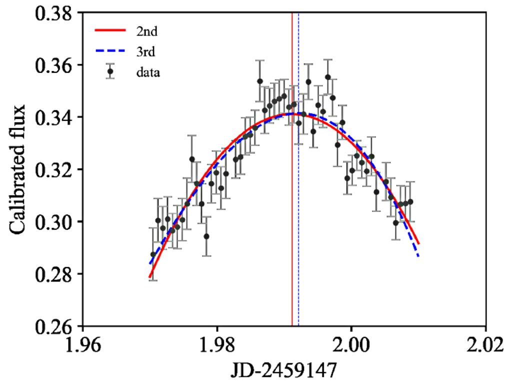

Figure 3. Parameter estimation of the time of hump maxima of MASTER J004527 on 26 Oct. 2020. The abscissa is the Julian date, and the ordinate is the flux of MASTER J004527 calibrated by the standard star in the FoV. The solid curve represents the second-order polynomial fit, and the dashed curve is the third-order fit. Vertical lines represent the estimated timing of the peak of the superhump. Detailed values related to the fit are tabulated in Table 4.

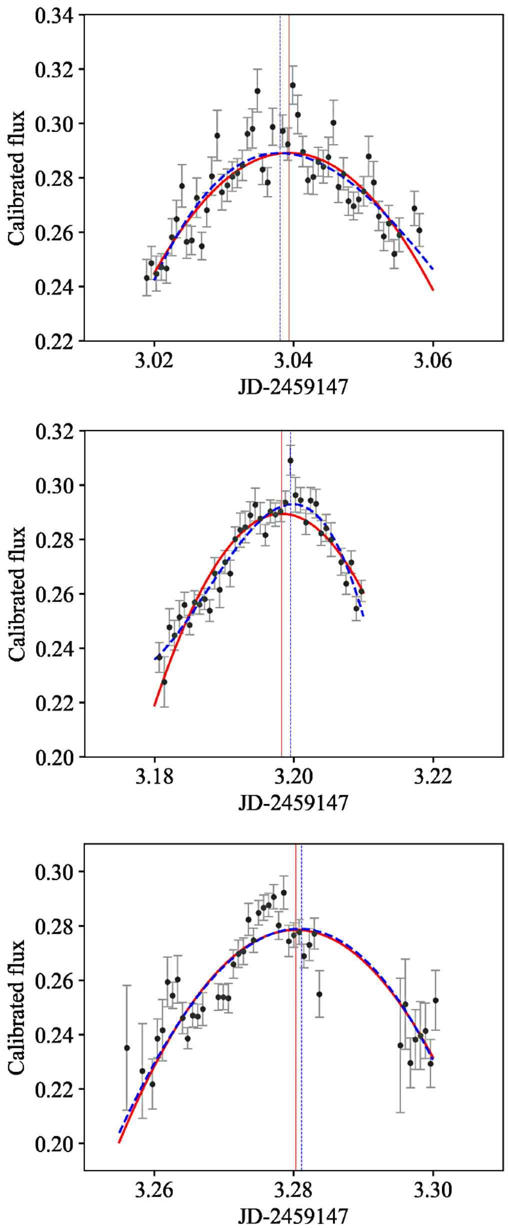

Figure 4. Same as Figure 3 but for the peaks on 27 Oct. 2020.

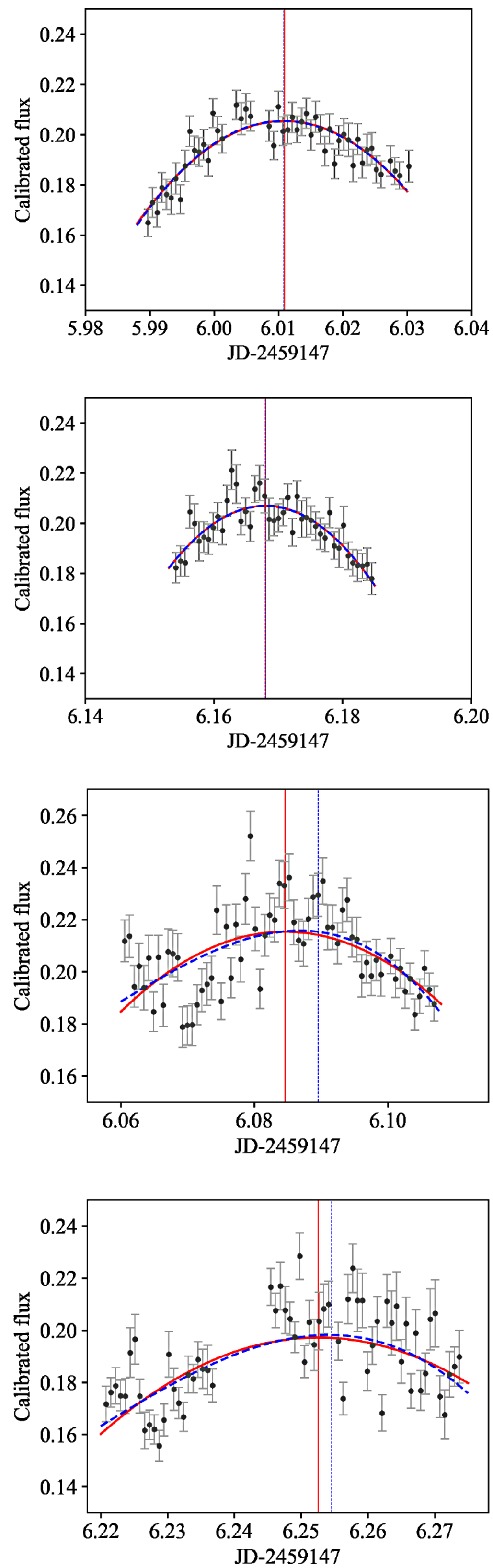

Figure 5. Same as Figure 3 but for the peaks on 30 Oct. 2020.

4. Results

4.1. Global behavior of the light curve

Figure 6 shows the light curves obtained from our observation and from all-sky surveys. We refer to the data obtained by the All-Sky Automated Survey for Supernovae (ASAS-SN) and the Zwicky Transient Facility Survey (ZTF). According to these observations, the plateau phase lasted about 12 days, during which MASTER J004527 dimmed by about 2 mag. We find no re-brightening after the superoutburst, which is typically observed in WZ Sge-type DNe. Furthermore, several small outbursts occurred after the superoutburst, according to the ASAS-SN data (Figure 7). We discuss this in more detail in section 5.2.

4.2. Peaks and periodic analysis

We then analyze the relation between E and O by a linear fitting. The period of the humps is estimated to be 0.08034 ± 0.00003 day, corresponding to 115.69 ± 0.05 min.

To examine the variation of the period of humps, we performed the so-called O–C diagram analysis. The name O–C stands for "Observed minus Calculated." It is expressed as deviations of phase in the cycle of variability. We followed the standard procedure for the analysis see, e.g., Sterken (2005). The period obtained from the linear fit is adopted as the value of the period P', and we calculated C as

$$C = T_0 + [E]P'. \tag{3}$$

We calculated O–C using the O obtained by observation and C obtained by calculation, and we made the O–C diagram (Figure 8).

The obtained quantities for the O–C analysis are listed in Table 3. Figure 8 is the O–C diagram of MASTER J004527 . As described in section 3.2, the abscissa represents the rounded value of the Epoch, [E], and the ordinate is the Observation data minus the Calculation data. However, since the data points are too few in Figure 8, it is difficult to discuss variation of the period only with the current data.

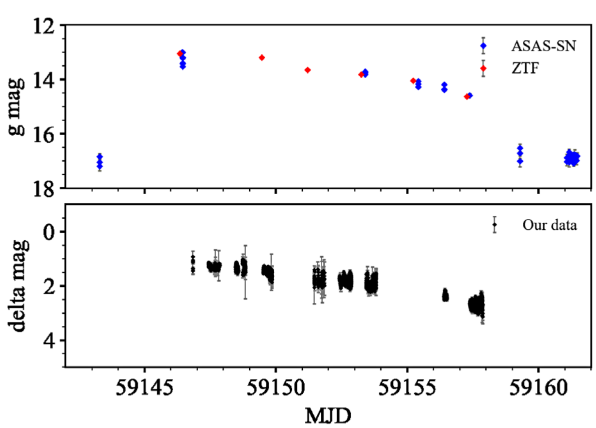

Figure 6. Light curves of the two all-sky surveys compared with our observed data. Upper panel: light curves from the ASAS-SN and the ZTF. Blue symbols represent the ASAS-SN data, while red ones are the ZTF data. The ordinate is in g magnitude. Lower panel: our observed light curve. The ordinate is expressed in Δmag, the difference between the measured brightness of MASTER J004527 and the standard star in the FoV. The abscissa is in MJD, an index of JD minus 2400000.5 days.

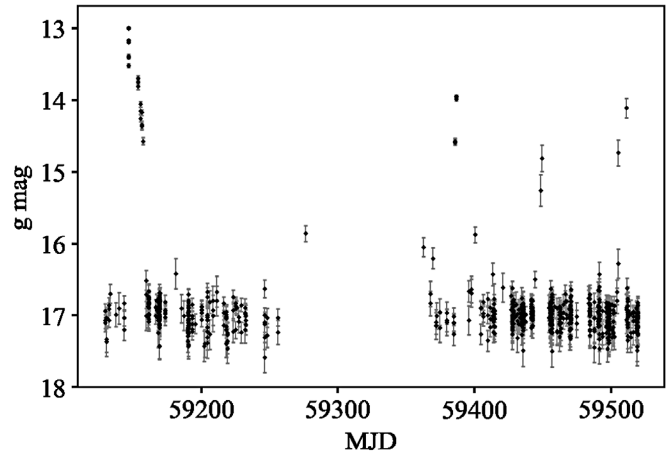

Figure 7. The light curve of MASTER J004527 for 391 days from MJD 59129 to MJD 59520 obtained by ASAS-SN. There are several outbursts without a hump after the superoutburst. The horizontal and vertical axes are the same as the upper panel in Figure 6.

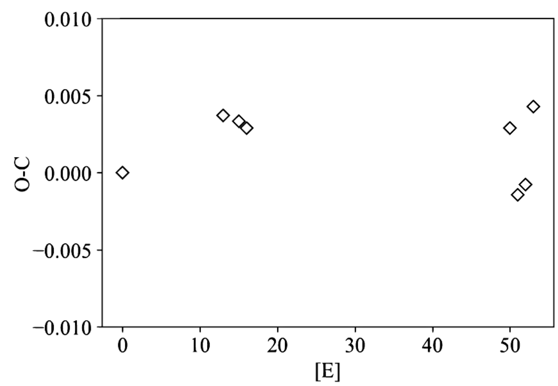

Figure 8. O–C diagram of MASTER J004527.

Table 3. Observed quantities for the O–C analysis.

O	*E*	*[E]*	*C*	*O–C*
1.9912 ± 0.0004	0	0	1.9912	0.0000
3.0393 ± 0.0006	13.01	13	3.0356	0.0037
3.1996 ± 0.0008	15.00	15	3.1963	0.0033
3.2795 ± 0.0007	15.99	16	3.2766	0.0029
6.0110 ± 0.0005	49.89	50	6.0081	0.0029
6.0870 ± 0.0131	50.83	51	6.0884	–0.0014
6.1679 ± 0.0005	51.83	52	6.1688	–0.0008
6.2534 ± 0.0101	52.89	53	6.2491	0.0043

5. Discussion

5.1. Examination of the light curve of the superoutburst

In the subclassification of SU UMa-type dwarf novae, one of the definitions of the WZ Sge type is the so-called "early superhumps" feature. The early superhumps are small-amplitude fluctuations of 0.1 to 0.5 magnitude that appear for about a week after the maximum magnitude. They are thought to be the result of tidal instability caused when the outer disk reaches a 3:1 resonance radius during an outburst (e.g., Osaki 1989; Hirose and Osaki 1990). In our observation, there was no variation that could be considered early superhumps, though the data points are not enough to give a definitive conclusion.

Comparison of our data with the mainstream sky survey data from ASAS-SN and ZTF from Figure 7 clearly shows that the light curves are consistent with each other. This confirms the reliability of the data in this work. Although the precise date and time of the outburst cannot be determined, at least the outburst occurred at some moment during 3.15477 days between 59143.2778 MJD (the last observation before the outburst) and 59146.43257 MJD (when the outburst was detected). Therefore, our observations should have started within 3.54926 days after the outburst at most. The first superhump-like feature was detected at 59147.69086 MJD, which means that the superhumps were detected between 1.25829 and 4.41296 days after the outburst. This means that, since usually the early superhumps appear approximately one week after the maximum, it is not very plausible that we have missed the early superhumps associated with this superoutburst. Then, we conclude that the early superhumps may not have occurred. Early superhumps were also not reported in the 2013 superoutburst (Kato 2015).

5.2. Normal outbursts after the surperoutburst

The ASAS-SN data in Figure 7 show that since the superoutburst in 2020, a number of humpless outbursts with a smaller amplitude have been detected. It is highly probable that they are normal outbursts. Generally, WZ Sge-type dwarf novae do not have normal outbursts (see Patterson *et al.* 1981). This is consistent with the classification of MASTER J004527 as a SU UMa-type DN.

5.3. Classification of MASTER J004527

Now we consider the classification of MASTER J004527. As discussed above, the estimated period of superhumps of MASTER J004527 is about 116 min, strongly supporting that it should be classified as a typical SU UMa-type DN (period ~ 90–120 min). In comparison, the period of WZ Sge type objects is about 80 min (e.g., Tanabe *et al.* 2018). The measured superhump period is too long for MASTER J004527 to be classified as a WZ Sge-type object (e.g., Vogt 1980).

In contrast, Kato (2015) proposed a measure of how many magnitudes brighter the superhumps are when they appear compared to the quiescent magnitude, and many WZ Sge-type objects have amplitudes of 7 magnitudes or brighter. The exact magnitude is not known from this observation, but considering the all-sky surveys data, the amplitude is considered to be about $\simeq 4$ mag. Again, this suggests that it has the characteristics of a SU UMa-type DNe. Putting all discussions together, we conclude that MASTER J004527 is an SU UMa-type DN.

6. Summary

MASTER OT J004527.52+503213.8 (MASTER J004527) is a dwarf nova (DN) discovered by the MASTER project in 2013. This DN is considered to be an SU UMa-type. In this study, we present an analysis to support the classification of MASTER J004527. At 18:20 UTC on 24 Oct. 2020, brightening of this object was reported to vsnet-alert by Denisenko (2020). MASTER J004527 had brightened to ~ 13 mag during the superoutburst, enough to be detected by the 23.5-cm Schmidt-Cassegrain telescope at Okayama University of Science Observatory. We conducted a photometric observation of MASTER J004527 soon after the alert through 4 Nov. 2020 and obtained the light curve. We provide our own photometric data publicly online through the URL mentioned in section 2.

A comparison of this observation and other all-sky surveys has shown that early superhumps may not have occurred. This indicates that MASTER J004527 is an SU UMa-type DN. Although we could not prove the change in period with the current data, we can also consider that MASTER J004527 belongs to the SU UMa type based on the change in period observed during the 2013 outburst (Kato 2015). In addition, the observation of multiple normal outbursts further supports that MASTER is an SU UMa-type DN.

In this study, we applied a method to calculate the peak of superhumps from polynomial fitting, instead of the standard PDM. Since PDM can only handle continuous data, our method is more suitable to analyze data with many missing data, as in this study. Our method has another advantage in that is more intuitive and easier to understand. Further, more data-scientific approach can be done. We mention some possible methods in Part A3 of Appendix A, but we leave it as our future work.

7. Acknowledgements

This work has been supported by the Japan Society for the Promotion of Science (JSPS) Grants-in-Aid for Scientific Research (19H05076 and 21H01128). This work has also been supported in part by the Collaboration Funding of the Institute of Statistical Mathematics "New Development of the Studies on Galaxy Evolution with a Method of Data Science." SC is supported by the Japan Society for the Promotion of Science (JSPS) under Grant No. 21J23611. We thank Shiro Ikeda for discussing detailed data analysis methods, and Makoto Uemura, Daisaku Nogami, and Agnieszka Pollo for important suggestions in the discussion. We are sincerely grateful to the All-Sky Automated Survey for Supernovae (ASAS-SN) and the Zwicky Transient Facility Survey (ZTF) for providing the data of MASTER J004527.

References

Akaike, H. 1974, *IEEE Trans. Automatic Control*, **19**, 716.
Banks, H., and Joyner, M. L. 2017, *Appl. Math. Lett.*, **74**, 33.
Collins, K. A., Kielkopf, J. F., Stassun, K. G., and Hessman, F. V. 2017, *Astron. J.*, **153**, 77.
Cooray, S., Takeuchi, T. T., Akahori, T., Miyashita, Y., Ideguchi, S., Takahashi, K., and Ichiki, K. 2021a, *Mon. Not. Roy. Astron. Soc.*, **500**, 5129.
Cooray, S., Takeuchi, T. T., Ideguchi, S., Akahori, T., Miyashita, Y., and Takahashi, K. 2021b, arXiv:2112.01444.
Cooray, S., Takeuchi, T. T., Yoda, M., and Sorai, K. 2020, *Publ. Astron. Soc. Japan*, **72**, 61.
Denisenko, D. 2013 vsnet-alert 16417 (September 19; http://ooruri.kusastro.kyoto-u.ac.jp/mailarchive/vsnet-alert/16417).
Denisenko, D. 2020, vsnet-alert 24843 (October 25; http://ooruri.kusastro.kyoto-u.ac.jp/mailarchive/vsnet-alert/24843).
Denisenko, D., *et al.* 2013, *Astron. Telegram*, No. 5399, 1.
Efron, B. 1982, *The Jackknife, the Bootstrap and Other Resampling Plans*, Society for Industrial and Applied Mathematics (SIAM), Philadelphia.
Gaia Collaboration. 2020, VizieR On-line Data Catalog: I/350, originally published in 2020A&A...649A...1G; doi:10.5270/esa-1ug.
Hirose, M., and Osaki, Y. 1990, *Publ. Astron. Soc. Japan*, **42**, 135.
Høg, E., *et al.* 2000, *Astron. Astrophys.*, **355**, L27.
Kato, T. 2015, *Publ. Astron. Soc. Japan*, **67**, 108.
Kennedy, M. R., *et al.* 2016, *Astron. J.*, **152**, 27.
La Dous, C. 1994, *Space Sci. Rev.*, **67**, 1.
Monet, D. G., *et al.* 2003, *Astron. J.*, **125**, 984.
Osaki, Y. 1989, *Publ. Astron. Soc. Japan*, **41**, 1005.
Osaki, Y. 1996, *Publ. Astron. Soc. Pacific*, **108**, 39.
Patterson, J., McGraw, J. T., Coleman, L., and Africano, J. L. 1981, *Astrophys. J.*, **248**, 1067.
Schwarz, G. 1978, *Ann. Statistics*, **6**, 461.
Stellingwerf, R. F. 1978, *Astrophys. J.*, **224**, 953.
Sterken, C. 2005, in *The Light-Time Effect in Astrophysics: Causes and cures of the O–C diagram*, ed. C. Sterken, ASP Conf. Ser. 335, Astronomical Society of the Pacific, San Francisco, 3.
Takeuchi, T. T. 2000, *Astrophys. Space Sci.*, **271**, 213.
Takeuchi, T. T., Yoshikawa, K., and Ishii, T. T. 2000, *Astrophys. J., Suppl. Ser.*, **129**, 1.
Tanabe, K., Akazawa, H., and Fukuda, N. 2018, *Inf. Bur. Var. Stars*, No. 6251, 1.
Vogt, N. 1980, *Astron. Astrophys.*, **88**, 66.

Appendix A

A1. Observation log

We show the observation log of our observation of MASTER J004527 in Table A1.

Table A1. Observation log.

Date (2020)	*Start (JST)*	*End (JST)*	*Number of Images*
24 Oct	28:51	29:05	14
25 Oct	19:29	29:10	468
26 Oct	20:01	28:43	286
27 Oct	21:27	29:04	360
29 Oct	19:53	28:56	342
30 Oct	18:59	29:18	598
31 Oct	19:33	29:49	532
03 Nov	18:32	20:54	142
04 Nov	18:07	29:21	636

A2. AIC and BIC

We first introduce the Akaike information criterion (AIC; Akaike 1974) and the Bayesian information criterion (BIC; Schwarz 1978) formally in the context of maximum likelihood estimation. Let $\ln \mathscr{L}(\theta \mid \{m_i : i = 1, ..., n\})$ be the log-likelihood where i is the number of photometric observations, m_i is the magnitude observed at time t_i, $\{\theta\} = (\theta_1, ..., \theta_k)$ denotes the parameters, and k is the number of parameters. In the classical maximum log-likelihood estimation, we search a set of parameters $\hat{\theta}$ that maximizes $\ln \mathscr{L}(\theta)$ under observed $\{t_i\}$. If we denote the maximum log-likelihood as $\ln \mathscr{L}_{max} \equiv \mathscr{L}(\hat{\theta})$, the AIC is generally defined as

$$\mathrm{AIC} \equiv -2(\ln \mathscr{L}_{max} - k)\,. \tag{A1}$$

Similarly, the BIC is defined as

$$\mathrm{BIC} \equiv -2\left(\mathrm{Ln}\, \mathscr{L}_{max} - \frac{k}{2} \ln n\right). \tag{A2}$$

A derivation geared to astronomers is given by Takeuchi (2000).

In the current work, we assumed a polynomial function to describe the shape of humps. Let t_i be the magnitude observed at time t_i. To describe the shape of the humps around the peak, we assume a polynomial model as

$$m_i = a_0 + a_1 t_1 + a_2 t_i^2 + ... + a_k t_i^k + \epsilon \equiv f(t_i | \{a_k\}) + \epsilon\,, \tag{A3}$$

where ϵ is a Gaussian noise with mean 0 and dispersion σ^2. We consider second and third order (i.e., k = 2 and 3). In order to judge which of the second and third order polynomial models describes the data better with taking into account the penalty of the increase of model parameters, we adopt Akaike's information criterion (AIC; Akaike 1974) and the Bayesian information criterion (BIC; Schwarz 1978). Under the assumption of Equation A3, the AIC and BIC become

Table A2. Estimated AICs and BICs for the polynomial fit.

Date	*2nd*		*Time of Maxima (JD–2459147)*		*3rd*		*Time of Maxima (JD–2459147)*	
(JST)	*AIC*	*BIC*		*Error*	*AIC*	*BIC*		*Error*
26 Oct 2020	–334.6	–340.7	1.9912	0.0004	–344.9	–339.1	1.9926	0.0009
27 Oct 2020	–318.1	–314.2	3.0393	0.0006	–319.8	–313.9	3.0381	0.0026
	–271.1	–267.7	3.1982	0.0004	–298.1	–293.1	3.1996	0.0008
	–231.3	–227.8	3.2795	0.0007	–230.8	–225.5	3.2797	0.0021
30 Oct 2020	–370.9	–367.1	6.0110	0.0005	–370.1	–364.3	6.0105	0.0039
	–330.1	–325.8	6.0845	0.0011	–356.0	–349.5	6.0870	0.0131
	–320.5	–317.0	6.1679	0.0005	–318.6	–313.3	6.1679	0.0005
	–297.2	–293.0	6.2524	0.0016	–306.6	–300.2	6.2534	0.0101

$$\mathrm{AIC}(k) = n \ln\left\{\frac{\sum_i [m_i - f(t_i|\{\hat{a_k}\})]^2}{n}\right\} + 2(k+1) + n(\ln 2\pi + 1), \quad (A4)$$

$$\mathrm{BIC}(k) = n \ln\left\{\frac{\sum_i [m_i - f(t_i|\{\hat{a_k}\})]^2}{n}\right\} + (k+1)\ln n + n(\ln 2\pi + 1), \quad (A5)$$

(for a derivation, see, e.g., Takeuchi *et al.* 2000; Banks and Joyner 2017). In practice, the last term n (ln 2π + 1) does not affect the evaluation and we can neglect it. The obtained AIC and BIC are tabulated in Table A2.

A3. Period estimation by PDM

As we mentioned in the main text, the PDM is widely used for similar studies. It is well known that some lengths of contiguous data are required, in order to have a secure result by the PDM. However, since we have significant gaps in the observations, clearly seen in Figure 1, the PDM is not an ideal method to have a reliable result. Here, just for a comparison, we applied it to a relatively continuous portion of the current data.

Periodic signals can be approximated more sparsely in the Fourier domain. Therefore, extrapolation techniques that impose sparsity in the Fourier domain can successfully reconstruct missing regions (e.g., Cooray *et al.* 2021a, b) and often perform better than interpolation techniques (e.g., Cooray *et al.* 2020).

The result is summarized in Table A3.

Table A3. Period obtained by PDM.

Date	*Period*
(JST)	*(JD–2459147)*
26 Oct 2020	0.0807272764
27 Oct 2020	0.0803726379
30 Oct 2020	0.0796680278

Infrared Photometric Distance to WZ Hya

Camdon Ritterby (ORCID 0000-0002-6321-6461)
Department of Physics and Astronomy, Washington State University, Pullman, WA 99164-2814; camdon.ritterby@wsu.edu

Michael L. Allen (ORCID 0000-0002-6047-3315)
Department of Physics and Astronomy, Washington State University, Pullman, WA 99164-2814; mlfa@wsu.edu (corresponding author)

Received August 24, 2022; revised March 29, 2023; accepted April 5, 2023

Abstract A distance to the RR Lyrae star WZ Hya was determined to test how well period-luminosity-metallicity (PLZ) relations agree with current parallax measurements from Gaia. We obtained 120 photometric observations in the B, V, ip, and zs filters from 16 February to 28 May 2022. Fluxes were extracted using six-aperture photometry methods. The period found for WZ Hya was 0.5377 ± 0.0005 day. Using the theoretical PLZ relations, a weighted average distance of 872 ± 47 parsecs was determined for the V, ip, and zs filters with a minimization technique. This distance is compared to the distances found using color excess values found in the literature, which distances were 942 ± 51 and 931 ± 50 parsecs, respectively. The Gaia Data Release 3 (DR3) parallax distance is 999 ± 16 parsecs. The distances determined using the PLZ relation are consistent with the parallax-determined value from Gaia within 1–2 standard deviations.

1. Introduction

RR Lyrae stars are variable stars that belong to the horizontal branch. Their periods range from 0.2 to 1.2 days (Dambis et al. 2013). These pulsating stars are used as standard candles that help us understand the structure of the Milky Way. RR Lyr standard candles use period-luminosity relations to measure distances, then Catelan *et al.* (2004) and Cáceres and Catelan (2008) derived theoretical period-luminosity-metallicity relations that use the infrared ip and zs filters and the visible Johnson V filter. The standard for geometric parallax distances is the Gaia survey (Gaia Collaboration 2022). The infrared PLZ relations have not yet been determined to agree with those values found in Gaia for many stars. This research provides the results of these relations using the RR Lyr star WZ Hya and compares them to the parallax measurements determined by the Gaia DR3 survey.

WZ Hya is classified as an RRab type variable sstar (Clube *et al.* 1969). RRab-type variable stars can be determined by looking at the shape of their light curves. Known as fundamental-mode pulsating RR Lyr stars, these variable stars have an asymmetric light curve that has a steep rise and a much slower decline in magnitude. This typically takes the shape of a shark tooth. These light curves are provided in Figure 2 and basic properties of WZ Hya are found in Table 1.

This paper will first discuss how observations for WZ Hya were set up using the Las Cumbres Observatory (LCO) via Michael Fitzgerald's OurSolarSiblings (OSS) research course. The data pipelines set up to analyze these observations are discussed, along with descriptions of the equipment used (section 2). Then, the results of the PLZ relation will be analyzed, specifically the period and the distance from Earth (section 3). Finally, a comparison is drawn to the distance produced by the Gaia DR3 survey using parallax (section 4).

We transformed Gaia's values for parallax, p (arcseconds), and parallax error Δp, to distance, d (parsecs), and distance error, Δd, using standard formulae:

$$d = \frac{1}{p}, \ |\Delta d| = \frac{1}{p^2} \Delta p. \quad (1)$$

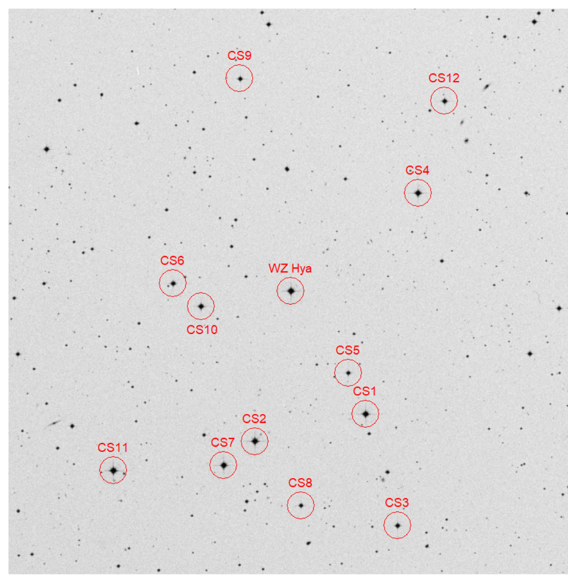

Figure 1. Field of WZ Hya with the 12 comparison stars used in data analysis. The image is 25 × 25 arcminutes. The image is from the Digitized Sky Survey (DSS) and is processed using SAOImageDS9. North is up and east is left.

2. Observations

WZ Hya was observed between February 16 and May 28, 2022. Figure 1 shows the field of WZ Hya and identifies the variable and comparison stars used. The star was observed through four filters: Johnson-Cousins B and V (Bessell 1993), SDSS ip (Sloan Digital Sky Survey; Fukugita *et al.* (1996)), and Pan-STARRS zs (Panoramic Survey Telescope and Rapid Response System; Tonry *et al.* (2012)). The star was observed with the Las Cumbres Observatory (LCO) network of robotic telescopes. The filter characteristics are summarized in Table 2.

Table 1. Basic properties of WZ Hya.

Property	*Value*	*Reference*	*Comments*
R.A. (J2000)	153.435053291387°	Gaia Collab. (2022)	Gaia DR3
Dec. (J2000)	–13.13816584777°	Gaia Collab. (2022)	
Spectral Type	A2	Barbier-Brossat *et al.* (1994)	
Variable Type	RRab	Clube *et al.* (1969)	
Parallax	1.0008 ± 0.0157 mas	Gaia Collab. (2022)	
Distance	999 ± 16 pc		From parallax; see text
Distance	982 ± 15 pc	Gaia Collab. (2022)	Photometric

Table 3 lists the location, telescope camera label, and the number of observations taken from all used telescopes. The WZ Hya dataset is shown in Appendix A and is also available through the AAVSO's public ftp site as noted in the Appendix.

Every observation of WZ Hya was taken using the 0.4-meter series of telescopes. Each was equipped with an SBIG STL-6303 CCD camera of format 3k × 2k pixels, with a pixel size of 0.571 arcsec and a field of view of 29.2 × 19.5 arcmins. Using the LCO observation portal, cadences were set up to provide an observation every four hours. In total, 120 observations of WZ Hya were recovered. All images produced by the LCO telescope network were usable.

Data gathered by the LCO telescope network needed to be optimized to allow data collection to still proceed without over-exposure occurring, avoiding errors in the photometric measurements being made. We used AstroImageJ ssoftware (Collins *et al.* 2017) on test images to measure approximate photon counts. Exposure times for our science run were calculated to collect 150,000 photons integrated. An exposure time was produced for each filter: 50 seconds for B, 20 seconds for ip, 18 seconds for V, and 80 seconds for zs.

The LCO's BANZAI data pipeline (Brown *et al.* 2013) took raw images from the telescope and corrected them using bad-pixel masking, bias subtraction, dark subtraction, flat field correction, and astrometric calibration. Source extraction and photometry were performed by the OurSolarSiblings (OSS) data pipeline (Fitzgerald 2018) automatically. The OSS pipeline trims and cleans up the images and then calculates a new World Coordinate System (WCS) value and applies it to the image. After this, six automated photometry methods are performed on each of the images, those being Dominion Astrophysical Observatory Photometry (DAO; Stetson 1987), DoPHOT (DOP; Schechter *et al.* 1993); Alonso-García *et al.* 2012), Source Extractor Aperture (SEX) and Source Extractor Kron (SEK) (Bertin and Arnouts 1996), Point Spread Function Extractor (PSX; Bertin 2011), and Aperture Photometry Tool (APT; Laher *et al.* 2012a, 2012b). For each star-like source, the results of these methods are then parsed into comma-separated variable files consisting of R.A., Dec., X and Y pixel values, counts, and errors in the counts.

Next, Astrosource software (Fitzgerald *et al.* 2020) was used to further process the data. Astrosource first identifies stars of sufficient signal-to-noise in the image. Then the least variable stars are chosen to become comparison stars. Next, the magnitudes of these calibration stars are extracted from photometric databases. Photometric databases used were APASS DR9 for the B and V ffilters (Henden *et al.* 2015), Skymapper DR 1.1 for the ip filter (Wolf *et al.* 2018), and Pan-STARRS for the zs filter (Magnier *et al.* 2020; Flewelling *et al.* 2020). Reduction to the magnitude system is performed and light curves are plotted for the observed variable star, WZ Hya, using differential photometry.

All calibration stars used are provided in Table 4 along with their R.A., Dec., and magnitude. Out of the six methods available, the SEK method provided the cleanest light curves and these magnitudes were used in this paper. Astrosource also creates a list of all magnitude measurements that were recovered in each method. The SEK method provided 103 in the B filter, 109 in the V filter, 46 in the ip filter, and 107 in the zs filter.

Table 2. Filters used.

Filter	*LCO Description (Name)*	*Wavelength Center (Å)*	*Width (Å)*
B	Bessell B (blue)	4361	890
V	Bessell V (visual)	5448	840
ip	SDSS i' (i-prime)	7545	1290
zs	Pan-STARRS z_s (z-short)	8700	1040

Note: The values for wavelength center, and width, (angstroms) are tabulated on LCO's webpages and are derived from transmission data.

Table 3. Telescope locations and the number of observations taken.

Location	*LCO Label*	*Number of Observations*
SAAO, Sutherland, South Africa	kb87	30
CTIO, Region IV, Chile	kb29	21
Haleakala Observatory, Maui, USA	kb27	15
CTIO, Region IV, Chile	kb26	12
Tiede Observatory, Tenerife, Spain	kb95	11
Siding Spring Observatory, NSW, Australia	kb88	9
McDonald Observatory, Texas, USA	kb55	8
Tiede Observatory, Tenerife, Spain	kb82	8
Tiede Observatory, Tenerife, Spain	kb56	3
Siding Spring Observatory, NSW, Australia	kb24	2
Tiede Observatory, Tenerife, Spain	kb96	1

Note: SAAO, South African Astronomical Observatory; CTIO, Cerro Tololo Inter-American Observatory.

3. Results

In this section, we will discuss the derivation of the period, metallicity, absolute magnitude, and apparent magnitude of WZ Hya. We will then discuss the calculated distance using these quantities.

Table 4. List of comparison stars shown in Figure 1 with their calibrated magnitudes from the three surveys listed in the text.

Label	*Name*	*R.A. (°)*	*Dec. (°)*	*B Magnitude*	*V Magnitude*	*ip Magnitude*	*zs Magnitude*
CS1	TYC 5496–399–1	153.2930114	–13.2281205	—	11.392 ± .0197	11.024 ± .0156	—
CS2	TYC 5496–179–1	153.3767936	–13.2490501	—	11.329 ± .0223	11.053 ± .0168	—
CS3	UCAC4 384–056646	153.2681133	–13.3101129	—	12.321 ± .0303	11.673 ± .0177	—
CS4	TYC 5496–549–1	153.2548302	–13.0648543	—	11.601 ± .0275	11.409 ± .0183	11.272 ± .2996
CS5	UCAC4 385–056463	153.3065883	–13.1980118	—	12.947 ± .0397	12.289 ± .0247	11.998 ± .2302
CS6	UCAC4 385–056484	153.4398068	–13.1333245	—	12.250 ± .0441	11.692 ± .0152	11.434 ± .2887
CS7	TYC 5496–502–1	153.4004762	–13.2669225	—	11.360 ± .0415	10.998 ± .0163	—
CS8	UCAC4 384–056658	153.3415656	–13.2961601	—	12.887 ± .0498	12.096 ± .0229	11.766 ± .2536
CS9	UCAC4 386–056121	153.3904497	–12.9817688	—	12.841 ± .0526	12.436 ± .0291	12.237 ± .2129
CS10	TYC 5496–594–1	153.4185244	–13.1498112	12.782 ± .03	—	11.131 ± .0121	—
CS11	TYC 5496–141–1	153.4836995	–13.2713872	—	—	10.636 ± .0221	—
CS12	TYC 5496–559–1	153.2353099	–12.9970765	—	—	11.303 ± .0181	—

3.1. Period

Period finding and light curves were produced by ASTROSOURCE. Two different methods were used to obtain the period, string length minimization (String) (Dworetsky 1983) and phase dispersion minimization method (PDM) (Stellingwerf 1978). These are both standard methods and have the advantage of being model-independent. The only assumption made is the repeating signal, in this case, the period. Altunin *et al.* (2020) developed a method that automates these processes across data sets, this being the method used within ASTROSOURCE. Figure 2 presents all four light curves provided through the PDM. These light curves show the characteristic "shark tooth" shape of an RRab-type star.

We now take a look to see if our light curves are adequately sampled to produce a convincing distance measurement. The curves produced for the B, V, and zs bands all have over 100 magnitude inputs, while the ip band only has 46 inputs. The light curves from all four bands clearly showcase the rise and fall of the apparent magnitude with several points clustered around the extrema and therefore are considered sufficient for determining a period and an average magnitude.

The period of WZ Hya was determined by taking the weighted average of the eight values in Table 5. This results in the value of 0.5377 ± 0.0005 day. This value closely resembles those of other studies listed in Table 6.

3.2. Fourier decomposition

Fourier decomposition of the observed light curves of RR Lyr stars is an important analysis technique because physical parameters of these stars are shown to be correlated with the so-called relative Fourier parameters (e.g., Jurcsik and Kovacs (1996), Kovács (2005), Arellano Ferro (2022)). We fit a sine series of the form:

$$m(t) = A_0 + \sum_{j=1}^{N} A_j \sin(j\omega(t - t_0) + \varphi_j) \quad (2)$$

where m(t) is the model magnitude at time t, t_0 is the epoch of maximum light, A_j are the amplitudes to be fit, $\omega = 2\pi / P$ is the frequency of variation, P is the period of variation, φ_j are the phase shifts to be fit, and N is the order of the fit. The relative Fourier parameters are defined:

$$A_{ij} = \frac{A_i}{A_j}, \quad (3)$$

$$\varphi_{ij} = j\varphi_i - i\varphi_j. \quad (4)$$

The data were period folded using the modal period 0.537729 day. We used the PYTHON3 package `scipy.optimize.leastsq` to minimize the residuals between the measured magnitudes and model magnitudes. The question of how many sines to fit is an open one; we decided upon N = 11 for B-, V-, and zs-band and N = 6 for ip-band for reasons discussed in the next two paragraphs.

As an upper limit to the order of the fit, N, we chose two times the ratio of the total number of data points to the number of data points in the peak. The rationale is derived from Nyquist-Shannon sampling theory. The light curve changes most rapidly near maximum light, i.e., the light curve is sharply peaked. It is crucial to estimate as precisely as possible the epoch of maximum light, t_0, because the values of the Fourier phase parameters depend sensitively upon the value of t_0. By Shannon's theorem, to sample adequately the shape of the light curve near the peak we need a high enough frequency so that two complete sine waves fit within the peak. How wide is the peak? To estimate the width we first estimated the amplitude of the light curve, then counted the number of data points whose values were brighter than the half-amplitude. The ratio of the number of data points in the peak to the total number of data points is thus an estimate of the full width at half maximum (FWHM) of the (phased) light curve. The inverse of this ratio is the number of times the light curve is wider than the FWHM. Twice this number is an upper limit to the order of the fit, N. In V-band there are 15 data points of 109 total representing the peak, so N ≈ 2 × 109 / 15 is approximately 14.

In practice, we found that N = 14 was an "over fit," i.e., the higher order sines try to fit the scatter. The reader's attention is directed to Figure 3, and note the light curve is poorly sampled near a phase of 0.1. At orders of N > 12 a prominent peak appears there; there are no data points to contribute to the value of χ^2 in the optimization process and thus constrain these higher orders of sine. The N = 11 fit in Figure 3 may also have the slightest of bumps at this location, but we ran into a different problem for fits of N < 11. For a lower order fit the

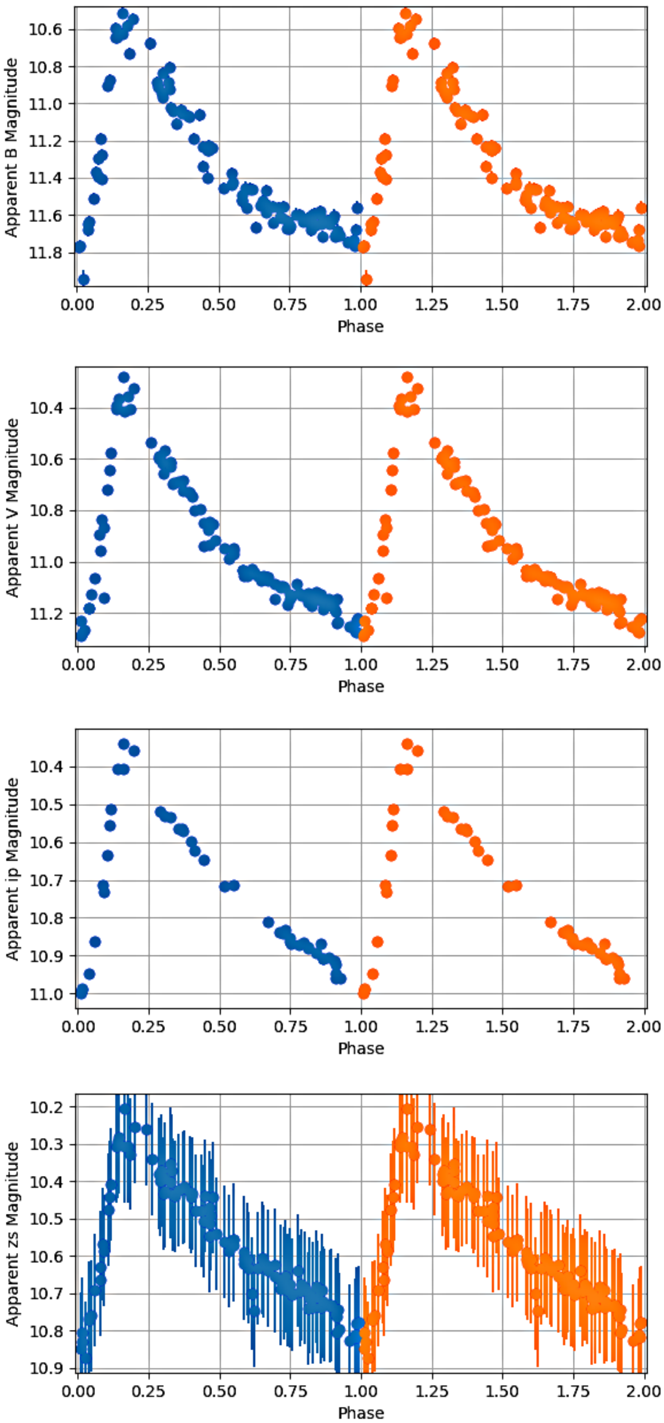

Figure 2. Light curves for WZ Hya in order from top to bottom: B, V, ip, and zs bands. All of these light curves are from the PDM method. Two full cycles are showcased to better visualize the shape of the curve. Calibrated magnitudes for each filter are shown in Table 7. Period values for each filter are provided in Table 5. No explicit choice was made for the value of phase.

Table 5. Period values in days determined through both PDM and String methods.

Filter	*PDM (days)*	*String (days)*
B	0.537635 ±.00114	0.537729 ±.001519
V	0.537920 ±.00114	0.537729 ±.001473
ip	0.537729 ±.001235	0.537729 ±.001758
zs	0.537729 ±.00114	0.537729 ±.001473

Note: PDM, phase dispersion minimization method; String, string length minimization method.

Table 6. List of known period values for WZ Hya from past studies.

Period (days)	*Source*
0.54	Joy (1950)
0.538	McNamara and Langford (1969)
0.53771535	Clube *et al.* (1969)
0.538	Jones (1973)
0.538	Hemenway (1975)
0.5377	Strauss (1976)
0.538	Preston *et al.* (1991)
0.5377229	Fernley *et al.* (1993)
0.538	Eggen (1994)
0.537718	Kovács (2005)
0.537713	Feast *et al.* (2008)
0.53772	Kolenberg and Bagnulo (2009)
0.5377	Dambis *et al.* (2013)
0.5373193	Skarka (2014)
0.537713	Gavrilchenko *et al.* (2014)
0.5377	Marsakov *et al.* (2018)

Table 7. Fourier decomposition parameters, and values derived therefrom, extracted from a least squares fit of a sine series to each light curve.

Filter	*A_0 (mag)*	*Amplitude (mag)*	*σ_{31} (rad*	*Epoch oft Maximum Light*
B	11.31 ± 0.09	0.73	—	—
V	10.91 ± 0.09	0.58	5.25	2459633.0312
ip	10.72 ± 0.15	0.37	—	—
zs	10.57 ± 0.14	0.29	—	—

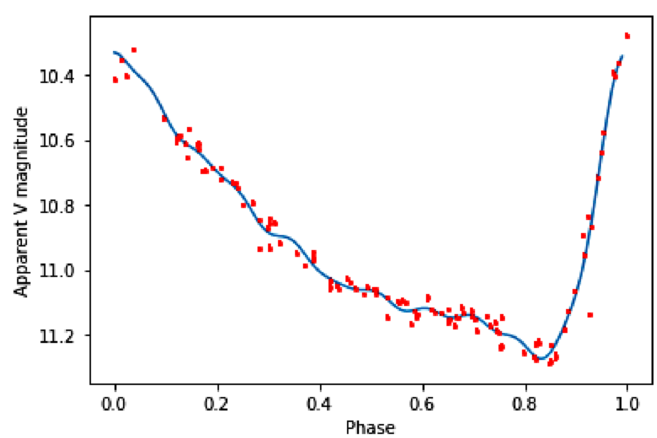

Figure 3. Phased light curve in V-band (points) with an 11th-order sine series fit (curve). Phase zero is at maximum light.

value of φ_1 experiences a large jump, and the inferred values of iron abundance are highly unrealistic. So we were left a single value, N = 11, that produced a reasonable fit for B, V, and zs light curves, an uncomfortably specific value, and perhaps an ungentle reminder that one can never have too much data. For the remaining filter, ip, there are about half as many total data points, and sine series at N > 6 showed noise-fitting. It is noted that the values of the intensity means, A_0, do not depend sensitively to the order of fit, and all values of A_0 were very close to the values of the various means discussed in section 3.4.

The relevant decomposition parameters for the purpose of this study are the zeroth order amplitudes, A_0, and the first and third order phases, φ_1 and φ_3. The zeroth order amplitude values for each filter are adopted as average apparent magnitudes, (m). The first and third order phases are extracted from the V-band data only and are used to compute iron abundance. The epoch of maximum light is a barycentric julian date (BJD) computed from the fit using the Python3 package `scipy.optimize.fmin`. The results are tabulated in Table 7.

3.3. Metallicity

Iron abundances found in other projects are showcased in Table 8, where a total of eight different values were found. The [Fe/H] of –1.40 from Eggen (1994) was derived photometrically by comparison with model atmospheres from Lester *et al.* (1986) assuming log(g) = 2.75. The –1.39 value from Fernley *et al.* (1998) uses Hipparcos data. The values of −1.30 (Layden 1994) and −0.89 (Norris 1986) were both derived using spectroscopy. The Gaia Data Release 3 (DR3) derives a [Fe/H] of –0.8574 (Gaia Collaboration 2022). We discovered that the value of –1.04 from Kovács (2005) appeared to be incorrect, as it is different than the value found in the references of that paper. The value of –0.59 from Ammons *et al.* (2006) also raised concern since it was derived using a training set of FGK dwarf stars only, not evolved stars, using Tycho data. The –1.32 value from Anderson and Francis (2012) uniquely assigns homogenized abundances to Hipparcos stars from a literature survey.

We derived an iron abundance value from the Fourier parameters thus (Jurcsik and Kovacs 1996):

$$[\mathrm{Fe}/\mathrm{H}] = -5.038 - 5.394\mathrm{P} + 1.345\varphi_{31}, \tag{5}$$

to obtain a value of [Fe/H] = –0.882. Our value is consistent with the larger of the historical values. The error on the φ_{31} term is large, of order 1 radian.

Using this iron abundance value, we can convert it into a metals/hydrogen ratio [M/H] via (Salaris *et al.* 1993):

$$[\mathrm{M}/\mathrm{H}] = [\mathrm{Fe}/\mathrm{H}] + \log(0.638 \times 10^{0.3} + 0.362). \tag{6}$$

This gives us a [M/H]} value of –0.668 which we can then apply to a conversion to log(Z) via (Catelan *et al.* 2004):

$$\log \mathrm{Z} = [\mathrm{M} / \mathrm{H}] - 1.765. \tag{7}$$

This gives us a log Z value of –2.43.

Table 8. List of derived metallicity values from past studies.

[Fe/H]	*Reference*
–1.40	Eggen (1994)
–1.39	Fernley *et al.* (1998)
–1.32	Anderson and Francis (2012)
–1.30	Layden (1994)
–1.04	Kovács (2005) (spurious?)
–0.89	Norris (1986)
–0.8574	Gaia Collaboration (2022)
–0.59	Ammons *et al.* (2006)

3.4. Apparent and absolute magnitude

An incomplete reading of the literature reveals four methods by which an average apparent magnitude can be computed for a variable star. These four are the magnitude-weight mean, $(\mathrm{m})_{\mathrm{mag}}$, the intensity-weighted mean, $(\mathrm{m})_{\mathrm{int}}$, the phase-weighted mean, $(\mathrm{m})_{\mathrm{pha}}$ (Saha and Hoessel 1990), and the mean derived from Fourier decomposition, which is called the intensity mean, $(\mathrm{m})_{\mathrm{fou}}$. For n data points with ith magnitude m_i at relative phase Φ_i the definitions are listed:

$$(\mathrm{m})_{\mathrm{mag}} = \frac{1}{\mathrm{n}} \sum^{\mathrm{n}} \mathrm{m}_i \tag{8}$$

$$(\mathrm{m})_{\mathrm{int}} = -2.5 \log \frac{1}{\mathrm{n}} \sum^{\mathrm{n}} 10^{-0.4\mathrm{m}_i} \tag{9}$$

$$(\mathrm{m})_{\mathrm{pha}} = -2.5 \log \frac{1}{2} \sum^{\mathrm{n}} (\Phi_{i+1} - \Phi_{i-1}) 10^{-0.4\mathrm{m}_i} \tag{10}$$

$$(\mathrm{m})_{\mathrm{fou}} = \mathrm{A}_0 \tag{11}$$

Note that the data must be phase-sorted before computing the phase-weighted mean.

Each mean has its own merits and the same goal, viz., to best approximate the flux of the "static" condition of the star. The values of the various means for our data are so close to each other as to be statistically indistinguishable. We adopt the Fourier decomposition amplitudes listed in Table 7 for the mean apparent magnitudes; to do so is consistent with modern practice and internally consistent with our computation of iron abundance.

Absolute magnitudes for WZ Hya were obtained using three magnitude-metallicity relations. The M_V-metallicity relation is from Catelan *et al.* (2004) while the M_i and M_z-metallicity relations are from Cáceres and Catelan (2008):

$$\mathrm{M}_\mathrm{V} = 2.288 + 0.882 \log \mathrm{Z} + 0.108(\log \mathrm{Z})^2 \tag{12}$$

$$\mathrm{M}_\mathrm{i} = 0.908 - 1.035 \log \mathrm{P} + 0.220 \log \mathrm{Z} \tag{13}$$

$$\mathrm{M}_\mathrm{z} = 0.839 - 1.295 \log \mathrm{P} + 0.211 \log \mathrm{Z} \tag{14}$$

In these equations, M is the absolute magnitude of the source star, P is the period (days), and Z is the metallicity.

3.5. Distance

Using the distance modulus equation, we can solve for our distance and interstellar extinction simultaneously by plugging in our apparent and absolute magnitudes:

$$d = 10^{(m - M - A + 5)/5} \tag{15}$$

In this equation, m is the average apparent magnitude, M is the absolute magnitude, and A is the value for interstellar extinction. The color excess E(B–V) was found using the three distances and their associated extinction values derived in each of the V, ip, and zs filters: d_V, d_{ip}, d_{zs}; A_V, A_{ip}, A_{zs}. This was done using the standard relations for extinction, e.g.,

$$R_\upsilon = \frac{A\upsilon}{E(B\text{–}V)} \tag{16}$$

where $R_\upsilon = 3.1$. A color excess of E(B–V) = 0.142 mag was derived by minimizing the standard deviation of the V, ip, and zs distances. Changing the color excess resulted in the distances having larger differences between each filter. If our distances were measured perfectly, we would expect a color excess value that gives identical distances in each filter. However, this did not happen, and we believe our value is a global minimum of the standard deviation.

An estimate of the maximum extinction along the line of sight to WZ Hya is provided by Schlafly and Finkbeiner (2011) and Schlegel *et al.* (1998) via online query of the NASA/IPAC Infrared Science Archive. They provide two mean extinction values, 0.0700 ± 0.0011 (Schlafly and Finkbeiner 2011) and 0.0814 ± 0.0012 (Schlegel *et al.* 1998). The distances determined using each of the different color excess values are provided in Table 9.

The final distance value calculated was an error-weighted average of the three distances in each filter. This is represented in the last row of Table 9, where we produced an average distance of 872 ± 47 parsecs. Comparing this value to the Gaia DR3 value of 999 ± 16 parsecs (Gaia Collaboration 2022), the difference between the calculated value and the Gaia DR3 value is nearly 2 standard deviations. When using the Schlafly and Finkbeiner (2011) and Schlegel *et al.* (1998) color excess values, we get an average distance of 942 ± 51 and 931 ± 50 parsecs, respectively. These two values are within 1 standard deviation of the Gaia DR3 distance value.

Table 9. Distances in each filter.

	Distances (pc)		
E(B–V)	0.142	0.0700 ± 0.0011	0.0814 ± 0.0012
V	866 ± 73	960 ± 81	945 ± 80
ip	898 ± 94	964 ± 101	953 ± 100
zs	862 ± 82	907 ± 86	900 ± 85

Note: Distances in each filter with its corresponding E(B–V) measurement; (d) represents the weighted average distance of the V, ip, and zs filters.

4. Conclusion

Using observations of the RR Lyr star WZ Hya, this research tested the infrared period-luminosity-metallicity (PLZ) relationships of Catelan *et al.* (2004) and Cáceres and Catelan (2008). The period was determined to be 0.5377 ± 0.0005 day. The photometric distance to WZ Hya was determined to be 872 ± 47 parsecs, 942 ± 51, and 931 ± 50 parsecs using the color excess derived using our minimization method, and the provided values from Schlafly and Finkbeiner (2011) and Schlegel *et al.* (1998) respectively. These values agreed with the Gaia DR3 value of 999 ± 16 within 1–2 standard deviations. The infrared PLZ relations yielded distances consistent with the Gaia parallax distance. For this particular star, the ip filter distance was closest to the Gaia distance; it will be interesting to see if this closest agreement is generally true.

5. Acknowledgements

Thank you to Michael Fitzgerald for creating the OurSolarSiblings RR Lyrae research course, providing access to an efficient pipeline, providing educational materials, and also providing telescope time with the Las Cumbres Observatory.

Many thanks to the editor and anonymous referee for the careful review and meaningful comments that improved the manuscript.

The DSS image is based on photographic data obtained using The UK Schmidt Telescope. The UK Schmidt Telescope was operated by the Royal Observatory Edinburgh, with funding from the UK Science and Engineering Research Council, until 1988 June, and thereafter by the Anglo-Australian Observatory. Original plate material is copyright (c) the Royal Observatory Edinburgh and the Anglo-Australian Observatory. The plates were processed into the present compressed digital form with their permission. The Digitized Sky Survey was produced at the Space Telescope Science Institute under US Government grant NAG W-2166.

This research has made use of SAOImageDS9, developed by Smithsonian Astrophysical Observatory.

This work has made use of data from the European Space Agency (ESA) mission Gaia (https://www.cosmos.esa.int/Gaia), processed by the Gaia Data Processing and Analysis Consortium (DPAC, https://www.cosmos.esa.int/web/Gaia/dpac/consortium). Funding for the DPAC has been provided by national institutions, in particular, the institutions participating in the Gaia Multilateral Agreement.

This research has made use of the NASA/IPAC Infrared Science Archive, which is funded by the National Aeronautics and Space Administration and operated by the California Institute of Technology.

This research has made use of the SIMBAD database, operated at CDS, Strasbourg, France.

This research has made use of the APASS database, located at the AAVSO web site. Funding for APASS has been provided by the Robert Martin Ayers Sciences Fund.

References

Alonso-García, J., Mateo, M., Sen, B., Banerjee, M., Catelan, M., Minniti, D., and von Braun, K. 2012, *Astron. J.*, **143**, 70 (DOI: 10.1088/0004-6256/143/3/70).

Altunin, I., Caputo, R., and Tock, K. 2020, *Astron. Theory Obs. Methods*, **1**, 1 (DOI: 10.32374/atom.2020.1.1).

Ammons, S. M., Robinson, S. E., Strader, J., Laughlin, G., Fischer, D., and Wolf, A. 2006, *Astrophys. J.*, **638**, 1004 (DOI: 10.1086/498490).

Anderson, E., and Francis, C. 2012, *Astron. Lett.*, **38**, 331 (DOI: 10.1134/S1063773712050015).

Arellano Ferro, A. 2022, *Rev. Mex. Astron. Astrofis.*, **58**, 257 (DOI: 10.22201/ia.01851101p.2022.58.02.08).

Barbier-Brossat, M., Petit, M., and Figon, P. 1994, *Astron. Astrophys., Suppl. Ser.*, **108**, 603.

Bertin, E. 2011, in *Astronomical Data Analysis Software and Systems XX*, eds. I. N. Evans, A. Accomazzi, D. J. Mink, A. H. Rots, ASP Conf. Proc. 442, Astronomical Society of the Pacific, San Francisco, 435.

Bertin, E., and Arnouts, S. 1996, *Astron. Astrophys., Suppl. Ser.*, 117, 393 (DOI: 10.1051/aas:1996164).

Bessell, M. S. 1993, in *Stellar Photometry—Current Techniques and Future Developments*, eds. C. J. Butler, I. Elliott, IAU Colloq. 136, Cambridge Univ. Press, Cambridge, 22.

Brown, T. M., *et al.* 2013, *Publ. Astron. Soc. Pacific,* **125**, 1031 (DOI: 10.1086/673168).

Cáceres, C., and Catelan, M. 2008, *Astrophys. J., Suppl. Ser.*, **179**, 242 (DOI: 10.1086/591231).

Catelan, M., Pritzl, B. J., and Smith, H. A. 2004, *Astrophys. J., Suppl. Ser.*, **154**, 633 (DOI: 10.1086/422916).

Clube, S. V. M., Evans, D. S., and Jones, D. H. P. 1969, *Mem. Roy. Astron. Soc.*, **72**, 101.

Collins, K. A., Kielkopf, J. F., Stassun, K. G., and Hessman, F. V. 2017, *Astron. J.*, **153**, 77 (DOI: 10.3847/1538-3881/153/2/77).

Dambis, A. K., Berdnikov, L. N., Kniazev, A. Y., Kravtsov, V. V., Rastorguev, A. S., Sefako, R., and Vozyakova, O. V. 2013, *Mon. Not. Roy. Astron. Soc.*, **435**, 3206 (DOI: 10.1093/mnras/stt1514).

Dworetsky, M. M. 1983, *Mon. Not. Roy. Astron. Soc.*, **203**, 917 (DOI: 10.1093/mnras/203.4.917).

Eggen, O. J. 1994, *Astron. J.*, **107**, 2131 (DOI: 10.1086/117024).

Feast, M. W., Laney, C. D., Kinman, T. D., van Leeuwen, F., and Whitelock, P. A. 2008, *Mon. Not. Roy. Astron. Soc.*, **386**, 2115 (DOI: 10.1111/j.1365-2966.2008.13181.x).

Fernley, J. A., Skillen, I., and Burki, G. 1993, *Astron. Astrophys., Suppl. Ser.*, **97**, 815

Fernley, J., Barnes, T. G., Skillen, I., Hawley, S. L., Hanley, C. J., Evans, D. W., Solano, E., and Garrido, R. 1998, *Astron. Astrophys.*, **330**, 515.

Fitzgerald, M. T. 2018, *Robotic Telesc. Student Res. Educ.Proc.*, **1**, 347.

Fitzgerald, M., Gomez, E., Salimpour, S., and Wibowo, R. 2020, *J. Open Source Software*, in review.

Flewelling, H. A., *et al.* 2020, *Astrophys. J., Suppl. Ser.*, **251**, 7 (DOI: 10.3847/1538-4365/abb82d).

Fukugita, M., Ichikawa, T., Gunn, J. E., Doi, M., Shimasaku, K., and Schneider, D. P. 1996, *Astron. J.*, **111**, 1748 (DOI: 10.1086/117915

Gaia Collaboration. 2022, VizieR Online Data Catalog, I/355.

Gavrilchenko, T., Klein, C. R., Bloom, J. S., and Richards, J. W. 2014, *Mon. Not. Roy. Astron. Soc.*, **441**, 715 (DOI: 10.1093/mnras/stu606).

Hemenway, M. K. 1975, *Astron. J.*, **80**, 199 (DOI: 10.1086/111732).

Henden, A. A., Levine, S., Terrell, D., and Welch, D. L. 2015, Amer. Astron. Soc. Meeting Abstr. 225, id.336.16.

Jones, D. H. P. 1973, *Astrophys. J., Suppl. Ser.*, **25**, 487 (DOI: 10.1086/190276).

Joy, A. H. 1950, *Publ. Astron. Soc. Pacific*, **62**, 60 (DOI: 10.1086/126230).

Jurcsik, J., and Kovacs, G. 1996, *Astron. Astrophys.*, **312**, 111.

Kolenberg, K., and Bagnulo, S. 2009, *Astron. Astrophys.*, **498**, 543 (DOI: 10.1051/0004-6361/200811591).

Kovács, G. 2005, *Astron. Astrophys.*, **438**, 227 (DOI: 10.1051/0004-6361:20052742).

Laher, R. R., Gorjian, V., Rebull, L. M., Masci, F. J., Fowler, J. W., Helou, G., Kulkarni, S. R., and Law, N. M. 2012a, *Publ. Astron. Soc. Pacific*, **124**, 737 (DOI: 10.1086/666883).

Laher, R. R., *et al.* 2012b, *Publ. Astron. Soc. Pacific*, **124**, 764 (DOI: 10.1086/666507).

Layden, A. C. 1994, *Astron. J.*, 108, 1016 (DOI: 10.1086/117132).

Lester, J. B., Gray, R. O., and Kurucz, R. L. 1986, *Astrophys. J., Suppl. Ser.*, **61**, 509 (DOI: 10.1086/191122

Magnier, E. A., *et al.* 2020, *Astrophys. J., Suppl. Ser.*, **251**, 3 (DOI: 10.3847/1538-4365/abb829).

Marsakov, V. A., Gozha, M. L., and Koval, V. V. 2018, *Astron. Rep.*, **62**, 50 (DOI: 10.1134/S1063772918010055).

McNamara, D. H., and Langford, W. R. 1969, *Publ. Astron. Soc. Pacific*, **81**, 141 (DOI: 10.1086/128753).

Norris, J. 1986, *Astrophys. J., Suppl. Ser.*, **61**, 667 (DOI: 10.1086/191128).

Preston, G. W., Shectman, S. A., and Beers, T. C. 1991, *Astrophys. J.*, **375**, 121 (DOI: 10.1086/170175).

Saha, A., and Hoessel, J. G. 1990, *Astron. J.*, **99**, 97 (DOI: 10.1086/115316).

Salaris, M., Chieffi, A., and Straniero, O. 1993, *Astrophys. J.*, **414**, 580 (DOI: 10.1086/173105).

Schechter, P. L., Mateo, M., and Saha, A. 1993, *Publ. Astron. Soc. Pacific*, **105**, 1342 (DOI: 10.1086/133316).

Schlafly, E. F., and Finkbeiner, D. P. 2011, *Astrophys. J.*, **737**, 103 (DOI: 10.1088/0004-637X/737/2/103).

Schlegel, D. J., Finkbeiner, D. P., and Davis, M. 1998, *Astrophys. J.*, **500**, 525 (DOI: 10.1086/305772).

Skarka, M. 2014, *Astron. Astrophys.*, **562A**, 90 (DOI: 10.1051/0004-6361/201322491).

Stellingwerf, R. F. 1978, *Astrophys. J.*, **224**, 953 (DOI: 10.1086/156444).

Stetson, P. B. 1987, *Publ. Astron. Soc. Pacific*, **99**, 191 (DOI: 10.1086/131977).

Strauss, F. M. 1976, *Publ. Astron. Soc. Pacific*, **88**, 531 (DOI: 10.1086/129980).

Tonry, J. L., *et al.* 2012, *Astrophys. J.*, **750**, 99 (DOI: 10.1088/0004-637X/750/2/99).

Wolf, C., *et al.* 2018, *Publ. Astron. Soc. Australia*, **35**, 10 (DOI: 10.1017/pasa.2018.5).

Appendix A. Data tables and source file locations.

Table A1. WZ Hya dataset.

JD	Magnitude	Mag. Error	Filter
2459631.32120815	11.68119776	0.03160651	B
2459631.38961681	10.90275832	0.03106498	B
2459631.52986586	11.05240500	0.03095381	B
2459631.90497966	11.36690333	0.03074839	B
2459632.11644435	11.25047690	0.03195777	B
2459632.31963406	11.59148747	0.03277155	B
2459632.46740585	10.87088978	0.03082018	B
2459632.65489512	11.39846061	0.03328912	B
2459632.84242209	11.63499130	0.03394055	B
2459633.02999621	10.51738172	0.03106159	B
2459633.33575260	11.55400480	0.03135752	B
2459633.40504647	11.57827082	0.03111393	B
2459633.96745447	11.62460656	0.03074584	B
2459634.71738339	10.94227464	0.03378873	B
2459634.90502241	11.54681989	0.03065391	B
2459635.35021620	11.24058850	0.03146099	B
2459635.46743325	11.55229917	0.03118107	B
2459641.59250689	11.18647574	0.03092746	B
2459656.50994394	11.68038804	0.03250783	B
2459656.52677103	11.60091458	0.03231762	B
2459656.70236651	10.73154939	0.03195103	B
2459657.63984314	11.70944913	0.03149046	B
2459697.85450335	11.56288489	0.03094733	B
2459698.22203357	11.06950416	0.03115582	B
2459698.36058325	11.52359494	0.03235234	B
2459698.49942127	11.71505990	0.03170587	B
2459698.74480662	11.03472327	0.03075865	B
2459699.46883935	11.61231692	0.03163601	B
2459699.81178139	11.10996455	0.03109777	B
2459700.20797593	11.27416993	0.03099031	B
2459700.56170047	11.67326501	0.03150321	B
2459700.93669469	11.23216378	0.03113684	B
2459701.60866620	11.64385517	0.03162460	B
2459701.87893299	10.54808932	0.03060532	B
2459702.21107926	11.61488492	0.03119212	B
2459702.25307245	11.64699553	0.03117435	B
2459702.46445447	10.90937105	0.03142435	B
2459702.62407697	11.51861527	0.03166141	B
2459703.01222885	10.83516455	0.03122663	B
2459703.20806666	11.54491682	0.03123967	B
2459703.37407174	11.73321993	0.03115290	B
2459703.56145459	10.80511083	0.03329113	B
2459704.21840146	11.37270534	0.03120304	B
2459704.34700364	11.60036503	0.03132903	B
2459704.50308852	11.39383704	0.03135875	B
2459704.82186830	11.58426964	0.03069995	B
2459705.20986664	11.06397141	0.03115627	B
2459705.24886522	11.25349236	0.03123569	B
2459705.43638178	11.63532744	0.03129773	B
2459705.62388413	10.62814720	0.03115146	B
2459705.83168486	11.43619693	0.03133891	B
2459706.41467827	11.66344575	0.03119400	B
2459706.61694132	11.77148836	0.03128924	B
2459707.37145955	11.18941986	0.03077553	B
2459707.61626139	11.71485261	0.03163603	B
2459707.84062034	10.88803630	0.03227036	B
2459708.20300464	11.74466829	0.03152550	B
2459708.25705697	11.51115410	0.03128736	B
2459708.52079102	11.42444598	0.03377139	B
2459708.62361516	11.67121932	0.03151273	B
2459708.81101966	11.40590600	0.03132924	B
2459709.21062183	11.60003075	0.03126306	B
2459711.24406055	11.45964726	0.03212920	B
2459711.24827957	11.46173082	0.03236761	B
2459711.46436722	11.94210063	0.04966275	B
2459711.62814068	10.92119465	0.03394172	B
2459711.81080307	11.47038469	0.03150432	B
2459715.53026930	11.52628126	0.03422700	B
2459715.53712212	11.45275452	0.03410839	B
2459715.74394376	11.76338112	0.03094872	B
2459715.92834665	10.88393288	0.03230447	B
2459716.19871550	11.62341197	0.03135328	B
2459716.31213507	11.64535232	0.03152462	B
2459716.47460922	11.04307744	0.03138095	B
2459716.74423077	11.65556754	0.03088464	B
2459716.84953994	11.68174912	0.03136323	B
2459717.37319755	11.76559009	0.03108308	B
2459717.50605679	10.67653244	0.03390063	B
2459717.59952549	11.06166094	0.03405958	B
2459717.97848694	10.64632403	0.03091745	B
2459718.36908144	11.64866183	0.03102339	B
2459719.36952073	11.61669957	0.03096378	B
2459719.47441348	11.68228870	0.03396045	B
2459720.37812455	11.55916872	0.03088135	B
2459720.58767248	11.56005704	0.03495183	B
2459720.61774372	11.63637107	0.03140771	B
2459721.20377867	10.59464812	0.03131397	B
2459721.38079223	11.22624726	0.03119094	B
2459721.54737673	11.59723452	0.03489259	B
2459721.74559132	10.64155750	0.03071132	B
2459724.45211563	10.58558601	0.03168327	B
2459724.53644186	11.02336458	0.03168203	B
2459725.37183316	11.63212235	0.03125886	B
2459725.47378102	11.29732681	0.03181294	B
2459725.74664321	11.49065338	0.03098182	B
2459725.86201528	11.63246256	0.03066522	B
2459726.37222211	11.63436081	0.03110716	B
2459726.45907937	11.60178023	0.03362850	B
2459726.74690490	11.34005042	0.03096944	B
2459726.78617987	11.45542248	0.03084804	B
2459727.45127671	11.65897289	0.03149027	B
2459727.53614328	11.70864622	0.03141469	B
2459727.74739230	10.96655069	0.03090420	B
2459631.32176487	11.23098219	0.00856189	V
2459631.39015043	10.64091303	0.00721569	V
2459631.53039949	10.72417289	0.00705874	V
2459632.11707044	10.87453853	0.01134212	V
2459632.32019080	11.11731306	0.00947455	V
2459632.46795089	10.57592942	0.00697907	V
2459632.65550975	10.93288188	0.01159176	V
2459632.84303669	11.16142437	0.01231007	V
2459633.03059999	10.27867799	0.00725113	V
2459633.33629775	11.10243631	0.00779396	V
2459633.40560320	11.12640516	0.00741145	V
2459633.96810466	11.16223956	0.00687267	V
2459634.71798657	10.61395811	0.01135391	V
2459634.90563778	11.07445225	0.00658723	V
2459635.35076154	10.85560333	0.00881935	V
2459635.46797837	11.08585632	0.00757545	V
2459641.59313320	10.83542052	0.00705794	V
2459656.51104560	11.17194067	0.00963212	V
2459656.52783905	11.14428889	0.00961167	V
2459656.70343464	10.40350315	0.00846187	V
2459656.89097394	10.98879612	0.00809554	V
2459657.40287331	10.91717737	0.00997281	V
2459657.83656025	10.58720370	0.00660642	V
2459697.85557120	11.09714568	0.00732102	V
2459698.22297260	10.73442405	0.00745519	V
2459698.36168461	11.05422447	0.00918399	V

Table continued on following pages

Table A1. WZ Hya dataset (cont.).

JD	*Magnitude*	*Mag. Error*	*Filter*
2459698.50049568	11.23969433	0.00861602	V
2459698.74586166	10.68447405	0.00651769	V
2459699.03989695	11.14771217	0.00980217	V
2459699.46993081	11.10195134	0.00847730	V
2459699.62965451	11.28136037	0.00778777	V
2459699.81285153	10.68612531	0.00704274	V
2459700.20891495	10.86889823	0.00726682	V
2459700.37622688	10.74723363	0.00694093	V
2459700.56277911	11.14551619	0.00837344	V
2459700.75464628	10.71708236	0.00883561	V
2459700.93783197	10.93734896	0.00887568	V
2459701.60962844	11.14611813	0.00839703	V
2459701.88005757	10.32340126	0.00646920	V
2459702.21201839	11.15215185	0.00765449	V
2459702.25402307	11.17305268	0.00766597	V
2459702.46556749	10.58925391	0.00848174	V
2459702.62514488	11.03482661	0.00925387	V
2459703.01338619	10.56776608	0.00727696	V
2459703.20901927	11.06038718	0.00766719	V
2459703.37501246	11.26942934	0.00771130	V
2459703.56240552	10.61354901	0.00961088	V
2459704.21934061	10.94614202	0.00768201	V
2459704.34794264	11.13112543	0.00783055	V
2459704.50418071	10.95543237	0.00825845	V
2459704.82294081	11.07248647	0.00710963	V
2459705.21081736	10.73000468	0.00781084	V
2459705.24981604	10.84387429	0.00757284	V
2459705.43747441	11.12169165	0.00766847	V
2459705.62483649	10.41454991	0.00729793	V
2459705.83275267	10.95852716	0.01709137	V
2459706.41577953	11.05726672	0.00819051	V
2459706.61791683	11.28995689	0.00787362	V
2459707.37259575	10.79954125	0.00702156	V
2459707.61722841	11.18693566	0.00846792	V
2459707.84168745	10.59820882	0.01846062	V
2459708.20395538	11.25515601	0.00826521	V
2459708.25799751	11.06648392	0.00786685	V
2459708.52174222	10.96959337	0.01075267	V
2459708.62457532	11.16709057	0.00814072	V
2459708.81208735	11.13919074	0.00878394	V
2459709.21158414	11.14890554	0.00771536	V
2459711.24501128	11.02939528	0.00921082	V
2459711.24921901	11.04083864	0.00950904	V
2459711.46546865	11.26678241	0.01718254	V
2459711.62909139	10.62733931	0.01019201	V
2459711.81186939	11.06169097	0.00818734	V
2459715.53080266	11.05629794	0.01122435	V
2459715.53766717	11.05015691	0.01140439	V
2459715.74461708	11.27660642	0.00738109	V
2459715.92895613	10.61621181	0.00873878	V
2459716.19926060	11.14692108	0.00792803	V
2459716.31268001	11.18195780	0.00811704	V
2459716.47522228	10.69353089	0.00811796	V
2459716.74484604	11.13306399	0.00713996	V
2459716.85017754	11.18345808	0.00770394	V
2459717.37382369	11.23152486	0.00742539	V
2459717.50660182	10.53477125	0.01066790	V
2459717.60007119	10.79610816	0.01092264	V
2459717.78764107	11.12338903	0.00692882	V
2459717.97910147	10.40680258	0.00730584	V
2459718.36970757	11.15434943	0.00725604	V
2459719.37013531	11.09513374	0.00721605	V
2459719.47494693	11.23484994	0.01076551	V
2459720.37878542	11.05745628	0.00728260	V
2459720.58820739	11.22309786	0.01167114	V
2459720.61831196	11.12943392	0.00791142	V
2459721.20432199	10.39271632	0.00773426	V
2459721.38140667	10.85896708	0.00754318	V
2459721.54791105	11.08756349	0.01157736	V
2459721.74619431	10.36299144	0.00659583	V
2459724.45271880	10.35538364	0.00837314	V
2459724.53705630	10.69822101	0.00860641	V
2459725.37245917	11.14425542	0.00761149	V
2459725.47439555	10.89453777	0.00890517	V
2459725.74724677	11.03215008	0.00731312	V
2459725.86262988	11.13448704	0.00667883	V
2459726.37284834	11.12660374	0.00731357	V
2459726.45961276	11.18783561	0.01025520	V
2459726.74750857	10.84896351	0.00721619	V
2459726.78679440	10.94964284	0.00706361	V
2459727.45191450	11.13825566	0.00834278	V
2459727.53675778	11.19343732	0.00829792	V
2459727.74800753	10.65509449	0.00711970	V
2459631.39053289	10.55648431	0.00550258	i
2459631.53077037	10.57147150	0.00529747	i
2459632.46832180	10.51417880	0.00536922	i
2459633.03102939	10.34082725	0.00504870	i
2459633.33666873	10.83253219	0.00592412	i
2459633.40597407	10.86805539	0.00567568	i
2459633.96853404	10.91254450	0.00486197	i
2459641.59358528	10.71475958	0.00541331	i
2459657.64048168	10.95837165	0.00639423	i
2459657.83613127	10.52081704	0.00458260	i
2459697.85515348	10.83825174	0.00550703	i
2459698.50005996	10.95926836	0.00648658	i
2459698.74543282	10.56608435	0.00450234	i
2459699.62927147	10.98523929	0.00546827	i
2459699.81241842	10.56391484	0.00555219	i
2459700.20854407	10.73064096	0.00591570	i
2459700.37578641	10.59950236	0.00516710	i
2459700.56233857	10.86244673	0.00621707	i
2459700.75421840	10.63401254	0.00693163	i
2459701.87961705	10.35774183	0.00460786	i
2459702.21164739	10.88185558	0.00592165	i
2459703.56203461	10.53556247	0.00662110	i
2459704.21896959	10.71268025	0.00576139	i
2459704.82249749	10.81136101	0.00540506	i
2459705.43703406	10.87886264	0.00572599	i
2459705.62446111	10.40582789	0.00508036	i
2459706.61752665	10.99825287	0.00561892	i
2459707.37212047	10.62262219	0.00530269	i
2459707.61685294	10.90823369	0.00598006	i
2459708.25763665	10.86089016	0.00612845	i
2459716.74526366	10.89395946	0.00533096	i
2459716.85061799	10.94597944	0.00577784	i
2459717.37426410	10.98983883	0.00570631	i
2459717.78807034	10.87161034	0.00526509	i
2459717.97953064	10.40772908	0.00512816	i
2459718.37014800	10.90677193	0.00541374	i
2459719.37058731	10.83969881	0.00545159	i
2459725.37289954	10.90442091	0.00556959	i
2459725.86305866	10.86428269	0.00493983	i
2459726.37328883	10.85175947	0.00544215	i
2459726.45999521	10.92425839	0.00736830	i
2459726.74793789	10.64778762	0.00534345	i
2459726.78722322	10.71529874	0.00508839	i
2459727.45234329	10.86710720	0.00684808	i
2459727.53718664	10.94756530	0.00643976	i
2459727.74844838	10.53023937	0.00543720	i

Table continued on next page

Table A1. WZ Hya dataset (cont.).

JD	*Magnitude*	*Mag. Error*	*Filter*
2459631.32285389	10.78203507	0.15050933	z
2459631.39125106	10.44145689	0.15037791	z
2459631.53148860	10.41457243	0.15036347	z
2459632.11829888	10.51429645	0.15107269	z
2459632.32127990	10.68290595	0.15045219	z
2459632.46905161	10.40879291	0.15037393	z
2459632.65671485	10.54846137	0.15069227	z
2459632.84425321	10.74078865	0.15071855	z
2459633.03180580	10.20578020	0.15035893	z
2459633.33738765	10.65440540	0.15040000	z
2459633.40669219	10.69151655	0.15038322	z
2459633.61219789	10.26104776	0.15079467	z
2459634.71919207	10.43255192	0.15059871	z
2459634.90687842	10.60521655	0.15032782	z
2459635.35185058	10.44398231	0.15045952	z
2459635.46906738	10.62479420	0.15040014	z
2459641.59438461	10.56951199	0.15034931	z
2459656.51183339	10.73745108	0.15048501	z
2459656.52865002	10.73805249	0.15049498	z
2459656.70421063	10.32752091	0.15043448	z
2459656.89175564	10.58843782	0.15048595	z
2459657.40367260	10.54138680	0.15061632	z
2459657.83733875	10.37171322	0.15032388	z
2459697.85635923	10.66794176	0.15036657	z
2459698.22369076	10.44339064	0.15038915	z
2459698.36248389	10.61391133	0.15046186	z
2459698.50127352	10.80727223	0.15042284	z
2459698.74664934	10.41908558	0.15031886	z
2459699.04074243	10.74314577	0.15058538	z
2459699.47071848	10.68866258	0.15042033	z
2459699.63037953	10.82987728	0.15036386	z
2459699.81363279	10.42392521	0.15035116	z
2459700.20964455	10.58593233	0.15040116	z
2459700.37702606	10.43449585	0.15034688	z
2459700.56355515	10.69399312	0.15040903	z
2459700.75543019	10.47759611	0.15047198	z
2459700.93864325	10.43936531	0.15036992	z
2459701.61035802	10.65538088	0.15041941	z
2459701.88085672	10.25586391	0.15032545	z
2459702.21274797	10.71225491	0.15039709	z
2459702.25475276	10.73110322	0.15039950	z
2459702.46635516	10.39809275	0.15048897	z
2459702.62593252	10.60782518	0.15048067	z
2459703.01419464	10.42832482	0.15036998	z
2459703.20974908	10.62612274	0.15040716	z
2459703.37574511	10.81123895	0.15039881	z
2459703.56313515	10.40234977	0.15041641	z
2459704.22007019	10.55545715	0.15038940	z
2459704.34867282	10.67777937	0.15040493	z
2459704.50496849	10.66550237	0.15039720	z
2459704.82371899	10.63877824	0.15036971	z
2459705.21154701	10.43029152	0.15041051	z
2459705.25054560	10.47100007	0.15040380	z
2459705.43827371	10.70135120	0.15039738	z
2459705.62556718	10.30622256	0.15035184	z
2459705.83352896	10.57153671	0.15175672	z
2459706.41656708	10.63273065	0.15039274	z
2459706.61864831	10.84991407	0.15036729	z
2459707.37338343	10.47932695	0.15036470	z
2459707.61795928	10.73177187	0.15038634	z
2459707.84248661	10.37995546	0.15039250	z
2459708.20468500	10.82645355	0.15044368	z
2459708.25873876	10.69276995	0.15041935	z
2459708.52247260	10.55779694	0.15048733	z
2459708.62530269	10.69138020	0.15038106	z
2459711.24574090	10.70157326	0.15054014	z
2459711.24994864	10.74628830	0.15056297	z
2459711.46625629	10.87348393	0.15095943	z
2459711.62980942	10.37257327	0.15044954	z
2459711.81265709	10.63315095	0.15041091	z
2459715.53189182	10.62255017	0.15049505	z
2459715.53875619	10.60998373	0.15049361	z
2459715.74582272	10.81938025	0.15035631	z
2459715.93015837	10.35294804	0.15044921	z
2459716.20034952	10.71395361	0.15042301	z
2459716.31378054	10.76464077	0.15041905	z
2459716.47647730	10.44080625	0.15039559	z
2459716.74604015	10.70996851	0.15035387	z
2459716.85139407	10.77317511	0.15035629	z
2459717.37505188	10.80698922	0.15037017	z
2459717.50770247	10.34136831	0.15046219	z
2459717.60116024	10.47915679	0.15044534	z
2459717.78884682	10.69365887	0.15035474	z
2459717.98034193	10.29610808	0.15034050	z
2459718.37093561	10.72408285	0.15034985	z
2459719.37137499	10.67300351	0.15036255	z
2459719.47605906	10.79635613	0.15046105	z
2459720.38002633	10.63225237	0.15034784	z
2459720.58929645	10.77713829	0.15050392	z
2459720.61943562	10.76084938	0.15037456	z
2459721.20541182	10.30646149	0.15039970	z
2459721.38265799	10.49055559	0.15035776	z
2459721.54900010	10.63911151	0.15046978	z
2459721.74741067	10.28383230	0.15033698	z
2459724.45392371	10.30699905	0.15045869	z
2459724.53827339	10.43729983	0.15043322	z
2459725.37368720	10.73404219	0.15036833	z
2459725.47560047	10.63040382	0.15041861	z
2459725.74846399	10.59045759	0.15035685	z
2459725.86383466	10.68653769	0.15032462	z
2459726.37407647	10.67511115	0.15035774	z
2459726.46071340	10.75733677	0.15046591	z
2459726.74871439	10.50824590	0.15036044	z
2459726.78799930	10.56199176	0.15034503	z
2459727.45313099	10.70535056	0.15045880	z
2459727.53795122	10.76124796	0.15041864	z
2459727.74922477	10.39382015	0.15037274	z

Table A2. Repository of the data files.

Available through the AAVSO ftp public datasets site
ftp://ftp.aavso.org/public/datasets/3850-Ritterby-511-wzhya/B-filter.txt
ftp://ftp.aavso.org/public/datasets/3850-Ritterby-511-wzhya/V-filter.txt
ftp://ftp.aavso.org/public/datasets/3850-Ritterby-511-wzhya/i-filter.txt
ftp://ftp.aavso.org/public/datasets/3850-Ritterby-511-wzhya/z-filter.txt

Recent Maxima of 89 Short Period Pulsating Stars

Gerard Samolyk
P.O. Box 20677, Greenfield, WI 53220; gsamolyk@wi.rr.com

Received January 25, 2023; accepted January 25, 2023

Abstract This paper contains times of maxima for 89 short period pulsating stars (primarily RR Lyrae and δ Scuti stars). This represents the CCD observations received by the AAVSO Short Period Pulsator (SPP) Section in 2022.

1. Recent observations

Table 1 contains times of maxima calculated from CCD observations made by participants in the AAVSO's Short Period Pulsator (SPP) Section. This list will be web-archived and made available through the AAVSO ftp site at:

ftp:ftp.aavso.org/public/datasets/gsamj511spp89.txt .

The error estimate is included. RR Lyr stars in this list, along with data from earlier AAVSO publications, are included in the GEOS database at:

http://rr-lyr.irap.omp.eu/dbrr/ .

This database does not include δ Scuti stars. These observations were reduced by the writer using the Peranso program (Vanmunster 2021). Column F indicates the filter used. A "C" indicates a clear filter.

The linear elements in the *General Catalogue of Variable Stars* (GCVS; Kholopov *et al*. 1985) were used to compute the O–C values for most stars. For a few exceptions where the GCVS elements are missing or are in significant error, light elements from another source are used: V799 Aur, V338 Boo, V377 Boo, V876 Cep, V488 Gem, EH Lib, and AN Lyn (AAVSO VSX site, Watson et al. 2014); RZ Cap and DG Hya (Samolyk 2010); V2416 Cyg (Samolyk 2018); and EF Cnc and GO Hya (GEOS Database).

In the case of AA LMi (Figure 1), the following light elements were calculated using a linear regression on the times of maxima listed in this paper.

$$\text{Time of maximum (JD)} = \underset{\pm 0.0015}{2458941.3878} + \underset{0.00000009}{0.05420027} * E \quad (1)$$

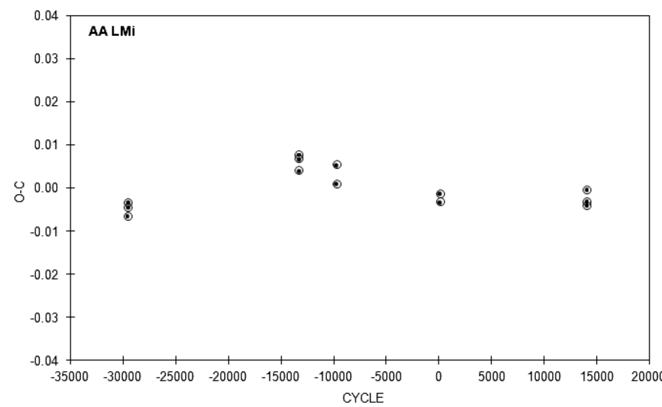

Figure 1. O–C plot for AA LMi using the light elements in Equation 1.

References

Groupe Européen d'Observation Stellaire (GEOS). 2021, GEOS RR Lyr Database, (http://rr-lyr.irap.omp.eu/dbrr/index.php).
Kholopov, P. N., *et al.* 1985, *General Catalogue of Variable Stars*, 4th ed., Moscow.
Samolyk, G. 2010, *J. Amer. Assoc. Var. Star Obs.*, **38**, 12.
Samolyk, G. 2018, *J. Amer. Assoc. Var. Star Obs.*, **46**, 70.
Vanmunster, T. 2021, light curve and period analysis software, Peranso v.2.50 (http://www.cbabelgium.com/peranso).
Watson, C., Henden, A. A., and Price, C. A. 2014, AAVSO International Variable Star Index VSX (Watson+, 2006–2014; https://www.aavso.org/vsx).

Table 1. Recent times of maxima of stars in the AAVSO Short Period Pulsator program.

Star	JD (max) Hel. 2400000 +	Cycle	O–C (day)	F	Observer	Error (day)
SW And	59815.7382	94247	–0.5650	V	G. Samolyk	0.0009
SW And	59941.3391	94531	–0.5715	V	T. Arranz	0.0011
XX And	59591.3542	28369	0.3032	V	T. Arranz	0.0011
XX And	59790.8342	28645	0.3050	V	G. Samolyk	0.0015
ZZ And	59823.8597	63108	0.0374	V	K. Menzies	0.0017
ZZ And	59838.8325	63135	0.0378	V	K. Menzies	0.0013
ZZ And	59907.5954	63259	0.0386	V	K. Menzies	0.0014
AC And	59790.8279	15874	0.4511	V	G. Samolyk	0.0012
AC And	59831.6571	15931	0.7397	V	G. Samolyk	0.0039
AC And	59915.3441	16049	0.5003	V	T. Arranz	0.0019
AC And	59937.3568	16080	0.4646	V	T. Arranz	0.0021
AT And	59813.8279	28319	–0.0014	V	G. Samolyk	0.0017
AT And	59863.7873	28400	–0.0121	V	G. Samolyk	0.0031
GM And	59934.5941	48522	0.0481	V	K. Menzies	0.0018
SW Aqr	59779.8217	75511	0.0022	V	G. Samolyk	0.0008
SW Aqr	59870.3045	75708	0.0022	V	T. Arranz	0.0006
TZ Aqr	59874.6152	39086	0.0148	V	G. Samolyk	0.0014
TZ Aqr	59888.3238	39110	0.0147	V	T. Arranz	0.0010
YZ Aqr	59853.7428	44370	0.0954	V	G. Samolyk	0.0012
AA Aqr	59875.6558	64260	–0.2070	V	G. Samolyk	0.0009
BO Aqr	59878.3532	26306	0.2479	V	T. Arranz	0.0011
BR Aqr	59917.5471	46239	–0.2519	V	G. Samolyk	0.0011
CY Aqr	59808.7370	417775	0.0181	V	G. Samolyk	0.0003
CY Aqr	59808.7982	417776	0.0183	V	G. Samolyk	0.0004
CY Aqr	59808.8595	417777	0.0186	V	G. Samolyk	0.0004
CY Aqr	59889.3078	419095	0.0183	V	T. Arranz	0.0003
CY Aqr	59889.3686	419096	0.0181	V	T. Arranz	0.0003
CY Aqr	59889.4299	419097	0.0184	V	T. Arranz	0.0004
CY Aqr	59912.3801	419473	0.0181	V	T. Arranz	0.0003
RV Ari	59830.7901	266442	–0.0032	V	G. Samolyk	0.0008
RV Ari	59830.8906	266443	0.0042	V	G. Samolyk	0.0009
RV Ari	59853.7866	266689	–0.0094	V	G. Samolyk	0.0005
RV Ari	59853.8860	266690	–0.0031	V	G. Samolyk	0.0009
RV Ari	59904.5527	267234	0.0018	V	G. Samolyk	0.0009
RV Ari	59904.6414	267235	–0.0026	V	G. Samolyk	0.0006
RV Ari	59904.7310	267236	–0.0062	V	G. Samolyk	0.0007
RV Ari	59909.5797	267288	–0.0001	V	G. Samolyk	0.0011
RV Ari	59909.6733	267289	0.0003	V	G. Samolyk	0.0005
RV Ari	59909.7581	267290	–0.0080	V	G. Samolyk	0.0003
TZ Aur	59585.7476	101317	0.0182	TG	G. Conrad	0.0009
TZ Aur	59611.5977	101383	0.0178	V	K. Menzies	0.0014
TZ Aur	59632.3568	101436	0.0182	V	T. Arranz	0.0005
TZ Aur	59659.3820	101505	0.0178	V	T. Arranz	0.0005
TZ Aur	59861.8780	102022	0.0180	V	K. Menzies	0.0008
TZ Aur	59914.7545	102157	0.0185	V	G. Samolyk	0.0008
BH Aur	59589.5783	36918	0.0131	V	G. Samolyk	0.0014
BH Aur	59612.3829	36968	0.0132	V	T. Arranz	0.0009
BH Aur	59618.3121	36981	0.0132	V	T. Arranz	0.0009
BH Aur	59851.8298	37493	0.0129	V	G. Samolyk	0.0011
BH Aur	59897.8952	37594	0.0133	V	K. Menzies	0.0009
V799 Aur	59625.3937	71278	0.0067	V	T. Arranz	0.0006
V799 Aur	59625.4696	71279	0.0065	V	T. Arranz	0.0005
RS Boo	59679.7257	47462	–0.0260	V	G. Samolyk	0.0008
RS Boo	59717.4567	47562	–0.0289	V	T. Arranz	0.0008
RS Boo	59731.4209	47599	–0.0263	V	T. Arranz	0.0005
RS Boo	59734.4404	47607	–0.0255	V	T. Arranz	0.0006
RS Boo	59751.4188	47652	–0.0273	V	T. Arranz	0.0005
ST Boo	59707.6753	65124	0.1306	V	G. Samolyk	0.0011
ST Boo	59762.4184	65212	0.1121	V	T. Arranz	0.0008
ST Boo	59775.4823	65233	0.1079	V	T. Arranz	0.0009
ST Boo	59780.4579	65241	0.1052	V	T. Arranz	0.0009
ST Boo	59785.4369	65249	0.1059	V	T. Arranz	0.0011
ST Boo	59790.4121	65257	0.1027	V	T. Arranz	0.0009
ST Boo	59795.3909	65265	0.1032	V	T. Arranz	0.0011
SW Boo	59686.7416	33329	0.6036	V	G. Samolyk	0.0013
SW Boo	59731.4211	33416	0.6061	V	T. Arranz	0.0007
SW Boo	59732.4527	33418	0.6107	V	T. Arranz	0.0009
SW Boo	59751.4498	33455	0.6072	V	T. Arranz	0.0009
SW Boo	59769.4244	33490	0.6083	V	T. Arranz	0.001
SZ Boo	59681.7815	61286	0.0162	V	G. Samolyk	0.0012
SZ Boo	59765.4321	61446	0.0157	V	T. Arranz	0.0008
TV Boo	59626.9102	112034	0.1199	V	K. Menzies	0.0018
TV Boo	59719.4227	112330	0.1148	V	T. Arranz	0.0012
TV Boo	59734.4313	112378	0.1205	V	T. Arranz	0.0012
TV Boo	59739.4581	112394	0.1464	V	T. Arranz	0.0025
TV Boo	59743.5050	112407	0.1300	V	T. Arranz	0.0018
TV Boo	59749.4599	112426	0.1463	V	T. Arranz	0.0018
TV Boo	59759.4505	112458	0.1350	V	T. Arranz	0.0019
TV Boo	59932.9026	113013	0.1166	V	K. Menzies	0.0012
TW Boo	59679.7038	61601	–0.1225	V	G. Samolyk	0.0011
TW Boo	59716.4298	61670	–0.1234	V	T. Arranz	0.0009
TW Boo	59724.4138	61685	–0.1235	V	T. Arranz	0.0009
TW Boo	59745.7049	61725	–0.1233	V	G. Samolyk	0.0011
UU Boo	59706.6787	51698	0.3927	V	G. Samolyk	0.0012
UU Boo	59767.4528	51831	0.3964	V	T. Arranz	0.0009
UY Boo	59636.9053	27350	0.8330	V	G. Samolyk	0.0013
UY Boo	59725.4149	27486	0.8289	V	T. Arranz	0.001
V338 Boo	59754.8463	17039	–0.1005	V	G. Samolyk	0.0009
V338 Boo	59757.8001	17045	–0.1110	V	G. Samolyk	0.0014
V338 Boo	59758.8248	17047	–0.0744	V	G. Samolyk	0.0024
V338 Boo	59762.8112	17055	–0.0404	V	G. Samolyk	0.0037
V338 Boo	59770.6501	17071	–0.1062	V	G. Samolyk	0.0029
V338 Boo	59774.6548	17079	–0.0539	V	G. Samolyk	0.0024
V338 Boo	59783.4854	17097	–0.1162	V	T. Arranz	0.0019
V377 Boo	59738.5797	7610	0.0010	V	T. Arranz	0.0004
UY Cam	59871.8824	91022	–0.0845	V	K. Menzies	0.0017
UY Cam	59914.6077	91182	–0.0859	V	G. Samolyk	0.0022
UY Cam	59914.8714	91183	–0.0893	V	G. Samolyk	0.0021
RW Cnc	59615.7906	36658	0.2557	V	G. Samolyk	0.0019
RW Cnc	59674.3416	36765	0.2564	V	T. Arranz	0.0009
RW Cnc	59686.3773	36787	0.2537	V	T. Arranz	0.0017
TT Cnc	59606.6400	34896	0.1427	V	K. Menzies	0.0021
TT Cnc	59675.3672	35018	0.1291	V	T. Arranz	0.0013
VZ Cnc	59671.3873	110863	0.0274	V	T. Arranz	0.0008
EF Cnc	59685.4090	30387	–0.0285	V	T. Arranz	0.0019
SS CVn	59637.8961	41828	–0.3853	V	K. Menzies	0.0005
SS CVn	59715.4211	41990	–0.3807	V	T. Arranz	0.0008
RV Cap	59797.6081	57878	–0.1817	V	T. Arranz	0.0007
RV Cap	59813.7321	57914	–0.1765	V	G. Samolyk	0.0015
RZ Cap	59831.6451	21064	0.0017	V	G. Samolyk	0.0011
VW Cap	59843.6274	109571	0.2449	V	G. Samolyk	0.0039
YZ Cap	59822.6729	58850	0.0286	V	G. Samolyk	0.0033
V876 Cep	59860.3552	48746	–0.0452	V	T. Arranz	0.0016
V876 Cep	59860.5072	48747	–0.0418	V	T. Arranz	0.0024
RR Cet	59597.3705	47766	0.0244	V	T. Arranz	0.0009
RR Cet	59831.8544	48190	0.0243	V	G. Samolyk	0.0009
RR Cet	59856.7401	48235	0.0238	V	G. Samolyk	0.0009
RU Cet	59886.6676	34216	0.1001	V	G. Samolyk	0.0031
RX Cet	59884.6626	34441	0.3443	V	G. Samolyk	0.0021
RZ Cet	59587.3022	50294	–0.2464	V	T. Arranz	0.0013
RZ Cet	59851.7948	50812	–0.2501	V	G. Samolyk	0.0019
RZ Cet	59853.8353	50816	–0.2521	V	G. Samolyk	0.0013
TY Cet	59934.6341	26284	–0.0110	V	G. Samolyk	0.0029
UU Cet	59906.5915	30851	–0.1894	V	G. Samolyk	0.0026
XX Cyg	59748.6985	113397	0.0048	V	G. Samolyk	0.0005
XX Cyg	59748.8332	113398	0.0046	V	G. Samolyk	0.0006
XX Cyg	59795.7664	113746	0.0048	V	G. Samolyk	0.0005
XX Cyg	59795.9015	113747	0.0050	V	G. Samolyk	0.0005
XX Cyg	59798.4642	113766	0.0053	V	T. Arranz	0.0004
XX Cyg	59799.5426	113774	0.0047	V	T. Arranz	0.0004

Table continued on following pages

Table 1. Recent times of maxima of stars in the AAVSO Short Period Pulsator program, cont.

Star	JD (max) Hel. 2400000 +	Cycle	O–C (day)	F	Observer	Error (day)
XZ Cyg	59728.8071	33442	–3.0143	V	G. Samolyk	0.0008
XZ Cyg	59743.7433	33474	–3.0125	V	G. Samolyk	0.0011
XZ Cyg	59751.6754	33491	–3.0143	V	G. Samolyk	0.0008
XZ Cyg	59757.7387	33504	–3.0181	V	G. Samolyk	0.0008
XZ Cyg	59778.7265	33549	–3.0318	V	G. Samolyk	0.0012
XZ Cyg	59793.6660	33581	–3.0267	V	G. Samolyk	0.0009
XZ Cyg	59797.3984	33589	–3.0279	V	T. Arranz	0.0006
XZ Cyg	59803.4646	33602	–3.0288	V	T. Arranz	0.0007
XZ Cyg	59804.3993	33604	–3.0275	V	T. Arranz	0.0007
XZ Cyg	59811.3989	33619	–3.0284	V	T. Arranz	0.0006
XZ Cyg	59817.4605	33632	–3.0339	V	T. Arranz	0.0008
XZ Cyg	59832.3790	33664	–3.0498	V	T. Arranz	0.0009
XZ Cyg	59839.3843	33679	–3.0450	V	T. Arranz	0.0009
XZ Cyg	59845.4538	33692	–3.0426	V	T. Arranz	0.0008
XZ Cyg	59847.3231	33696	–3.0401	V	T. Arranz	0.0007
XZ Cyg	59853.3915	33709	–3.0388	V	T. Arranz	0.0008
XZ Cyg	59860.3885	33724	–3.0423	V	T. Arranz	0.0007
XZ Cyg	59867.3846	33739	–3.0467	V	T. Arranz	0.0007
DM Cyg	59778.7169	40957	0.1049	V	G. Samolyk	0.0011
DM Cyg	59798.4509	41004	0.1055	V	T. Arranz	0.0009
DM Cyg	59806.4303	41023	0.1075	V	T. Arranz	0.0010
DM Cyg	59811.4657	41035	0.1046	V	T. Arranz	0.0006
DM Cyg	59819.4426	41054	0.1042	V	T. Arranz	0.0007
DM Cyg	59824.4835	41066	0.1067	V	T. Arranz	0.0006
DM Cyg	59827.4219	41073	0.1061	V	T. Arranz	0.0006
DM Cyg	59840.4363	41104	0.1049	V	T. Arranz	0.0007
DM Cyg	59843.3760	41111	0.1055	V	T. Arranz	0.0007
DM Cyg	59856.3936	41142	0.1075	V	T. Arranz	0.0009
DM Cyg	59861.4285	41154	0.1041	V	T. Arranz	0.0007
DM Cyg	59893.3386	41230	0.1048	V	T. Arranz	0.0010
DM Cyg	59909.2951	41268	0.1066	V	T. Arranz	0.0008
V2416 Cyg	59748.6196	109788	0.0033	V	G. Samolyk	0.0008
V2416 Cyg	59748.6745	109789	0.0023	V	G. Samolyk	0.0011
V2416 Cyg	59748.7308	109790	0.0028	V	G. Samolyk	0.0009
V2416 Cyg	59748.7849	109791	0.0010	V	G. Samolyk	0.0009
V2416 Cyg	59748.8433	109792	0.0034	V	G. Samolyk	0.0009
V2416 Cyg	59795.7338	110631	0.0025	V	G. Samolyk	0.0012
V2416 Cyg	59795.7881	110632	0.0009	V	G. Samolyk	0.0012
V2416 Cyg	59795.8474	110633	0.0044	V	G. Samolyk	0.0011
V2416 Cyg	59799.5328	110699	0.0010	V	T. Arranz	0.0007
V2416 Cyg	59799.5902	110700	0.0025	V	T. Arranz	0.0011
V2416 Cyg	59799.6461	110701	0.0025	V	T. Arranz	0.0013
RW Dra	59666.8445	45808	0.3116	V	G. Samolyk	0.0008
RW Dra	59770.4495	46042	0.2740	V	T. Arranz	0.0013
RW Dra	59778.4368	46060	0.2888	V	T. Arranz	0.0012
RW Dra	59782.4409	46069	0.3066	V	T. Arranz	0.0011
RW Dra	59786.4353	46078	0.3148	V	T. Arranz	0.0008
RW Dra	59829.4000	46175	0.3165	V	T. Arranz	0.0009
XZ Dra	59687.7923	37271	–0.1014	V	K. Menzies	0.0007
XZ Dra	59730.6818	37361	–0.0966	V	G. Samolyk	0.0014
XZ Dra	59796.4386	37499	–0.0964	V	T. Arranz	0.0009
XZ Dra	59806.4468	37520	–0.0946	V	T. Arranz	0.0011
XZ Dra	59826.4565	37562	–0.0978	V	T. Arranz	0.0009
XZ Dra	59827.4095	37564	–0.0978	V	T. Arranz	0.0009
XZ Dra	59848.3846	37608	–0.0886	V	T. Arranz	0.0008
RX Eri	59613.3073	64574	–0.0091	V	T. Arranz	0.0009
RX Eri	59932.7706	65118	–0.0078	V	G. Samolyk	0.0013
SV Eri	59610.3559	33703	1.1668	V	T. Arranz	0.0031
SV Eri	59893.7499	34100	1.1837	V	G. Samolyk	0.0019
BB Eri	59630.3147	35218	0.3560	V	T. Arranz	0.0011
RR Gem	59632.3766	45999	–0.7187	V	T. Arranz	0.0006
RR Gem	59638.3348	46014	–0.7201	V	T. Arranz	0.0005
RR Gem	59659.3915	46067	–0.7209	V	T. Arranz	0.0006
GQ Gem	59632.5912	51363	–0.2227	V	K. Menzies	0.0021
V488 Gem	59940.4264	57885	–0.0265	V	T. Arranz	0.0009
V488 Gem	59940.5193	57886	–0.0269	V	T. Arranz	0.0007
TW Her	59643.8855	95342	–0.0216	V	K. Menzies	0.0006
TW Her	59768.5614	95654	–0.0209	V	T. Arranz	0.0007
TW Her	59784.5446	95694	–0.0218	V	T. Arranz	0.0007
TW Her	59792.5376	95714	–0.0208	V	T. Arranz	0.0006
VX Her	59715.6976	83372	–0.1278	V	G. Samolyk	0.0008
VX Her	59751.6713	83451	–0.1286	V	G. Samolyk	0.0007
VX Her	59779.4483	83512	–0.1293	V	T. Arranz	0.0008
VZ Her	59706.7446	52047	0.1009	V	G. Samolyk	0.0009
VZ Her	59753.8583	52154	0.0995	V	G. Samolyk	0.0007
VZ Her	59771.4725	52194	0.1006	V	T. Arranz	0.0005
VZ Her	59775.4354	52203	0.1006	V	T. Arranz	0.0008
AR Her	59681.7705	38782	–1.2024	V	G. Samolyk	0.0011
AR Her	59696.8378	38814	–1.1760	V	G. Samolyk	0.0011
AR Her	59706.6973	38835	–1.1871	V	G. Samolyk	0.0008
AR Her	59712.7992	38848	–1.1955	V	G. Samolyk	0.0009
AR Her	59728.7938	38882	–1.1819	V	G. Samolyk	0.0013
AR Her	59745.6937	38918	–1.2030	V	G. Samolyk	0.0008
AR Her	59749.4343	38926	–1.2226	V	T. Arranz	0.0013
AR Her	59751.7804	38931	–1.2267	V	G. Samolyk	0.0008
AR Her	59764.5140	38958	–1.1838	V	T. Arranz	0.0011
AR Her	59765.4618	38960	–1.1761	V	T. Arranz	0.0016
AR Her	59781.3989	38994	–1.2199	V	T. Arranz	0.0012
AR Her	59788.4434	39009	–1.2259	V	T. Arranz	0.0016
DL Her	59679.8632	36292	0.0767	V	G. Samolyk	0.0013
DL Her	59692.8638	36314	0.0615	V	K. Menzies	0.0019
DL Her	59740.7856	36395	0.0614	V	K. Menzies	0.0016
DL Her	59743.7476	36400	0.0653	V	G. Samolyk	0.0017
DL Her	59767.4023	36440	0.0549	V	T. Arranz	0.0012
DL Her	59774.5061	36452	0.0591	V	T. Arranz	0.0018
DL Her	59777.4658	36457	0.0607	V	T. Arranz	0.0013
DL Her	59780.4333	36462	0.0701	V	T. Arranz	0.0016
DL Her	59793.4465	36484	0.0675	V	T. Arranz	0.0009
DL Her	59796.3996	36489	0.0624	V	T. Arranz	0.0009
DL Her	59809.4124	36511	0.0594	V	T. Arranz	0.0012
DY Her	59679.8687	176547	–0.0373	V	G. Samolyk	0.0007
DY Her	59686.8538	176594	–0.0379	V	G. Samolyk	0.0007
DY Her	59715.6883	176788	–0.0378	V	G. Samolyk	0.0007
DY Her	59743.6308	176976	–0.0380	V	G. Samolyk	0.0007
DY Her	59758.6428	177077	–0.0378	V	G. Samolyk	0.0006
DY Her	59761.4676	177096	–0.0370	V	T. Arranz	0.0008
DY Her	59774.6947	177185	–0.0381	V	G. Samolyk	0.0007
LS Her	59753.7113	137555	0.0098	V	G. Samolyk	0.0017
LS Her	59759.4558	137580	–0.0159	V	T. Arranz	0.0021
SZ Hya	59636.6655	35287	–0.3421	V	G. Samolyk	0.0029
SZ Hya	59650.6814	35313	–0.2945	V	G. Samolyk	0.0012
SZ Hya	59671.6281	35352	–0.3002	V	G. Samolyk	0.0014
SZ Hya	59704.3970	35413	–0.3029	V	T. Arranz	0.0011
UU Hya	59665.7175	38534	0.0296	V	G. Samolyk	0.0016
DG Hya	59582.9040	9557	0.0415	V	G. Samolyk	0.0019
DG Hya	59673.4197	9677	0.0481	V	T. Arranz	0.0014
DH Hya	59654.6521	58238	0.1309	V	G. Samolyk	0.0013
GO Hya	59637.7122	8039	0.0039	V	G. Samolyk	0.0023
RR Leo	59658.6762	36170	0.2085	V	G. Samolyk	0.0008
RR Leo	59675.4140	36207	0.2078	V	T. Arranz	0.0008
RR Leo	59898.9036	36701	0.2151	V	K. Menzies	0.0006
SS Leo	59673.4291	28566	–0.1255	V	T. Arranz	0.0011
ST Leo	59650.7415	66378	–0.0184	V	G. Samolyk	0.0009
ST Leo	59722.4400	66528	–0.0175	V	T. Arranz	0.0007
TV Leo	59679.6541	33645	0.1384	V	G. Samolyk	0.0017
TV Leo	59694.4557	33667	0.1372	V	T. Arranz	0.0011
WW Leo	59666.6320	41112	0.0633	V	G. Samolyk	0.0018
WW Leo	59934.8957	41557	0.0608	V	K. Menzies	0.0018
AA Leo	59650.8928	33499	–0.1295	V	G. Samolyk	0.0017
AA Leo	59708.3629	33595	–0.1303	V	T. Arranz	0.0009

Table continued on next page

Table 1. Recent times of maxima of stars in the AAVSO Short Period Pulsator program, cont.

Star	JD (max) Hel. 2400000 +	Cycle	O–C (day)	F	Observer	Error (day)	Star	JD (max) Hel. 2400000 +	Cycle	O–C (day)	F	Observer	Error (day)
AA LMi	57334.8311	–29641	–0.0064	V	G. Samolyk	0.0024	SZ Lyn	59911.8547	180756	0.0465	V	G. Samolyk	0.0007
AA LMi	57334.8885	–29640	–0.0033	V	G. Samolyk	0.0021	SZ Lyn	59911.9741	180757	0.0453	V	G. Samolyk	0.0006
AA LMi	57334.9416	–29639	–0.0044	V	G. Samolyk	0.0013	AN Lyn	59672.3913	156517	–0.0240	V	T. Arranz	0.0014
AA LMi	58216.5744	–13373	0.0069	V	G. Samolyk	0.0036	AN Lyn	59672.4884	156518	–0.0251	V	T. Arranz	0.0013
AA LMi	58216.6296	–13372	0.0078	V	G. Samolyk	0.0012	RR Lyr	59696.8378	29591	–0.7654	V	G. Samolyk	0.0013
AA LMi	58216.6801	–13371	0.0042	V	G. Samolyk	0.0022	RR Lyr	59799.4294	29772	–0.7769	V	T. Arranz	0.0009
AA LMi	58409.9054	–9806	0.0055	V	G. Samolyk	0.0021	RZ Lyr	59733.7974	36285	–0.0555	V	G. Samolyk	0.0011
AA LMi	58409.9552	–9805	0.0011	V	G. Samolyk	0.0021	RZ Lyr	59791.5570	36398	–0.0662	V	T. Arranz	0.0007
AA LMi	58941.3847	0	–0.0031	V	T. Arranz	0.0015	EN Lyr	56182.5277	26593	0.1143	V	K. Menzies	0.0016
AA LMi	58941.4408	1	–0.0012	V	T. Arranz	0.0013	ST Oph	59810.3824	69687	–0.0297	V	T. Arranz	0.0008
AA LMi	59699.3756	13985	–0.0030	V	T. Arranz	0.0011	AV Peg	59790.8321	40987	0.2283	V	G. Samolyk	0.0007
AA LMi	59699.4326	13986	–0.0002	V	T. Arranz	0.0010	AV Peg	59854.4692	41150	0.2343	V	T. Arranz	0.0008
AA LMi	59699.4831	13987	–0.0038	V	T. Arranz	0.0013	BH Peg	59915.3864	32060	–0.1292	V	T. Arranz	0.0016
U Lep	59903.8000	31904	0.0373	V	G. Samolyk	0.0011	DY Peg	59830.7169	210194	–0.0236	V	G. Samolyk	0.0006
EH Lib	59738.4578	297465	0.0038	V	T. Arranz	0.0005	DY Peg	59830.7896	210195	–0.0239	V	G. Samolyk	0.0006
EH Lib	59738.5465	297466	0.0041	V	T. Arranz	0.0005	DY Peg	59830.8630	210196	–0.0234	V	G. Samolyk	0.0005
EH Lib	59739.4302	297476	0.0037	V	T. Arranz	0.0004	DY Peg	59875.5664	210809	–0.0238	V	G. Samolyk	0.0004
EH Lib	59739.5185	297477	0.0035	V	T. Arranz	0.0005	DY Peg	59875.6395	210810	–0.0236	V	G. Samolyk	0.0005
EH Lib	59740.4028	297487	0.0037	V	T. Arranz	0.0005	DY Peg	59875.7128	210811	–0.0232	V	G. Samolyk	0.0004
EH Lib	59740.4908	297488	0.0033	V	T. Arranz	0.0004	DF Ser	59747.6725	68620	0.1174	V	G. Samolyk	0.0011
EH Lib	59740.5792	297489	0.0033	V	T. Arranz	0.0005	DF Ser	59788.3849	68713	0.1148	V	T. Arranz	0.0007
EH Lib	59741.3755	297498	0.0039	V	T. Arranz	0.0005	RV UMa	59654.7819	31148	0.1380	V	G. Samolyk	0.0011
EH Lib	59741.4635	297499	0.0035	V	T. Arranz	0.0004	RV UMa	59725.4675	31299	0.1466	V	T. Arranz	0.0009
EH Lib	59741.5515	297500	0.0031	V	T. Arranz	0.0005	RV UMa	59726.4010	31301	0.1439	V	T. Arranz	0.0009
SZ Lyn	59610.6284	178257	0.0369	V	K. Menzies	0.0009	RV UMa	59755.4194	31363	0.1426	V	T. Arranz	0.0013
SZ Lyn	59671.3800	178761	0.0389	V	T. Arranz	0.0005	RV UMa	59762.4380	31378	0.1403	V	T. Arranz	0.0013
SZ Lyn	59872.9201	180433	0.0446	V	K. Menzies	0.0007	RV UMa	59923.9165	31723	0.1381	V	K. Menzies	0.0014
SZ Lyn	59885.8187	180540	0.0460	V	G. Samolyk	0.0006	AE UMa	59690.4032	280015	–0.0005	V	T. Arranz	0.0004
SZ Lyn	59885.9388	180541	0.0456	V	G. Samolyk	0.0006							

Recent Minima of 228 Eclipsing Binary Stars

Gerard Samolyk
P.O. Box 20677, Greenfield, WI 53220; gsamolyk@wi.rr.com

Received March 3, 2023; accepted March 8, 2023

Abstract This paper continues the publication of times of minima for eclipsing binary stars. Times of minima presented were determined from observations received by the AAVSO Eclipsing Binaries Section from August 2022 through January 2023.

1. Recent observations

The accompanying list (Table 1) contains times of minima calculated for 228 variable stars calculated from recent CCD observations made by participants in the AAVSO's eclipsing binary program. These observations were reduced by the observers or the writer using the method of Kwee and van Woerden (1956).

The linear elements in the *General Catalogue of Variable Stars* (GCVS; Kholopov *et al.* 1985) were used to compute the O–C values for most stars. For a few exceptions where the GCVS elements are missing or are in significant error, light elements from another source are used: CD Cam (Baldwin and Samolyk 2007), CW Cas (Samolyk 1992), EF Ori (Baldwin and Samolyk 2005), GU Ori (Samolyk 1985).

The light elements used for QX And, V376 And EK Aqr, V688 Aql, V719 Aql, V889 Aql, V644 Aur, LZ Lyr, and GR Psc are from Kreiner (2004).

The light elements used for BN Ari, V641 Aur, CW CMi, CX CMi, EX CMi, V1261 Cas, V700 Cyg, V2477 Cyg, PS Del, V502 Oph, and VZ Psc are from Paschke (2014).

The light elements used for V731 Cep and V495 Vul are from Nelson (2014).

The light elements used for V765 Cas, V796 Cep, V3135 Cyg, V479 Lac, V505 Lac, V589 Lyr, and V882 Per are from Watson *et al.* (2014).

The standard error is included when available. Column F indicates the filter used; a "C" indicates a clear filter.

This list will be web-archived and made available through the AAVSO ftp site at:

ftp://ftp.aavso.org/public/datasets/gsamj511eb228.txt.

This list, along with the eclipsing binary data from earlier AAVSO publications, is also included in the Lichtenknecker Database administrated by the Bundesdeutsche Arbeitsgemeinschaft für Veränderliche Sterne e.V. (BAV; Walter *et al.* 2015).[1]

References

Baldwin, M. E., and Samolyk, G. 2005, *Observed Minima Timings of Eclipsing Binaries No. 10*, AAVSO, Cambridge, MA.

Baldwin, M. E., and Samolyk, G. 2007, *Observed Minima Timings of Eclipsing Binaries No. 12*, AAVSO, Cambridge, MA.

Kholopov, P. N., *et al.* 1985, *General Catalogue of Variable Stars*, 4th ed., Moscow.

Kreiner, J. M. 2004, *Acta Astron.*, **54**, 207 (http://www.as.up.krakow.pl/ephem/).

Kwee, K. K., and van Woerden, H. 1956, *Bull. Astron. Inst. Netherlands*, **12**, 327.

Nelson, R. 2014, Eclipsing Binary O–C Files (http://www.aavso.org/bob-nelsons-o-c-files).

Paschke, A. 2014, "O–C Gateway" (http://var.astro.cz/ocgate/).

Samolyk, G. 1985, *J. Amer. Assoc. Var. Star Obs.*, **14**, 12.

Samolyk, G. 1992, *J. Amer. Assoc. Var. Star Obs.*, **21**, 34.

Walter, F., Hübscher, J., and Grimm, W. 2015, *Lichtenknecker-Database of the BAV: Collection of Times of Minima of Eclipsing Binaries*, Bundesdeutsche Arbeitsgemeinschaft für Veränderliche Sterne e.V. (BAV), Berlin.[1]

Watson, C., Henden, A. A., and Price, C. A. 2014, AAVSO International Variable Star Index VSX (Watson+, 2006–2014; http://www.aavso.org/vsx).

[1] Walter *et al.* (2015), https://www.bav-astro.eu/index.php/veroeffentlichungen/service-for-scientists/lkdb-engl

Table 1. Recent times of minima of stars in the AAVSO eclipsing binary program.

Star	JD (min) Hel. 2400000 +	Cycle	O–C (day)	F	Observer	Standard Error (day)
RT And	59845.6103	29739	–0.0135	V	G. Samolyk	0.0001
RT And	59884.6038	29801	–0.0136	V	G. Samolyk	0.0001
RT And	59910.3896	29842	–0.0139	V	T. Arranz	0.0003
RT And	59918.5659	29855	–0.0137	V	G. Samolyk	0.0001
RT And	59944.3520	29896	–0.0137	V	T. Arranz	0.0001
TT And	59875.6254	2247	–0.0129	V	L. Hazel	0.0006
TW And	59852.7142	5053	–0.0732	V	G. Samolyk	0.0001
TW And	59881.5745	5060	–0.0723	V	G. Samolyk	0.0001
UU And	59830.8384	12232	0.1257	V	G. Samolyk	0.0002
UU And	59906.6413	12283	0.1275	V	G. Samolyk	0.0002
WZ And	59852.7075	27284	0.0955	V	G. Samolyk	0.0002
XZ And	59798.6867	26392	0.2143	V	L. Hazel	0.0003
XZ And	59874.6951	26448	0.2151	V	L. Hazel	0.0003
AB And	59795.6709	71367	–0.0554	V	G. Samolyk	0.0001
AB And	59795.8382	71367.5	–0.0541	V	G. Samolyk	0.0001
AB And	59851.5954	71535.5	–0.0548	V	G. Samolyk	0.0001
AB And	59906.5226	71701	–0.0557	V	G. Samolyk	0.0001
AB And	59916.3126	71730.5	–0.0565	V	T. Arranz	0.0003
AD And	59796.8074	21085.5	–0.0757	V	G. Samolyk	0.0001
AD And	59884.5768	21174.5	–0.0778	V	G. Samolyk	0.0002
BD And	59845.7276	53755	0.0145	V	G. Samolyk	0.0002
BX And	59808.8246	38157	–0.1241	V	G. Samolyk	0.0003
DS And	59813.8139	23425	0.0053	V	G. Samolyk	0.0002
DS And	59893.6448	23504	0.0052	V	G. Samolyk	0.0001
DS And	59934.5719	23544.5	0.0063	V	G. Samolyk	0.0002
DS And	59960.3412	23570	0.0074	V	T. Arranz	0.0004
EP And	59857.6359	42610	0.0912	V	L. Hazel	0.0006
EP And	59976.4358	42904	0.0835	V	T. Arranz	0.0001
KP And	59877.6176	6026	0.0837	V	L. Hazel	0.0006
QX And	59813.8232	17744.5	0.0131	V	G. Samolyk	0.0004
QX And	59893.5798	17938	0.0145	V	G. Samolyk	0.0003
QX And	59893.7851	17938.5	0.0137	V	G. Samolyk	0.0003
QX And	59934.5898	18037.5	0.0134	V	G. Samolyk	0.0002
V376 And	59926.5759	9298	0.0058	V	K. Menzies	0.0004
RY Aqr	59809.7503	9654	–0.1622	V	L. Hazel	0.0003
RY Aqr	59815.6497	9657	–0.1626	V	L. Hazel	0.0003
RY Aqr	59894.3105	9697	–0.1655	V	T. Arranz	0.0001
CX Aqr	59778.8628	41953	0.0188	V	G. Samolyk	0.0001
CX Aqr	59875.6048	42127	0.0192	V	G. Samolyk	0.0001
CX Aqr	59888.3924	42150	0.0191	V	T. Arranz	0.0001
CZ Aqr	59851.7189	19102	–0.0770	V	G. Samolyk	0.0001
EK Aqr	59852.7295	23987	0.0522	V	G. Samolyk	0.0003
XZ Aql	59795.7509	8364	0.1800	V	G. Samolyk	0.0002
XZ Aql	59810.7252	8371	0.1800	V	L. Hazel	0.0006
OO Aql	59803.6530	41813	0.0841	V	G. Samolyk	0.0001
OP Aql	59791.6118	1370	0.0037	V	T. Arranz	0.0003
V342 Aql	59799.4319	6040	–0.0764	V	T. Arranz	0.0002
V346 Aql	59821.5335	16182	–0.0166	V	T. Arranz	0.0001
V346 Aql	59822.6401	16183	–0.0163	V	G. Samolyk	0.0001
V346 Aql	59863.5753	16220	–0.0166	V	G. Samolyk	0.0002
V688 Aql	59810.5748	1879	–0.0006	V	T. Arranz	0.0006
V719 Aql	59828.5053	1085	–0.0050	V	T. Arranz	0.0002
V889 Aql	59805.4857	656	0.0273	V	T. Arranz	0.0003
RX Ari	59909.5769	20892	0.0608	V	G. Samolyk	0.0001
SS Ari	59842.8136	51269	–0.4673	V	L. Hazel	0.0006
SS Ari	59977.3944	51600.5	–0.4734	V	T. Arranz	0.0001
BN Ari	59982.3354	28248	–0.0523	V	T. Arranz	0.0001
RY Aur	59852.8657	7912	0.0091	V	L. Hazel	0.0006
RY Aur	59934.6316	7942	0.0133	V	G. Samolyk	0.0003
TT Aur	59856.9046	28974	–0.0157	V	G. Samolyk	0.0006
AP Aur	59848.8470	30569	1.9242	V	L. Hazel	0.0006
AP Aur	59875.8964	30616.5	1.9312	V	G. Samolyk	0.0002
BF Aur	59867.6965	12152	0.0329	V	L. Hazel	0.0003
EM Aur	59909.7607	15872	–1.1422	V	G. Samolyk	0.0002
EP Aur	59853.8399	56758	0.0258	V	G. Samolyk	0.0001
EP Aur	59877.7765	56798.5	0.0266	V	L. Hazel	0.0009
EP Aur	59934.8092	56895	0.0270	V	G. Samolyk	0.0001
FW Aur	59880.7977	2390	–0.0047	V	L. Hazel	0.0009
HP Aur	59818.7973	11992	0.0739	V	L. Hazel	0.0006
HP Aur	59952.5452	12086	0.0774	V	G. Samolyk	0.0004
IM Aur	59824.7992	15481	–0.1367	V	L. Hazel	0.0006
V641 Aur	59876.7989	17038	–0.0035	V	L. Hazel	0.0006
V644 Aur	59629.6731	9135	–0.0009	V	K. Menzies	0.0002
SV Cam	59863.6926	29118	0.0666	V	L. Hazel	0.0006
SV Cam	59875.5523	29138	0.0649	V	L. Hazel	0.0003
CD Cam	59914.6718	9359	–0.0274	V	G. Samolyk	0.0005
R CMa	59934.8171	13773	0.1476	V	G. Samolyk	0.0005
RT CMa	59914.7895	25731	–0.8048	V	G. Samolyk	0.0001
SX CMa	59917.9139	19592	0.0437	V	G. Samolyk	0.0003
TZ CMa	59884.9063	17139	–0.2377	V	G. Samolyk	0.0002
EG CMa	59909.9077	2936	0.0234	V	L. Hazel	0.0006
AK CMi	59857.8718	29610	–0.0252	V	L. Hazel	0.0003
CW CMi	59876.9156	24427	–0.0739	V	L. Hazel	0.0006
CX CMi	59907.8541	7091.5	0.0433	V	L. Hazel	0.0009
EX CMi	59919.8183	17811.5	0.0205	V	L. Hazel	0.0006
RW Cap	59812.4724	5055	–0.8741	V	T. Arranz	0.0003
TY Cap	59796.7198	10540	0.1069	V	G. Samolyk	0.0001
TY Cap	59826.6139	10561	0.1086	V	L. Hazel	0.0006
TY Cap	59849.3890	10577	0.1085	V	T. Arranz	0.0002
RZ Cas	59822.6778	13907	0.0715	V	G. Samolyk	0.0002
TV Cas	59851.7858	8413	–0.0344	V	G. Samolyk	0.0008
TW Cas	59879.6074	12512	0.0302	V	G. Samolyk	0.0002
ZZ Cas	59822.6613	21218	0.0104	V	G. Samolyk	0.0002
AB Cas	59804.6387	12503	0.1529	V	L. Hazel	0.0003
BS Cas	59803.6462	8175	–0.0325	V	L. Hazel	0.0006
BZ Cas	59805.7060	14253	0.3590	V	L. Hazel	0.0006
CW Cas	59836.6212	57092	–0.1530	V	G. Samolyk	0.0003
CW Cas	59836.7824	57092.5	–0.1512	V	G. Samolyk	0.0002
CW Cas	59884.7692	57243	–0.1535	V	G. Samolyk	0.0001
CW Cas	59952.5284	57455.5	–0.1529	V	G. Samolyk	0.0002
CW Cas	59969.2669	57508	–0.1548	V	T. Arranz	0.0001
CW Cas	59969.4287	57508.5	–0.1524	V	T. Arranz	0.0001
DZ Cas	59893.5657	40081	–0.2305	V	G. Samolyk	0.0004
GT Cas	59882.6736	10884	0.2219	V	L. Hazel	0.0006
GT Cas	59885.6567	10885	0.2152	V	G. Samolyk	0.0002
IR Cas	59791.6617	25603	0.0194	V	G. Samolyk	0.0002
IR Cas	59917.5889	25788	0.0198	V	G. Samolyk	0.0001
IS Cas	59831.6046	16864	0.0765	V	G. Samolyk	0.0002
IV Cas	59894.3055	19068	–0.1567	V	T. Arranz	0.0002
MM Cas	59884.7198	21134	0.1318	V	G. Samolyk	0.0002
OR Cas	59887.6290	12585	–0.0405	V	L. Hazel	0.0006
OR Cas	59967.3588	12649	–0.0362	V	T. Arranz	0.0001
OX Cas	59918.5701	7491.5	0.0238	V	G. Samolyk	0.0006
PV Cas	59831.7877	11199.5	–0.0039	V	G. Samolyk	0.0001
PV Cas	59853.6421	11212	–0.0304	V	G. Samolyk	0.0002
PV Cas	59917.5599	11248.5	–0.0047	V	G. Samolyk	0.0001
V364 Cas	59800.8388	16504.5	–0.0250	V	G. Samolyk	0.0002
V364 Cas	59937.3996	16593	–0.0257	V	T. Arranz	0.0002
V375 Cas	59853.6550	17111	0.3211	V	G. Samolyk	0.0004
V380 Cas	59829.7073	25186	–0.0755	V	G. Samolyk	0.0006
V380 Cas	59886.7107	25228	–0.0775	V	G. Samolyk	0.0002
V523 Cas	59798.7382	79499.5	0.1424	V	L. Hazel	0.0003
V523 Cas	59802.5959	79516	0.1442	V	L. Hazel	0.0003
V523 Cas	59802.7125	79516.5	0.1440	V	L. Hazel	0.0003
V523 Cas	59802.8292	79517	0.1438	V	L. Hazel	0.0003
V523 Cas	59966.2991	80216.5	0.1471	V	T. Arranz	0.0001
V523 Cas	59966.4163	80217	0.1474	V	T. Arranz	0.0001
V765 Cas	59905.3414	1071.5	–0.0212	V	T. Arranz	0.0004
V765 Cas	59909.6270	1074	–0.0251	V	T. Arranz	0.0008
V765 Cas	59910.4853	1074.5	–0.0246	V	T. Arranz	0.0007
V765 Cas	59916.4936	1078	–0.0216	V	T. Arranz	0.0003
V765 Cas	59917.3482	1078.5	–0.0248	V	T. Arranz	0.0005
V765 Cas	59947.3782	1096	–0.0208	V	T. Arranz	0.0002
V1261 Cas	59967.2949	18756.5	0.0219	V	T. Arranz	0.0005

Table continued on following pages

Table 1. Recent times of minima of stars in the AAVSO eclipsing binary program, cont.

Star	JD (min) Hel. 2400000 +	Cycle	O–C (day)	F	Observer	Standard Error (day)
U Cep	59796.8114	6119	0.2506	V	G. Samolyk	0.0002
U Cep	59831.7146	6133	0.2512	V	G. Samolyk	0.0002
U Cep	59831.7199	6133	0.2565	V	L. Hazel	0.0003
WZ Cep	59803.6543	76089.5	–0.2428	V	G. Samolyk	0.0002
XX Cep	59948.3239	6464	0.0426	V	T. Arranz	0.0001
ZZ Cep	59832.6843	14896	–0.0195	V	G. Samolyk	0.0002
ZZ Cep	59858.3893	14908	–0.0161	V	T. Arranz	0.0001
DK Cep	59909.3594	26695	0.0251	V	T. Arranz	0.0002
EG Cep	59867.6131	31716	0.0046	V	L. Hazel	0.0006
GW Cep	59836.7553	67282.5	0.0192	V	L. Hazel	0.0006
NW Cep	59860.4743	797	–0.0124	V	T. Arranz	0.0002
V338 Cep	59870.3873	7487	0.0410	V	T. Arranz	0.0001
V731 Cep	59958.3580	657.5	–0.1568	V	T. Arranz	0.0004
V796 Cep	59831.8742	16282	–0.0358	V	L. Hazel	0.0006
SS Cet	59887.8290	5863	0.0787	V	L. Hazel	0.0003
SS Cet	59893.7792	5865	0.0810	V	G. Samolyk	0.0002
TT Cet	59881.7623	56252	–0.0927	V	G. Samolyk	0.0001
TT Cet	59947.3652	56387	–0.0940	V	T. Arranz	0.0001
TW Cet	59949.2750	55470.5	–0.0363	V	T. Arranz	0.0001
Y Cyg	59863.6361	16824	–0.0861	V	G. Samolyk	0.0005
SW Cyg	59798.6813	3921	–0.3948	V	L. Hazel	0.0003
SW Cyg	59821.5425	3926	–0.3993	V	T. Arranz	0.0001
UW Cyg	59815.5677	4673	0.0349	V	T. Arranz	0.0004
WW Cyg	59813.5419	5858	0.1651	V	T. Arranz	0.0001
ZZ Cyg	59852.5922	23627	–0.0854	V	L. Hazel	0.0003
AE Cyg	59796.6483	15694	–0.0043	V	G. Samolyk	0.0002
AE Cyg	59866.4306	15766	–0.0035	V	T. Arranz	0.0002
BR Cyg	59863.5556	13751	0.0006	V	L. Hazel	0.0006
BR Cyg	59863.5569	13751	0.0019	V	G. Samolyk	0.0001
CG Cyg	59804.7484	32290	0.0834	V	L. Hazel	0.0003
CG Cyg	59830.6247	32331	0.0829	V	G. Samolyk	0.0001
CG Cyg	59834.4116	32337	0.0830	V	T. Arranz	0.0001
CG Cyg	59852.7162	32366	0.0845	V	L. Hazel	0.0006
DK Cyg	59793.6415	46302	0.1439	V	G. Samolyk	0.0002
DK Cyg	59854.3628	46431	0.1461	V	T. Arranz	0.0001
DK Cyg	59854.5982	46431.5	0.1461	V	T. Arranz	0.0002
DO Cyg	59846.6144	8982	–0.0643	V	L. Hazel	0.0003
DO Cyg	59853.4542	8986	–0.0646	V	T. Arranz	0.0001
KR Cyg	59812.4930	36332	0.0284	V	T. Arranz	0.0001
KR Cyg	59839.5376	36364	0.0282	V	T. Arranz	0.0001
KV Cyg	59868.3965	10708	0.0640	V	T. Arranz	0.0002
MY Cyg	59889.3357	6502	0.0009	V	T. Arranz	0.0001
V346 Cyg	59797.6678	8789	0.2123	V	G. Samolyk	0.0003
V387 Cyg	59843.6184	49732	0.0172	V	G. Samolyk	0.0001
V387 Cyg	59865.3986	49766	0.0172	V	T. Arranz	0.0001
V388 Cyg	59793.6687	20768	–0.1532	V	G. Samolyk	0.0001
V388 Cyg	59819.4378	20798	–0.1552	V	T. Arranz	0.0001
V401 Cyg	59795.5358	27389	0.1039	V	T. Arranz	0.0003
V445 Cyg	59833.5381	10107	0.3362	V	T. Arranz	0.0001
V456 Cyg	59808.5813	16716	0.0595	V	T. Arranz	0.0001
V456 Cyg	59850.4648	16763	0.0570	V	T. Arranz	0.0001
V466 Cyg	59805.6304	22299.5	0.0089	V	L. Hazel	0.0003
V466 Cyg	59840.4185	22324.5	0.0079	V	T. Arranz	0.0001
V477 Cyg	59808.4388	6655	–0.0475	V	T. Arranz	0.0001
V488 Cyg	59823.5321	54643.5	–0.2710	V	T. Arranz	0.0002
V488 Cyg	59839.5064	54672	–0.2714	V	T. Arranz	0.0002
V548 Cyg	59813.6253	8507	0.0124	V	G. Samolyk	0.0004
V548 Cyg	59824.4570	8513	0.0127	V	T. Arranz	0.0002
V700 Cyg	59810.6389	95591.5	–0.0361	V	T. Arranz	0.0002
V700 Cyg	59829.3832	95656	–0.0375	V	T. Arranz	0.0001
V700 Cyg	59829.5299	95656.5	–0.0361	V	T. Arranz	0.0002
V704 Cyg	59868.4675	38424.5	0.0427	V	T. Arranz	0.0002
V753 Cyg	59818.6516	54630	0.0858	V	L. Hazel	0.0003
V753 Cyg	59823.4128	54640	0.0851	V	T. Arranz	0.0001
V995 Cyg	59465.4118	9311	0.6853	V	T. Arranz	0.0002
V995 Cyg	59810.3764	9408	0.6912	V	T. Arranz	0.0006
V995 Cyg	59817.4887	9410	0.6910	V	T. Arranz	0.0001
V1034 Cyg	59830.5952	17291	0.0223	V	G. Samolyk	0.0004
V1034 Cyg	59839.3888	17300	0.0235	V	T. Arranz	0.0001
V2477 Cyg	59747.8100	26522	0.0025	V	L. Hazel	0.0006
V2477 Cyg	59809.4375	26720	0.0025	V	T. Arranz	0.0001
V2477 Cyg	59809.5941	26720.5	0.0034	V	T. Arranz	0.0001
V2551 Cyg	59812.6457	34461.5	–0.1108	V	T. Arranz	0.0001
V2551 Cyg	59823.5495	34506.5	–0.1116	V	T. Arranz	0.0002
V3135 Cyg	59811.4490	969	–0.0013	V	T. Arranz	0.0002
W Del	59808.6660	3429	–0.0004	V	G. Samolyk	0.0001
TT Del	59843.3979	5089	–0.1457	V	T. Arranz	0.0001
TY Del	59830.6578	14164	0.0915	V	G. Samolyk	0.0001
TY Del	59866.3919	14194	0.0918	V	T. Arranz	0.0001
YY Del	59801.6330	21236	0.0150	V	G. Samolyk	0.0001
YY Del	59813.5296	21251	0.0153	V	T. Arranz	0.0001
YY Del	59820.6679	21260	0.0157	V	L. Hazel	0.0006
FZ Del	59824.6237	36389	–0.0286	V	L. Hazel	0.0003
FZ Del	59865.3505	36441	–0.0289	V	T. Arranz	0.0001
PS Del	59832.3872	9156	–0.0123	V	T. Arranz	0.0002
RZ Dra	59808.6760	28375	0.0764	V	G. Samolyk	0.0002
UZ Dra	59797.7056	5589	0.0035	V	G. Samolyk	0.0001
UZ Dra	59833.5801	5600	0.0037	V	T. Arranz	0.0001
BH Dra	59800.4364	10885	–0.0036	V	T. Arranz	0.0001
S Equ	59811.6880	5010	0.0991	V	L. Hazel	0.0003
S Equ	59818.5586	5012	0.0975	V	T. Arranz	0.0001
S Equ	59842.6113	5019	0.0975	V	G. Samolyk	0.0001
TZ Eri	59974.3180	6738	0.3870	V	T. Arranz	0.0001
YY Eri	59906.8025	56999.5	0.1727	V	G. Samolyk	0.0001
YY Eri	59917.7333	57033.5	0.1727	V	G. Samolyk	0.0001
YY Eri	59976.5675	57216.5	0.1735	V	G. Samolyk	0.0001
RW Gem	59863.8282	14504	0.0018	V	L. Hazel	0.0006
AL Gem	59880.8632	24118	0.1146	V	L. Hazel	0.0003
BD Gem	59910.6943	20100	–0.0524	V	L. Hazel	0.0006
CW Gem	59927.7425	18950	0.3860	V	L. Hazel	0.0006
FG Gem	59893.7562	40032	–0.0199	V	L. Hazel	0.0006
RT Lac	59932.3303	2968	–0.5169	V	T. Arranz	0.0003
RW Lac	59937.2704	3981	–0.0344	V	T. Arranz	0.0002
SW Lac	59840.4785	45414	–0.0882	V	L. Corp	0.0001
SW Lac	59855.5520	45461	–0.0885	V	T. Arranz	0.0001
SW Lac	59856.3547	45463.5	–0.0876	V	T. Arranz	0.0002
SW Lac	59856.5140	45464	–0.0887	V	T. Arranz	0.0001
TW Lac	59819.7101	6031	0.5136	V	L. Hazel	0.0006
VX Lac	59801.8354	13535	0.0904	V	G. Samolyk	0.0001
VX Lac	59867.3795	13596	0.0904	V	T. Arranz	0.0001
AR Lac	59874.7285	9218	–0.0480	V	G. Samolyk	0.0004
AW Lac	59803.6608	29032	0.2234	V	G. Samolyk	0.0002
AW Lac	59857.3753	29079	0.2240	V	T. Arranz	0.0001
CM Lac	59856.6978	20459	–0.0036	V	G. Samolyk	0.0002
CO Lac	59801.6925	20923	0.0122	V	G. Samolyk	0.0002
CO Lac	59845.6166	20951.5	–0.0166	V	G. Samolyk	0.0003
CO Lac	59954.3693	21022	0.0104	V	T. Arranz	0.0002
DG Lac	59813.6490	6936	–0.2578	V	G. Samolyk	0.0002
DG Lac	59824.6865	6941	–0.2530	V	L. Hazel	0.0006
DG Lac	59917.3510	6983	–0.2629	V	T. Arranz	0.0002
GX Lac	59857.3826	3164	–0.0456	V	T. Arranz	0.0002
V479 Lac	58767.6296	21211	–0.0146	V	K. Alton	0.0004
V479 Lac	58767.6297	21211	–0.0145	R	K. Alton	0.0002
V479 Lac	58767.6299	21211	–0.0143	B	K. Alton	0.0002
V479 Lac	58767.8016	21211.5	–0.0155	B	K. Alton	0.0004
V479 Lac	58767.8018	21211.5	–0.0153	V	K. Alton	0.0002
V479 Lac	58767.8020	21211.5	–0.0151	R	K. Alton	0.0002
V479 Lac	58769.7041	21217	–0.0146	B	K. Alton	0.0003
V479 Lac	58769.7041	21217	–0.0146	R	K. Alton	0.0003
V479 Lac	58769.7042	21217	–0.0145	V	K. Alton	0.0002
V479 Lac	58773.6796	21228.5	–0.0153	B	K. Alton	0.0004
V479 Lac	58773.6798	21228.5	–0.0151	V	K. Alton	0.0002
V479 Lac	58773.6800	21228.5	–0.0149	R	K. Alton	0.0003
V479 Lac	58773.8534	21229	–0.0143	R	K. Alton	0.0006

Table continued on next page

Table 1. Recent times of minima of stars in the AAVSO eclipsing binary program, cont.

Star	JD (min) Hel. 2400000 +	Cycle	O–C (day)	F	Observer	Standard Error (day)	Star	JD (min) Hel. 2400000 +	Cycle	O–C (day)	F	Observer	Standard Error (day)
V479 Lac	58773.8535	21229	–0.0143	V	K. Alton	0.0002	RT Per	59910.5996	31239	0.1247	V	L. Hazel	0.0006
V479 Lac	58773.8537	21229	–0.0140	B	K. Alton	0.0005	RT Per	59974.3048	31314	0.1249	V	T. Arranz	0.0001
V505 Lac	59893.3586	18127.5	0.0124	V	T. Arranz	0.0001	RV Per	59851.7727	9022	0.0105	V	G. Samolyk	0.0001
Y Leo	59909.8552	8584	–0.0954	V	G. Samolyk	0.0001	RV Per	59855.7185	9024	0.0093	V	L. Hazel	0.0006
Z Lep	59874.8624	32656	–0.2056	V	G. Samolyk	0.0001	ST Per	59886.5815	6589	0.3260	V	G. Samolyk	0.0001
RR Lep	59843.8272	32189	–0.0467	V	L. Hazel	0.0006	ST Per	59976.6240	6623	0.3258	V	G. Samolyk	0.0001
RR Lep	59875.8637	32224	–0.0502	V	G. Samolyk	0.0003	XZ Per	59816.8361	14162	–0.0837	V	L. Hazel	0.0003
RY Lyn	59884.8451	11845	–0.0308	V	G. Samolyk	0.0002	DK Per	59857.7595	19319	0.0011	V	L. Hazel	0.0003
SW Lyn	59874.8259	24686	0.0868	V	L. Hazel	0.0003	IT Per	59885.6282	19888	–0.0565	V	G. Samolyk	0.0003
RV Lyr	59803.5655	3967	–0.2972	V	T. Arranz	0.0001	IU Per	59874.9067	16643	0.0020	V	G. Samolyk	0.0001
UZ Lyr	59805.4185	8521	–0.0577	V	T. Arranz	0.0001	KW Per	59904.5671	18792	0.0190	V	G. Samolyk	0.0001
BV Lyr	59804.5404	14715	0.0393	V	T. Arranz	0.0002	KW Per	59975.3429	18868	0.0191	V	T. Arranz	0.0001
BV Lyr	59815.5177	14721	0.0388	V	T. Arranz	0.0002	LS Per	59874.6392	7024	–0.7091	V	L. Hazel	0.0006
BV Lyr	59826.4962	14727	0.0393	V	T. Arranz	0.0001	V432 Per	59856.8740	74591.5	0.0627	V	G. Samolyk	0.0001
LZ Lyr	59796.5363	4528	0.0141	V	T. Arranz	0.0001	V432 Per	59956.5348	74901.5	0.0532	V	T. Arranz	0.0003
V589 Lyr	59795.5255	12221	0.414	V	T. Arranz	0.0004	V882 Per	59857.6837	5002	0.0557	V	L. Hazel	0.0009
Beta Lyr	59770.87	833	3.11	B	G. Samolyk	0.03	Y Psc	59941.3610	3799	–0.0288	V	T. Arranz	0.0001
Beta Lyr	59770.87	833	3.11	R	G. Samolyk	0.03	RV Psc	59905.5555	64124	–0.0722	V	G. Samolyk	0.0003
Beta Lyr	59770.87	833	3.11	V	G. Samolyk	0.03	RV Psc	59970.3718	64241	–0.0729	V	T. Arranz	0.0001
Beta Lyr	59777.30	833.5	3.07	R	G. Samolyk	0.04	VZ Psc	59907.3285	61529.5	–0.0005	V	T. Arranz	0.0004
Beta Lyr	59777.32	833.5	3.09	B	G. Samolyk	0.04	GR Psc	59970.3616	17200.5	–0.0127	V	T. Arranz	0.0002
Beta Lyr	59777.40	833.5	3.17	V	G. Samolyk	0.05	RW PsA	59882.5137	70895	–0.1141	V	L. Hazel	0.0006
RW Mon	59934.8924	13774	–0.0961	V	G. Samolyk	0.0001	UZ Pup	59934.8403	19275.5	–0.0123	V	G. Samolyk	0.0001
AT Mon	59907.7862	16412	0.0100	V	L. Hazel	0.0006	V505 Sgr	59837.5987	12999	–0.1394	V	G. Samolyk	0.0001
V502 Oph	59844.3161	25021	0.0010	V	L. Corp	0.0005	CC Ser	59795.4122	43241	1.2181	V	T. Arranz	0.0002
EF Ori	59885.8929	4653	0.0121	V	G. Samolyk	0.0004	RW Tau	59890.7769	5131	–0.3225	V	L. Hazel	0.0003
EF Ori	59906.9442	4666	0.0106	V	G. Samolyk	0.0004	RW Tau	59918.4652	5141	–0.3226	V	T. Arranz	0.0001
EQ Ori	59855.7874	16275	–0.0333	V	L. Hazel	0.0003	RZ Tau	59917.7668	53506	0.1093	V	G. Samolyk	0.0001
ER Ori	59885.8611	43125.5	0.1655	V	G. Samolyk	0.0001	AC Tau	59915.7969	6988	0.2352	V	L. Hazel	0.0006
ET Ori	59975.5808	35009	–0.0066	V	G. Samolyk	0.0004	AH Tau	59977.3193	86916	–0.0038	V	T. Arranz	0.0001
FR Ori	59906.8703	36284	0.0551	V	G. Samolyk	0.0001	AM Tau	59881.7141	7157	–0.0813	V	L. Hazel	0.0006
FZ Ori	59932.7049	39772	–0.0205	V	G. Samolyk	0.0002	CT Tau	59855.8307	21672	–0.0746	V	L. Hazel	0.0006
GU Ori	59881.8462	35718.5	–0.0761	V	G. Samolyk	0.0005	CT Tau	59881.8354	21711	–0.0762	V	G. Samolyk	0.0002
GU Ori	59885.8484	35727	–0.0747	V	G. Samolyk	0.0002	EQ Tau	59822.8859	57447.5	–0.0559	V	G. Samolyk	0.0002
GU Ori	59906.7924	35771.5	–0.0760	V	G. Samolyk	0.0003	EQ Tau	59874.7702	57599.5	–0.0566	V	K. Menzies	0.0003
U Peg	59840.5075	62247	–0.1810	V	L. Corp	0.0002	V Tri	59881.5857	60504	–0.0050	V	G. Samolyk	0.0001
U Peg	59851.5642	62276.5	–0.1803	V	G. Samolyk	0.0001	X Tri	59906.6869	17914	–0.1157	V	G. Samolyk	0.0001
U Peg	59863.7437	62309	–0.1812	V	G. Samolyk	0.0001	X Tri	59907.6585	17915	–0.1156	V	L. Hazel	0.0003
U Peg	59893.5393	62388.5	–0.1807	V	G. Samolyk	0.0001	RS Tri	59881.5973	11494	–0.0583	V	G. Samolyk	0.0001
U Peg	59914.5262	62444.5	–0.1816	V	G. Samolyk	0.0001	RV Tri	59842.6869	18323	–0.0520	V	L. Hazel	0.0006
U Peg	59932.3288	62492	–0.1811	V	T. Arranz	0.0002	RV Tri	59885.6458	18380	–0.0521	V	G. Samolyk	0.0001
TY Peg	59845.6852	6272	–0.5026	V	G. Samolyk	0.0001	ZZ UMa	59909.7716	10420	–0.0016	V	G. Samolyk	0.0001
TY Peg	59901.3426	6290	–0.5052	V	T. Arranz	0.0003	AF UMa	59903.8888	6297	0.6650	V	G. Samolyk	0.0003
UX Peg	59822.7844	12558	0.0051	V	G. Samolyk	0.0002	W UMi	59801.6628	15354	–0.2340	V	G. Samolyk	0.0004
UX Peg	59836.6873	12567	0.0065	V	L. Hazel	0.0003	RU UMi	59917.8197	34903	–0.0153	V	G. Samolyk	0.0001
UX Peg	59861.4004	12583	0.0057	V	T. Arranz	0.0001	Z Vul	59800.5813	6865	–0.0183	V	T. Arranz	0.0003
UX Peg	59918.5513	12620	0.0058	V	G. Samolyk	0.0002	RR Vul	59844.4106	4912	–0.0648	V	T. Arranz	0.0001
BB Peg	59856.7423	44515.5	–0.0378	V	G. Samolyk	0.0001	RS Vul	59844.4071	6038	0.0179	V	T. Arranz	0.0004
BB Peg	59863.6107	44534.5	–0.0380	V	G. Samolyk	0.0002	AW Vul	59842.6764	16811	–0.0433	V	G. Samolyk	0.0002
BB Peg	59905.5446	44650.5	–0.0383	V	G. Samolyk	0.0001	BE Vul	59808.4718	12691	0.1004	V	T. Arranz	0.0001
BG Peg	59874.6206	7346	–2.5785	V	G. Samolyk	0.0003	BE Vul	59842.6167	12713	0.1003	V	G. Samolyk	0.0001
BX Peg	59801.6290	55653.5	–0.1471	V	G. Samolyk	0.0002	BE Vul	59842.6175	12713	0.1011	V	L. Hazel	0.0006
BX Peg	59801.7677	55654	–0.1486	V	G. Samolyk	0.0001	BE Vul	59856.5850	12722	0.1002	V	G. Samolyk	0.0001
BX Peg	59849.4387	55824	–0.1491	V	T. Arranz	0.0001	BO Vul	59824.3836	12249	0.0032	V	T. Arranz	0.0001
BX Peg	59858.4129	55856	–0.1484	V	T. Arranz	0.0002	BO Vul	59851.6264	12263	0.0039	V	G. Samolyk	0.0001
BX Peg	59858.5523	55856.5	–0.1492	V	T. Arranz	0.0003	BS Vul	59793.4606	34712	–0.0391	V	T. Arranz	0.0001
DI Peg	59800.8552	20517	0.0219	V	G. Samolyk	0.0001	BT Vul	59797.6194	21377	0.0070	V	G. Samolyk	0.0003
EU Peg	59954.3397	36017	0.0517	V	T. Arranz	0.0002	BT Vul	59828.4324	21404	0.0076	V	T. Arranz	0.0002
GP Peg	59822.8117	19049	–0.0617	V	G. Samolyk	0.0001	BU Vul	59796.7040	46157	0.0111	V	G. Samolyk	0.0001
GP Peg	59914.5192	19143	–0.0623	V	G. Samolyk	0.0002	BU Vul	59808.6531	46178	0.0113	V	G. Samolyk	0.0001
GP Peg	59921.3489	19150	–0.0619	V	T. Arranz	0.0002	BU Vul	59823.4471	46204	0.0115	V	T. Arranz	0.0001
KW Peg	59801.6802	14261.5	0.2523	V	G. Samolyk	0.0004	BU Vul	59874.6553	46294	0.0104	V	G. Samolyk	0.0001
KW Peg	59849.4403	14320	0.2540	V	T. Arranz	0.0001	CD Vul	59801.7816	19749	–0.0034	V	G. Samolyk	0.0001
KW Peg	59858.4201	14331	0.2535	V	T. Arranz	0.0002	CD Vul	59886.5655	19873	–0.0039	V	G. Samolyk	0.0001
RT Per	59875.7736	31198	0.1241	V	G. Samolyk	0.0002	V495 Vul	59818.5018	2048	0.0212	V	T. Arranz	0.0003
RT Per	59875.7753	31198	0.1258	V	L. Hazel	0.0003							

Minima of 126 Eclipsing Binary Stars

Stephen P. Cook
Project Worldview, 910 Oak Terrace Drive, Prescott, AZ 86301; scook@projectworldview.org

Received April 16, 2023; accepted May 22, 2023

Abstract Previously unpublished times of minima for 126 eclipsing binary stars are reported based on the author's CCD photometry—typically conducted in the 2015–2023 time frame.

1. Presenting the TOM and accompanying data

The accompanying list (Table 1) contains times of minima (TOM) for 126 eclipsing binary (EB) stars derived from CCD observations made by the author, nearly all using a 130-mm f/5 reflector with ST6 CCD imager and V filter. An observed TOM (and associated mean error) was the end result of applying the method of Kwee and van Woerden (1956) and making a heliocentric correction. The raw data starting point for this are all available online, identified by observer code CK in the AAVSO International Database (Kafka 2015–2023).

Table 1 will be web-archived and made available through the AAVSO ftp site at:
ftp://ftp.aavso.org/public/datasets/3885-Cook-511-eb126.txt.

Using the linear elements (epoch and period) and associated cycle number (all presented in Table 1), a computed TOM was determined, and subtracted from the observed TOM to get the O–C values also displayed there. The elements used (for all of the stars except four) are from the Krakow Astronomica group's TIDAK database (Kreiner 2004).

These elements provide the historical average ephemeris presented in the lower left corners of the O–C diagrams found on the webpages for thousands of EB stars on this website. Note sometimes these have an epoch similar, if not identical to, that given in the *General Catalogue of Variable Stars* (GCVS; Kholopov *et al.* 1985). They are not to be confused with current best prediction ephemeris elements also found in the TIDAK database web pages and referred to as the light elements. The four stars which are exceptions—where the elements used are from the AAVSO Variable Star Index (VSX; Watson *et al.* 2014)—are V1811 Aql, V830 Cep, V667 Ser, and V1417 Tau.

2. Acknowledgements

The author wishes to thank Gerry Samolyk for helping him appreciate some of the fine points in applying the method of Kwee and van Woerden, and Lew Cook for putting together the heliocentric correction calculation spreadsheet, which he has made heavy use of.

References

Kafka, S. 2015–2023, Observations from the AAVSO International Database (https://www.aavso.org/data-download).

Kholopov, P. N. *et al.* 1985, *General Catalogue of Variable Stars*, 4th Ed. Moscow

Kreiner, J. M. 2004, *Acta Astron.*, **54**, 207 (https://www.as.up.krakow.pl/ephem/).

Kwee, K. K., and van Woerden, H. 1956, *Bull. Astron. Inst. Netherlands*, **12**, 327.

Watson, C., Henden, A. A., and Price, C. A. 2014, AAVSO International Variable Star Index VSX (Watson+, 2006–2014; https://www.aavso.org/vsx).

Table 1. Recent times of minima of stars in the AAVSO eclipsing binary program.

Star	*Heliocentric Min.* JD 2400000+	*Mean Error* (d)	*Cycle*	*O–C,* (d)	*Epoch* JD 2400000+	*Period* (d)
AP And	59209.6911	0.0005	20566	0.0046	26565.4660	1.5872907
QX And	59924.7004	0.0008	31877.5	0.0631	46785.7432	0.41216827
ST Aqr	59892.6678	0.0017	23888	–0.1969	41236.2786	0.78100243
BX Aqr	59838.7880	0.0024	22217	0.1744	25855.3749	1.5296052
EE Aqr	59131.7629	0.0004	35959	–0.0025	40828.7802	0.508995945
EL Aqr	59527.8411	0.0013	23687.5	0.0041	48124.6444	0.48140127
V 889 Aql	59093.7614	0.0013	1875	0.7900	38241.5539	11.120756
V889 Aql	59842.7884	0.0067	1942.5	–0.8340	38241.5539	11.120756
V1719 Aql	59449.7596	0.0047	1843.5	–0.0672	51421.7530	4.3548
V1719 Aql	59460.6617	0.0041	1846	–0.0521	51421.7530	4.3548
V1811 Aql	59435.7873	0.0022	1846	–0.0007	53153.8500	3.403
TX Ari	59978.7458	0.0030	11730	0.0842	28409.4053	2.6913262
WW Aur	58897.7025	0.0041	6930	0.0138	41399.3043	2.525019399
GI Aur	59984.6687	0.0022	27890	–0.0010	26297.5048	1.20785819
HL Aur	59983.7279	0.0017	19390	–0.0063	47913.3495	0.622505659
V364 Aur	59616.6825	0.0023	29709	0.0068	38849.3589	0.69902443
V364 Aur	59983.6691	0.0015	30234	0.0056	38849.3589	0.69902443
MT Boo	59045.6840	0.0040	20883	0.0484	51416.4378	0.36533055
S Cnc	59292.5489	0.0043	2352	–0.0919	36985.0310	9.484528
SW Cnc	59347.6931	0.0010	16036	–0.0262	30495.6503	1.7992061
TX Cnc	59292.7538	0.0012	64945	0.0135	34426.4633	0.382882085
VZ CVn	59334.7041	0.0011	24279	0.0003	38880.5821	0.842461458
VZ CVn	59703.6998	0.0007	24717	–0.0022	38880.5821	0.842461458
GG CVn	59708.7750	0.0008	16080.5	–0.0163	53502.5511	0.38594821
AF Cap	59157.6899	0.0026	3522	0.0356	38252.4046	5.9356189
TV Cas	59891.6797	0.0012	9295	–0.1238	43043.6189	1.81260727
XX Cas	59178.7492	0.0011	7385	0.0147	36527.6220	3.0671784
CR Cas	59163.7306	0.0018	6562	0.2350	40526.2180	2.8401825
CR Cas	59200.6107	0.0019	6575	0.1928	40526.2180	2.8401825
DN Cas	59173.6559	0.0022	7696	–0.0001	41388.5640	2.3109527
DO Cas	59216.6656	0.0011	36938	0.0168	33926.4585	0.684665936
DZ Cas	59922.6158	0.0021	40118	–0.0308	28434.5740	0.7848864
V380 Cas	59202.6485	0.0009	1397	0.0003	55410.4377	2.71453867
V520 Cas	59932.7443	0.0035	38271	0.0088	41186.3670	0.48983221
V520 Cas	59935.6839	0.0021	38277	0.0094	41186.3670	0.48983221
V523 Cas	59813.9279	0.0003	79564.5	0.0721	41220.3880	0.2336905
V541 Cas	59522.7072	0.0006	14904	0.0053	45962.3067	0.90984938
V559 Cas	59610.7115	0.0016	11548	0.0068	41357.5595	1.58063259
V1112 Cas	59140.6914	0.0016	3646	0.0018	51378.6320	2.12892419
V1112 Cas	59206.6871	0.0014	3677	0.0009	51378.6320	2.12892419
V1141 Cas	59267.4195	0.0041	1118	0.4622	51542.5020	6.9091729
V1160 Cas	59144.7573	0.0015	3588	0.0024	51490.8753	2.13318828
SU Cep	59431.6766	0.0017	36727.5	–0.0059	26325.4637	0.901401369
WX Cep	59136.6082	0.0015	10078	0.0096	25088.5362	3.3784543
XZ Cep	59124.7288	0.0005	6492	–0.0385	26033.4391	5.0972471
AI Cep	59431.7336	0.0020	7782	0.0650	26550.2890	4.2253122
CQ Cep	59822.6930	0.0028	16674	–0.0873	32456.6654	1.64124475
CW Cep	59220.6778	0.0010	6431	0.0052	41669.5719	2.7291402
EG Cep	59124.7508	0.0005	24869	0.0107	45580.5475	0.544621521
FS Cep	59870.7048	0.0029	24445	0.0795	26930.4500	1.347522
GI Cep	59109.6623	0.0019	21427	–0.0716	36875.4104	1.03767786
GI Cep	59112.7782	0.0012	21430	–0.0687	36875.4104	1.03767786
GW Cep	59867.6831	0.0007	66541.5	0.0164	38652.1923	0.31883072
IP Cep	59873.7538	0.0046	25655	–0.0043	36812.4193	0.89890231
V358 Cep	59872.6787	0.0029	30944	–0.0808	45241.4702	0.47283122
V711 Cep	59220.6701	0.0028	6276	–0.0112	51034.5337	1.30435749
V800 Cep	59872.8061	0.0030	6885	–0.0021	51486.5470	1.2180481
V830 Cep	59870.6445	0.0067	32850.5	–0.0118	51325.6500	0.260118
V898 Cep	59123.6978	0.0016	2699.5	–0.2957	51363.5464	2.874772
V919 Cep	59116.6826	0.0011	4223	–0.0206	51295.7840	1.8519818
V922 Cep	59117.6276	0.0007	2101	–0.1423	51606.7550	3.5749714
V957 Cep	59429.7582	0.0012	3985	–0.0808	51504.7300	1.988735
EK Com	59344.7605	0.0013	37294	–0.0150	49398.9783	0.266686256
WZ Cyg	59142.7104	0.0007	31340	0.0266	40825.4880	0.584467
CV Cyg	59134.7086	0.0013	35265	–0.1577	24454.4669	0.98342264
V366 Cyg	59798.8519	0.0024	23092	0.0044	34489.5930	1.0960183
V370 Cyg	59882.6530	0.0016	32604	–0.0128	34629.4740	0.77454275
V753 Cyg	59518.6524	0.0017	27000	–0.0018	33804.4633	0.95237744

Table continued on next page

Table 1. Recent times of minima of stars in the AAVSO eclipsing binary program, cont.

Star	Heliocentric Min. JD 2400000+	Mean Error (d)	Cycle	O–C, (d)	Epoch JD 2400000+	Period (d)
V787 Cyg	59515.6992	0.0006	28170	–0.0019	16457.4260	1.52851527
V859 Cyg	59530.5842	0.0019	61484	0.0689	34629.4141	0.40500132
V1061 Cyg	59102.7849	0.0021	13955	–0.0118	26355.2150	2.3466558
AL Del	59878.6447	0.0039	22936	–0.0107	25807.5191	1.48548728
LS Del	59826.6619	0.0042	33081	0.0196	47790.4317	0.36384059
RR Dra	59837.6100	0.0026	15121	0.5692	17026.3840	2.8312054
RZ Dra	57973.7132	0.0008	25044	0.0098	44177.5609	0.55087616
SX Dra	59769.6263	0.0079	2914	0.5404	44705.6607	5.1693292
AR Dra	59706.7506	0.0011	24914	0.0257	42868.9122	0.67583739
AU Dra	59828.6658	0.0011	17580	–0.0345	50770.3112	0.51526673
BE Dra	59830.7043	0.0009	45002	0.0235	36317.3829	0.52249451
BF Dra	59361.8889	0.0024	1078	0.1033	47276.3491	11.21098
BS Dra	59364.7019	0.0009	5322	0.0112	41461.4248	3.36401088
V391 Dra	59769.6797	0.0030	6869	–0.0073	51310.7020	1.23147256
V441 Dra	59136.7674	0.0017	2684	–0.0092	51338.6830	2.9054
BZ Eri	60003.6329	0.0020	25848	–0.0031	42836.1697	0.664170006
AY Gem	59994.7288	0.0030	7651	–0.0116	36631.3219	3.05364246
LT Her	57975.6807	0.0020	15885	–0.0002	40755.7797	1.08403533
RX Hya	59348.6401	0.0013	6969	0.3520	43447.7480	2.28161
FW Hya	58607.6838	0.0016	16314	–0.0045	51982.0292	0.40613333
VY Lac	59139.6617	0.0005	23653	–0.0025	34629.3871	1.036243903
CN Lac	59523.7848	0.0039	11657.5	–0.0316	52093.8126	0.63735825
V Lep	59279.7061	0.0019	37758.5	0.1415	18873.6810	1.07011358
Y Leo	57874.6742	0.0004	14344	–0.0737	33689.4880	1.68608895
RW Leo	59377.8170	0.0069	9541	–0.0362	43324.7374	1.68254017
AG Leo	59684.6124	0.0056	9737	0.1050	26651.5918	3.3925147
AL Leo	59732.7347	0.0013	7417	0.0038	47824.6206	1.60551575
DU Leo	59685.6901	0.0008	8250	0.0098	48348.6580	1.37418452
EX Leo	59711.6964	0.0025	27439	0.0122	48499.9966	0.40860409
RZ Lyn	59691.7104	0.0014	29687	–0.0475	25643.3519	1.14691299
UV Lyn	59690.6657	0.0013	46795	0.0938	40271.5304	0.41498112
CD Lyn	60036.6739	0.0047	2432	–0.0168	54504.5210	2.27474081
UZ Lyr	57974.6718	0.0004	7553	–0.0166	43689.9496	1.89126689
EW Lyr	57630.8227	0.0005	15975	–0.0255	26499.6986	1.94874176
PR Mon	60026.7274	0.0037	3169	–0.0868	51870.6227	2.573743
VY Mic	59150.6111	0.0023	1563	–0.0421	52216.5600	4.4364
RV Oph	59817.7651	0.0015	9715	–0.0034	23997.3830	3.68712152
ER Ori	57443.6640	0.0005	33899.5	0.0721	43090.5353	0.423400246
EW Ori	60021.6744	0.0004	4682	–0.0925	27543.4670	6.9368432
DF Peg	59169.6680	0.0043	1746	–0.1010	33505.6467	14.69881
ER Peg	59181.5448	0.0012	6003	–0.0504	45526.5879	2.2746972
GH Peg	59171.6293	0.0012	12724	0.0009	26647.3450	2.5561367
KL Per	59629.6659	0.0018	10701	–0.0113	35840.3580	2.2230931
NZ Per	59607.6530	0.0026	33436	–0.0121	28247.3520	0.9379206
V427 Per	59620.6679	0.0029	7927	0.0189	37345.3430	2.810055
AQ Psc	59930.7234	0.0015	20179	–0.0858	50333.4784	0.47560983
DV Psc	59971.6267	0.0007	27614	–0.0091	51451.7177	0.308536181
RZ Pyx	58587.6192	0.0022	18384.5	0.0150	46522.3407	0.656273684
TX Pyx	58612.6690	0.0021	17969	–0.2458	48500.6294	0.56276284
CU Sge	59847.6705	0.0009	21744	–0.0020	42633.4813	0.79167546
CW Sge	59847.7932	0.0045	33840	0.0683	37501.1608	0.66035946
RS Sct	59166.6209	0.0016	22175	–0.0367	44437.1717	0.664238371
RS Sct	59170.6051	0.0008	22181	–0.0379	44437.1717	0.664238371
RS Sct	49573.7207	0.0014	7733	–0.0063	44437.1717	0.664238371
V667 Ser	59877.6512	0.0012	2248	0.0044	57681.5070	0.9769305
RZ Tau	57428.6806	0.0008	47518	0.1047	37676.5928	0.415673705
AH Tau	59978.6423	0.0017	84636.5	–0.0589	31822.3653	0.33267368
GW Tau	59635.6886	0.0007	66636	–0.1400	16900.2260	0.64132905
V1130 Tau	59661.7031	0.0007	8816.5	0.0077	52618.4781	0.798867726
V1241 Tau	59250.6587	0.0008	38528	0.0044	27531.6838	0.823270623
V1417 Tau	59970.7240	0.0013	5726	0.0179	54439.7050	0.965945
UX UMa	58637.7133	0.0008	159131	–0.0061	27341.2240	0.196671267
CX Vir	59372.7347	0.0014	44607	0.0357	26092.4440	0.74607696
DM Vir	59737.7841	0.0023	4315	–0.0002	39589.1817	4.66943281
FQ Vir	59792.7328	0.0008	10525	0.0124	51903.1506	0.74960283
AW Vul	59433.8079	0.0009	16304	–0.0296	46285.4605	0.806450989
BT Vul	59434.7185	0.0015	21059	0.0127	35402.1750	1.1412
CD Vul	59451.7040	0.0010	19237	–0.0074	46298.5050	0.6837452